



5-2000

## Heteroepitaxial growth of oxides via solution chemical techniques

Jonathan Sherman Morrell

Follow this and additional works at: [https://trace.tennessee.edu/utk\\_graddiss](https://trace.tennessee.edu/utk_graddiss)

---

### Recommended Citation

Morrell, Jonathan Sherman, "Heteroepitaxial growth of oxides via solution chemical techniques. " PhD diss., University of Tennessee, 2000.  
[https://trace.tennessee.edu/utk\\_graddiss/8354](https://trace.tennessee.edu/utk_graddiss/8354)

This Dissertation is brought to you for free and open access by the Graduate School at TRACE: Tennessee Research and Creative Exchange. It has been accepted for inclusion in Doctoral Dissertations by an authorized administrator of TRACE: Tennessee Research and Creative Exchange. For more information, please contact [trace@utk.edu](mailto:trace@utk.edu).

To the Graduate Council:

I am submitting herewith a dissertation written by Jonathan Sherman Morrell entitled "Heteroepitaxial growth of oxides via solution chemical techniques." I have examined the final electronic copy of this dissertation for form and content and recommend that it be accepted in partial fulfillment of the requirements for the degree of Doctor of Philosophy, with a major in Chemistry.

Ziling Ben Xue, Major Professor

We have read this dissertation and recommend its acceptance:

David B. Beach, J. L. Adcock, Robert J. Hinde, Joseph E. Spruiell

Accepted for the Council:

Carolyn R. Hodges

Vice Provost and Dean of the Graduate School

(Original signatures are on file with official student records.)

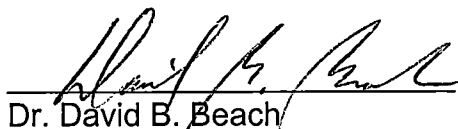
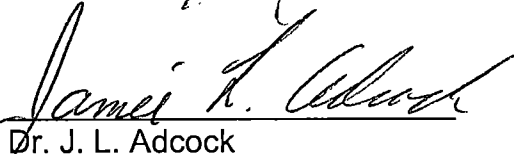
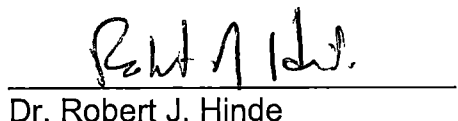
To the Graduate Council:

I am submitting herewith a dissertation written by Jonathan Sherman Morrell entitled "Heteroepitaxial Growth of Oxides via Solution Chemical Techniques." I have examined the final copy of this dissertation for form and content and recommend that it be accepted in partial fulfillment of the requirements for the degree of Doctor of Philosophy, with a major in Chemistry.




Dr. Ziling Ben Xue, Major Professor

We have read this dissertation  
and recommend its acceptance:

  
Dr. David B. Beach  
Dr. J. L. Adcock  
Dr. Robert J. Hinde  
Dr. Joseph E. Spruiell

Accepted for the Council:

  
Associate Vice Chancellor and  
Dean of The Graduate School

**HETEROEPITAXIAL GROWTH OF OXIDES VIA SOLUTION CHEMICAL  
TECHNIQUES**

A Dissertation

Presented for the

Doctor of Philosophy Degree

The University of Tennessee, Knoxville

Jonathan Sherman Morrell

May 2000

This Dissertation is dedicated to my parents

Eli Jonathan and Sara Lee O'Dell Morrell

and to my grandparents

Edward Jonathan and Ruth Morrell

and

Webb and Sara Bertha O'Dell.

## ACKNOWLEDGMENTS

Many people provided technical assistance in the progress of this work. First of all I would like to thank Dr. David B. Beach [Chemical and Analytical Sciences Division, Oak Ridge National Laboratory (ORNL)], for his expert guidance during the course of this work. I also thank Dr. Ziling Ben Xue for his support in allowing me to have the opportunity to work at ORNL. Special thanks go to my committee for their careful reading of this dissertation.

For technical assistance, I wish to thank Dr. Eliot Specht (Metals and Ceramics Division, ORNL) for help with the x-ray diffraction experiments; Dr. M. Parans Paranthaman (Chemical and Analytical Sciences Division, ORNL), Dr. Dominic Lee, Dr. John Mathis and Dr. Pinwong Pon (Metals and Ceramics Division, ORNL), for deposition of yttrium barium copper oxide, cerium oxide and yttrium stabilized zirconium films; Dr. Catherine E. Vallet (Chemical and Analytical Sciences Division, ORNL) for atomic force microscopy measurements; Dr. Thomas Chirayil (Chemical and Analytical Sciences Division, ORNL), for assistance with scanning electron microscopy; and Mr. Patrick M. Martin (Metals and Ceramics Division, ORNL), for critical current and critical temperature measurements on the superconducting films.

Finally, I am inexpressibly grateful to my parents, Mr. and Mrs. Eil Jonathan Morrell, for their support and patience through these years of higher education. I would also like to thank the following for their support: my

brothers, Benjamin and Andrew Morrell; my grandparents, Mr. and Mrs. Webb O'Dell and Mr. and Mrs. Edward Jonathan Morrell; and my friends, Bill V. Blevins and Chris Harris. At last, put in chief place, I would like to thank Holly C. Dorman for all her love, encouragement, support, and understanding through these last few years at UT.

This work was supported by the U. S. Department of Energy, Division of Basic Energy Sciences, Office of Science, under contract No. DE-AC05-96OR22464, and was performed at the Oak Ridge National Laboratory.

## ABSTRACT

An all-alkoxide solution chemistry utilizing methoxyethoxide-metal complexes in 2-methoxyethanol was developed to deposit epitaxial thin-films of metal oxides on single-crystal oxide and textured metal substrates. The speciation within these solutions was studied using Nuclear Magnetic Resonance (NMR) spectroscopy. Film precursor gels were studied using IR spectroscopy and thermal analysis. Approximate temperature ranges for film crystallization were determined from powders prepared from the film coating solutions. Film structure was determined using X-ray diffraction and film morphology was studied using scanning electron microscopy (SEM), and atomic force microscopy (AFM).

A number of technologically interesting systems were prepared using this general technique. Bismuth-containing ferroelectric materials of the general formula  $(\text{Sr or Ba})\text{Bi}_2(\text{Nb or Ta})_2\text{O}_9$  were synthesized. Films were deposited on polycrystalline silver, (100) strontium titanate, and (100) lanthanum aluminate single-crystal oxide substrates by spin coating techniques. Excellent epitaxy was achieved on the oxide substrates.

Several systems which may be used for buffer layers for superconducting thin-films were synthesized. Rare earth gallates and rare-earth aluminates (where Ln = La, Pr, Nd, Gd, Y) were synthesized. The crystallization of powders under reducing and oxidizing conditions, deposition of polycrystalline films on silver substrates, deposition of epitaxial films on single crystal oxide substrates



using solution deposition was studied. In addition, rare-earth aluminates were deposited on roll-textured nickel using spin-coating and dip-coating techniques. Tetragonal perovskites in the general form  $ABCO_4$  (where A = Sr; B = La or Pr; C = Al or Ga) were prepared on single crystal oxide substrates. Chemical solution epitaxy was used to deposit films of rare-earth oxides (Ln = Sm, Eu, Gd, Tb, Dy, Ho, Er, Tm, Yb, and Lu) on roll-textured nickel.

Superconducting thin-films of yttrium barium copper oxide (YBCO) were grown on several solution-deposited buffer layers. The high critical currents and transition temperatures of the YBCO thin-films were measured and found satisfactory, thus demonstrating the viability of the technique.

## TABLE OF CONTENTS

CHAPTER	PAGE
1: INTRODUCTION .....	1
1.1. Thin-Films .....	1
1.1.1. Importance and Significance to Industry .....	1
1.1.2. Physical Methods of Deposition .....	1
1.1.3. Chemical Methods of Deposition .....	2
1.2. Epitaxial Films .....	3
1.2.1. Definition of Epitaxy .....	3
1.3. Solution Routes versus Physical Routes .....	6
1.3.1. Utility .....	6
1.3.2. Cost of Solution Routes versus Physical Routes .....	6
1.3.3. Advantages of Solution Routes .....	7
1.3.4. Disadvantages of Solution Routes .....	8
1.4. Solution Based Growth Techniques .....	9
1.5. Coating Methods .....	13
1.5.1. Spin-Coating .....	13
1.5.2. Dip-Coating .....	14
1.6. Characterization of Powders and Thin-Films .....	16
1.6.1. X-Ray Diffraction .....	16

1.6.2. Analysis Techniques for Film Thickness and Surface	
Structure .....	19
1.7. Materials and Substrates .....	20
1.7.1. Single Crystal Oxide Substrates .....	20
1.7.2. Ferroelectrics .....	22
1.7.3. High Temperature Superconductors .....	23
1.7.4. Nickel Substrates .....	25
1.7.5. Buffer Layers .....	26
2. EPITAXIAL GROWTH OF BISMUTH CONTAINING FERROELECTRIC	
MATERIALS .....	28
2.1. Introduction .....	28
2.2. Experimental Details .....	32
2.2.1. General Procedures .....	32
2.2.2. Solution Preparation of Strontium and Barium 2-	
Methoxyethoxide .....	32
2.2.3. Solution Preparation of Niobium and Tantalum 2-	
Methoxyethoxide .....	32
2.2.4. Solution Preparation of Bismuth 2-Methoxyethoxide .....	33
2.2.5. Powder and Film Preparation .....	34
2.2.6. Preparation for Electrical Characterization .....	36

2.3. Results and Discussion .....	36
2.3.1. Analysis of NMR Data .....	36
2.3.2. XRD Analysis of Bismuth Containing Perovskite Powders ..	43
2.3.3. XRD Analysis of Bismuth Containing Perovskite Films on Silver Substrates .....	50
2.3.4. Electrical Characterization .....	53
2.3.5. XRD Analysis of Bismuth Containing Perovskite Films on Strontium Titanate and Lanthanum Aluminate .....	55
2.3.6. Out-of-Plane and In-Plane Texture Analysis of Bismuth Containing Perovskites on Strontium Titanate and Lanthanum Aluminate .....	59
2.4. Conclusion .....	63
3. EPITAXIAL GROWTH OF RARE-EARTH GALLATES AND AA'GaO <sub>3</sub> MIXED METAL OXIDE THIN-FILMS .....	65
3.1. Introduction .....	65
3.2. Experimental Details .....	67
3.2.1. General Procedures .....	67
3.2.2. Preparation of Gallium Isopropoxide .....	67
3.2.3. Preparation of Rare-Earth Isopropoxides .....	68
3.2.4. Preparation of Methoxyethoxide Solutions .....	69

3.2.5. Powder and Film Preparation . . . . .	71
3.2.6. Application of Yttrium Barium Copper Oxide Superconductor . . . . .	72
3.2.7. Critical Current and Critical Temperature Measurements . . . . .	73
3.3. Results and Discussion . . . . .	74
3.3.1. XRD Analysis of Rare-Earth Gallate Powders . . . . .	74
3.3.2. XRD Analysis of Rare-Earth Gallate Films on Silver Substrates . . . . .	81
3.3.3. XRD Analysis of Rare-Earth Gallate Films on Strontium Titanate and Lanthanum Aluminate . . . . .	81
3.3.4. Out-of-Plane and In-Plane Texture Analysis of Rare-Earth Gallates on Strontium Titanate and Lanthanum Aluminate . . . . .	88
3.3.5. Analysis of $\text{YBa}_2\text{Cu}_3\text{O}_{7.5}$ PLD Film on Solution Deposited $\text{NdGaO}_3$ on (100) Strontium Titanate . . . . .	93
3.4. Conclusion . . . . .	96
4. EPITAXIAL GROWTH OF RARE-EARTH ALUMINATES AND $\text{A}_x\text{A}'_{(1-x)}\text{B}_y\text{B}'_{(1-y)}\text{O}_3$ MIXED METAL OXIDE THIN-FILMS . . . . .	100
4.1. Introduction . . . . .	100
4.2. Experimental Details . . . . .	102
4.2.1. General Procedures . . . . .	102
4.2.2. Preparation of Rare-Earth Isopropoxides . . . . .	103

4.2.3. Preparation of Gallium Isopropoxide .....	103
4.2.4. Preparation of Methoxyethoxide Solutions .....	104
4.2.5. Powder and Film Preparation .....	107
4.3. Results and Discussion .....	108
4.3.1. NMR Study of Lanthanum Aluminum 2-Methoxyethoxide Solution .....	108
4.3.2. Gelation and Crystallization .....	108
4.3.3. XRD Analysis of Rare-Earth Aluminate Powders .....	113
4.3.4. XRD Analysis of Rare-Earth Aluminate Films on Silver Substrates .....	124
4.3.5. XRD Analysis of Rare-Earth Aluminate Films on Strontium Titanate and Lanthanum Aluminate .....	126
4.3.6. Out-of-Plane and In-Plane Texture Analysis of Rare-Earth Aluminates on Strontium Titanate and Lanthanum Aluminate .....	129
4.3.7. Analysis of Rare-Earth Aluminate Films on Roll-Textured Nickel .....	135
4.4. Conclusion .....	137
5. EPITAXIAL GROWTH OF TETRAGONAL PEROVSKITE (ABCO <sub>4</sub> ) THIN-FILMS .....	141

5.1. Introduction .....	141
5.2. Experimental Details .....	143
5.2.1. General Procedures .....	143
5.2.2. Preparation of Gallium Isopropoxide .....	144
5.2.3. Preparation of Lanthanum and Praseodymium Isopropoxide .....	145
5.2.4. Preparation of Methoxyethoxide Solutions .....	146
5.2.5. Powder and Film Preparation .....	146
5.2.6. Deposition of Yttrium Barium Copper Oxide Superconductor .....	147
5.2.7. Critical Current and Critical Temperature Measurements ...	148
5.3. Results and Discussion .....	149
5.3.1. XRD Analysis of Tetragonal Perovskite Powders .....	149
5.3.2. XRD Analysis of Tetragonal Perovskite Films on Silver Substrates .....	155
5.3.3. XRD Analysis of Tetragonal Perovskite Films on Strontium Titanate and Lanthanum Aluminate .....	155
5.3.4. Out-of-Plane and In-Plane Texture Analysis of Tetragonal Perovskites on Strontium Titanate and Lanthanum Aluminate .....	162

5.3.5. Analysis of YBCO PLD Film on Solution Deposited Strontium Praseodymium Gallate on (100) Strontium Titanate and Strontium Lanthanum Gallate on (100) Lanthanum Aluminate .....	166
5.4. Conclusion .....	169
 6. EPITAXIAL GROWTH OF RARE-EARTH OXIDES ( $\text{Ln}_2\text{O}_3$ and $\text{CeO}_2$ ) ON ROLL-TEXTURED NICKEL .....	 171
6.1. Introduction .....	171
6.2. Experimental Details .....	176
6.2.1. General Procedures .....	176
6.2.2. Preparation of Rare-Earth Isopropoxides .....	176
6.2.3. Preparation of Rare-Earth Acetates .....	177
6.2.4. Preparation of Methoxyethoxide Solutions .....	177
6.2.5. Preparation of Substrates and Films .....	178
6.2.6. Application of Yttrium Barium Copper Oxide Superconductor .....	179
6.2.7. Critical Current and Critical Temperature Measurements ...	180
6.3. Results and Discussion .....	181
6.3.1. Study of the Coating Solutions .....	181



6.3.2. XRD Analysis of Rare-Earth Oxide Films on Roll-Textured Nickel .....	183
6.3.3. Out-of-Plane and In-Plane Texture Analysis of Rare-Earth Oxides on Nickel .....	194
6.3.4. Film Morphology and Surface Structure .....	196
6.3.5. Analysis of $\text{YBa}_2\text{Cu}_3\text{O}_{7-\delta}$ PLD Film on Solution Deposited Rare- Earth Oxide Buffer Layers on Roll-Textured Nickel .....	204
6.4. Conclusion .....	209
7. SUMMARY .....	210
REFERENCES .....	216
VITA .....	225

## LIST OF FIGURES

FIGURE	PAGE
1.1. Epitaxial and Non-Epitaxial Relationship Between Film and Substrate . . .	5
1.2. Examples of Pole Figures in a Cubic System with no In-Plane Texture and One or Two In-Plane Textures . . . . .	18
2.1. Lattice Structure of $\text{SrBi}_2\text{Ta}_2\text{O}_9$ . . . . .	29
2.2. $\{^1\text{H}\}^{13}\text{C}$ 100 MHz NMR of Metal Methoxyethoxides . . . . .	38
2.3. $\{^1\text{H}\}^{13}\text{C}$ 100 MHz NMR of Double Metal Methoxyethoxides . . . . .	39
2.4. $\{^1\text{H}\}^{13}\text{C}$ 100 MHz NMR of SBT, SBN, BBT, and BBN Methoxyethoxides . . . . .	40
2.5. Structure of $\text{Ta}(\text{OCH}_2\text{CH}_2\text{OCH}_3)_5$ and $\text{SrTa}_2(\text{OCH}_2\text{CH}_2\text{OCH}_3)_{12}$ . . . . .	42
2.6. Theta/2-Theta XRD of $\text{SrBi}_2\text{Ta}_2\text{O}_9$ Powders . . . . .	44
2.7. Theta/2-Theta XRD of $\text{SrBi}_2\text{Nb}_2\text{O}_9$ Powders . . . . .	45
2.8. Theta/2-Theta XRD of $\text{BaBi}_2\text{Nb}_2\text{O}_9$ Powders . . . . .	46
2.9. Theta/2-Theta XRD of $\text{BaBi}_2\text{Ta}_2\text{O}_9$ Powders . . . . .	47
2.10. Theta/2-Theta XRD of $\text{BaBiTa}_{2.85}\text{O}_{9.64}$ Powders . . . . .	49
2.11. Theta/2-Theta XRD of $\text{BaBi}_2\text{Ta}_2\text{O}_9$ Powders with and without 10% Excess Bi at 850 °C and 950 °C . . . . .	51
2.12. Theta/2-theta XRD of SBT, SBN, BBN, and BBT on Ag at 850 °C . . . . .	52
2.13. Plot of Dielectric Constants and Leakage Currents of SBT on Evaporated Silver at Various Temperatures . . . . .	54

2.14. Theta/2-Theta XRD of SBT, SBN, BBN, and BBT on SrTiO <sub>3</sub> at 850 °C .	57
2.15. Theta/2-Theta XRD of SBT, SBN, BBN, and BBT on LaAlO <sub>3</sub> at 850 °C .	58
2.16. Omega Scan and Phi Scan of SrBi <sub>2</sub> Nb <sub>2</sub> O <sub>9</sub> on SrTiO <sub>3</sub> . . . . .	61
2.17. Pole Figure of SrBi <sub>2</sub> Nb <sub>2</sub> O <sub>9</sub> on SrTiO <sub>3</sub> about the (105) Reflection . . . . .	62
2.18. Plot of FWHM of Phi Scans (in Degrees) Versus % Lattice Mismatch . .	64
3.1. <sup>1</sup> H NMR Spectra of Gallium Isopropoxide and Gallium Methoxyethoxide . . . . .	70
3.2. Theta/2-Theta XRD of NdGaO <sub>3</sub> Powders . . . . .	75
3.3. Theta/2-Theta XRD of PrGaO <sub>3</sub> Powders . . . . .	76
3.4. Theta/2-Theta XRD of LaGaO <sub>3</sub> Powders . . . . .	77
3.5. Theta/2-Theta XRD of NdGaO <sub>3</sub> Powders Annealed in Forming Gas . . . .	78
3.6. Theta/2-Theta XRD of PrGaO <sub>3</sub> Powders Annealed in Forming Gas . . . .	79
3.7. Theta/2-Theta XRD of LaGaO <sub>3</sub> Powders Annealed in Forming Gas . . . .	80
3.8. Theta/2-Theta XRD of GdGaO <sub>3</sub> and YGaO <sub>3</sub> Powders at 850 °C . . . . .	82
3.9. Theta/2-Theta XRD of LaGaO <sub>3</sub> , PrGaO <sub>3</sub> , and NdGaO <sub>3</sub> on Ag at 850 °C	83
3.10. Theta/2-Theta XRD of LaGaO <sub>3</sub> , PrGaO <sub>3</sub> , and NdGaO <sub>3</sub> on SrTiO <sub>3</sub> at 850 °C . . . . .	85
3.11. Theta/2-Theta XRD of La <sub>0.5</sub> Y <sub>0.5</sub> GaO <sub>3</sub> and La <sub>0.5</sub> Nd <sub>0.5</sub> GaO <sub>3</sub> on SrTiO <sub>3</sub> at 850 °C . . . . .	86
3.12. Theta/2-Theta XRD of LaGaO <sub>3</sub> on SrTiO <sub>3</sub> at 850 °C with a Longer Dwell Time . . . . .	89

3.13. Theta/2-Theta XRD of LaGaO <sub>3</sub> , PrGaO <sub>3</sub> , NdGaO <sub>3</sub> and La <sub>0.5</sub> Nd <sub>0.5</sub> GaO <sub>3</sub> on LaAlO <sub>3</sub> at 850 °C .....	90
3.14. Theta/2-Theta XRD of GdGaO <sub>3</sub> and YGaO <sub>3</sub> on SrTiO <sub>3</sub> at 850 °C .....	91
3.15. Theta/2-Theta XRD of GdGaO <sub>3</sub> and YGaO <sub>3</sub> on LaAlO <sub>3</sub> at 850 °C .....	92
3.16. Omega Scan and Phi Scan of NdGaO <sub>3</sub> on SrTiO <sub>3</sub> .....	94
3.17. Pole Figures of NdGaO <sub>3</sub> on SrTiO <sub>3</sub> and LaAlO <sub>3</sub> about the (220) Reflection .....	95
3.18. Theta/2-Theta XRD of YBCO/NdGaO <sub>3</sub> on SrTiO <sub>3</sub> .....	97
3.19. Critical Current Density (J <sub>c</sub> ) versus Applied Magnetic Field (H) at 77K for YBCO/NdGaO <sub>3</sub> on SrTiO <sub>3</sub> .....	98
3.20. Resistivity versus Temperature for a YBCO Film Deposited on SrTiO <sub>3</sub> with a NdGaO <sub>3</sub> Buffer Layer .....	99
4.1. <sup>1</sup> H NMR Spectra of Aluminum Isopropoxide and Aluminum Methoxyethoxide .....	106
4.2. <sup>1</sup> H NMR Spectra of Mixed Lanthanum and Aluminum Alkoxide Precursor .....	109
4.3. IR Spectra of Lanthanum Aluminum Methoxyethoxide Solutions with 2 Equivalents (Top Trace) and 6 Equivalents (Bottom Trace) of Water ..	111
4.4. TGA/DTA Plot of Lanthanum Aluminate Gel with 2 Equivalents (Top Trace) and 6 Equivalents (Bottom Trace) of Water .....	112
4.5. Theta/2-Theta XRD of LaAlO <sub>3</sub> Powders .....	114
4.6. Theta/2-Theta XRD of PrAlO <sub>3</sub> Powders .....	115

4.7. Theta/2-Theta XRD of NdAlO <sub>3</sub> Powders .....	116
4.8. Theta/2-Theta XRD of GdAlO <sub>3</sub> Powders .....	117
4.9. Theta/2-Theta XRD of YAlO <sub>3</sub> Powders .....	118
4.10. Theta/2-Theta XRD of LaAlO <sub>3</sub> Powders Annealed in Forming Gas ....	119
4.11. Theta/2-Theta XRD of PrAlO <sub>3</sub> Powders Annealed in Forming Gas ....	120
4.12. Theta/2-Theta XRD of NdAlO <sub>3</sub> Powders Annealed in Forming Gas ...	121
4.13. Theta/2-Theta XRD of GdAlO <sub>3</sub> Powders Annealed in Forming Gas ...	122
4.14. Theta/2-Theta XRD of YAlO <sub>3</sub> Powders Annealed in Forming Gas ....	123
4.15. Theta/2-Theta XRD of LaAlO <sub>3</sub> , PrAlO <sub>3</sub> , NdAlO <sub>3</sub> , GdAlO <sub>3</sub> , and YAlO <sub>3</sub> on Ag at 850 °C .....	125
4.16. Theta/2-Theta XRD of LaAlO <sub>3</sub> , PrAlO <sub>3</sub> , NdAlO <sub>3</sub> , GdAlO <sub>3</sub> , and YAlO <sub>3</sub> on SrTiO <sub>3</sub> at 850 °C .....	127
4.17. Theta/2-Theta XRD of PrAlO <sub>3</sub> , NdAlO <sub>3</sub> , GdAlO <sub>3</sub> , and YAlO <sub>3</sub> on LaAlO <sub>3</sub> at 850 °C .....	128
4.18. Theta/2-Theta XRD of Layered YAlO <sub>3</sub> /GdAlO <sub>3</sub> /PrAlO <sub>3</sub> /LaAlO <sub>3</sub> on SrTiO <sub>3</sub> at 850 °C .....	130
4.19. Theta/2-Theta XRD of LaAl <sub>0.5</sub> Ga <sub>0.5</sub> O <sub>3</sub> and La <sub>0.5</sub> Y <sub>0.5</sub> Al <sub>0.5</sub> Ga <sub>0.5</sub> O <sub>3</sub> on SrTiO <sub>3</sub> at 850 °C .....	131
4.20. Phi Scan of NdAlO <sub>3</sub> on SrTiO <sub>3</sub> about the (220) Reflection .....	133
4.21. Pole Figure of PrAlO <sub>3</sub> on SrTiO <sub>3</sub> about the (220) Reflection .....	134
4.22. Theta/2-Theta XRD of LaAlO <sub>3</sub> , PrAlO <sub>3</sub> , NdAlO <sub>3</sub> , GdAlO <sub>3</sub> , and YAlO <sub>3</sub> on Ni .....	136

4.23. Pole Figure of $\text{LaAlO}_3$ on Ni about the (110) Reflection	139
4.24. Phi Scan of $\text{NdAlO}_3$ on Ni about the (220) Reflection	140
5.1. Structure of $\text{ABCO}_4$ Compounds	142
5.2. Theta/2-Theta XRD of $\text{SrLaGaO}_4$ Powders	150
5.3. Theta/2-Theta XRD of $\text{SrPrGaO}_4$ Powders	151
5.4. Theta/2-Theta XRD of $\text{SrLaAlO}_4$ Powders	152
5.5. Theta/2-Theta XRD of $\text{SrPrAlO}_4$ Powders	153
5.6. Theta/2-Theta XRD of $\text{SrLaGaO}_4$ , $\text{SrPrGaO}_4$ , $\text{SrLaAlO}_4$ , and $\text{SrPrAlO}_4$ on Ag at 850 °C	156
5.7. Theta/2-Theta XRD of $\text{SrLaGaO}_4$ and $\text{SrPrGaO}_4$ on $\text{SrTiO}_3$ at 850 °C	158
5.8. Theta/2-Theta XRD of $\text{SrLaAlO}_4$ and $\text{SrPrAlO}_4$ on $\text{SrTiO}_3$ at 850 °C	159
5.9. Theta/2-Theta XRD of $\text{SrLaGaO}_4$ and $\text{SrPrGaO}_4$ on $\text{LaAlO}_3$ at 850 °C	160
5.10. Theta/2-Theta XRD of $\text{SrLaAlO}_4$ and $\text{SrPrAlO}_4$ on $\text{LaAlO}_3$ at 850 °C	161
5.11. Omega Scan and Phi Scan of $\text{SrLaGaO}_4$ on $\text{SrTiO}_3$	164
5.12. Pole Figure of $\text{SrLaAlO}_4$ on $\text{SrTiO}_3$ about the (105) Reflection	165
5.13. Theta/2-Theta XRD of $\text{YBCO}/\text{SrLaGaO}_4/\text{SrTiO}_3$ and $\text{YBCO}/\text{SrPrGaO}_4/\text{LaAlO}_3$ at 850 °C	167
5.14. Resistivity versus Temperature for a YBCO Film Deposited on $\text{SrTiO}_3$ with a $\text{SrLaGaO}_4$ Buffer Layer	168
5.15. Critical Current ( $I_c$ ) versus Voltage Plot of $\text{YBCO}/\text{SrPrGaO}_4$ on $\text{SrTiO}_3$	170
6.1. RABiTS standard architecture (left) and proposed architecture (right)	174

6.2. Phase Diagram of Rare-Earth Oxide Transitions as a Function of Cation Radius .....	175
6.3. IR Spectra of Ytterbium Containing Compounds .....	182
6.4. Theta/2-Theta XRD of Gd <sub>2</sub> O <sub>3</sub> on Ni at 1160 °C by Two Different Routes .....	184
6.5. Theta/2-Theta XRD of Yb <sub>2</sub> O <sub>3</sub> on Ni at 1160 °C by Two Different Routes .....	185
6.6. Theta/2-Theta XRD of Sm <sub>2</sub> O <sub>3</sub> , Eu <sub>2</sub> O <sub>3</sub> , and Tb <sub>2</sub> O <sub>3</sub> on Ni .....	186
6.7. Theta/2-Theta XRD of Dy <sub>2</sub> O <sub>3</sub> , Er <sub>2</sub> O <sub>3</sub> , and Ho <sub>2</sub> O <sub>3</sub> on Ni .....	187
6.8. Theta/2-Theta XRD of Tm <sub>2</sub> O <sub>3</sub> and Lu <sub>2</sub> O <sub>3</sub> on Ni .....	188
6.9. Theta/2-Theta XRD of Eu <sub>2</sub> O <sub>3</sub> on Ni at 1160 °C with One to Four Spin-Coats .....	191
6.10. Theta/2-Theta XRD of Eu <sub>2</sub> O <sub>3</sub> and Yb <sub>2</sub> O <sub>3</sub> on Ni at 1160 °C .....	192
6.11. Theta/2-Theta XRD of CeO <sub>2</sub> and Eu <sub>2</sub> O <sub>3</sub> /CeO <sub>2</sub> on Ni at 1050 °C .....	193
6.12. Omega Scan and Phi Scan of Gd <sub>2</sub> O <sub>3</sub> on Ni .....	195
6.13. Gd <sub>2</sub> O <sub>3</sub> and Yb <sub>2</sub> O <sub>3</sub> Pole Figures about the (222) Reflection for Two Different Solution Routes .....	197
6.14. Eu <sub>2</sub> O <sub>3</sub> , Tb <sub>2</sub> O <sub>3</sub> , Dy <sub>2</sub> O <sub>3</sub> , and Ho <sub>2</sub> O <sub>3</sub> Pole Figures about the (222) Reflection .....	198
6.15. Pole Figures of Er <sub>2</sub> O <sub>3</sub> and Tm <sub>2</sub> O <sub>3</sub> on Ni about the (222) Reflection, and CeO <sub>2</sub> on Ni about the (111) Reflection .....	199
6.16. Low Magnification SEM of Gd <sub>2</sub> O <sub>3</sub> on Ni .....	200

6.17. High Magnification SEM of $Gd_2O_3$ on Ni .....	201
6.18. AFM of the Surface of an Annealed Roll-Textured Nickel Substrate ...	202
6.19. AFM of the Surface of a 600 Å $Gd_2O_3$ Film Deposited on Roll-Textured Nickel .....	203
6.20. Theta/2-Theta XRD of YBCO/ $CeO_2$ /YSZ/ $Gd_2O_3$ on Ni .....	206
6.21. Theta/2-Theta XRD of YBCO/ $CeO_2$ /YSZ/ $Eu_2O_3$ on Ni .....	207
6.22. Critical Current and Critical Temperature Plots of YBCO/ $CeO_2$ /YSZ/ $Eu_2O_3$ /Ni and YBCO/ $CeO_2$ /YSZ/ $Gd_2O_3$ /Ni .....	208



## LIST OF TABLES

TABLE	PAGE
1.1. Listing of Space Groups, Lattice Parameters, and Coefficient of Thermal Expansion for Oriented Substrates . . . . .	21
2.1. $\{^1\text{H}\}^{13}\text{C}$ Resonances (ppm) of Bismuth Containing Perovskite Methoxyethoxides . . . . .	41
2.2. Lattice Constants for $(\text{Sr,Ba})\text{Bi}_2(\text{Nb,Ta})_2\text{O}_9$ Powders . . . . .	48
2.3. Lattice Constants of $\text{SrBi}_2\text{Nb}_2\text{O}_9$ , $\text{SrBi}_2\text{Ta}_2\text{O}_9$ , $\text{BaBi}_2\text{Nb}_2\text{O}_9$ , and $\text{BaBi}_2\text{Ta}_2\text{O}_9$ on $\text{SrTiO}_3$ and $\text{LaAlO}_3$ . . . . .	56
2.4. Full-Width at Half-Maximum Values for $(\text{Sr,Ba})\text{Bi}_2(\text{Nb,Ta})_2\text{O}_9$ on $\text{SrTiO}_3$ and $\text{LaAlO}_3$ . . . . .	60
3.1. Full-Width at Half-Maximum for Rare-Earth Gallate Films . . . . .	87
4.1. Full-Width at Half-Maximum for Rare-Earth Aluminate Films . . . . .	132
4.2. Full-Width at Half-Maximum for $\text{LaAlO}_3$ , $\text{PrAlO}_3$ , and $\text{NdAlO}_3$ Films on Ni . . . . .	138
5.1. Lattice Constants ( $\text{\AA}$ ) for Epitaxial Tetragonal Perovskites . . . . .	154
5.2. Full-Width at Half-Maximum for Tetragonal Perovskite Films on $\text{SrTiO}_3$ and $\text{LaAlO}_3$ . . . . .	163
6.1. Lattice Constants and Full-Width at Half-Maximum for Rare-Earth Oxide Films on Roll-Textured Nickel . . . . .	190

## LIST OF ABBREVIATIONS

AFM	atomic force microscopy
BBN	barium bismuth niobate
BBT	barium bismuth tantalate
BSCCO	barium strontium calcium copper oxide
CVD	chemical vapor deposition
DTA	differential thermal analysis
FTIR	Fourier transform infrared
FWHM	full-width at half-maximum
GAO	gadolinium aluminate
GGO	gadolinium gallate
HTS	high temperature superconductors
IBAD	ion beam assisted deposition
$I_c$	critical current
IR	infrared
$J_c$	critical current density
LAO	lanthanum aluminate
LGO	lanthanum gallate
Ln	rare-earth
LPE	liquid phase epitaxy
M	molarity
MBE	molecular beam epitaxy

MOCVD	metal-organic chemical vapor deposition
MOD	metal-organic deposition
NAO	neodymium aluminate
NGO	neodymium gallate
NMR	nuclear magnetic resonance
PAO	praseodymium aluminate
PDC	powder diffraction card
PGO	praseodymium gallate
PLD	pulsed-laser deposition
PT	lead titanate
PZT	lead zirconium titanate
RABITS	rolled aligned biaxially textured substrates
RPM	rotations per minute
SBN	strontium bismuth niobate
SBT	strontium bismuth tantalate
SEM	scanning electron microscopy
SLA	strontium lanthanum aluminate
SLG	strontium lanthanum gallate
SPA	strontium praseodymium aluminate
SPG	strontium praseodymium gallate
STO	strontium titanate
TBCCO	thallium barium calcium copper oxide

T <sub>c</sub>	critical temperature
TEM	transmission electron microscopy
TGA	thermal gravimetric analysis
THF	tetrahydrofuran
XRD	X-ray diffraction
YAO	yttrium aluminate
YBCO	yttrium barium copper oxide
YGO	yttrium gallate
YSZ	yttrium stabilized zirconium

# CHAPTER 1

## INTRODUCTION

### 1.1. Thin-Films

#### 1.1.1. Importance and Significance to Industry

A film is a structure with a large surface-to-volume ratio and may consist of a pure material, mixed composite, or a layered structure of dissimilar materials. Thin-films are often defined as having thicknesses of a micrometer or less, and several thin-films may be present in one electronic or optical device. Devices based on thin-film technology employ films which are electrically conductive, insulating, or semiconducting, and sales of both thin-film deposition equipment and devices based on thin-films are in the multi-billion dollar range.<sup>1</sup> Of particular interest, and the topic of this research, is the search for newer, better, and more cost-effective methods of deposition.

#### 1.1.2. Physical Methods of Deposition

Several physical methods are used to deposit thin-films. They include evaporation,<sup>2</sup> pulsed-laser deposition,<sup>3</sup> sputtering,<sup>4</sup> and molecular beam epitaxy.<sup>5</sup> Evaporation consists of generating a flux of atoms or molecules using e-beam or thermal evaporation sources. In the case of multi-cationic films, the flux must be controlled to produce the correct stoichiometry of the film, and

each element used in the film requires a separate source due to differences in vapor pressures for various elements.<sup>6</sup> Pulsed-laser deposition involves a pulsed laser hitting a target of the material to be deposited. Each pulse is focused on the target and ablates a small amount of the target material in a forward plume. This plume provides the flux for film growth.<sup>7</sup> Sputtering involves the creation of energetic ions in a plasma which bombard a target of the material to deposit. Atoms are ejected from the target and deposit on a substrate.<sup>6</sup> Molecular beam epitaxy (MBE) consists of heating the elements of the material to be deposited to their evaporation point in specially designed "cells" which forms molecular beams. In each beam, the flux can be controlled and epitaxial films are produced by rastering the beam across the substrate.<sup>8</sup> All four of these methods have been used to produce high quality films, but they rely on relatively expensive and maintenance-intensive vacuum technology.

### **1.1.3. Chemical Methods of Deposition**

The most widely used method of chemical deposition, metal-organic chemical vapor deposition (MOCVD),<sup>9</sup> involves the use of cations which are delivered as constituents of volatile inorganic or organometallic molecules. Film growth is produced when the molecules decompose on the heated substrate.<sup>6</sup> Unlike physical methods of deposition, MOCVD is not line-of-sight,

allowing the coating of complex shapes. In addition, because a chemical reaction occurs on the growth surface, MOCVD allows selective growth<sup>10</sup> and self-limiting growth of multi-cationic films.<sup>11</sup> Virtually all of the epitaxial films in both Group IV and Group III-Group V semiconductor manufacture are produced by MOCVD.

A less widely used chemical deposition method is chemical solution deposition. In this technique, solutions of cations are used to coat substrates to form a pre-ceramic film which is then pyrolyzed to give a ceramic film. This technique will be discussed in detail in later sections of this dissertation.

## **1.2. Epitaxial Thin-Films**

### **1.2.1. Definition of Epitaxy**

The primary emphasis of the research described in this dissertation is the deposition of epitaxial thin-films. Epitaxy is defined from the Greek words "epi," placed or resting upon, and "taxis," arrangement. Thus, epitaxy is the growth of crystals on a crystalline substrate that determines their orientation.<sup>8</sup> The term epitaxy was first termed by Royer<sup>12</sup> in 1928 when he used X-ray diffraction to demonstrate that oriented growth requires lattice planes in the thin-film and substrate to be similar in structure. Dey and Barlingay<sup>13</sup> classified epitaxial films into three types. The first, Type A, is a highly oriented polycrystalline film, where there is complete z-axis (perpendicular to the

surface) orientation and random orientations in the x-y plane. Type B is crystalline in nature with single crystal-like texture, and the z-axis orientation is completely oriented with low angle boundaries in the x-y plane. The last, Type C, is an epitaxial film that is a single crystal and is fully aligned both in-plane and out-of-plane.<sup>13</sup> Figure 1.1 shows a diagram of epitaxial and non-epitaxial relationships between the film and substrate.

There are several possible mechanisms for epitaxial growth of thin-films by solution techniques. In case of bismuth containing compounds or lead-containing compounds with highly mobile cations, it has been observed that one crystalline phase may be converted to another crystalline phase upon annealing. For example, Lange *et al.*<sup>14</sup> has shown that the epitaxial growth of lead titanate proceeds from a metastable pyrochlore phase to the desired perovskite phase. Another possible mechanism has been proposed by Ng and Cima<sup>15</sup> in which a polycrystalline film is formed prior to epitaxial growth. Once grains growing with a particular orientation in the polycrystalline film reach the size of the film's thickness, they consume other grains of other orientations forming an epitaxial film. This has been observed in metallic films,<sup>16</sup> but may not be applicable to the refractory materials of this study. Another mechanism proposed by Ng and Cima<sup>15</sup> involves the formation of an amorphous film which undergoes nucleation and forms at the film/substrate interface. Once nucleation has occurred over the entire substrate surface, the crystallized



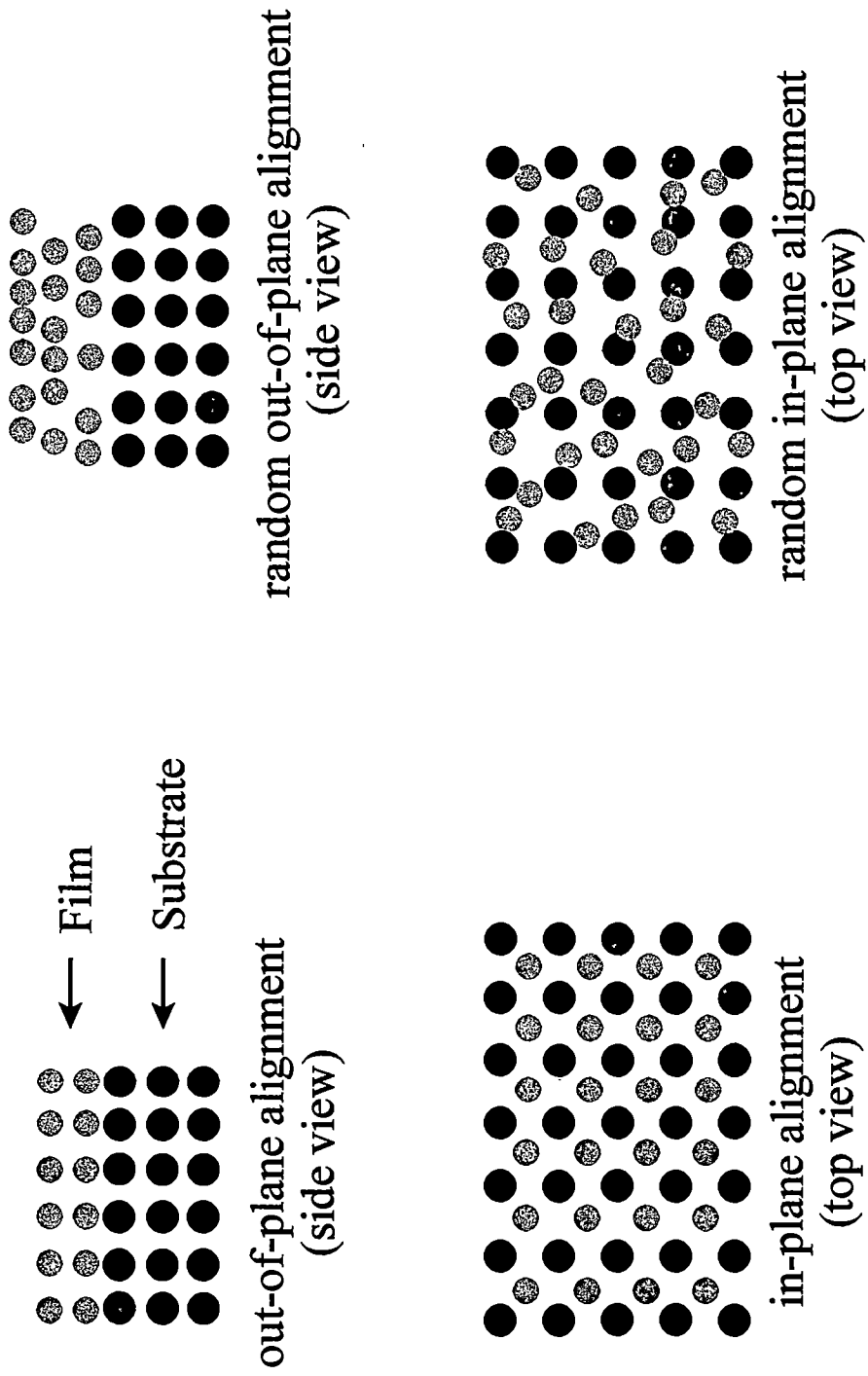


Figure 1.1. Epitaxial and non-epitaxial relationship between film and substrate.

nuclei begin to grow upwards throughout the rest of the amorphous solid regions of the film. Given the high melting points of the materials, the low processing temperatures used, and the low mobility of most cationic species of this dissertation, we favor this growth mechanism.

### **1.3. Solution Routes versus Physical Routes**

#### **1.3.1. Utility**

A new method of depositing epitaxial oxide thin-films is solution deposition. Solution deposition can be used in device applications such as non-volatile memories, pyroelectric detectors and field-emission displays.<sup>17</sup> Some of the materials that are currently produced by solution deposition are cuprate superconductors<sup>17</sup> and strontium titanate films on silicon.<sup>18</sup>

#### **1.3.2. Cost of Solution Routes versus Physical Routes**

The cost of producing epitaxial thin-films by solution routes is drastically cheaper than physical routes. Equipment for physical routes often costs hundreds of thousands of dollars to build and requires extensive maintenance. Unlike the physical routes, solution routes have low equipment costs, utilize a high percentage of the precursor material, have lower energy costs, and thus are more friendly to the environment.

### 1.3.3. Advantages of Solution Routes

Solution routes have several advantages over physical routes. First, control of the purity of the starting materials and careful preparation of the solutions can result in precise control of the stoichiometry of the solution. Typically, one part in a thousand accuracy can be obtained when nonvolatile elements are incorporated in a film. Other physical methods do not achieve this accuracy of film composition, especially for multicationic films involving elements of different weight or size. An example would be lanthanum aluminate which is extremely difficult to ablate or sputter. Also, preferential ablating or sputtering occurs over the course of deposition and the composition of the target may change and repeated calibrations are often required.

A second advantage of solution deposition is that it is a non-vacuum technique which is highly desirable for a number of applications. An example would be high  $T_c$  and  $J_c$  superconductors where the conductor and buffer layers could be applied by a solution technique such as dip-coating and processed in a continuous manner. This would allow superconductors to be made in long, continuous lengths.

Intimate mixing is another advantage of solution routes. In order to form mixed metal species and to control the rate of hydrolysis to achieve preceramic films, proper ligand systems and solvents must be chosen. This allows reactants in the coating solutions to be mixed at the molecular level and leads

to lower crystallization temperatures. Higher temperatures and longer processing times in conventional ceramic processes are observed due to solid-state diffusion. In a multi-cation solution process, mixing the reactants at the molecular level places them in close contact allowing for shorter diffusion distances, and, after the loss of organic material typically between 350 °C and 850 °C, crystallization can occur. Because the temperature of this solution process is generally several hundred degrees Celsius below those in typical ceramic processes, it has three advantages: (a) it allows for the formation and study of metastable (kinetic) phases; (b) it allows for the use of thermally sensitive substrates; and (c) it allows for the use of rapid thermal processing. Rapid thermal processing uses optical heating with rates up to 200 °C per second and has two unparalleled advantages. First, it allows for the use of substrates which would be damaged by prolonged heating at high temperatures, and second, it can be used to selectively heat the substrate. Rather than random crystallization from the bulk of the film, this process promotes epitaxial crystallization at the substrate and film interface.

#### **1.3.4. Disadvantages to Solution Routes**

The use of an oxidizing ambient and a general lack of processing knowledge are two disadvantages of solution deposition. Most ceramics prepared from solution deposition are fired in an oxidizing atmosphere. For a

number of applications such as epitaxial growth on metals and semiconductors, however, it is necessary to prevent the formation of an amorphous surface oxide which would cause a loss of epitaxy. In order to prevent surface oxidation, the precursor solution must be completely decomposed and the amorphous coating must be crystallized under reducing conditions. The other disadvantage of the solution deposition is the insufficient knowledge of the relationship between solution chemistry and the final microstructure of the ceramic film. This lack of knowledge is due mainly to the relative immaturity of the field, and did not cause difficulties in carrying out the researches of this dissertation.

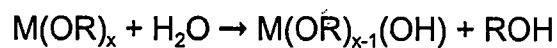
#### **1.4. Solution Based Growth Techniques**

Chemical solution depositions for thin-film development may be classified into three categories. The first, sol-gel processing, uses alkoxides and an alcohol as solvent.<sup>19,20,21</sup> Chelating processes, the second method, also utilizes alkoxide compounds and modifying ligands such as acetic acid.<sup>22,23,24</sup> The third method, metal-organic deposition (MOD), uses water-insensitive metal carboxylate compounds.<sup>25,26,27</sup> These three methods are discussed in more detail below.

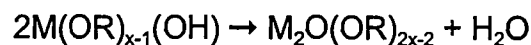
The term sol-gel has been used to describe a technique where there is a transition from a fluid-like property, "sol," to a semisolid or viscoelastic material,

the "gel." Sol-gel chemistry has been used to deposit a thin-layer of precursor molecules that decompose to low-density, polycrystalline films upon annealing.<sup>28</sup> Francis<sup>29</sup> stated that two different types of sol-gel processes can be distinguished. The first is a colloidal sol-gel which is a dispersion and aggregation of colloidal particles 1-100 nm in size. The second is a polymeric sol-gel which is the polymerization of a solution containing metal-organic compounds.<sup>29</sup> The metal-organic solutions can be hydrolyzed and polymerized by condensation reactions to form metal-oxygen-metal bonds (M-O-M).<sup>30,31</sup> A simple example of how hydrolysis and condensation reactions work is shown here:

Hydrolysis:



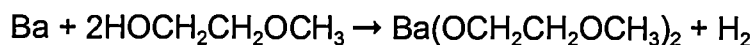
Condensation:



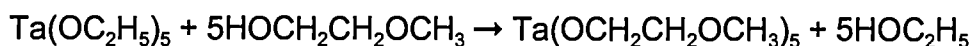
The polymeric sol-gel method used in the following chapters was first developed by Payne *et al.*<sup>19</sup> Payne's work was primarily concerned with lead titanate (PT) and lead zirconium titanate (PZT), but we found this chemistry to be quite general and have extended its use to aluminates, gallates, tantalates,

niobates, and rare-earth compounds. This method involves an all-alkoxide sol-gel with 2-methoxyethanol as the solvent and methoxyethoxide as the ligand. The 2-methoxyethanol can either directly react with a metal or readily undergo ligand exchange reactions with metal methoxides, ethoxides, and isopropoxides. Examples of formation of 2-methoxyethoxide complexes are given in the following reaction schemes.

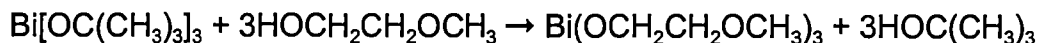
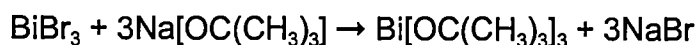
1. Direct reaction of the alcohol with metal:



2. Alcohol Exchange (condensation):



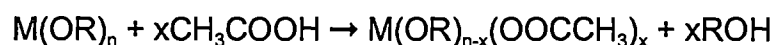
3. Metathesis followed by an alcohol exchange:



Several factors are known to affect sol-gel reactions, and it is important to carefully control the reactions. Solution viscosity, substrate wetting, solids content, solution gelation, and solution precipitation all play important roles in

whether a solution coats uniformly over a substrate when deposited, and whether a precise stoichiometry can be achieved.

Another approach to solution deposition involves the use of chelate alkoxide hybrid compounds. These routes utilize molecular modification of alkoxide complexes by reacting them with chelating ligands such as acetic acid, acetylacetone, and amines as in the following reaction.



The principal advantage of the chelate process is that it makes precursor solutions more stable in air by reducing the number of hydrolysis-sensitive alkoxide ligands in the precursor complexes. However, a certain drawback exists. Even though the chelate process may be faster than an all alkoxide process, its chemistry is quite complex as several reactions may occur, including chelation, esterification, hydrolysis, and condensation. Despite this drawback, chelate process is still a common method for obtaining thin-films on several different substrates.<sup>32</sup>

A third approach to solution deposition is metal-organic decomposition (MOD) which involves the use of water-insensitive metal carboxylate compounds. The precursor solution is a mixture of the starting compounds. It does not show any oligomerization, and the precursor species in solution have



a strong resemblance to the starting molecules. Although solution synthesis is straightforward, this process still possesses two disadvantages. The organic ligands in the precursor molecules are usually large. Thus, cracking develops during annealing of the product thin-films due to weight loss and shrinkage. Another disadvantage is that the reactivity of carboxylate precursors is limited. As a result, process flexibility is restricted to reactions such as hydrolysis and condensation. Despite these disadvantages, MOD has been shown to develop thin-films.<sup>32</sup>

## **1.5. Coating Methods**

### **1.5.1. Spin-Coating**

A thin-film can be formed by spin-coating the sol-gel liquid at a set rate. The spin-coating process involves four steps: deposition of the liquid, spin-up, spin-off, and evaporation or annealing.<sup>33</sup> The process begins by flooding the surface of a substrate with a specific solution. During the spin-up step, the substrate, which is fixed to the spin-coater by a vacuum, spins allowing all excess liquid to be driven outward from the center due to centrifugal force. Then the process reaches the spin-off stage, when the spin-rate is constant. The excess liquid that has been pushed to the end of the substrate leaves as droplets during the spin-off stage. The film typically becomes thinner the longer the substrate is spun. Since the film is thinner after spin-off, it has a greater

resistance to flow, and concentrations of the non-volatile components and viscosity increase. The final step, evaporation or annealing, becomes the primary mechanism of thinning by heating the substrate at a desired temperature.<sup>34</sup>

Scriven<sup>35</sup> reports that an advantage of spin-coating is that the liquid on the substrate tends to become uniform in thickness during spin-off and remains uniform if the viscosity does not vary over the substrate. This uniformity is due to centrifugal and viscous forces. Centrifugal force drives the liquid radially outward, while viscous force or friction acts radially inward. Yoldas<sup>36</sup> described the thickness of an initially uniform film during spin-off with Equation 1.1:

$$h(t) = \frac{h_0}{\left(1 + \frac{4\rho\omega^2 h_0^2 t}{3\eta}\right)^{\frac{1}{2}}} \quad (\text{Eq. 1.1})$$

where  $h_0$  is the initial thickness,  $t$  is time,  $\rho$  is the density,  $\omega$  is the angular velocity, and  $\eta$  is the liquid viscosity.

### 1.5.2. Dip-Coating

Dip-coating differs from spin-coating in that the depositing film is withdrawn vertically from the solution at a fixed velocity and acceleration, and

the film is thinned by gravitational draining. Unlike the spin-coating, this method allows long substrates to be coated. However, the dip-coated film is usually not fully uniform, and it shows a well-defined drying line at the end of the substrate.

The thickness of the film is related to the position of the streamline dividing the upward and downward moving layers.<sup>35</sup> In the film deposition, a competition arises among six forces: (1) viscous drag upward on the liquid by the moving substrate; (2) force of gravity; (3) resultant force of surface tension in the concavely shaped meniscus; (4) inertial force of the boundary layer liquid arriving at the deposition region; (5) surface tension gradient; and (6) the disjoining pressure.<sup>34</sup> When the liquid viscosity,  $\eta$ , and the speed of substrate removal from the solution are low and cannot lower the curvature of the gravitational meniscus, the film thickness,  $h$ , balances the viscous drag,  $\eta U_0$ , to liquid-vapor surface tension,  $\gamma_{LV}$ , and gravity force,  $\rho gh$ , according to the relationship Equation 1.2, derived by Landau and Levich:<sup>37</sup>

$$h = \frac{0.94(\eta U_0)^{\frac{2}{3}}}{\gamma_{LV}^{1/6} (\rho g)^{\frac{1}{2}}} \quad (\text{Eq. 1.2})$$

This formula shows that as the velocity,  $\eta$ , is increased, the film thickness,  $h$ , also increases.

## 1.6. Characterization of Powders and Thin-Films

### 1.6.1. X-Ray Diffraction

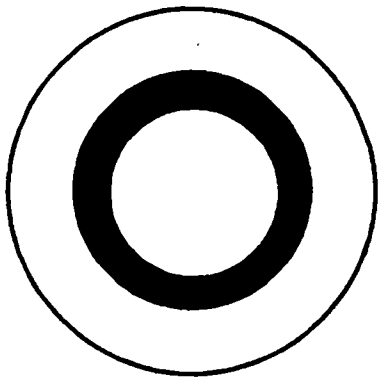
The German physicist Roentgen first discovered X-rays in 1895, and in 1912, the phenomenon of X-ray diffraction by crystals was discovered.<sup>38</sup> X-rays are produced when high-speed electrons collide with a metal target. X-ray diffraction is an interaction between X-rays and the geometry of crystals, revealing details of a solid structure around  $10^{-8}$  cm in size. X-ray wavelengths are measured in angstroms (Å) and X-rays have wavelengths ranging from 0.5 to 2.5 Å. Diffraction consists of a beam that is composed of a number of scattered rays mutually reinforcing one another. From this, Bragg's Law (Equation 1.3) was developed:

$$\lambda = 2d\sin\theta \quad (\text{Eq. 1.3})$$

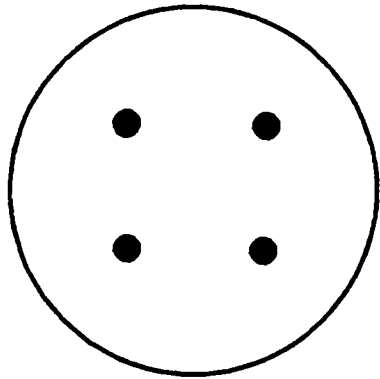
$\lambda$  is the wavelength of X-rays,  $d$  is the distance between planes in a crystal lattice, and  $\theta$  is the angle between a diffracted beam and the crystal. The angle between the diffracted beam and the transmitted beam is  $2\theta$ . The diffraction pattern is obtained from the diffracted angles of planes producing  $(hkl)$  reflections.<sup>38</sup> The  $(hkl)$  reflections refer to  $c$ -axis orientation and are obtained from  $\theta/2$ - $2\theta$  scans of a crystalline material. In the following chapters, a Phillips 1701 diffractometer equipped with a copper anode ( $K_{\alpha} =$

1.542 Å) using Bragg-Brentano geometry was used to obtain powder and thin-film theta/2-theta scans of crystalline material. The scan parameters were 50 kV accelerating voltage, 30 mA filament current, step size of 0.03° and a dwell time of one second. The theta/2-theta scans were analyzed to determine the reflections and phases by the Jade software (Materials Data, Inc., Livermore, CA).

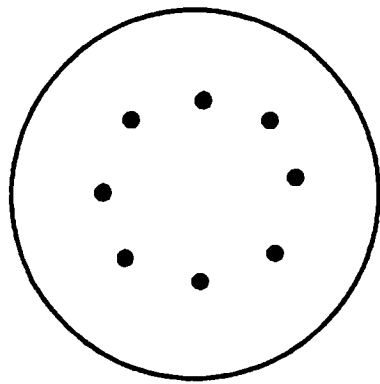
Omega scans (out-of-plane epitaxy; *c*-axis), phi scans (in-plane epitaxy; *a* and *b*-axis), and pole figures of a sample are obtained with a four-circle diffractometer. The four circles are 2-theta, omega, chi and phi. The four-circle diffractometer is also used to determine the full-width at half-maximum (fwhm) of a sample. The fwhm is the mosaic character or the measure of orientation present in a material. Pole figures, used to determine the in-plane texture in a sample, are obtained by scanning 360° in phi at intervals from 0° to 90° in chi. If no in-plane texture is observed in a sample, a ring is produced in phi at an angle of chi. If in-plane texture is observed, peaks will be prominent. If a pole figure shows single in-plane orientation and is cube-on-cube, four peaks at chi of 45° spaced 90° in phi are observed. If a cube-on-cube sample has two in-plane orientations, the pole figure will show 8 peaks at chi of 45° spaced 45° in phi as observed in lanthanum aluminate on nickel.<sup>39</sup> Examples of pole figures with no in-plane texture and one or two in-plane textures are shown in Figure 1.2. In the current studies, all omega scans, phi scans, and pole figures were



No in-plane texture



Single in-plane texture



Two in-plane textures

Figure 1.2. Examples of pole figures in a cubic system with no in-plane texture and one or two in-plane textures.

obtained on a Picker 4-Circle Diffractometer equipped with a copper anode ( $K_{\alpha}$  = 1.542 Å). The operating accelerating voltage was 40 kV and the filament current was 38 mA. Difftech 122D software was used to obtain the omega scans, phi scans and pole figures (Diffraction Technology Inc., Mitchell, Canberra, Australia, <http://www.difftech.com.au/>).

### **1.6.2. Analysis Techniques for Film Thickness and Surface Structure**

Several techniques are used to determine the thickness and surface structure of a film. The least time consuming techniques are profilometry and ellipsometry. In order to use profilometry, the film must be etched to expose the surface of the substrate. The sample is then placed under a probe and adjusted so that the probe can move across both the film and substrate. As the thickness is determined, the probe moves over the etch in the film. In ellipsometry, the sample is placed on a sample holder and a Class II helium-neon laser is used to analyze the thickness of the film. The laser travels through a polarizer prism striking the surface of the sample at an angle of incidence ( $\phi$ ), and then proceeds through an analyzer prism to a photodetector and extinction meter. The thickness is determined by the measurement of the index of refraction from the substrate and film. A more accurate technique to determine the thickness of a sample is transmission electron microscopy (TEM). TEM is capable of observing microstructural

features between 1,000 to 450,000 times and provides a resolution of less than one nm. However, TEM sample preparation is often tedious.

Scanning electron microscopy (SEM) is usually used to observe surface structure. SEM can obtain images of surface features at 10 to 100,000 times with resolution between 3 to 100 nm by controlling the beam diameter. SEM reveals surface features by converging an electron beam to a small point and then scanning it across a sample. These SEM images show grain boundaries and surface morphology including defects, pin-holes, and film coverage of a sample. Secondary, Auger, and backscattered electrons are emitted as well by the incident electron beams and detected to reveal the compositions of the sample surface. A Hitachi S-4100 Field Emission SEM was used in the current studies to obtain surface images of samples in the following chapters.

## **1.7. Materials and Substrates**

### **1.7.1. Single Crystal Oxide Substrates**

Several different types of oriented single crystal oxide substrates are used in the current studies for epitaxial growth of thin-films. They include (100) strontium titanate, (100) lanthanum aluminate, (100) yttrium stabilized zirconia, and (100) magnesium oxide. Their space groups, lattice parameters, dielectric constants, and coefficients of thermal expansion are listed in Table 1.1. The dielectric constants, coefficients of thermal expansion, and lattice parameters



**Table 1.1.** Listing of space groups, lattice parameters, and coefficients of thermal expansion for oriented single crystal oxide substrates.

Substrate	Space Group <sup>1</sup>	Lattice Parameters <sup>2</sup> (Å)			Dielectric Constant <sup>2</sup> $\epsilon$	Coefficient of Thermal Expansion <sup>2</sup> (ppm/°C)
		a	b	c		
LaAlO <sub>3</sub>	R3m	3.793			23	-
SrTiO <sub>3</sub>	Pm3m	3.905			277	10.4
Y <sub>0.1</sub> Zr <sub>0.9</sub> O <sub>2</sub>	Fm3m	3.607			27.5	9.2
MgO	Fm3m	4.213			9.62	12.6
Ni	Fm3m	3.524			-	13.0
YBa <sub>2</sub> Cu <sub>3</sub> O <sub>7</sub>	Pmmm	3.817	3.883	11.633	700 at 25 °C <sup>3</sup> 30 at 4.3 K	12.0

<sup>1</sup>Source: *Powder Diffraction Files*, International Center for Diffraction Data.

<sup>2</sup>Source: Giess, E. A.; Sandstrom, R. L.; Gallagher, W. J.; Gupta, A.; Shinde, S. L.; Cook, R. F.; Cooper, E. I.; O'Sullivan, E. J. M.; Roldan, J. M.; Segmuller, A. P.; Angiello, J. *IBM J. Res. Develop.* **1990**, *34*, 916.

<sup>3</sup>Source: Testardi, L. R.; Moulton, W. G.; Mathais, H.; Ng, H. K.; Rey, C. M. *Phys. Rev. B* **1988**, *37*, 2324.

were reported by Giess *et al.*<sup>40</sup> The space groups were obtained from their respective Powder Diffraction Cards (PDC).

### 1.7.2. Ferroelectrics

Ferroelectrics do not contain iron as the name suggests. They are solid insulators and piezoelectric. Piezoelectricity is a property in which materials acquire electric polarization either under external mechanical stress or when the materials change size or shape due to the application of external electric fields. Ferroelectrics have a spontaneous electric polarization, and when an electric field is applied, the polarization can be reversed in a process known as switching. The first material known to be ferroelectric was Rochelle salt ( $\text{NaKC}_4\text{H}_4\text{O}_6 \cdot 4\text{H}_2\text{O}$ ), but now many are known including ferroelectric solid solutions. Other ferroelectrics include perovskite structures of the formula  $\text{ABO}_3$  (e.g.,  $\text{CaTiO}_3$ ,  $\text{BaTiO}_3$ ,  $\text{PbTiO}_3$ ), and compounds having oxygen octahedra such as  $\text{Cd}_2\text{Nb}_2\text{O}_7$  and  $\text{PbNb}_2\text{O}_6$ . Ferroelectrics are useful in transducers, capacitors, frequency controls, thermal meters, and non-volatile memory (devices which retain information when power is interrupted).<sup>41</sup>

Most non-volatile memory materials, particularly the various compositions of PZT, exhibit polarization fatigue and increased dielectric loss on switching beyond  $10^6$  read-write cycles.<sup>42</sup> A memory material must be capable of switching more than  $10^{12}$  cycles in order to replace or supplant

current semiconductor memory.<sup>43</sup> The fatigue observed in most ferroelectrics is a decrease in the amount of charge which is switched each time the ferroelectric is polarized. Three microscopic causes have been observed to give this problem. First, stress relaxation or charged defects result in pinning of 180° domains.<sup>44</sup> This is caused by relaxation of 90° domains to 180° domains as mechanical stresses are released internally resulting in reduction of the net polarization.<sup>42</sup> Another problem is poling of charged defect pairs,<sup>45</sup> such as lead-vacancies and oxygen-vacancy neighbors. This involves the dipoles becoming aligned due to repeated application of large electric fields. The electric fields prolong the time needed to reverse causing reduction in the switched lattice polarization.<sup>46</sup> The last problem is space-charge accumulation at the electrode-ferroelectric interface. This leads to oxidation of the platinum electrode and valence conversion in the ferroelectric metal ions.<sup>47</sup> One method to fix the space-charge accumulation is to use perovskites that have bismuth oxide layers.<sup>43</sup> These bismuth-containing layered perovskite oxides exhibit high charge retention, fatigue-free properties, and low leakage currents.<sup>43</sup> These types of materials will be discussed in detail in Chapter 2.

### **1.7.3. High Temperature Superconductors**

A superconductor is an alloy or compound that has exceptional electrical and magnetic properties. Any conductor that has zero resistance to electrical

current can be classified as a superconductor since the current can flow without a loss of energy. All superconductors are diamagnetic in that they repel all magnetic fields by generating currents that produce opposing fields. In superconductors, electrons form pairs which enable them to flow around imperfections and impurities. There are several current and potential uses for superconductors such as power cable wire, motors and generators, powerful magnets for magnetic resonance imaging, and levitating trains.

The first superconducting transition in a material at a temperature higher than 30 K was observed in the compound  $\text{La}_{2-x}\text{Ba}_x\text{CuO}_{4-\delta}$  prepared by Bednorz and Müller in 1986.<sup>48</sup> Since then, other layered copper materials with superconducting transition temperatures,  $T_c$ , higher than the boiling point of liquid nitrogen (77 K) have been observed. Such high temperature superconductors (HTS) include  $\text{Ba}_x\text{La}_{5-x}\text{Cu}_5\text{O}_9$ ,  $\text{YBa}_2\text{Cu}_3\text{O}_{7-x}$  (YBCO),  $\text{Bi}_2\text{Sr}_2\text{Ca}_2\text{Cu}_3\text{O}_{10}$  (BSCCO), and  $\text{TlBa}_2\text{Ca}_2\text{Cu}_3\text{O}_x$  (TBCCO). BSCCO has been used in the manufacture of the first generation wire using the powder-in-tube production technique.<sup>49</sup> The advantage of using these high temperature superconductors (HTS) lies in the platelike microstructures that form after mechanical rolling and drawing, but these HTS exhibit a lower  $T_c$  in the presence of magnetic fields greater than one Tesla.<sup>50</sup> YBCO, which maintains its critical temperature ( $T_c$ ) under high magnetic field, is being actively studied,

and is the primary candidate to make second generation wire or coated conductors.

Several different methods have been used to produce HTS on a substrate. They include evaporation,<sup>2</sup> molecular beam epitaxy (MBE),<sup>5</sup> pulsed-laser deposition,<sup>3</sup> sputtering,<sup>4</sup> metal-organic chemical vapor deposition (MOCVD),<sup>9</sup> and liquid phase epitaxy (LPE).<sup>51</sup> Pulsed-laser deposition was used to apply YBCO to the buffered substrates in this dissertation principally for the following advantages of pulsed-laser deposition: stoichiometric transfer of material from the target, one target for all the elements, rotation of the target to produce uniform films over large areas, deposition rates higher than 100 Å/s,<sup>6</sup> and the ability to grow epitaxial films on a different number of substrates. The space group, lattice parameters, dielectric constant,<sup>52</sup> and coefficient of thermal expansion of YBCO are listed in Table 1.1.

#### **1.7.4. Nickel Substrates**

High temperature superconductors (HTS) have been grown on many types of substrates including strontium titanate and magnesium oxide. Two distinctly different approaches to inexpensive substrates have been pursued in order to achieve alignment in coated superconductors. One approach is a technique known as Ion Beam Assisted Deposition (IBAD), which involves the deposition of a textured buffer layer on a randomly oriented, oxidation resistant

metal tape using multiple ion beams.<sup>53</sup> The second approach is a technique known as Rolling-Assisted Biaxially Textured Substrates (RABiTS).<sup>54,55</sup> Goyal *et al.*<sup>55</sup> were the first to develop RABiTS as one of the most common HTS substrates. RABiTS are biaxially textured and have chemical and structural surfaces for epitaxial growth of superconducting material. These roll-textured substrates are produced thermomechanically to give a cubic texture. Roll-textured nickel substrates are formed by rolling randomly oriented, polycrystalline high purity nickel rod. After rolling, the surface was found to be as smooth as the substrates manufactured by mechanical or chemical means. The roll-textured nickel must meet several criteria for use in HTS, which include close crystallographic lattice match with the HTS film, chemical compatibility with a buffer layer, thermal stability, and a close match of coefficients of thermal expansion. The space group, lattice parameter, and coefficient of thermal expansion of nickel are listed in Table 1.1.

#### **1.7.5. Buffer Layers**

Buffer layers are films that lie between the substrate and the active layer of any material. They prevent the chemical reaction of the substrate with the active layer and/or the diffusion of atoms from the substrate to the active layer. For example, the nickel substrates discussed in the previous section require buffer layers to prevent the exchange of copper atoms for nickel atoms (which

destroys superconductivity) and the buffer must prevent the diffusion of nickel through the YBCO layer and the diffusion of oxygen to the nickel substrate.

In addition to these requirements for chemical stability and diffusion preventions, epitaxial buffer layers have additional requirements. They must be epitaxial and biaxially aligned with low full-width at half-maximum for their in-plane and out-of-plane texture. In order to be epitaxial, they must exhibit small lattice mismatch with the substrate and have a low thermal expansion coefficient mismatch with the substrate and active layer to allow for temperature changes during processing. By using several buffer layers, it is possible to "engineer" the lattice constant of a given substrate to meet the requirements of the active layer. Finally, they must be smooth, continuous with no pin-holes, and crack-free. Chapters 3 through 6 discuss different types of buffer layers used on (100) strontium titanate, (100) lanthanum aluminate, and nickel.

## CHAPTER 2

# EPITAXIAL GROWTH OF BISMUTH-CONTAINING FERROELECTRIC MATERIALS

### 2.1. Introduction

Layered perovskites containing bismuth were first discovered by Aurivillius<sup>56</sup> and possess several interesting electrical properties.<sup>57</sup> They have the general composition  $\text{Bi}_2\text{A}_{n-1}\text{B}_n\text{O}_{3n+3}$  ( $n = 1$  to  $3$ )<sup>57</sup> and have two structural layers consisting of a  $(\text{Bi}_2\text{O}_2)^{2+}$  layer between double perovskite layers of the general form  $(\text{A}_{n-1}\text{B}_n\text{O}_{3n+1})$ .<sup>57-58</sup> The "A" site is occupied by a large, dodecahedrally coordinated ion such as  $\text{Ca}^{2+}$ ,  $\text{Sr}^{2+}$ ,  $\text{Mg}^{2+}$ ,  $\text{Ba}^{2+}$ ,  $\text{Pb}^{2+}$ ,  $\text{Bi}^{3+}$ , or a rare earth ion, while the "B" site is occupied by an octahedrally coordinated ion such as  $\text{Ga}^{3+}$ ,  $\text{Al}^{3+}$ ,  $\text{Ti}^{4+}$ ,  $\text{Ta}^{5+}$ , or  $\text{Nb}^{5+}$ . A representative example of this structure is strontium bismuth tantalate whose structure is depicted in Figure 2.1.

The bismuth containing layered perovskites discussed in this chapter have an orthorhombic structure. (These materials are often treated as having a tetragonal structure due to the near equivalence of the  $a$  and  $b$  axes.) These materials are highly anisotropic in their dielectric response because electronic polarization occurs in the  $a$ - $b$  plane of the  $(\text{A}_{n-1}\text{B}_n\text{O}_{3n+1})$  layer, and not along the  $c$ -axis.<sup>59</sup> Because of this anisotropy, highly textured films are beneficial for



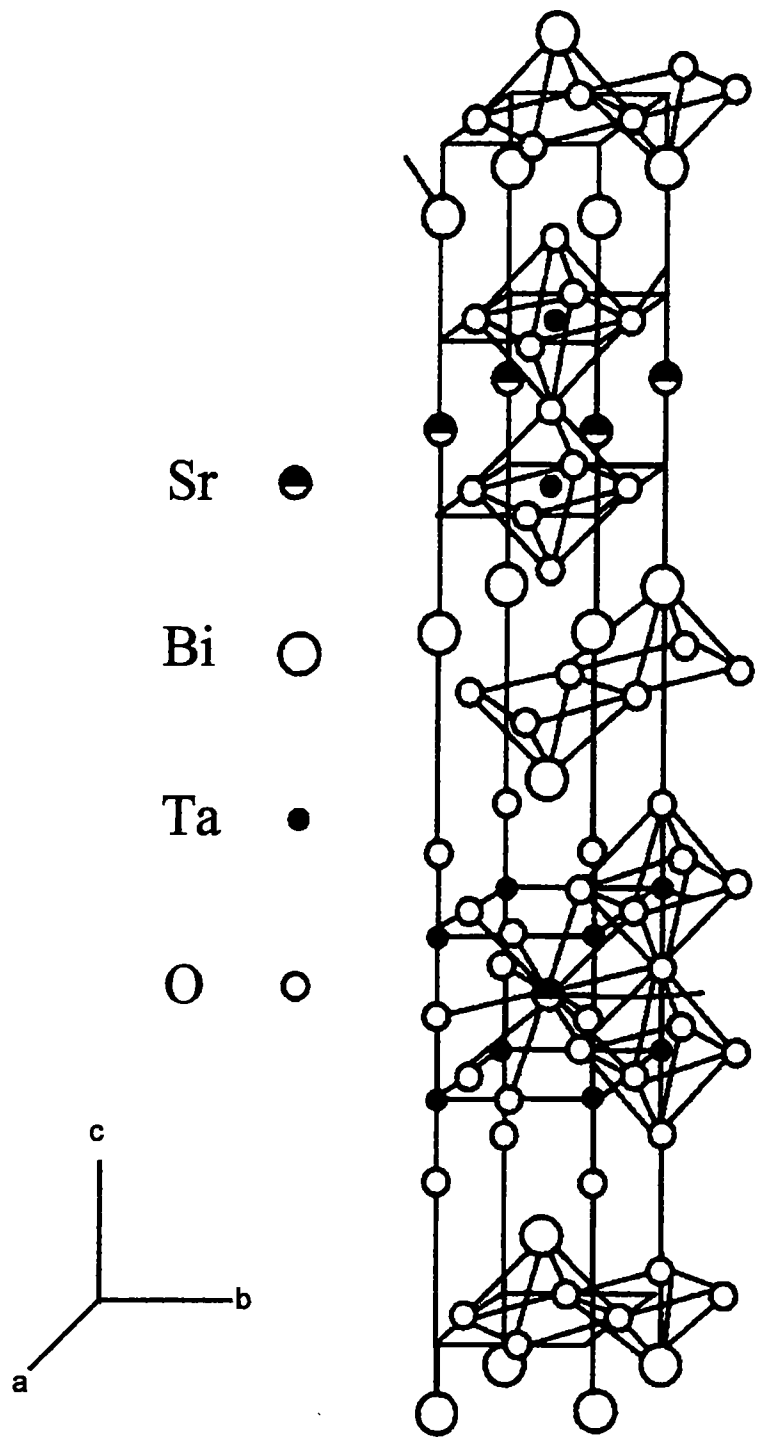


Fig. 2.1. Lattice structure of  $\text{SrBi}_2\text{Ta}_2\text{O}_9$ .

studies of fundamental properties and comparison of bulk properties with thin-film properties.

Interest in bismuth layered perovskite phases has increased over the last six years following the work of Aruajo and Scott.<sup>43</sup> These researchers demonstrated that, unlike lead zirconium titanate (PZT), these layered perovskites are fatigue-free for  $10^{12}$  polarization cycles. In comparison, lead zirconium titanate, a commonly used electronic ferroelectric material, exhibits severe polarization fatigue and degradation when deposited on noble metal electrodes. This fatigue-free property allows the materials to serve as primary memory in electronic storage applications.

Thin-films are important in integrating the electrooptic element in electrooptical applications. In the bismuth-containing materials, due to the anisotropy of the dielectric response, a light beam in the plane of the material may be modulated by the application of an electric field whereas a beam perpendicular to the material will be unaffected. In addition, this integration process requires epitaxial films since they do not have grain boundaries which would scatter radiation.

A number of physical techniques have been used to deposit bismuth layered perovskites such as  $\text{SrBi}_2\text{Ta}_2\text{O}_9$  (SBT). These techniques include pulsed laser deposition<sup>3</sup> and sputtering.<sup>4,60</sup> Other methods of preparing bismuth layered perovskite thin-films include chemical techniques such as Metal

Organic Deposition (MOD),<sup>25-27,61</sup> acetate-alkoxide hybrid sol-gel,<sup>62</sup> and Metal Organic Chemical Vapor Deposition (MOCVD).<sup>9,63</sup>

Epitaxial films of strontium barium tantalate and strontium barium niobate have been produced by several different techniques. Nagahma *et al.*<sup>64,65</sup> have shown that epitaxial thin-films of SBT and SBN can be produced by MOD technique which utilized metal ethylhexanoates in organic solvent. Lange *et al.*<sup>66</sup> have shown epitaxial growth of patterned SBT lines by a "channel stamping method", again using the same MOD chemistry. Sputtering and MOCVD, two more common methods, have also been used to deposit epitaxial films of SBT.<sup>67,68</sup>

Solution routes to epitaxial thin-films have been the subject of a review by Lange.<sup>28</sup> The following sections of this chapter provide the experimental procedures and results for all-alkoxide precursor solutions of SrBi<sub>2</sub>Ta<sub>2</sub>O<sub>9</sub> (SBT), SrBi<sub>2</sub>Nb<sub>2</sub>O<sub>9</sub> (SBN), BaBi<sub>2</sub>Ta<sub>2</sub>O<sub>9</sub> (BBT), and BaBi<sub>2</sub>Nb<sub>2</sub>O<sub>9</sub> (BBN). Powders of all four compounds were prepared and characterized. All four compounds were deposited on silver substrates and (100) oriented single-crystals of SrTiO<sub>3</sub> and LaAlO<sub>3</sub>, and characterized by X-ray diffraction. LaAlO<sub>3</sub> was indexed as if it were cubic, and the films were treated as if they were tetragonal to simplify analysis of peak reflections. The sol-gel chemistry used was pioneered by Payne *et al.*<sup>19</sup> and involves the preparation of metal methoxyethoxide complexes in 2-methoxyethanol.

## **2.2. Experimental Details**

### **2.2.1. General Procedures**

All manipulations were performed under dry argon atmosphere with the use of either standard Schlenk techniques or a glove box. NMR spectra were recorded on a Bruker AC-400 Fourier transform spectrometer, and were referenced to tetramethylsilane. Tetrahydrofuran was dried over sodium/benzophenone and distilled before use. Strontium metal (Alfa Aesar, 99.9%), barium metal (Alfa Aesar, 99.9%), niobium ethoxide (Alfa Aesar, 99.999%), tantalum ethoxide (Alfa Aesar, 99.999%), and bismuth tribromide (Alfa Aesar, 99.0%) were used as received.

### **2.2.2. Solution Preparation of Strontium and Barium 2-Methoxyethoxide**

Solutions were prepared with 2.19 g of strontium metal (25 mmole) or 3.43 g of barium metal (25 mmole) in 50 mL of 2-methoxyethanol. The solutions were refluxed for 1 h under inert atmosphere. The strontium metal took several minutes to dissolve, while the barium metal dissolved virtually instantaneously.

### **2.2.3. Solution Preparation of Niobium and Tantalum 2-Methoxyethoxide.**

Solutions were prepared by the reaction of 7.94 g of niobium ethoxide,  $\text{Nb}(\text{OCH}_2\text{CH}_3)_5$  (25 mmol), or 10.15 g of tantalum ethoxide,  $\text{Ta}(\text{OCH}_2\text{CH}_3)_5$  (25 mmol), with 2-methoxyethanol. The ethoxides were dissolved in 75 mL of 2-

methoxyethanol in a 250 mL Schlenk flask and refluxed for 1 h. Approximately 50 mL of solvent was removed by distillation at atmospheric pressure to promote ligand exchange of the ethoxide to the methoxyethoxide ligand. During the distillation, the temperature of the still-head climbed from 85 °C to 124 °C, the boiling point of 2-methoxyethanol. The solution was rediluted with 30 mL of 2-methoxyethanol, refluxed for 1 h and approximately 30 mL of solvent was removed by distillation to ensure complete ligand exchange. The solutions were placed in a 50 mL volumetric flask, and their volumes were adjusted to 50 mL with 2-methoxyethanol.

#### **2.2.4. Solution Preparation of Bismuth 2-Methoxyethoxide**

Bismuth tris-*t*-butoxide was prepared by the method described by Massiani et al.<sup>69</sup> A 250 mL Schlenk flask with a magnetic stir bar was charged with 1.2 g of crushed sodium metal, 3.85 g of *t*-butyl alcohol (CH<sub>3</sub>)<sub>3</sub>COH, and 100 mL of dry tetrahydrofuran (THF) and allowed to reflux overnight. Another Schlenk flask was charged with 8.5 g of BiBr<sub>3</sub> and 60 mL of THF, and this solution was added to the sodium *t*-butoxide solution. The mixture was stirred for 24 h under argon, and the solvent was then removed under reduced pressure (0.1 torr) to yield a solid compound. The solid compound was transferred in a dry box to a sublimer. Bismuth tris-*t*-butoxide was obtained (5.53 g, 70% yield), by vacuum sublimation at 80 °C and 0.5 torr. Bismuth tris-*t*-butoxide (5.35 g) was dissolved in 60 mL of 2-methoxyethanol and refluxed

for 1 h at 140 °C. Two-thirds of the solvents, consisting of 2-methoxyethanol and t-butanol, were removed by distillation at atmospheric pressure. An additional 40 mL of 2-methoxyethanol was added to the flask. The cycles of reflux, distillation, and redilution was repeated two more times to insure complete ligand exchange. Solution volume was then adjusted to 50 mL for each stock solution.

### 2.2.5. Powder and Film Preparation

Perovskite stock solutions were prepared for the synthesis of each of the following oxides: strontium bismuth tantalate ( $\text{SrBi}_2\text{Ta}_2\text{O}_9$ ), strontium bismuth niobate ( $\text{SrBi}_2\text{Nb}_2\text{O}_9$ ), barium bismuth tantalate ( $\text{BaBi}_2\text{Ta}_2\text{O}_9$ ), and barium bismuth niobate ( $\text{BaBi}_2\text{Nb}_2\text{O}_9$ ). The solutions were weighed, and their molalities were determined from the number of moles of the precursors in each of the stock solutions. Mixtures of the stock solutions were prepared gravimetrically to ensure accurate stoichiometry. The mixtures were then refluxed for 1 h. Hydrolysis was carried out using a 1 M water solution in 2-methoxyethanol. Powders and films were prepared by partially hydrolyzing the solutions with one mole equivalent of water per four mole equivalents of  $(\text{Sr,Ba})\text{Bi}_2(\text{Nb,Ta})_2\text{O}_9$ . Powders were prepared by decomposing the solutions at 300 °C, ground the resulting solid with a mortar and pestle, and fired at 650-950 °C in air. Film substrates, strontium titanate ( $\text{SrTiO}_3$ ) (100), and lanthanum aluminate ( $\text{LaAlO}_3$ ) (100), were heated for 1 h in oxygen at 1000 °C and 800 °C, respectively, prior

to coating. Silver foil was cleaned with 0.06 micron extra pure alumina. The hydrolyzed stock solutions were applied to the substrates through a 0.2  $\mu\text{m}$  syringe filter and spun for 30 sec at 2,000 rpm on a photo-resist spinner. The coated substrates were placed in a preheated, Thermolyne furnace at temperatures ranging from 650  $^{\circ}\text{C}$  to 850  $^{\circ}\text{C}$  for 20 min in air. Each coat was approximately 70 nm thick, and the coating and firing process was repeated four times.

X-ray diffraction was used to determine film structure and orientation. Theta/2-theta scans were obtained from a diffractometer. A Picker 4-circle diffractometer was used to obtain omega scans (rocking curves), phi scans, and pole figures. Lattice parameters of bismuth containing perovskite powders were determined for two different space groups [ $I4/mmm$  (tetragonal) and  $Fmmm$  (orthorhombic)] using cell refinements calculated by JADE software. Lattice parameters of bismuth containing perovskite films on (100) strontium titanate and (100) lanthanum aluminate with a tetragonal cell were determined by calculating the  $c$ -axis lattice constant. The  $c$ -axis lattice constant is the slope of the line obtained from theta/2-theta by plotting corrected values of  $d$  (referenced to the substrate reflections) against  $1/l$ . Equation 2.1 was used to determine the  $a$ -axis lattice constant from the film (105) reflection [referenced to the substrate (110) reflection].

$$a = \sqrt{\frac{h^2 + k^2}{1/d^2 - l^2/c^2}} \quad (\text{Eq. 2.1})$$

### 2.2.6. Preparation for Electrical Characterization

SBT thin-films were spin-coated on evaporated silver (1000 Å) on oxidized silicon. Capacitors for electrical characterization were formed by depositing a top electrode of platinum by e-beam evaporation through a contact mask. These electrodes were ~300 μm in diameter and 1000 Å thick. Capacitance measurements were made using an HP 4194A impedance analyzer at 1 MHz, and leakage current measurements were made using a Keithly 602 electrometer at a field of 150 kV/cm.

## 2.3. Results and Discussion

### 2.3.1. Analysis of NMR Data

An NMR investigation was conducted on the solutions used to produce the oxides SrBi<sub>2</sub>Ta<sub>2</sub>O<sub>9</sub>, SrBi<sub>2</sub>Nb<sub>2</sub>O<sub>9</sub>, BaBi<sub>2</sub>Ta<sub>2</sub>O<sub>9</sub>, and BaBi<sub>2</sub>Nb<sub>2</sub>O<sub>9</sub>. The information obtained helped determine the reason for the phase purity observed using metal methoxyethoxide precursor solutions comparable to other precursors. This study also helped clarify if “double alkoxides” of the formula AB<sub>2</sub>(OCH<sub>2</sub>CH<sub>2</sub>OCH<sub>3</sub>)<sub>12</sub> would form from the reactions between A(OCH<sub>2</sub>CH<sub>2</sub>OCH<sub>3</sub>)<sub>2</sub> (A = Sr, Ba) and B(OCH<sub>2</sub>CH<sub>2</sub>OCH<sub>3</sub>)<sub>5</sub> (B = Nb, Ta). {<sup>1</sup>H}<sup>13</sup>C



NMR was used instead of  $^1\text{H}$  NMR because lines in the proton spectrum were moderately broad due to the oligomeric nature of the species containing bismuth and tantalum. Figure 2.2 shows the  $\{^1\text{H}\}^{13}\text{C}$  spectra of strontium, barium, bismuth, niobium and tantalum methoxyethoxides. Figure 2.3 shows the  $\{^1\text{H}\}^{13}\text{C}$  spectra of the "double alkoxide" products formed between  $\text{A}(\text{OCH}_2\text{CH}_2\text{OCH}_3)_2$  (A = Sr, Ba) and  $\text{B}(\text{OCH}_2\text{CH}_2\text{OCH}_3)_5$  (B = Nb, Ta). Figure 2.4 shows the  $\{^1\text{H}\}^{13}\text{C}$  spectra of the four coating solutions containing  $\text{Bi}(\text{OCH}_2\text{CH}_2\text{OCH}_3)_3$ . Tetramethylsilane (TMS) was used as an internal standard in all solutions. Table 2.1 summarizes all resonances observed for these alkoxides. Methoxy methyl resonances (labeled carbon "a") were observed at 58 to 60 ppm in all the spectra, and as expected, these resonances are relatively insensitive to the cations to which they are bonded.<sup>70</sup> The resonances of the methylene carbon (labeled carbon "b") adjacent to the methoxy methyl group (or  $\gamma$ -carbon) were observed, in the range of 74 to 76 ppm, which were also relatively insensitive to the cations to which they are bonded. The resonances of the  $\alpha$ -carbon (labeled carbon "c") were fairly sensitive to the cation environment and appear between 62 and 72 ppm. Two broad  $\alpha$ -carbon resonances occurred at 65 and 72 ppm for  $\text{Ta}(\text{OCH}_2\text{CH}_2\text{OCH}_3)_5$ . This was indicative of terminal and bridging alkoxides of a dimer (Figure 2.5) undergoing exchange on the NMR timescale. In the NMR spectrum of a solution containing 1 equivalent of  $\text{A}(\text{OCH}_2\text{CH}_2\text{OCH}_3)_2$  (A = Sr, Ba) and 2 equivalents of  $\text{B}(\text{OCH}_2\text{CH}_2\text{OCH}_3)_5$  (B = Nb, Ta), the broad  $\alpha$ -carbon

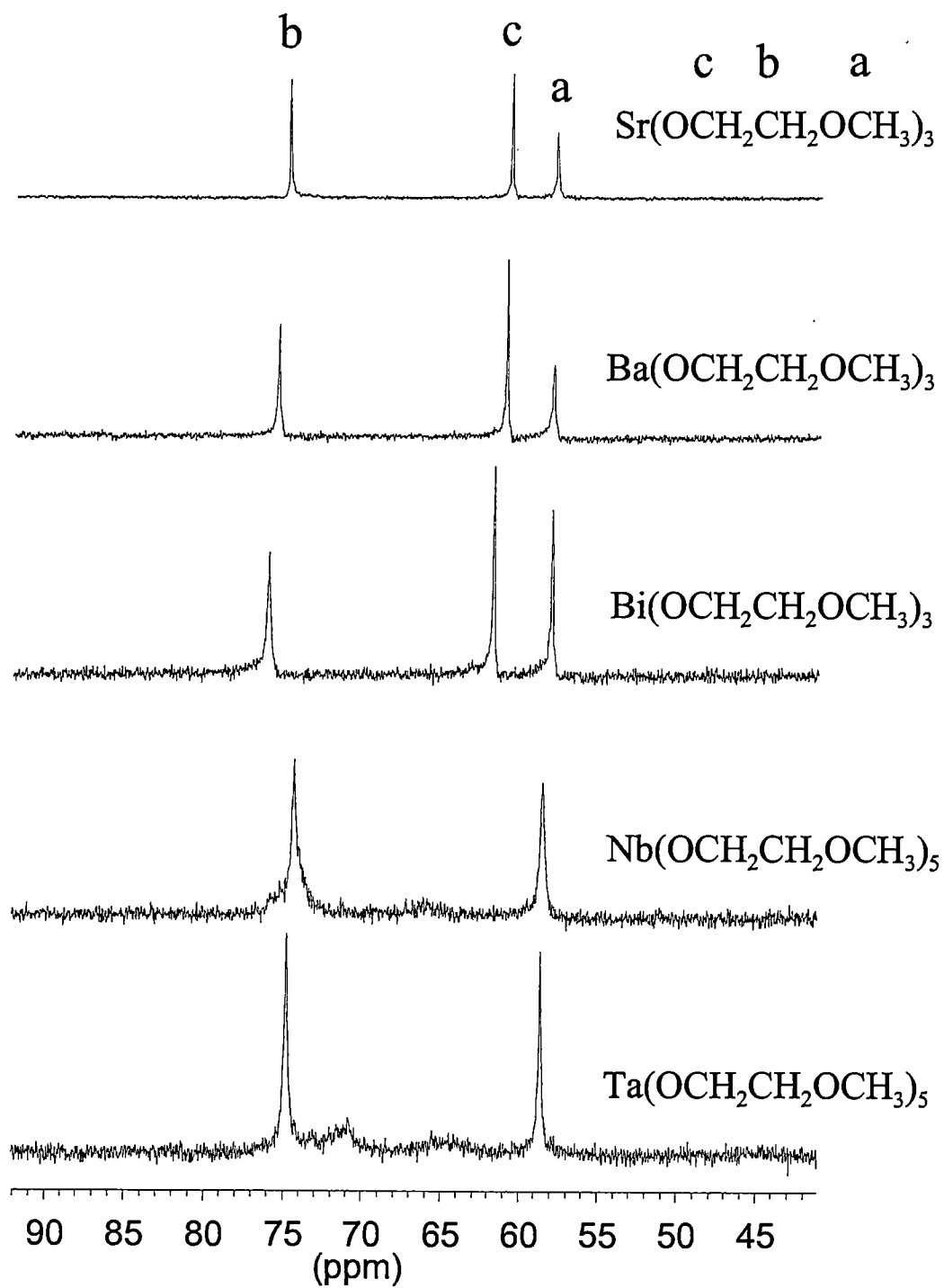


Figure 2.2.  $\{^1\text{H}\}^{13}\text{C}$  100 MHz NMR of metal methoxyethoxides at 23 °C.

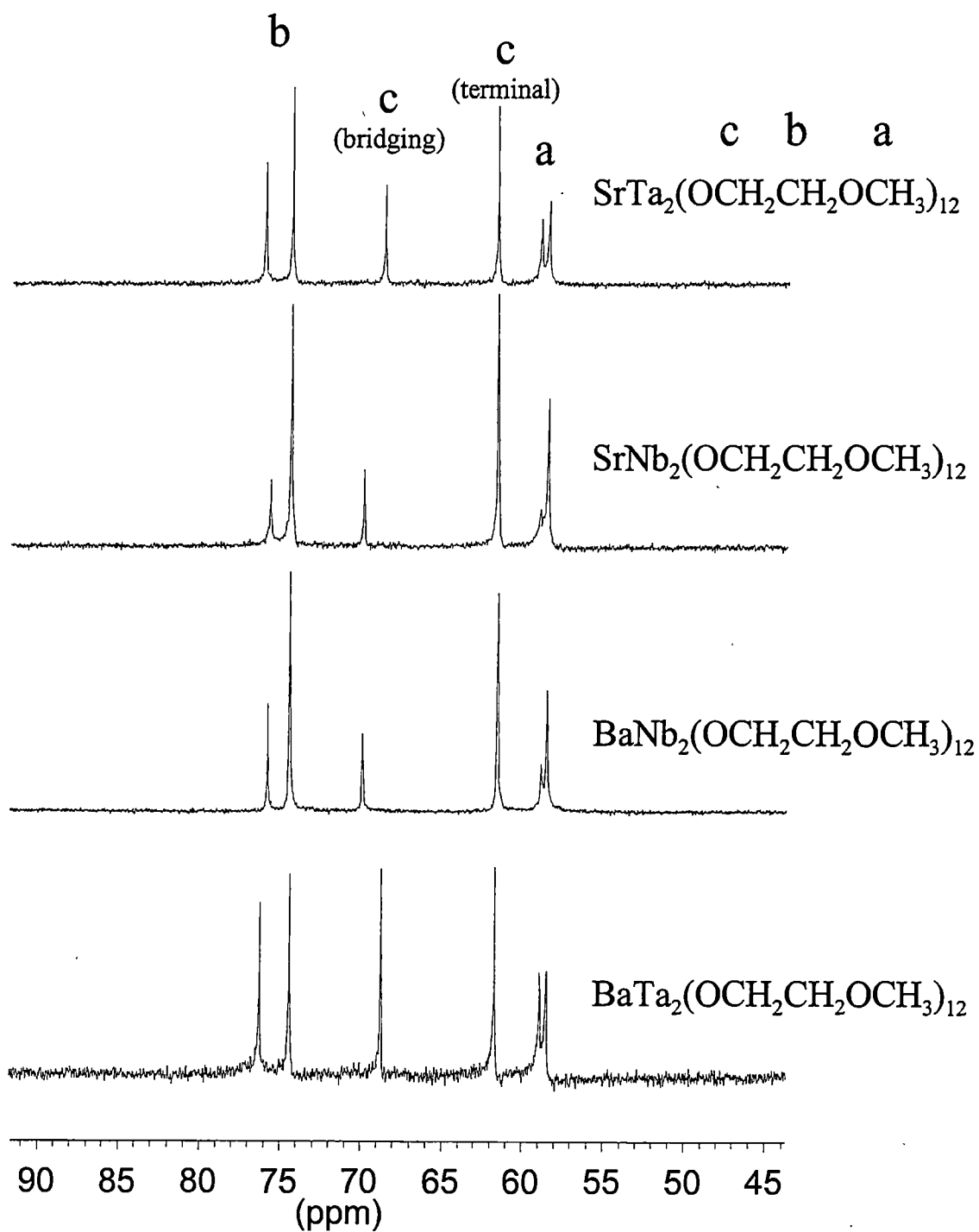


Figure 2.3.  $\{^1\text{H}\}^{13}\text{C}$  100 MHz NMR of “double metal methoxyethoxides” at 23 °C.

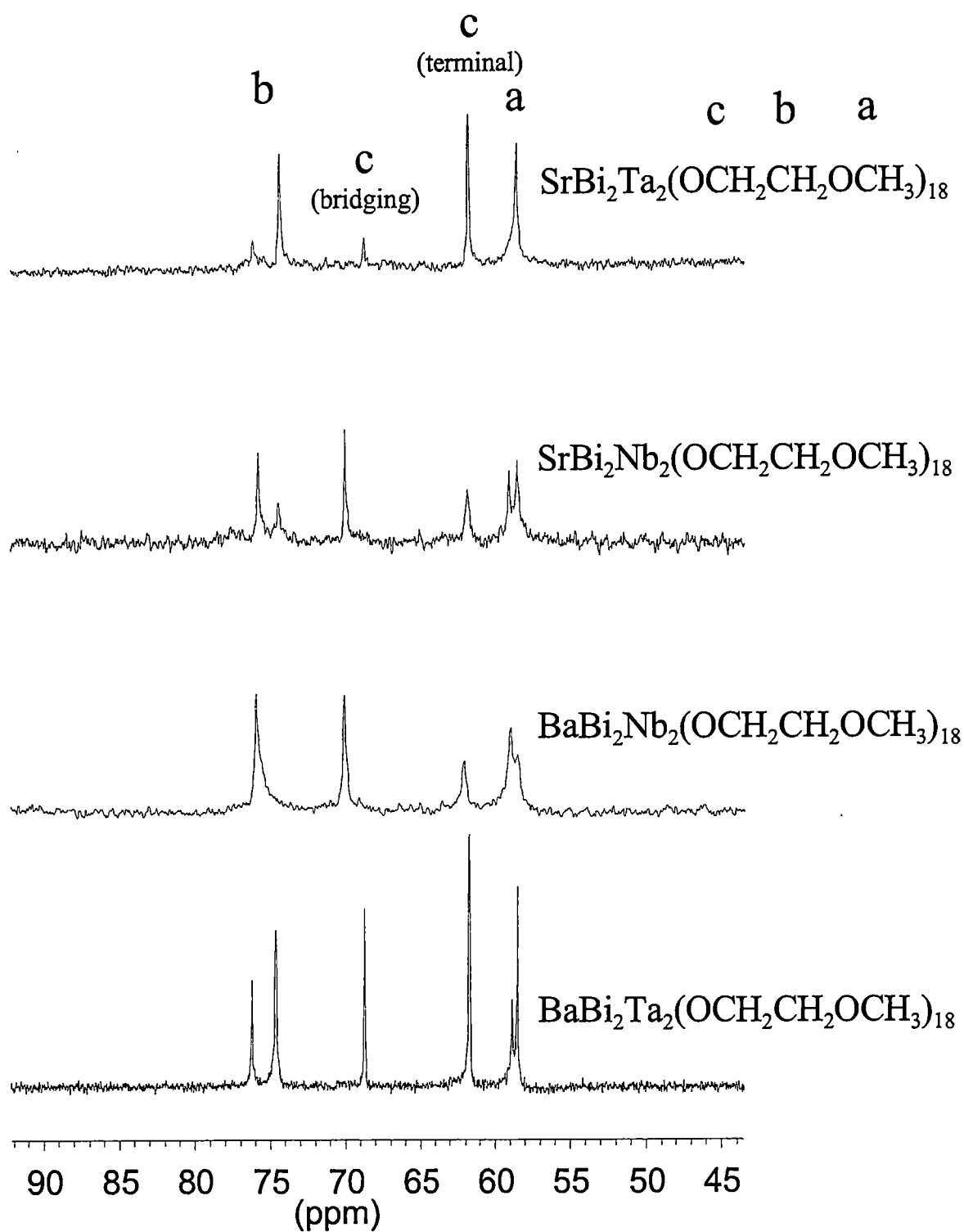


Figure 2.4.  $\{^1\text{H}\}^{13}\text{C}$  100 MHz NMR of SBT, SBN, BBT, and BBN methoxyethoxides at 23 °C.

**Table 2.1.  $\{^1\text{H}\}^{13}\text{C}$  resonances (ppm) of bismuth-containing perovskite methoxyethoxides.**

Metal Alkoxide	methoxy methyl resonances	methylene carbon adjacent to the methoxy group	methylene carbon attached to the ethoxide oxygen (terminal ligand)	methylene carbon attached to the ethoxide oxygen (bridging ligand)
$\text{Sr}(\text{OCH}_2\text{CH}_2\text{OCH}_3)_2$	58.62	75.69	61.53	-
$\text{Ba}(\text{OCH}_2\text{CH}_2\text{OCH}_3)_2$	58.51	77.32	61.26	-
$\text{Bi}(\text{OCH}_2\text{CH}_2\text{OCH}_3)_3$	58.38	76.41	62.10	-
$\text{Nb}(\text{OCH}_2\text{CH}_2\text{OCH}_3)_5$	58.69	74.55	65.96	71.40
$\text{Ta}(\text{OCH}_2\text{CH}_2\text{OCH}_3)_5$	58.60	74.79	64.09	70.81
<b>Double Alkoxides</b>				
$\text{SrTa}_2(\text{OCH}_2\text{CH}_2\text{OCH}_3)_{12}$	58.46 and 58.94	74.38 and 76.04	61.60	68.61
$\text{SrNb}_2(\text{OCH}_2\text{CH}_2\text{OCH}_3)_{12}$	58.46 and 58.94	74.40 and 75.68	61.57	69.88
$\text{BaTa}_2(\text{OCH}_2\text{CH}_2\text{OCH}_3)_{12}$	58.47 and 58.82	74.37 and 76.23	61.63	68.71
$\text{BaNb}_2(\text{OCH}_2\text{CH}_2\text{OCH}_3)_{12}$	58.46 and 58.86	74.43 and 75.80	61.52	69.92
<b>Bismuth Containing Alkoxides</b>				
$\text{SrBi}_2\text{Ta}_2(\text{OCH}_2\text{CH}_2\text{OCH}_3)_{18}$	58.46 and 58.94	74.32 and 76.10	61.68	68.67
$\text{SrBi}_2\text{Nb}_2(\text{OCH}_2\text{CH}_2\text{OCH}_3)_{18}$	58.44 and 58.97	74.39 and 75.75	61.74	68.95
$\text{BaBi}_2\text{Ta}_2(\text{OCH}_2\text{CH}_2\text{OCH}_3)_{18}$	58.45 and 58.82	74.39 and 75.75	61.65	68.68
$\text{BaBi}_2\text{Nb}_2(\text{OCH}_2\text{CH}_2\text{OCH}_3)_{18}$	58.36 and 58.87	74.61 and 76.21	61.97	70.00

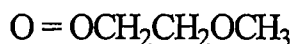
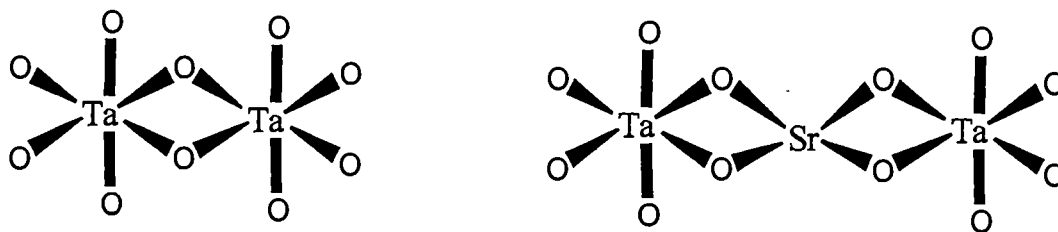
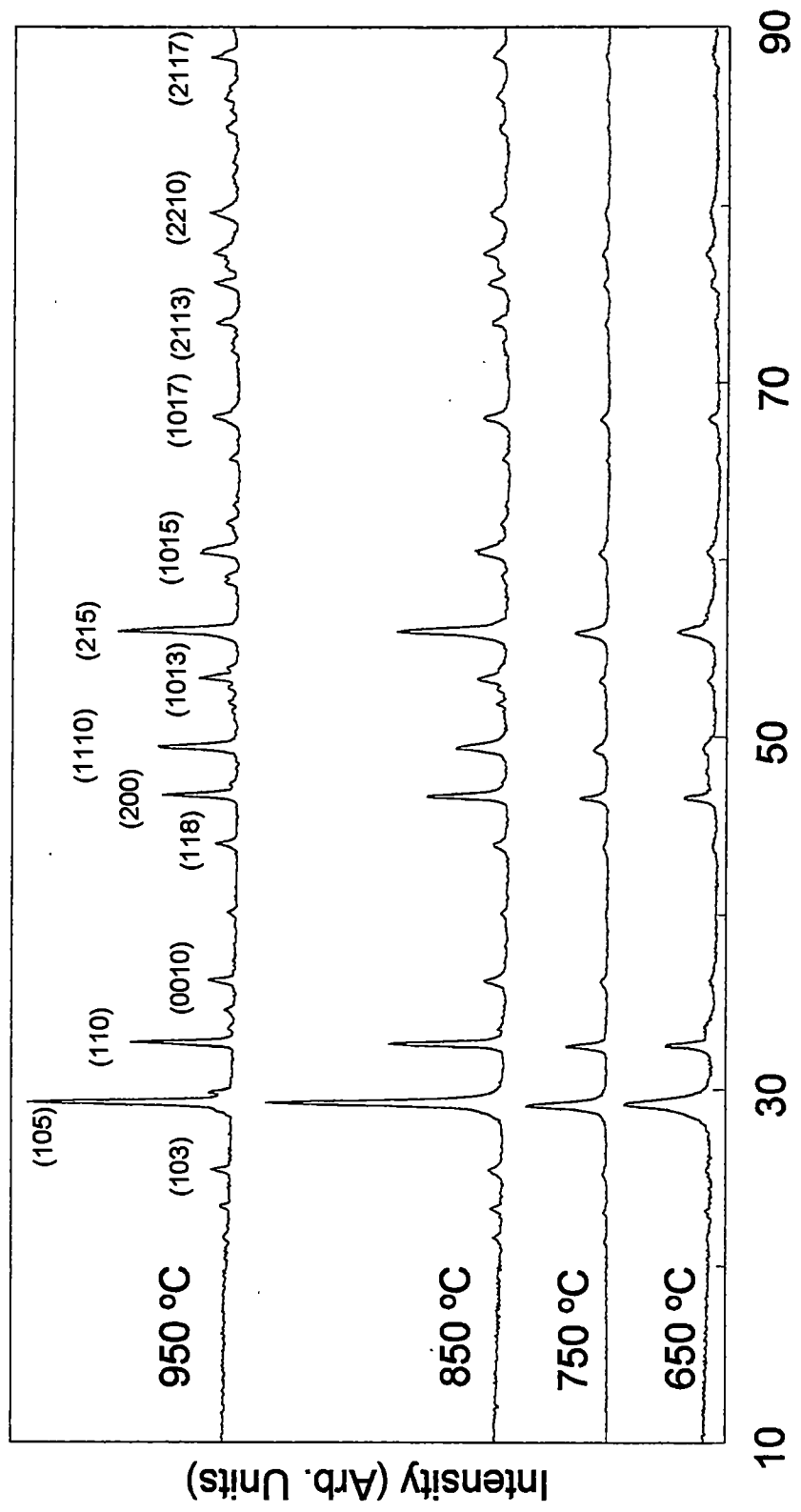


Figure 2.5. Structure of  $\text{Ta}(\text{OCH}_2\text{CH}_2\text{OCH}_3)_5$  dimer and  $\text{SrTa}_2(\text{OCH}_2\text{CH}_2\text{OCH}_3)_{12}$ .

resonances of  $\text{B}(\text{OCH}_2\text{CH}_2\text{OCH}_3)_5$  ( $\text{B} = \text{Nb}, \text{Ta}$ ) disappeared, and new peaks around 69 ppm and 62 ppm were observed, suggesting the formation of a mixed or "double" alkoxide  $\text{AB}_2(\text{OCH}_2\text{CH}_2\text{OCH}_3)_{12}$  ( $\text{A} = \text{Sr}, \text{Ba}$ ;  $\text{B} = \text{Nb}, \text{or Ta}$ ). The peak around 69 ppm was assigned to the  $\alpha$ -carbon (carbon c) of the bridging ligands (Figure 2.5). This same peak was observed in the coating solution containing  $\text{Bi}(\text{OCH}_2\text{CH}_2\text{OCH}_3)_3$ . The peak at 62 ppm, which was observed in both the double alkoxides and the coating solutions, was from the terminal ligands. The ratio of integrals between the peaks at 62 ppm and 69 ppm was approximately 2:1, which is consistent with the terminal and bridging ligand assignments (Figure 2.5). The addition of  $\text{Bi}(\text{OCH}_2\text{CH}_2\text{OCH}_3)_3$  to the double alkoxide solutions  $(\text{Sr or Ba})\text{Nb}_2(\text{OCH}_2\text{CH}_2\text{OCH}_3)_{12}$  and  $\text{SrTa}_2(\text{OCH}_2\text{CH}_2\text{OCH}_3)_{12}$  broadened the peaks (Figure 2.5) suggesting exchanges between these double alkoxides and  $\text{Bi}(\text{OCH}_2\text{CH}_2\text{OCH}_3)_3$ . Such exchange is perhaps less pronounced between  $\text{Bi}(\text{OCH}_2\text{CH}_2\text{OCH}_3)_3$  and  $\text{BaTa}_2(\text{OCH}_2\text{CH}_2\text{OCH}_3)_{12}$ . The nature of the exchange was not studied further.

### 2.3.2. XRD Analysis of Bismuth Containing Perovskite Powders

All peaks here were indexed in a tetragonal cell. Figures 2.6 to 2.9 show the X-ray diffraction (XRD) patterns of SBT, SBN, BBN, and BBT powders fired between 650 °C and 950 °C. It was observed that the crystallization starts at 650 °C, and the solid was well crystalized by 850 °C. Table 2.2 contains lattice constants of two space groups ( $I4/mmm$  and  $Fmmm$ ) for the four perovskite powders. Only one phase was observed in these powders, in contrast to the powders from acetate-alkoxide precursors that have two or more phases obtained by Boyle *et al.*<sup>62</sup> Phase formation was, in most cases, insensitive to bismuth content, as powders containing ten percent excess bismuth showed only one phase formation and no difference in crystallinity. The only irregularity in the powders was observed in BBT. The diffraction pattern of BBT showed a change in relative intensities upon heating from 850 °C to 950 °C when compared to the other three metal oxide powders. A bismuth deficient pyrochlore phase consisting of the stoichiometry  $BaBiTa_{2.85}O_{9.64}$ , a phase first observed by Rodriguez *et al.*,<sup>71</sup> was prepared for comparison. Figure 2.10 shows the theta/2-theta scans for  $BaBiTa_{2.85}O_{9.64}$ . At 650 °C the XRD of  $BaBiTa_{2.85}O_{9.64}$  was in excellent agreement with its strontium analog (SBT).<sup>71</sup>  $BaBiTa_{2.85}O_{9.64}$  decomposed to the Aurivillius phase and various tantalum oxides at 850 °C (Figure 2.10). This indicates that bismuth deficient compounds do not form at higher temperatures and are thermodynamically unfavorable. Such changes are probably due to cation exchange in the



2-Theta

Figure 2.6. Theta/2-theta XRD of SrBi<sub>2</sub>Ta<sub>2</sub>O<sub>9</sub> powders.



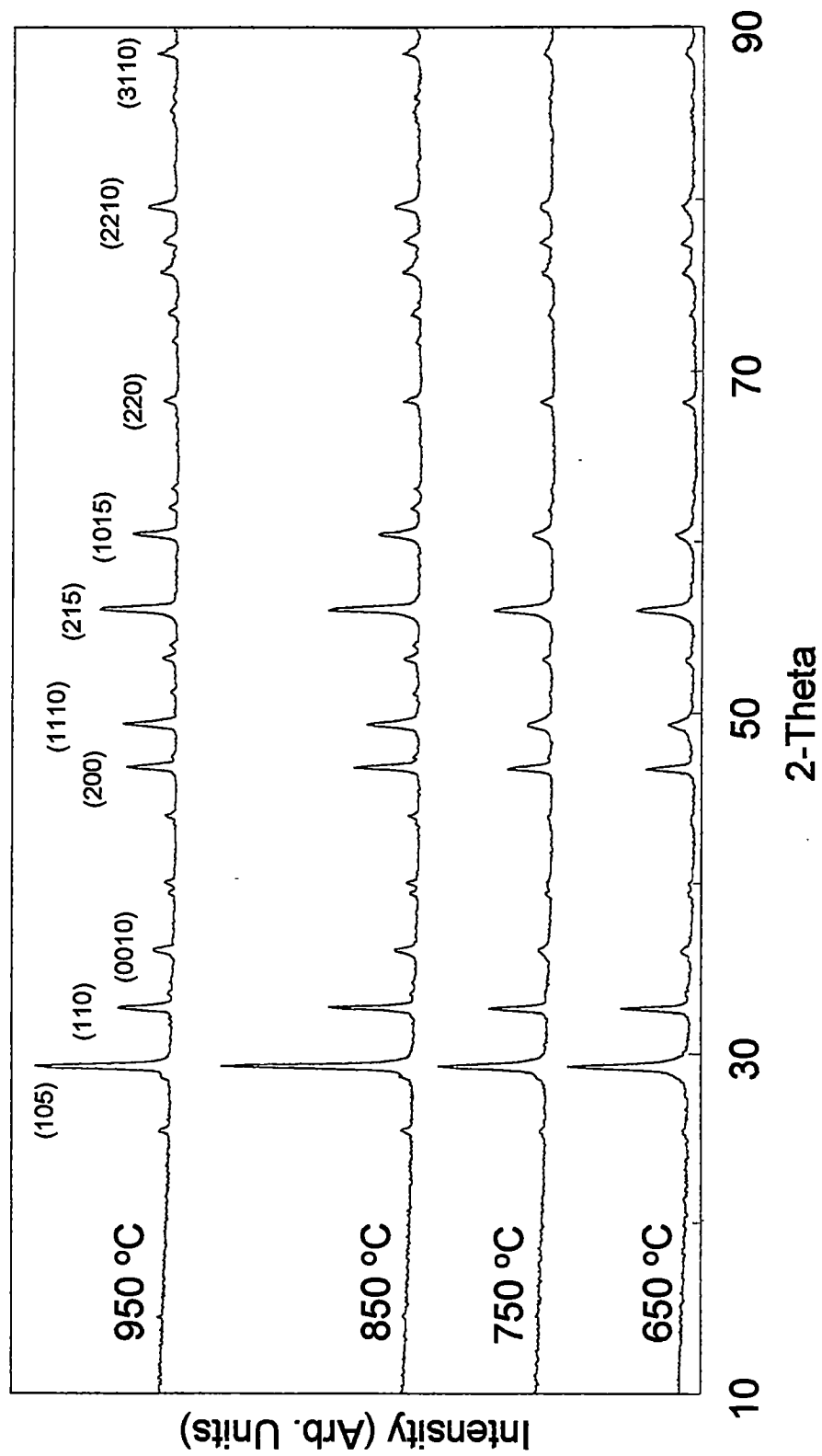
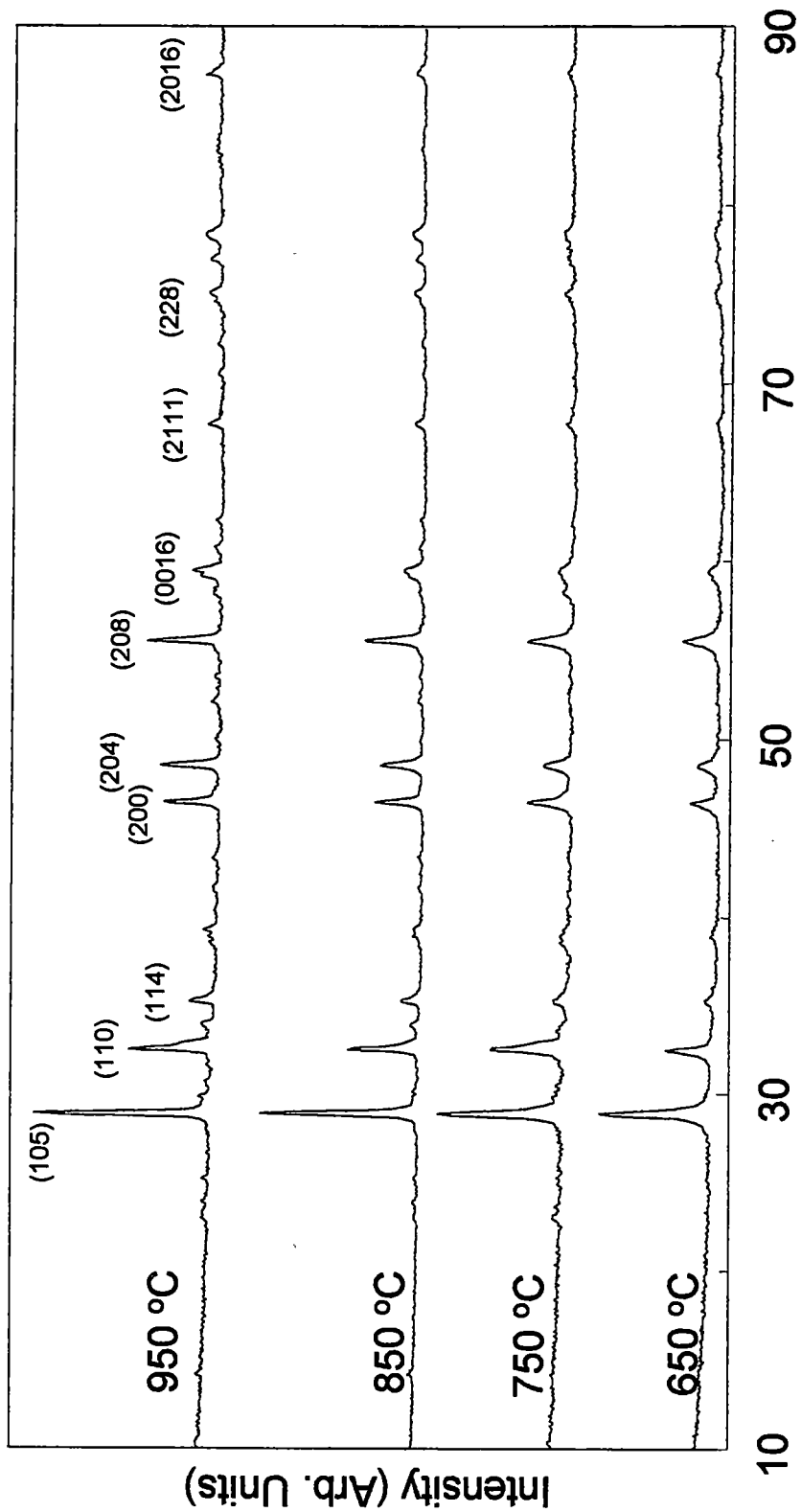
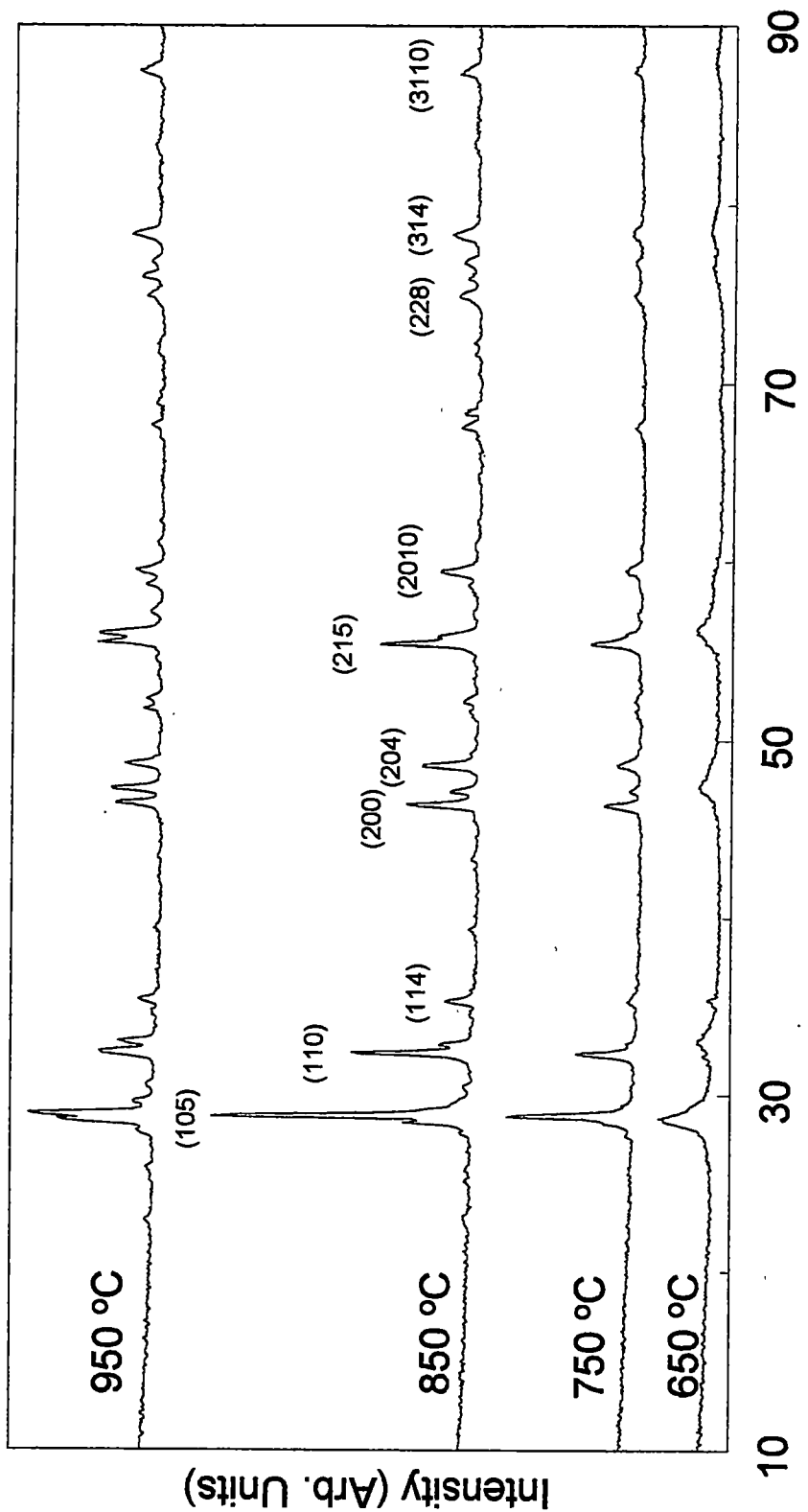


Figure 2.7. Theta/2-theta XRD of SrBi<sub>2</sub>Nb<sub>2</sub>O<sub>9</sub> powders.



2-Theta

Figure 2.8. Theta/2-theta XRD of BaBi<sub>2</sub>Nb<sub>2</sub>O<sub>9</sub> powders.



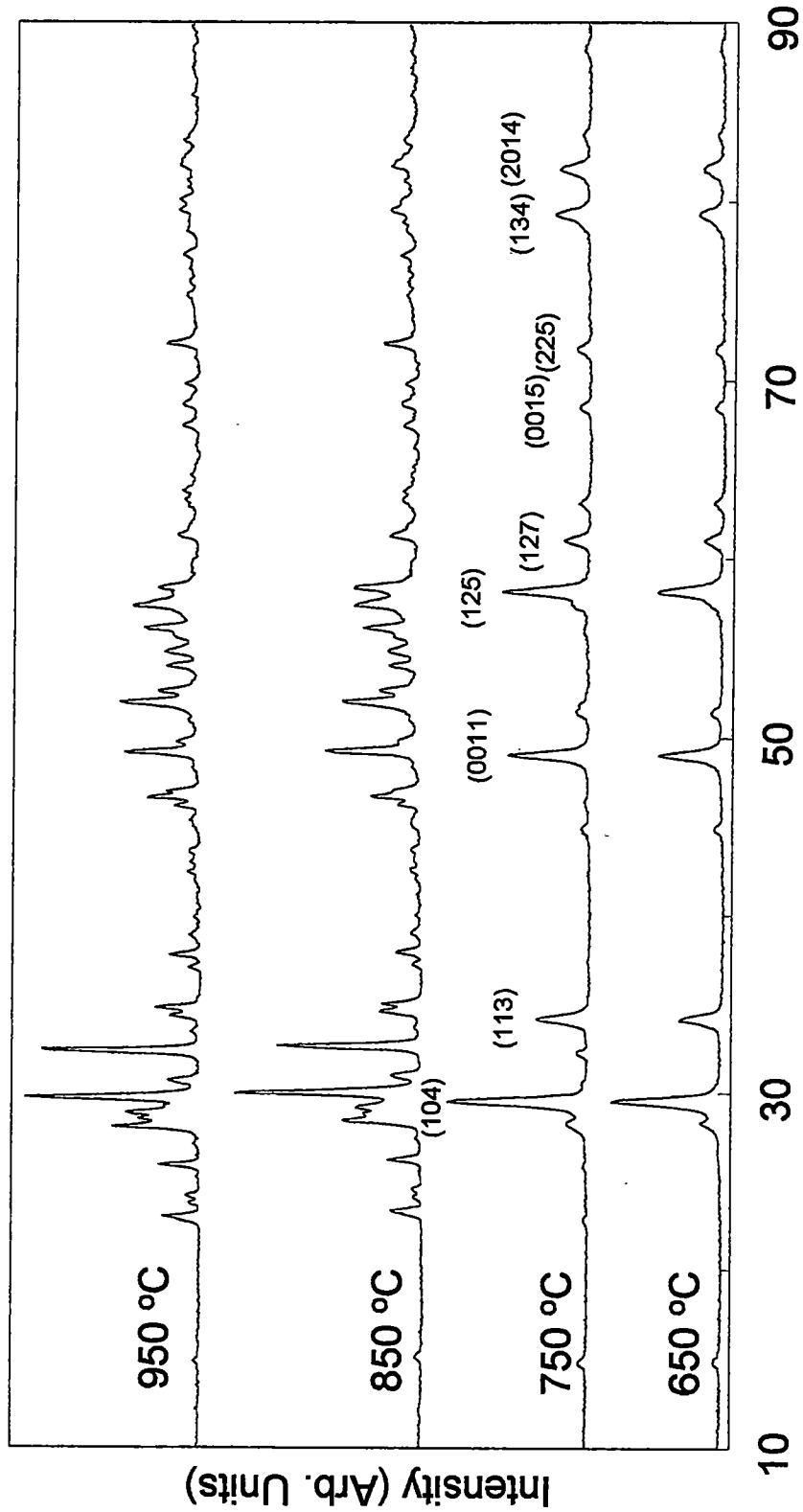
2-Theta

Figure 2.9. Theta/2-theta XRD of BaBi<sub>2</sub>Ta<sub>2</sub>O<sub>9</sub> powders.

**Table 2.2.** Lattice constants for (Sr,Ba)Bi<sub>2</sub>(Nb,Ta)<sub>2</sub>O<sub>9</sub> powders.

Compound	<i>I4mmm</i>		<i>Fmmm</i>		
	<i>a</i>	<i>c</i>	<i>a</i>	<i>b</i>	<i>c</i>
SrBi <sub>2</sub> Nb <sub>2</sub> O <sub>9</sub>	3.885(1)*	25.00(1)	3.869(3)	3.893(3)	24.88(2)
SrBi <sub>2</sub> Ta <sub>2</sub> O <sub>9</sub>	3.898(1)	25.24(1)	3.875(3)	3.912(3)	25.11(2)
BaBi <sub>2</sub> Nb <sub>2</sub> O <sub>9</sub>	3.908(2)	24.93(2)	3.901(2)	3.923(3)	24.97(2)
BaBi <sub>2</sub> Ta <sub>2</sub> O <sub>9</sub>	3.922(2)	25.27(1)	3.895(4)	3.936(4)	25.11(2)

\*Uncertainty in the last digit indicated parenthetically.



2-Theta

Figure 2.10. Theta/2-theta XRD of BaBiTa<sub>2.85</sub>O<sub>9.64</sub> powders.

material. A difference pattern resembling a bismuth deficient pyrochlore phase was observed when subtracting the 850 °C diffractogram from the 950 °C diffractogram.<sup>71</sup> The presence of 10% excess bismuth helps prevent the decomposition of BBT and the formation of bismuth deficient pyrochlore phase. Figure 2.11 shows BBT powders with 10% excess bismuth, and the theta/2-theta scans show approximately the same changes in intensities as with regular bismuth containing BBT powder upon heating from 850 °C to 950 °C.

### **2.3.3. XRD Analysis of Bismuth Containing Perovskite Films on Silver Substrates**

Silver substrates were used in order to find a more inert electrode material and to avoid difficulties associated with excess bismuth.<sup>72</sup> There is also considerable technological interest in these materials because polycrystalline films on noble metal electrodes have been shown to be fatigue free, a problem which limited the utility of materials such as lead zirconium titanate (PZT) in nonvolatile electronic memory. Films of the bismuth containing perovskites were spin-coated on silver coupons approximately 0.13 mm thick. These films were annealed in air in order to observe the temperature dependence of crystallization. The crystallization started at 650 °C and full crystallization was observed at 850 °C. Figure 2.12 shows the theta/2-theta scans of SBT, SBN, BBN and BBT on silver at 850 °C. Each film on the silver sheets showed strong c-axis orientation with more than an order of magnitude

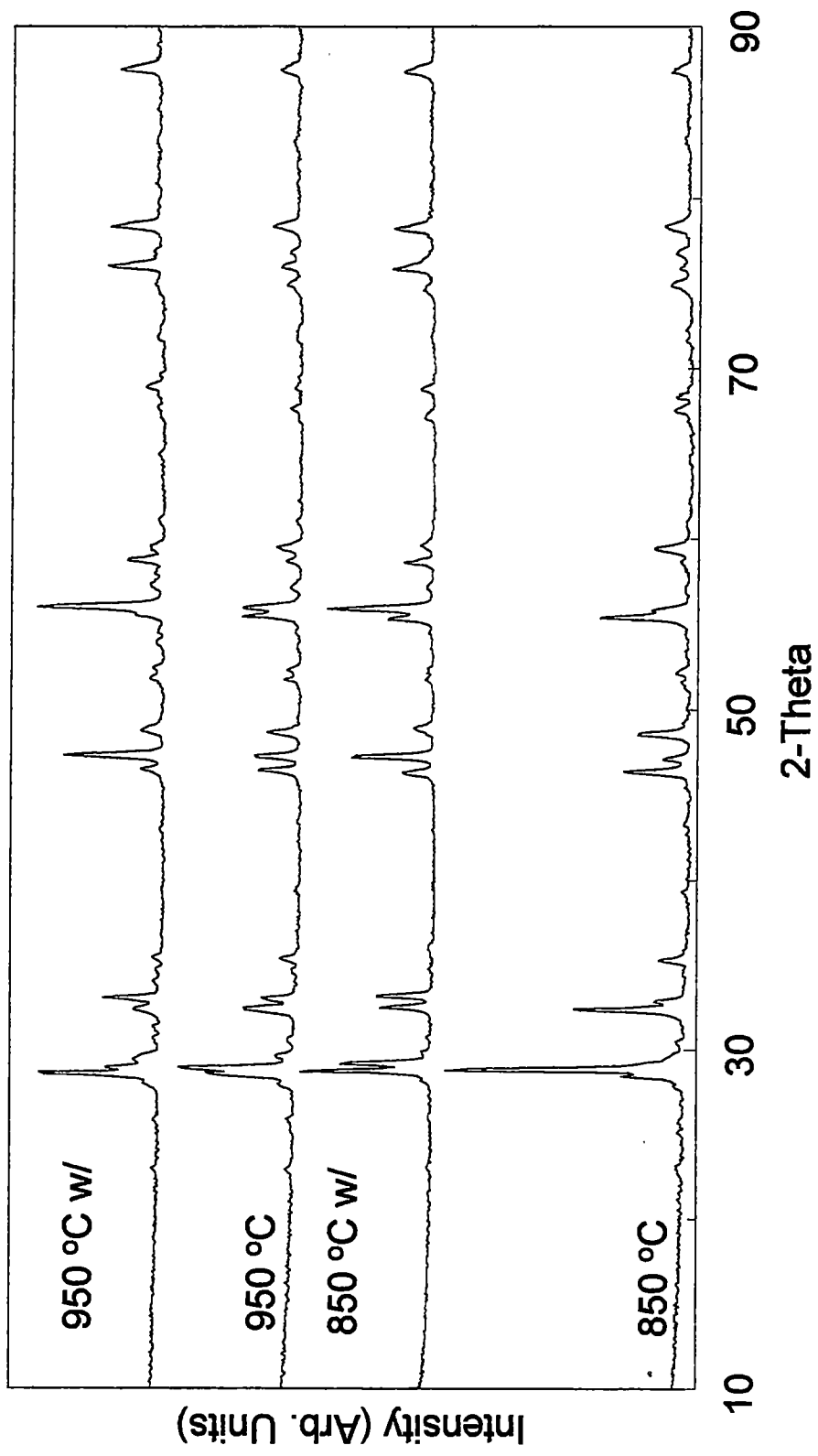


Figure 2.11. Theta/2-theta XRD of BaBi<sub>2</sub>Ta<sub>2</sub>O<sub>9</sub> powders with and without 10% excess Bi at 850 °C and 950 °C.

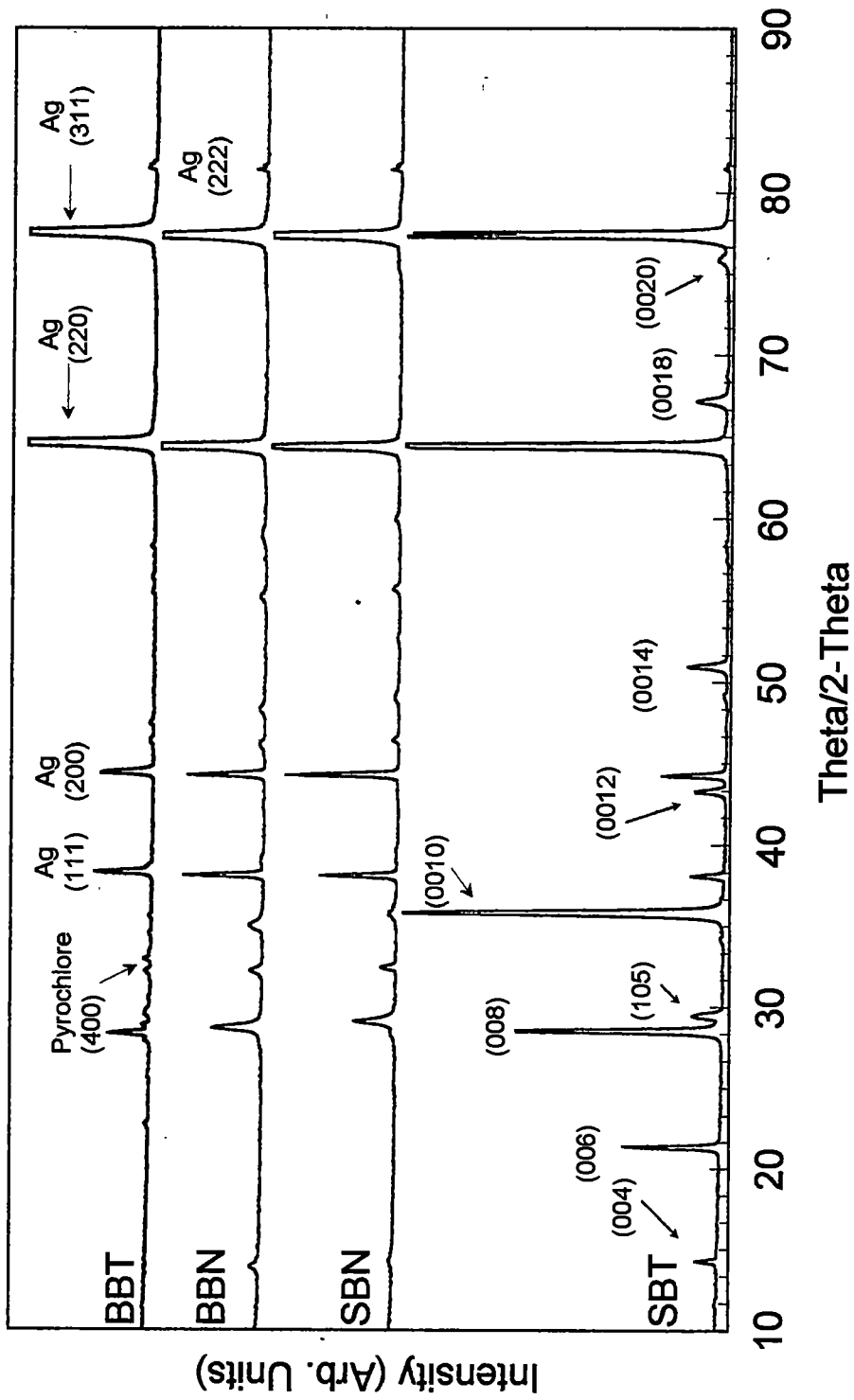


Figure 2.12. Theta/2-Theta XRD of SBT, SBN, BBN, and BBT on Ag at 850 °C.



increase in intensity of the (00 $l$ ) lines. Phi-scans about the (107) reflection were conducted on the films, and no in-plane orientation was observed. The silver sheet showed indications of preferred orientation, and the (220) and (311) reflections were nearly five times more intense than randomly oriented silver. These results indicate that the silver sheets may act as a template for crystallization of the bismuth containing perovskites.

#### **2.3.4. Electrical Characterization**

Dielectric constants and leakage currents for stoichiometric SBT films 2000 Å thick on evaporated silver as a function of temperature are shown in Figure 2.13. The maximum dielectric constant at an annealing temperature of 850 °C was 280, lower than the best value of 347 obtained on platinum,<sup>61</sup> and the leakage current was  $1 \times 10^{-6}$  A/cm<sup>2</sup> at 850 °C. The addition of excess bismuth would probably improve these values. Also, it was necessary to anneal the samples for relatively long times (30 min) in pure oxygen to obtain insulating materials. Rapid thermal processing, which is very useful in lead titanate-based dielectrics, was of limited value in processing these films. It was also difficult to obtain samples much thinner than 2000 Å that had leakage currents sufficiently low to allow reliable dielectric measurements. Prolonged heating, even at 650 °C, in an oxidizing ambient, may make these materials difficult to integrate into standard silicon technology.

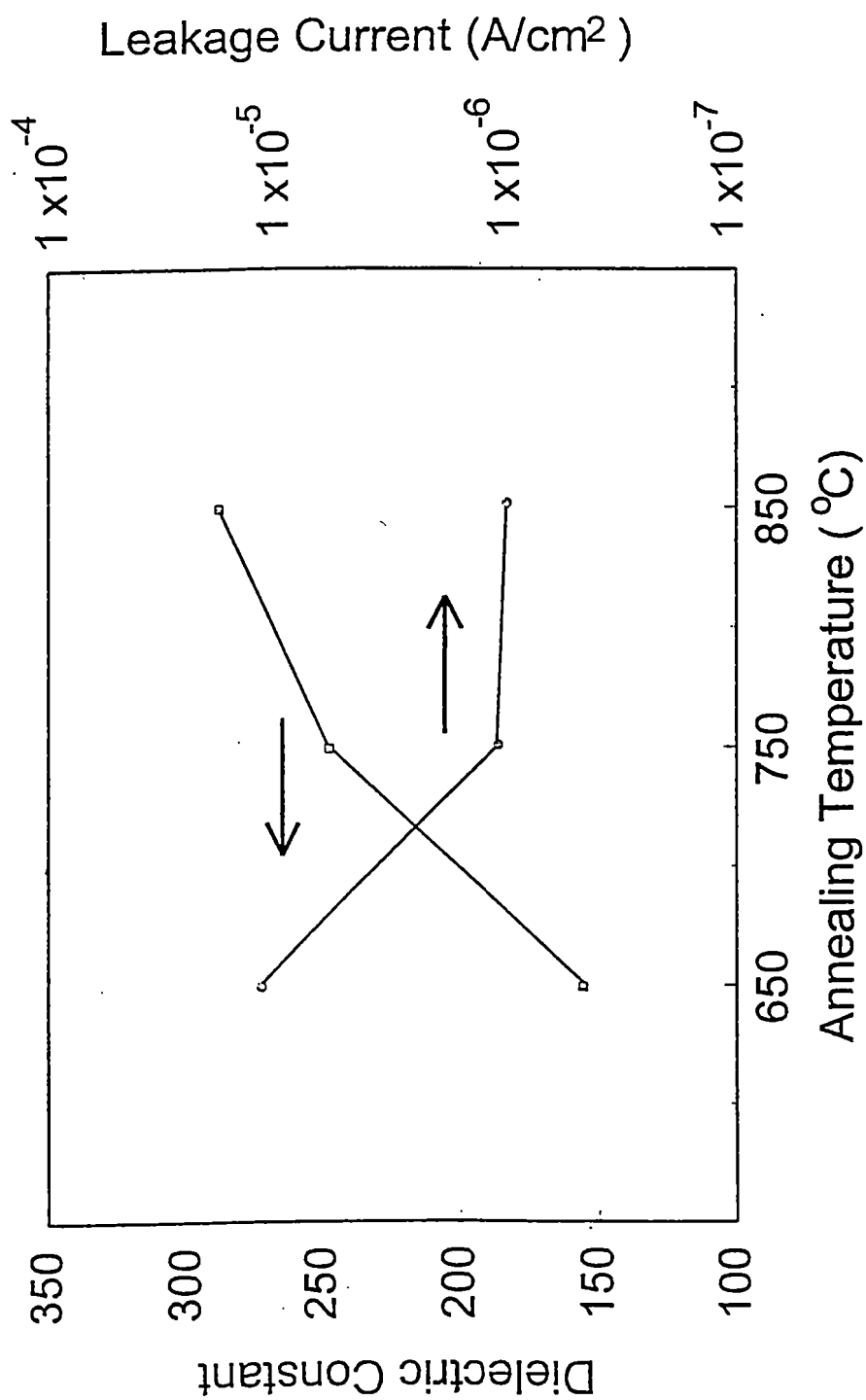


Figure 2.13. Plot of dielectric constants and leakage currents of SBT on evaporated silver at various temperatures.

### 2.3.5. XRD Analysis of Bismuth Containing Perovskite Films on Strontium Titanate and Lanthanum Aluminate

During the course of this investigation, it was observed that commercially obtained single-crystal substrates were mis-cut by 1 to 2°. The XRD peaks of the single-crystal oxide substrates, strontium titanate and lanthanum aluminate, had fwhm values of less than 0.5°. The combination of this mis-cut and the narrowness of the peaks made it difficult to align the (*h*00) peaks of the substrate, and therefore, some of the (*h*00) reflections were not observed in the XRD data.

Solutions of SBT, SBN, BBN, and BBT were each deposited on strontium titanate and lanthanum aluminate. Table 2.3 shows lattice constants for each of the perovskites on (100) strontium titanate and (100) lanthanum aluminate. Out-of-plane orientation was determined by theta/2-theta scans using a four circle diffractometer at chi slightly less than 90°. Since the substrate peaks are slightly narrower than the film peaks, the substrate peaks can be almost completely suppressed. Spectra of films on strontium titanate and lanthanum aluminate are shown in Figures 2.14 and 2.15, respectively. Besides a few small peaks of the bismuth deficient pyrochlore phase, mostly (002 $\ell$ ) reflections were observed for films on strontium titanate and were consistent with strong *c*-axis oriented Aurivillius compounds. For films on lanthanum aluminate, all the films except BBT showed the desired phase. The diffractogram of BBT showed

**Table 2.3.** Lattice constants of SrBi<sub>2</sub>Nb<sub>2</sub>O<sub>9</sub>, SrBi<sub>2</sub>Ta<sub>2</sub>O<sub>9</sub>, BaBi<sub>2</sub>Nb<sub>2</sub>O<sub>9</sub>, and BaBi<sub>2</sub>Ta<sub>2</sub>O<sub>9</sub> on SrTiO<sub>3</sub> and LaAlO<sub>3</sub>.

Film	<i>a</i> (Å)	<i>c</i> (Å)
STO	3.905	
SBN on STO	3.82(1)*	25.0(1)
SBT on STO	3.85(1)	25.0(1)
BBN on STO	3.92(1)	25.6(1)
BBT on STO	3.96(1)	25.5(1)
LAO	3.793	
SBN on LAO	3.82(1)	25.0(1)
SBT on LAO	3.86(1)	25.0(1)
BBN on LAO	3.93(1)	25.6(1)

\* Uncertainty in the last digit indicated parenthetically.

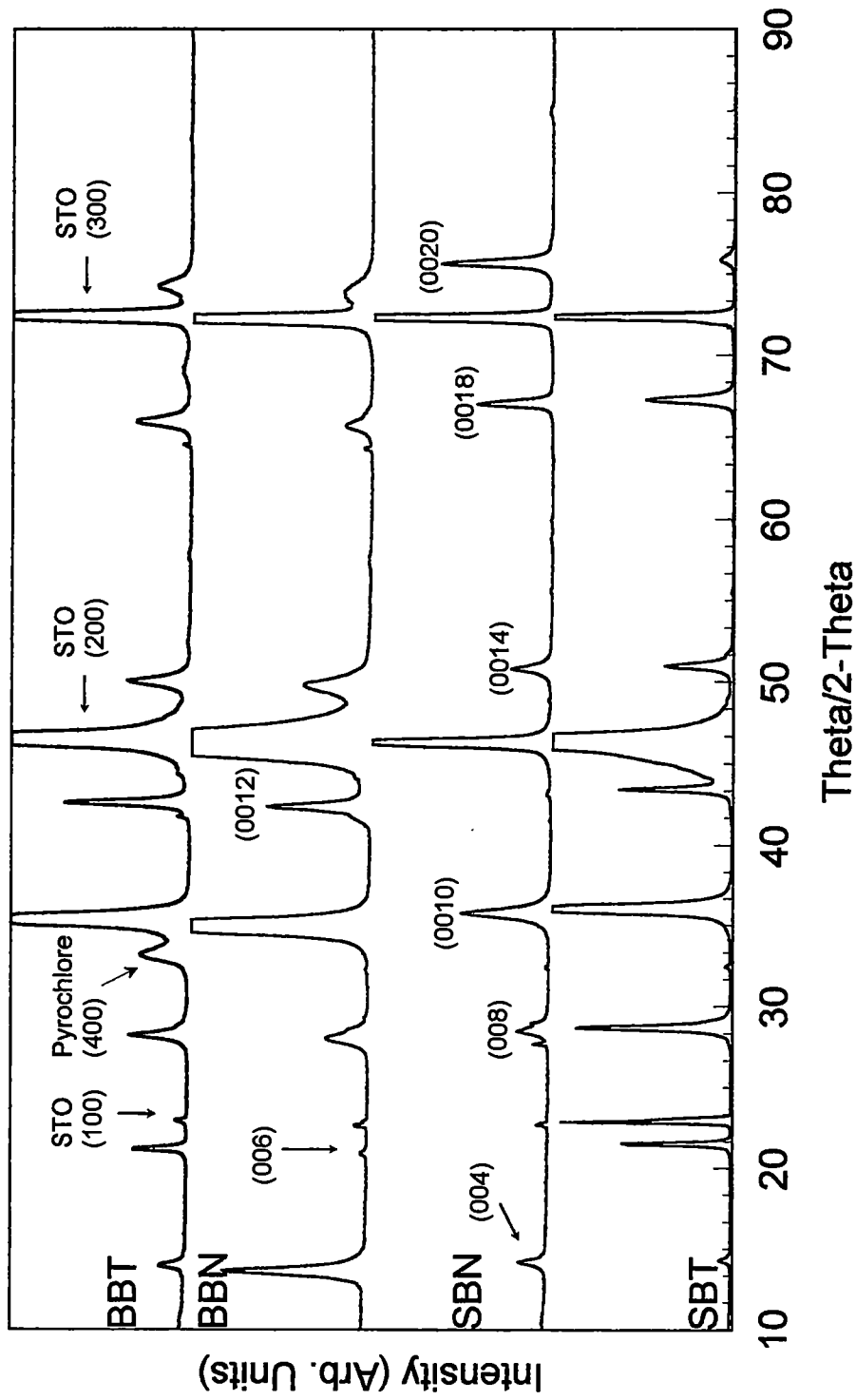


Figure 2.14. Theta/2-Theta XRD of SBT, SBN, BBN, and BBT on SrTiO<sub>3</sub> at 850 °C.

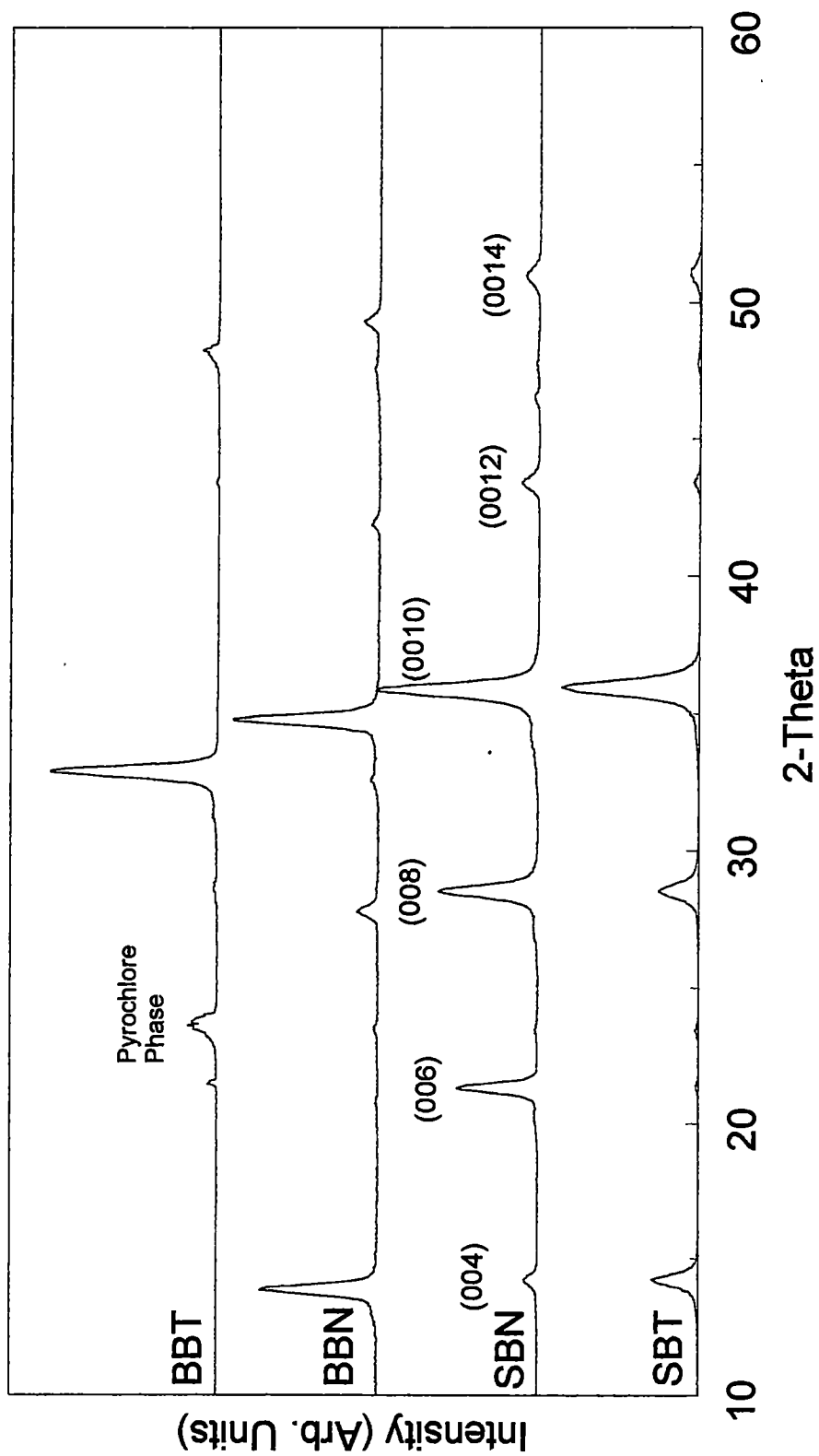


Figure 2.15. Theta/2-theta XRD of SBT, SBN, BBN, and BBT on LaAlO<sub>3</sub> at 850 °C.

only a single intense peak which is not consistent with its c-axis lattice parameter obtained from the powder studies.

### **2.3.6. Out-of-Plane and In-Plane Texture Analysis of Bismuth Containing Perovskites on Strontium Titanate and Lanthanum Aluminate**

Omega scans (rocking curves) about the (0010) reflection were used to measure the mosaic character (degree of crystallinity) of the film. Table 2.4 shows the full width at half maximum (fwhm) of the out-of-plane peaks and illustrates the fact that all of the films on both strontium titanate and lanthanum aluminate showed excellent out-of-plane orientation. A representative omega scan of SBT on (100) strontium titanate about the (0010) reflection is shown in Figure 2.16.

Pole figures about the (105) plane with chi at 39° and phi at 0° were obtained to help determine the nature of the in-plane epitaxy. Figure 2.17 shows a representative pole figure of SBN on (100) strontium titanate about the (105) reflection. The expected four-fold symmetry of the tetragonal bismuth perovskites was observed. In order to assess the quality of the in-plane epitaxy, phi scans were obtained. A representative phi scan of SBT on (100) strontium titanate about the (105) reflection is shown in Figure 2.16. Table 2.4 reports all fwhm values of the phi scans for the bismuth containing perovskites on strontium titanate and lanthanum aluminate. The in-plane peak widths are

**Table 2.4.** Full-width at half-maximum values for (Sr,Ba)Bi<sub>2</sub>(Nb,Ta)<sub>2</sub>O<sub>9</sub> on SrTiO<sub>3</sub> and LaAlO<sub>3</sub>.

Film	out-of-plane fwhm (°) about the (0010) reflection	in-plane fwhm (°) about the (105) reflection
SBN on STO	0.39(5)*	0.48(5)
SBT on STO	0.36(5)	0.45(5)
BBN on STO	0.88(5)	0.74(5)
BBT on STO	0.92(5)	0.82(5)
SBN on LAO	1.00(5)	0.84(5)
SBT on LAO	1.41(5)	1.02(5)
BBN on LAO	1.62(5)	1.14(5)

\*Uncertainty in the last digit indicated parenthetically.



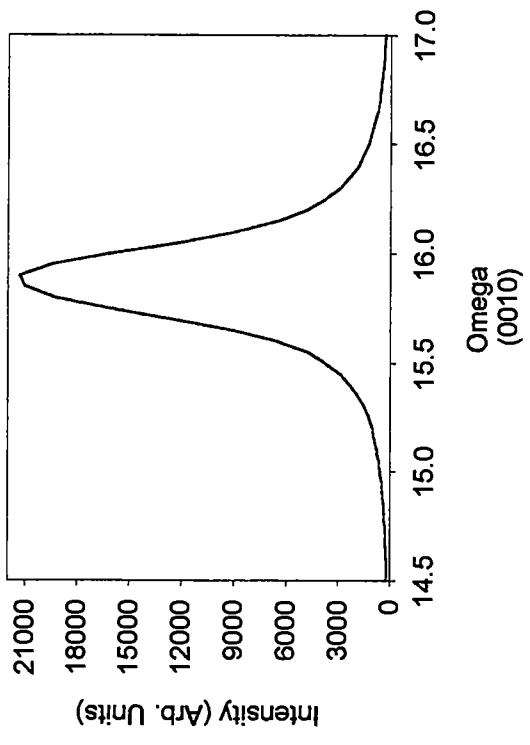
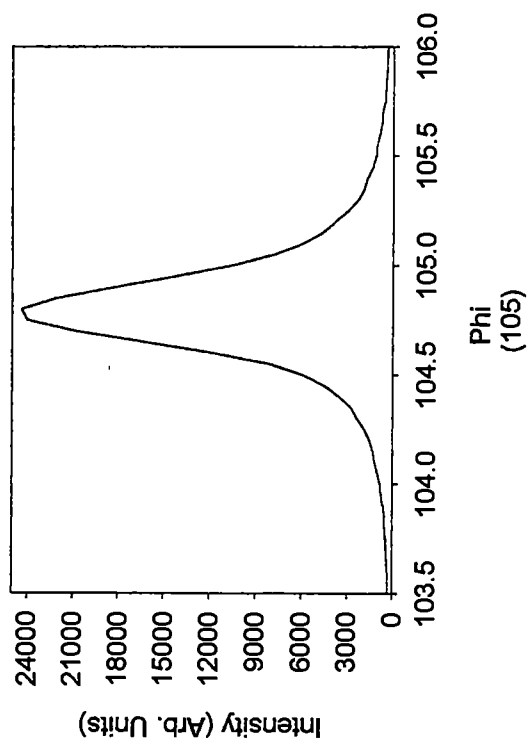
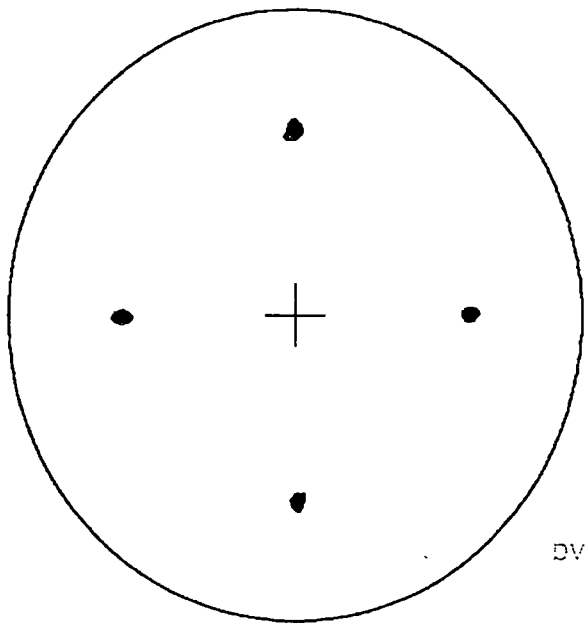


Figure 2.16. Omega scan and phi scan of SrBi<sub>2</sub>Nb<sub>2</sub>O<sub>9</sub> on SrTiO<sub>3</sub>.



DV 1

$\text{SrBi}_2\text{Nb}_2\text{O}_9$  on  $\text{SrTiO}_3$   
(105) reflection

Figure 2.17. Pole figure of  $\text{SrBi}_2\text{Nb}_2\text{O}_9$  on  $\text{SrTiO}_3$  about the (105) reflection.

proportional to the lattice mismatch between the film and the substrate and are significantly larger than those of the out-of-plane peaks.

The measured values of lattice mismatch of the in-plane lattice constants were plotted against the fwhm of phi scans in Figure 2.18. There was a good correlation between the lattice mismatch and film quality. It appeared from the plot that the film quality is degraded more by compressive stress than by tensile stress. In addition, the difficulty in growing the desired phase of BBT on lanthanum aluminate may be due to the larger lattice constant mismatch.

#### **2.4. Conclusion**

High quality bismuth-containing ferroelectric films have been produced (through novel sol-gel chemistry). The solution synthesis was shown to be simple and inexpensive in producing these important films with anisotropic electrical and optical properties. SBT films on silver substrates had a dielectric constant of 280 and leakage currents of  $1 \times 10^{-6} \text{ A/cm}^2$  at an annealing temperature of 850 °C.

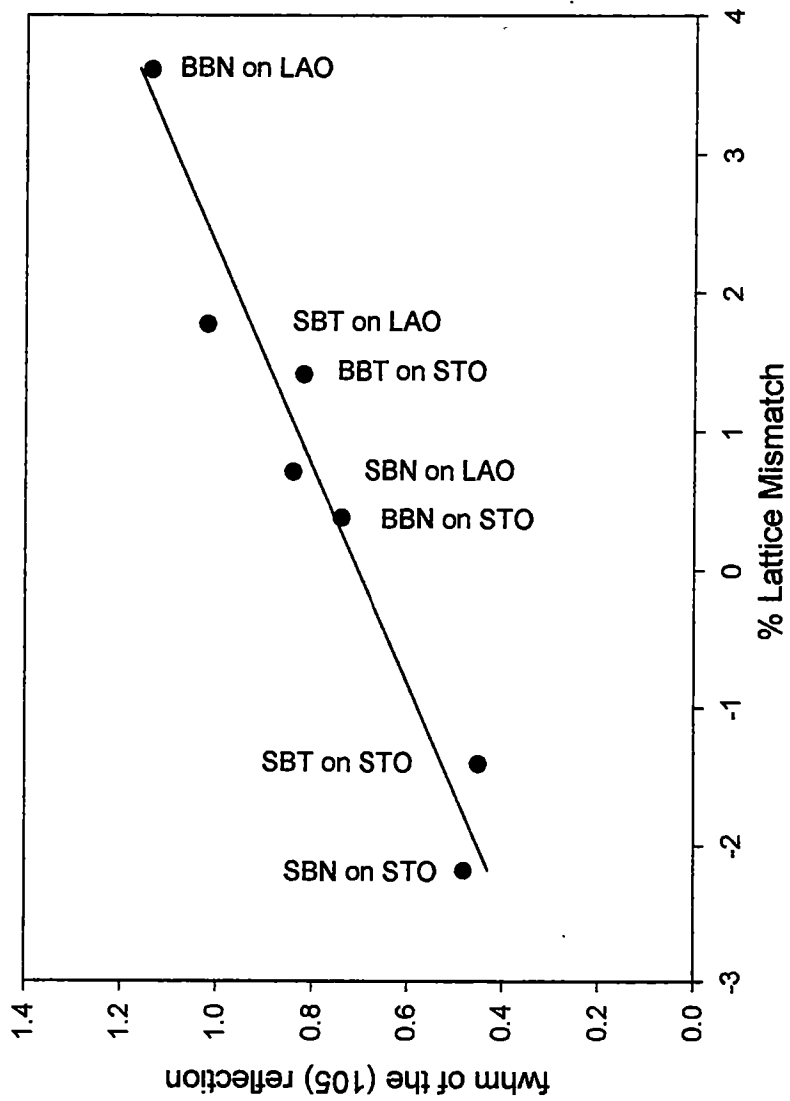


Figure 2.18. Plot of fwhm of phi scans (in degrees) versus % lattice mismatch.

## CHAPTER 3

### EPITAXIAL GROWTH OF RARE-EARTH GALLATES AND $AA'GaO_3$

#### MIXED METAL OXIDE THIN-FILMS

##### 3.1. Introduction

Thin-films of copper oxide-based high temperature superconductors (HTS) often require the use of buffer layer(s) between the superconducting layer and the substrate on which they are grown. There are several requirements for buffer layers in order to achieve high critical currents in HTS materials. The buffer layers must be chemically compatible with the superconducting film and the substrate, have good mechanical properties, and, in the case of epitaxial films, have good lattice match to the superconducting layer. Other requirements for thin-films used in HTS-based microwave devices are low dielectric loss ( $\tan \delta$ ) and a low dielectric constant ( $\epsilon$ ). Buffer layers consisting of neodymium gallate, praseodymium gallate and lanthanum gallate have been shown to meet these requirements. A review of their properties and their suitability as substrates for HTS has been published.<sup>40</sup> Heteroepitaxial buffer layers of a desired material on a readily available substrate have been used as an alternative to producing single-crystal substrates.

There have been, to our knowledge, no reports of heteroepitaxial growth of these buffer layers using physical deposition methods. This is perhaps due

to difficulties in stoichiometric evaporation, sputtering or ablation of rare-earth gallate targets. The sputtering or ablation rates of rare-earth atoms are significantly different from those of gallium. Metal Organic Chemical Vapor Deposition (MOCVD) has been used to grow heteroepitaxial films of neodymium gallate<sup>73</sup> and praseodymium gallate<sup>74</sup> on lanthanum aluminate. Growth of multicationic films by MOCVD is often difficult as single metal precursors usually decompose at different rates, leading to poor control of stoichiometry. Solution synthesis, in comparison, is known to provide accurate control of film stoichiometry and to produce high quality films.

Solution routes to epitaxial thin-films have been the subject of a review by Lange.<sup>28</sup> The following sections of this chapter provide the experimental procedures and results for powders (under oxidizing or reducing conditions) and solution deposition of neodymium gallate, praseodymium gallate, lanthanum gallate, gadolinium gallate, yttrium gallate, and mixed rare-earth metal gallates  $\text{La}_{0.5}\text{Nd}_{0.5}\text{GaO}_3$  and  $\text{La}_{0.5}\text{Y}_{0.5}\text{GaO}_3$ . The rare-earth gallate solutions were deposited on silver foil, (100) strontium titanate, and (100) lanthanum aluminate. Epitaxial growth of rare-earth gallate thin-films on roll-textured nickel was unsuccessful. The structural properties of thin-films on these substrates were studied by X-ray diffraction (XRD). Results of copper oxide-based high temperature superconductors with neodymium gallate as a buffer layer are also discussed. The sol-gel chemistry used here was

pioneered by Payne *et al.*,<sup>19</sup> and is based on solutions of metal methoxyethoxide complexes in 2-methoxyethanol.

## 3.2. Experimental Details

### 3.2.1. General Procedures

All manipulations were performed under dry argon atmosphere with the use of either standard Schlenk techniques or a glove box. <sup>1</sup>H NMR spectra were recorded on a Bruker AC-400 Fourier transform spectrometer, and were referenced to residual benzene-*d*<sub>6</sub>. Lanthanum isopropoxide (Gelest, 99.9%), neodymium metal (Alfa Aesar, 99.9%), praseodymium metal (Alfa Aesar, 99.9%), gadolinium metal (Alfa Aesar, 99.9%), yttrium metal (Alfa Aesar, 99.9%) and gallium trichloride (Alfa Aesar, 99.9%) were used as received. Benzene was dried over sodium/benzophenone and distilled before use.

### 3.2.2. Preparation of Gallium Isopropoxide, Ga(OPr)<sup>i</sup><sub>3</sub>

Gallium isopropoxide, Ga(*i*-OC<sub>3</sub>H<sub>7</sub>)<sub>3</sub>, was prepared from the reaction of gallium trichloride and sodium isopropoxide first reported by Mehrotra.<sup>75</sup> A 250 mL Schlenk flask with a magnetic stir bar and condenser was charged with 4.88 g (0.212 mol) of crushed sodium metal, 18 mL of dry isopropanol and 100 mL of dry benzene. The mixture was refluxed at 85 °C overnight to insure complete reaction of the sodium and isopropanol. Another 250 mL Schlenk flask was

charged with 12.0 g (68 mmol) of  $\text{GaCl}_3$  and 50 mL of benzene. The  $\text{GaCl}_3$  was allowed to dissolve in benzene, and added dropwise to the  $\text{NaOPr}^i$  solution from the top of the condenser via a syringe to maintain a gentle reflux. The mixture then refluxed for 8 h, and filtered afterwards. The volatiles in the filtrate were removed at 23 °C under vacuum to give a viscous oil. A microdistillation apparatus was attached to the Schlenk flask and the solution was distilled under reduced pressure. Approximately 8.8 g (66.8 mmol, 52%) of  $\text{Ga}(\text{i-OC}_3\text{H}_7)_3$  were collected at 137-141 °C and 0.1 torr. The gallium isopropoxide was placed in an inert atmosphere drybox and allowed to harden from a colorless viscous liquid to a semi-solid wax. (Oliver and Worrall<sup>76</sup> have attributed this change in state to conversion of the initially formed trimer to a more stable tetrameric oligomer.)

### 3.2.3. Preparation of Rare-Earth Isopropoxides

Lanthanum, praseodymium, neodymium, gadolinium, and yttrium isopropoxide were prepared by a literature method through the reaction of the metals directly with dry isopropanol in the presence of mercuric catalysts.<sup>77</sup> Commercial powders of these metals failed to react with dry isopropanol in the presence of a catalyst. Metal filings were obtained by using a rasp to file the metal under an inert atmosphere. The appropriate metal filings [1.736 g (12.5 mmol) of lanthanum, 1.76 g (12.5 mmol) of praseodymium, 1.803 g (12.5 mmol)



of neodymium, 1.966 g (12.5 mmol) of gadolinium, and 1.112 g (12.5 mmol) of yttrium], were added to a 250 mL Schlenk flask with 90 mL of dry isopropanol, a magnetic stir bar, 5 mg of  $\text{Hg}(\text{OOCCH}_3)_2$ , and 5 mg of  $\text{HgCl}_2$ . The mixtures were allowed to reflux overnight at 85 °C and then filtered. The solvent was removed at reduced pressure to give an off-white solid. The lanthanum, praseodymium, neodymium, gadolinium, and yttrium isopropoxides were extracted using a Soxhlet extractor with dry isopropanol and then purified by recrystallization. Yields ranged between 50-70%.

#### **3.2.4. Preparation of Methoxyethoxide Solutions**

The isopropoxides thus prepared were reacted with 90 mL of 2-methoxyethanol to undergo an exchange reaction between the isopropoxide ligand and the methoxyethoxide ligand. Each solution was refluxed for 1 h at 124 °C, and 60 mL of the solvent was then removed by distillation at atmospheric pressure. The solvent removed by distillation was replaced with fresh 2-methoxyethanol. The ligand exchange process was repeated two more times to insure complete ligand exchange. Nuclear magnetic resonance (NMR) was used to verify the ligand exchange. The  $^1\text{H}$  NMR spectra of gallium isopropoxide/methoxyethoxide are shown in Figure 3.1. The NMR spectra show only proton peaks associated with the methoxyethoxide ligand, implying that the ligand exchange was complete.

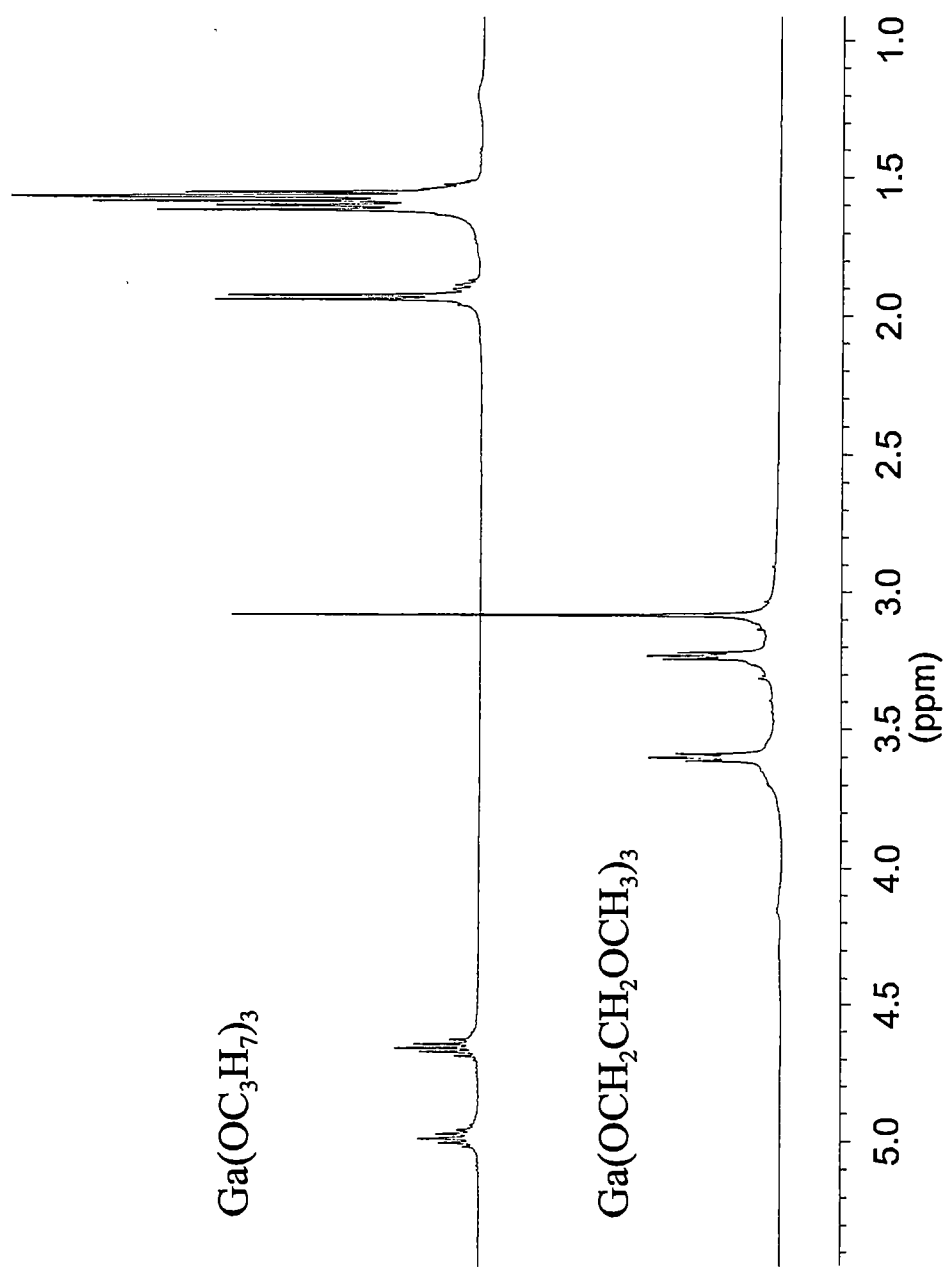


Figure 3.1.  $^1\text{H}$  NMR spectra of gallium isopropoxide and gallium methoxyethoxide.

Each solution was adjusted to 50 mL, and its molality was calculated based on the moles of isopropoxide used and the weight of the solutions. (The use of molality rather than molarity allowed the gravimetric preparation of small volumes of solutions with high accuracy.) Solutions were mixed from the individual stock solutions with the appropriate stoichiometry and refluxed for 1 h to insure proper mixing. The following rare-earth gallium oxides were prepared from the stock solutions: lanthanum gallate ( $\text{LaGaO}_3$ ), praseodymium gallate ( $\text{PrGaO}_3$ ), neodymium gallate ( $\text{NdGaO}_3$ ), gadolinium gallate ( $\text{GdGaO}_3$ ), yttrium gallate ( $\text{YGaO}_3$ ), and  $\text{La}_{0.5}\text{Nd}_{0.5}\text{GaO}_3$  of the general form  $\text{A}_x\text{A}'_{(1-x)}\text{GaO}_3$ .

### 3.2.5. Powder and Film Preparation

The stock solutions were mixed in a ratio of one part hydrolysis solution (1.0 M water in 2-methoxyethanol) to four parts of the stock solution, resulting in a partially hydrolyzed coating solution. Powders were prepared by the addition of excess water to the coating solution followed by the decomposition of the resultant gels at 300 °C. The gels were crushed, ground with a mortar and pestle, and fired (in air for 1 h) at the temperatures indicated in the following section. Each substrate, strontium titanate (100) or lanthanum aluminate (100), was heated for 1 h in oxygen at 1000 °C and 800 °C, respectively, prior to coating. Silver foil was polished with 0.06 micron extra pure alumina abrasive and cleaned in distilled water. The hydrolyzed stock solutions were applied to

the substrates through a 0.2  $\mu\text{m}$  syringe filter and spin coated using a photo-resist spinner for 30 seconds at 2,000 rotations per minute (rpm). The substrates were placed in a preheated, Thermolyne furnace at 850  $^{\circ}\text{C}$  for 20 min in air. Each coat was approximately 70 nm thick, and this coating and firing procedure was repeated four times.

### **3.2.6. Application of Yttrium Barium Copper Oxide Superconductor**

A neodymium gallate buffer layer was deposited by dip-coating a (100) strontium titanate substrate in a 0.25 M solution. The parameters for the dip-coating process consisted of a withdrawal acceleration of 1 mm/s and an initial velocity of 5 mm/s. This produced a film approximately 25 nm thick. The sample was annealed in air at 850  $^{\circ}\text{C}$  for 20 min. The YBCO superconductor was deposited on the neodymium gallate buffer layer by pulsed laser deposition (PLD), using a XeCl excimer laser operating at a wavelength of 308 nm, focused to produce a 3  $\text{J}/\text{cm}^2$  fluence at the YBCO target. The laser-pulse repetition rate was 5 Hz and 6000 laser pulses were required to obtain a film thickness of 250 nm. During the deposition of the YBCO, the strontium titanate temperature was maintained at 780  $^{\circ}\text{C}$  and the oxygen pressure was set at 200 mTorr. The YBCO target was rotated at 21 rpm to minimize both the rate of cone formation and the change in stoichiometry on the surface of the YBCO during laser ablation. After the deposition was completed, the sample was

cooled at a rate of 5 °C/min in 300 Torr of oxygen to 500 °C to ensure full oxygen uptake by the YBCO. Once the temperature reached 500 °C, additional oxygen was added to bring the pressure to 500 Torr, and the temperature and pressure was maintained for 1 h. Finally, the substrate was cooled to room temperature at a rate of 1 °C /min.

### **3.2.7. Critical Current and Critical Temperature Measurements**

In order to obtain critical current ( $I_c$ ) and critical temperature ( $T_c$ ) measurements, four silver electrical contacts, approximately one-half micron thick, were sputtered on a YBCO thin-film surface. The samples were then annealed for 30 min at 500 °C in flowing oxygen to ensure low contact resistance.

The property of resistivity was used to find the critical temperature at a constant current. A four-probe AC measurement was conducted in conjunction with a closed cycle helium refrigerator. Samples were cooled under vacuum to a low temperature, and then slowly warmed. Voltage was measured every 0.2 K during warm up. The  $T_c$  was the temperature reached when resistance first occurred, i.e., when any voltage was detected.

To find the critical current, the sample was put in a constant temperature bath of liquid nitrogen. Current was applied and slowly increased while the

voltage was monitored. When a voltage is first detected at a particular current, the sample is no longer considered to be superconducting.

### **3.3. Results and Discussion**

#### **3.3.1. XRD Analysis of Rare-Earth Gallate Powders**

The annealing behaviors of neodymium gallate, praseodymium gallate and lanthanum gallate powders were evaluated under both oxidizing and reducing conditions. The powders were annealed under reducing conditions to observe their phase behavior. This helped determine if epitaxial growth on substrates sensitive to surface oxidation was possible. Figures 3.2-3.4 show X-ray diffraction patterns of powders annealed at several temperatures for 1 h in air. Figures 3.5-3.7 show X-ray diffraction patterns of powders annealed at several temperatures for 1 h in 4% H<sub>2</sub> in argon. (For simplicity in determining epitaxial relationships between the cubic substrates and the orthorhombic films, X-ray peaks were indexed in a cubic crystal symmetry. Not all of the orthorhombic peaks could be indexed due to the increase in symmetry on going from orthorhombic to cubic.) The data showed that the onset of crystallization occurred at temperatures 100 °C higher under reducing conditions, and all three powders showed one phase. The gadolinium gallate and yttrium gallate powders did not form one phase. They were each a mixture between the garnet Ln<sub>3</sub>Ga<sub>5</sub>O<sub>12</sub> and a two to one phase (Ln<sub>4</sub>Ga<sub>2</sub>O<sub>9</sub>) of the rare-earth gallate. Figure

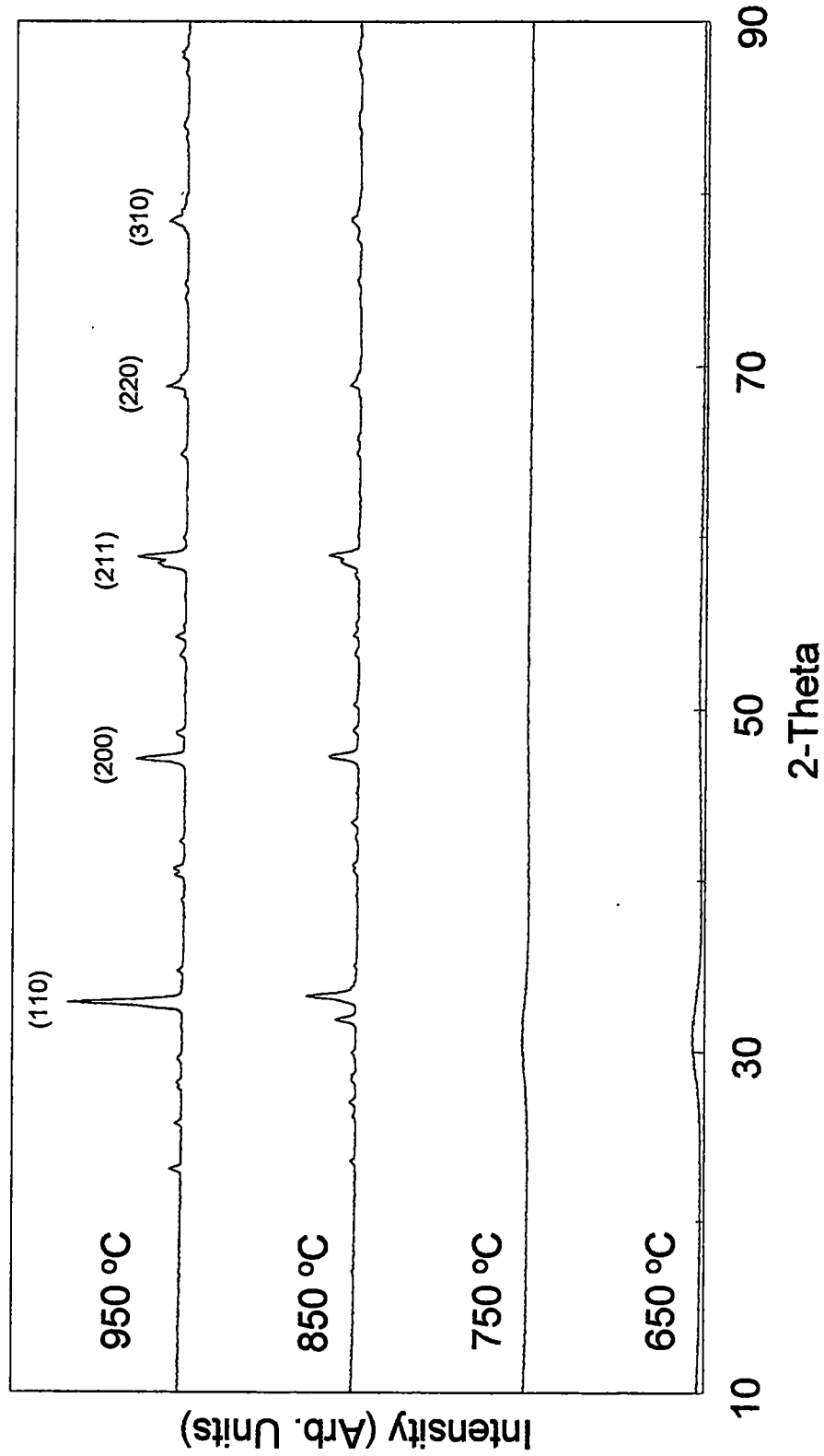
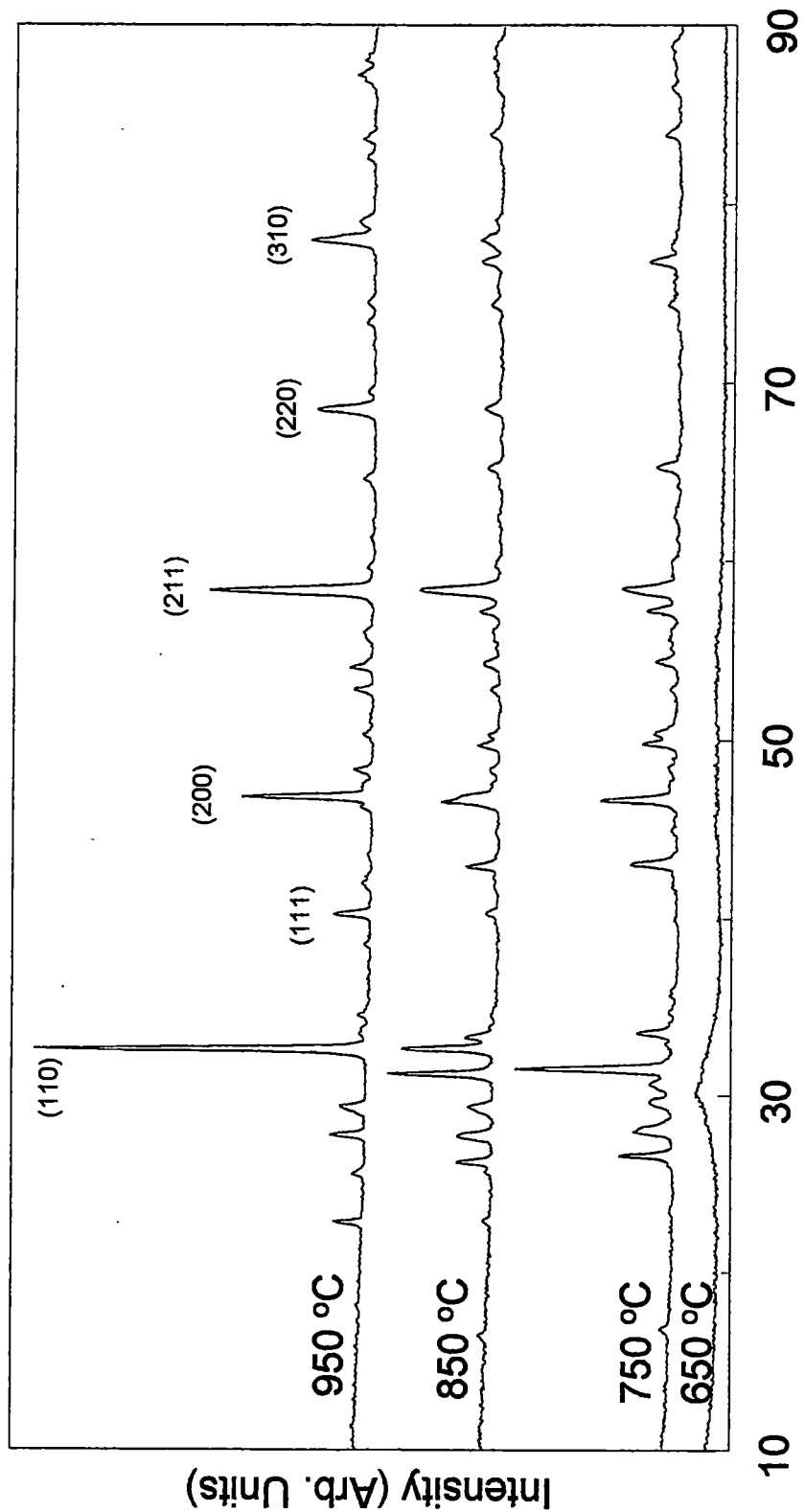


Figure 3.2. Theta/2-theta XRD of NdGaO<sub>3</sub> powders.



2-Theta

Figure 3.3. Theta/2-theta XRD of PrGaO<sub>3</sub> powders.



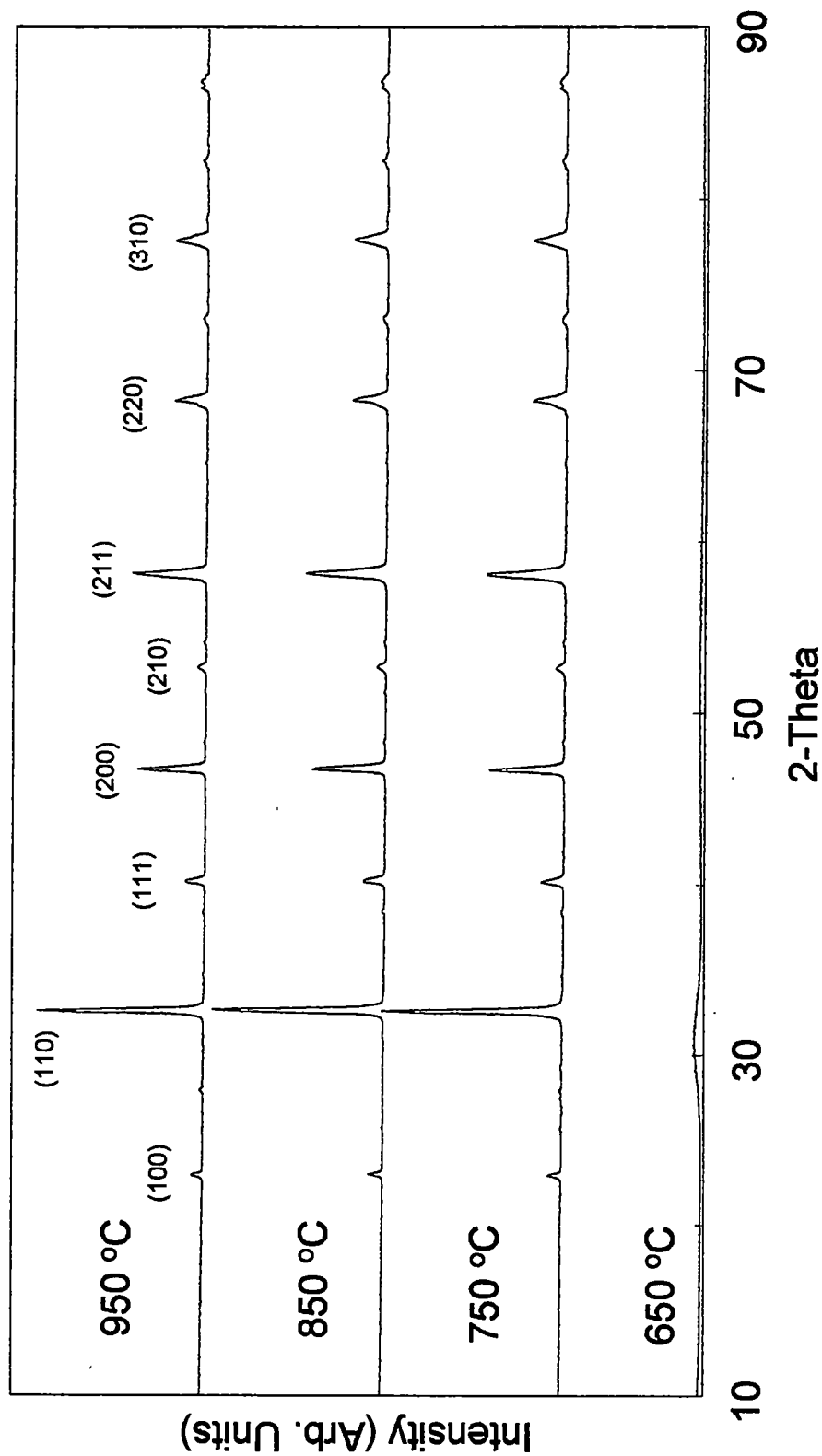


Figure 3.4. Theta/2-theta XRD of LaGaO<sub>3</sub> powders.

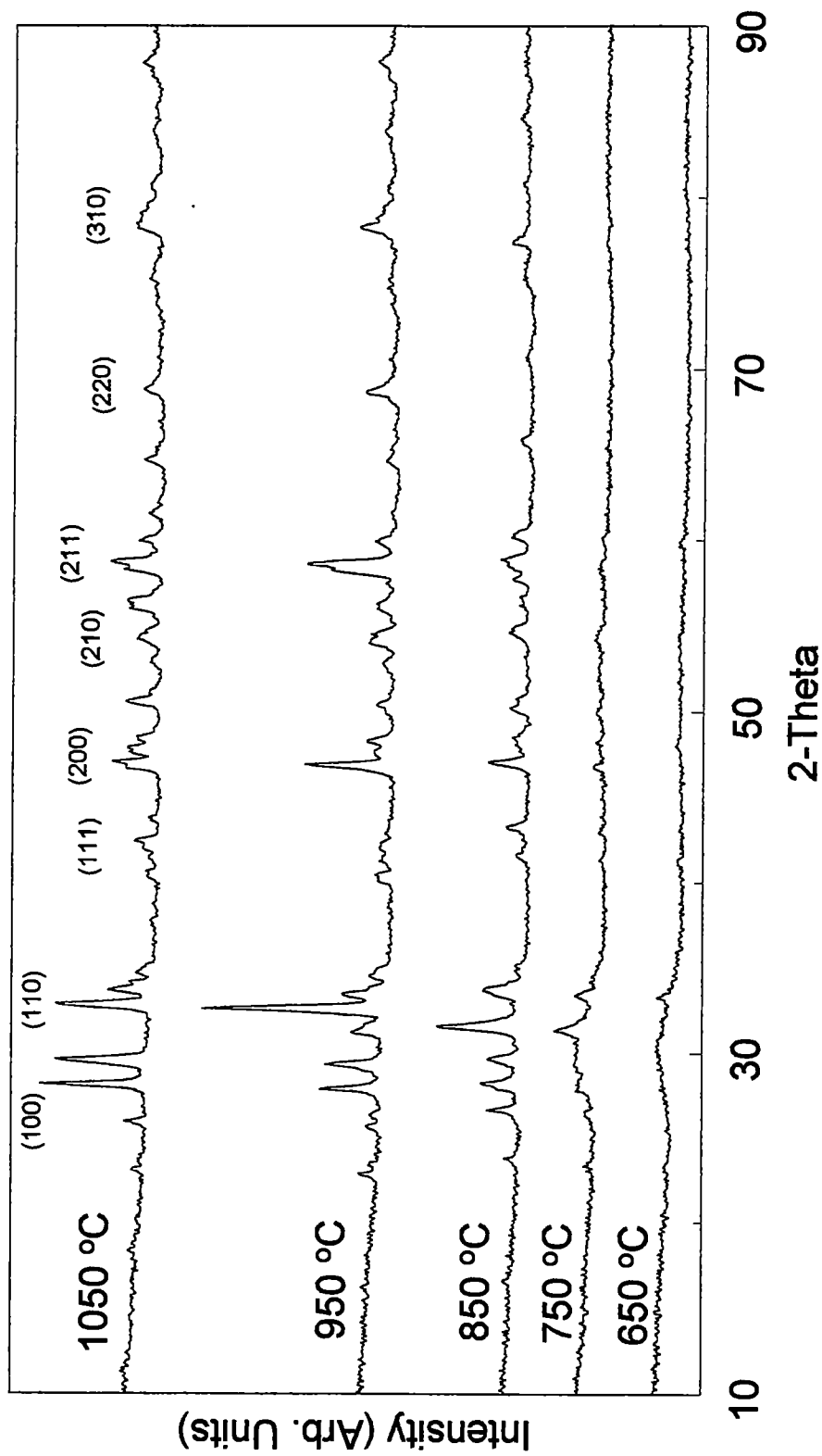


Figure 3.5. Theta/2-theta XRD of NdGaO<sub>3</sub> powders annealed in forming gas.

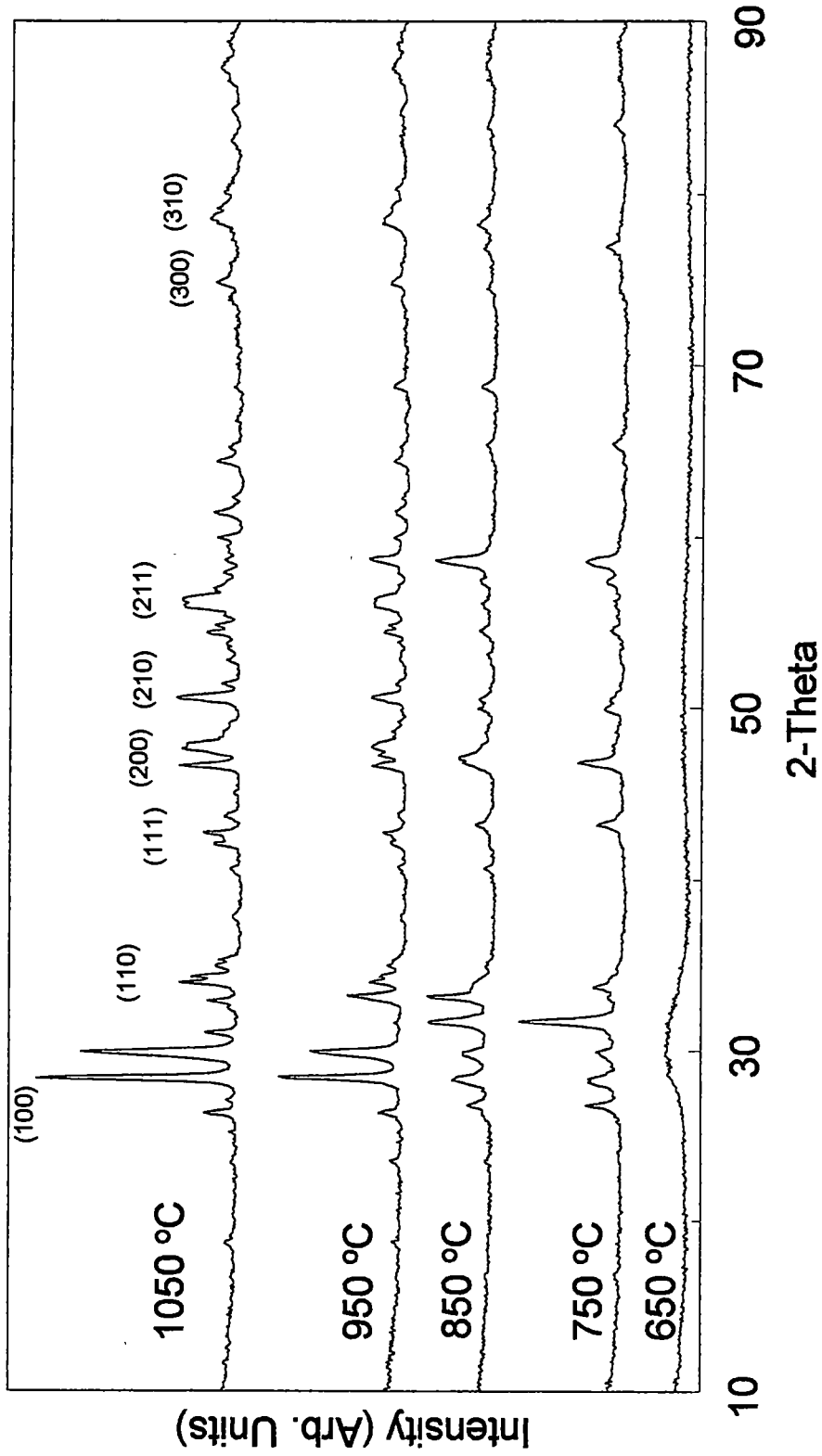


Figure 3.6. Theta/2-theta XRD of PrGaO<sub>3</sub> powders annealed in forming gas.

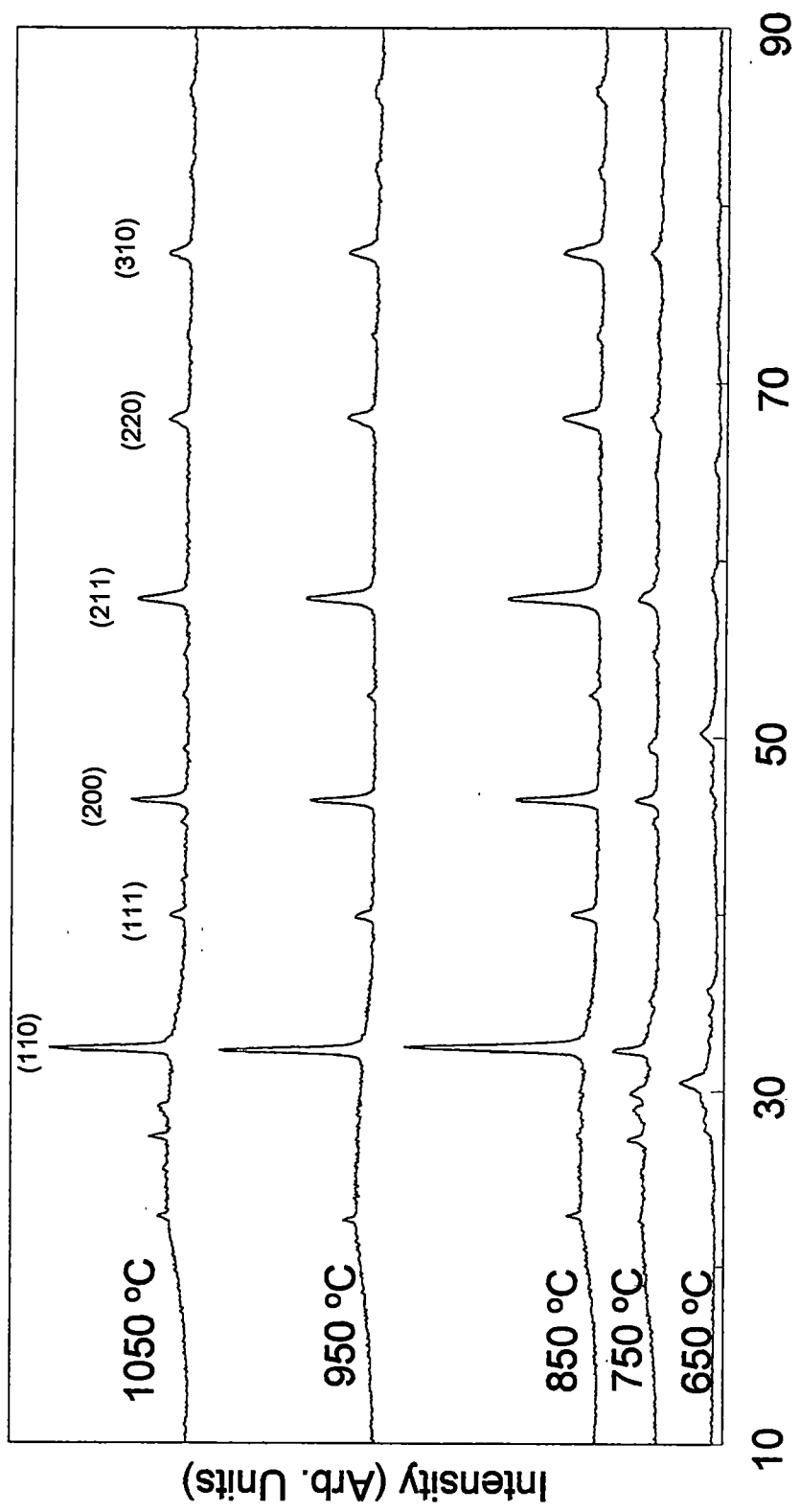


Figure 3.7. Theta/2-theta XRD of LaGaO<sub>3</sub> powders annealed in forming gas.

3.8 shows this mixed phase for the gadolinium gallate and yttrium gallate powders at 850 °C. Since neither had a single phase, they were not annealed under reducing conditions.

### **3.3.2. XRD Analysis of Rare-Earth Gallates on Silver Substrates**

Films were deposited on silver coupons using spin-coating in order to determine the coating characteristics of the solutions. Solutions of approximately 0.25 M gave films that were crack-free and continuous. Film thickness was built up by deposition of successive layers and each layer was annealed at 850 °C for 20 min in air. The thickness was found to be 600-700 Å per layer by etching a step in the films and measuring the step height with an Alpha Step Profilometer. Figure 3.9 shows X-ray diffraction data for polycrystalline films of neodymium gallate, praseodymium gallate, and lanthanum gallate on silver. There were no secondary phases observed and the intensities were similar to the powder theta/2-theta scans.

### **3.3.3. XRD Analysis of Rare-Earth Gallates on Strontium Titanate and Lanthanum Aluminate**

During the course of this investigation, it was observed that commercially obtained single-crystal substrates were mis-cut by 1 to 2°. The XRD peaks of the single-crystal oxide substrates, strontium titanate and lanthanum aluminate,

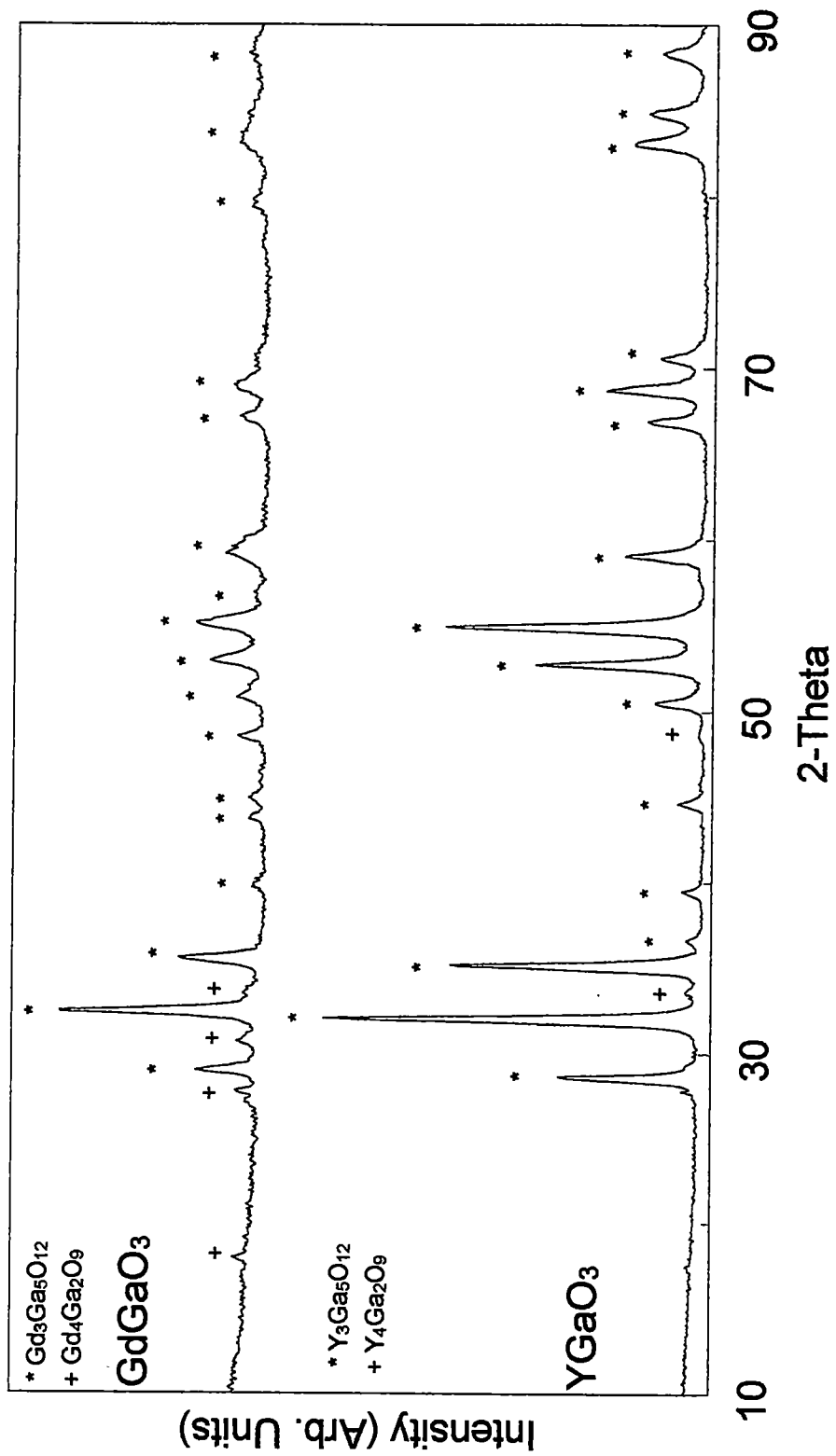


Figure 3.8. Theta/2-theta XRD of GdGaO<sub>3</sub> and YGaO<sub>3</sub> powders at 850 °C.

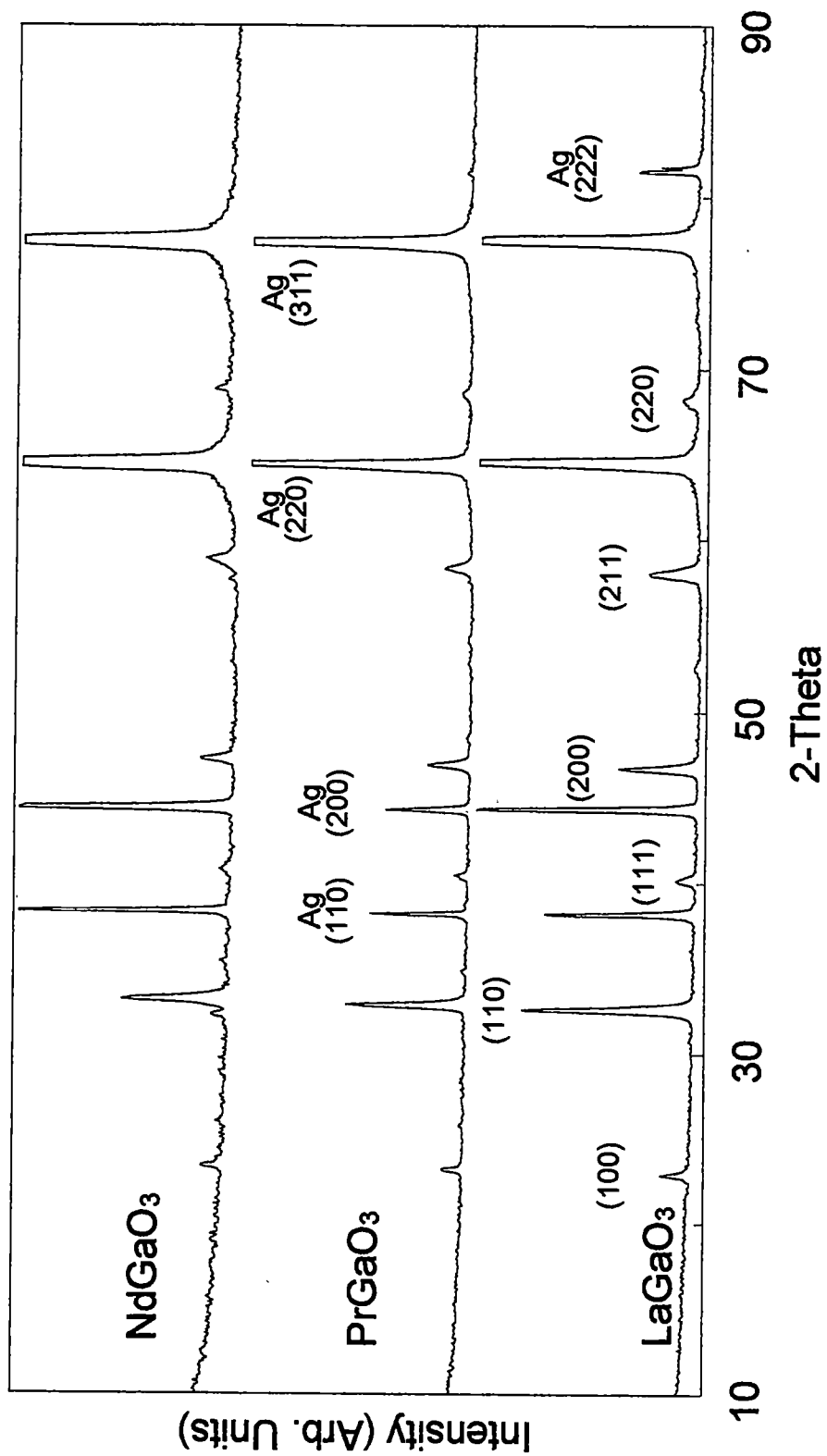


Figure 3.9. Theta/2-theta XRD of LaGaO<sub>3</sub>, PrGaO<sub>3</sub>, and NdGaO<sub>3</sub> on Ag at 850 °C.

had fwhm values of less than  $0.5^\circ$ . The combination of this mis-cut and the narrowness of the peaks made it difficult to align the ( $h00$ ) peaks of the substrate, and therefore, some of the ( $h00$ ) reflections were not observed in the XRD data.

Optical microscopy was conducted on spin-coated rare-earth gallate films on strontium titanate and lanthanum aluminate with a thickness of approximately  $280 \text{ \AA}$ , and the films were smooth and continuous. The out-of-plane orientations of the films were determined using X-ray diffraction, and they were indexed as pseudo-cubic. Figure 3.10 shows theta/2-theta scans of primarily ( $h00$ ) reflections of neodymium gallate, praseodymium gallate, and lanthanum gallate on (100)  $\text{SrTiO}_3$ , and Figure 3.11 shows the theta/2-theta scans of  $\text{La}_{0.5}\text{Nd}_{0.5}\text{GaO}_3$  and  $\text{La}_{0.5}\text{Y}_{0.5}\text{GaO}_3$  on (100)  $\text{SrTiO}_3$ . The peak at  $32.5^\circ$  in all five theta/2-theta scans was the (110) reflection. This might indicate the presence of a small component (less than 1%) of randomly oriented material. However, several other observations were not consistent with this hypothesis. First, the  $32.5^\circ$  peak was also observed in the uncoated substrate after cleaning. Second, the absence of a (111) reflection near  $40^\circ$  makes it unlikely that there was a significant amount of randomly oriented material in the film. Table 3.1 shows the lattice constants of all three rare-earth gallates, the two substrates, strontium titanate, and lanthanum aluminate and their lattice mismatch between the film and substrate. In Figure 3.10, the lattice constant



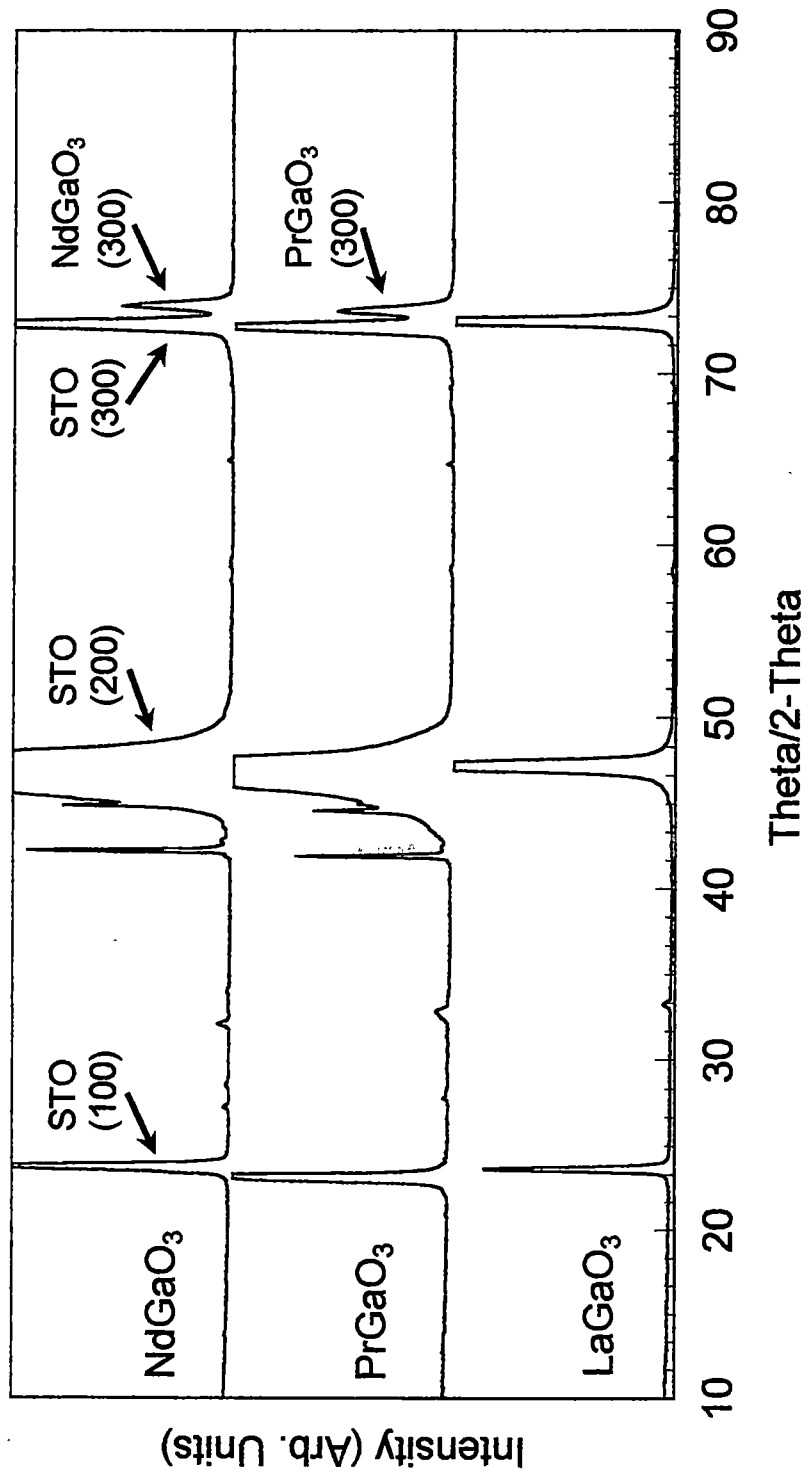


Figure 3.10. Theta/2-Theta XRD of LaGaO<sub>3</sub>, PrGaO<sub>3</sub>, and NdGaO<sub>3</sub> on SrTiO<sub>3</sub> at 850 °C.

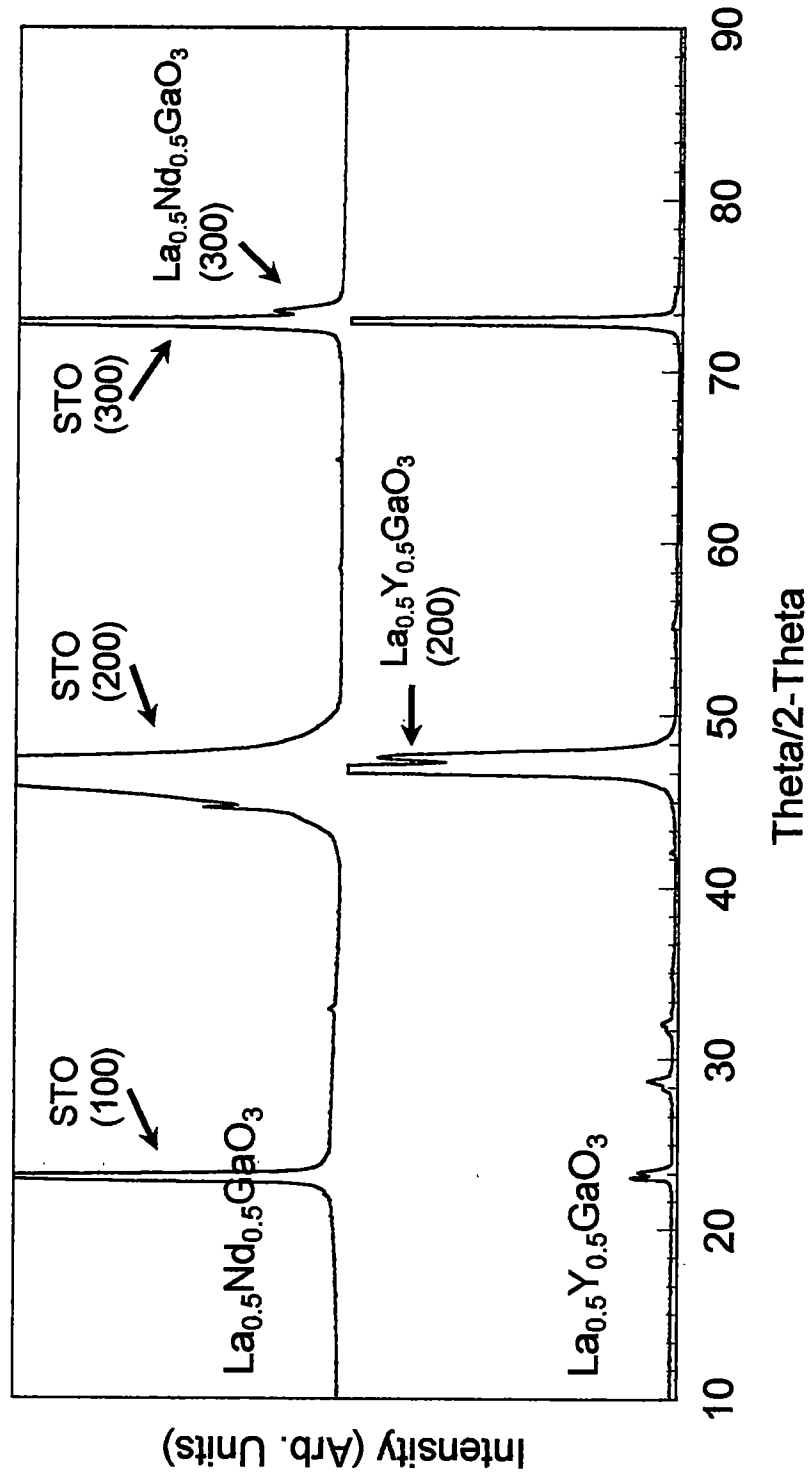


Figure 3.11. Theta/2-Theta XRD of  $\text{La}_{0.5}\text{Y}_{0.5}\text{GaO}_3$  and  $\text{La}_{0.5}\text{Nd}_{0.5}\text{GaO}_3$  on  $\text{SrTiO}_3$  at  $850^\circ\text{C}$ .

**Table 3.1.** Full-width at half-maximum for rare-earth gallate films.

	SrTiO <sub>3</sub>	LaAlO <sub>3</sub>	LaGaO <sub>3</sub>	PrGaO <sub>3</sub>	NdGaO <sub>3</sub>
Lattice constant <sup>1</sup>	3.905 Å	3.793 Å	3.885 Å	3.850 Å	3.837 Å
fwhm of (300) rocking curve on SrTiO <sub>3</sub>			-	0.51(5)* °	0.62(5) °
fwhm of (300) rocking curve on LaAlO <sub>3</sub>			0.92(5) °	0.58(5) °	0.42(5) °
fwhm of (220) phi scan on SrTiO <sub>3</sub>			-	0.65(5) °	0.74(5) °
fwhm of (220) phi scan on LaAlO <sub>3</sub>			1.21(5) °	0.64(5) °	0.49(5) °
lattice constant mismatch with SrTiO <sub>3</sub>			-0.5%	-1.4%	-1.7%
lattice constant mismatch with LaAlO <sub>3</sub>			2.4%	1.5%	1.2%

\*Uncertainty in the last digit indicated parenthetically.

<sup>1</sup>Giess, E. A.; Sandstrom, R. L.; Gallagher, W. J.; Gupta, A.; Shinde, S. L.; Cook, R. F.; Cooper, E. I.; O'Sullivan, E. J. M.; Roldan, J. M.; Segmuller, A. P.; Angilello, J. *IBM J. Res. Develop.* **1990**, *34*, 916.

mismatch for lanthanum gallate on strontium titanate was extremely small (approximately 0.5%), and the peaks from the film could not be resolved from the  $\theta/2\text{-}\theta$  scan with the normal scan rate. In order to distinguish between the  $\text{LaGaO}_3$  and  $\text{SrTiO}_3$  peaks, a longer data collection time was used. Figure 3.12 shows the  $\theta/2\text{-}\theta$  scan with the (002) reflection of  $\text{LaGaO}_3$  and  $\text{SrTiO}_3$ . Figure 3.13 shows  $\theta/2\text{-}\theta$  scans of neodymium gallate, praseodymium gallate, lanthanum gallate and  $\text{La}_{0.5}\text{Nd}_{0.5}\text{GaO}_3$  on (100) lanthanum aluminate. A high degree of out-of-plane orientation was indicated by mostly ( $h00$ ) reflections. The mixed metal gallate film,  $\text{La}_{0.5}\text{Y}_{0.5}\text{GaO}_3$ , on (100) strontium titanate showed only partial epitaxy, while  $\text{La}_{0.5}\text{Nd}_{0.5}\text{GaO}_3$  showed a single epitaxy (Figure 3.11). Gadolinium gallate and yttrium gallate were also deposited on (100) strontium titanate and (100) lanthanum aluminate. They showed only random epitaxy (Figures 3.14 and 3.15, respectively). This was due to the high lattice constant mismatch between the films and the substrates.

#### **3.3.4. Out-of-Plane and In-Plane Texture Analysis of Rare-Earth Gallates on Strontium Titanate and Lanthanum Aluminate**

Omega scans (rocking curves) about the (300) reflection were used to measure the mosaic character (degree of crystallinity) of the film. Table 3.1 shows the full width at half maximum (fwhm) of the out-of-plane peaks and

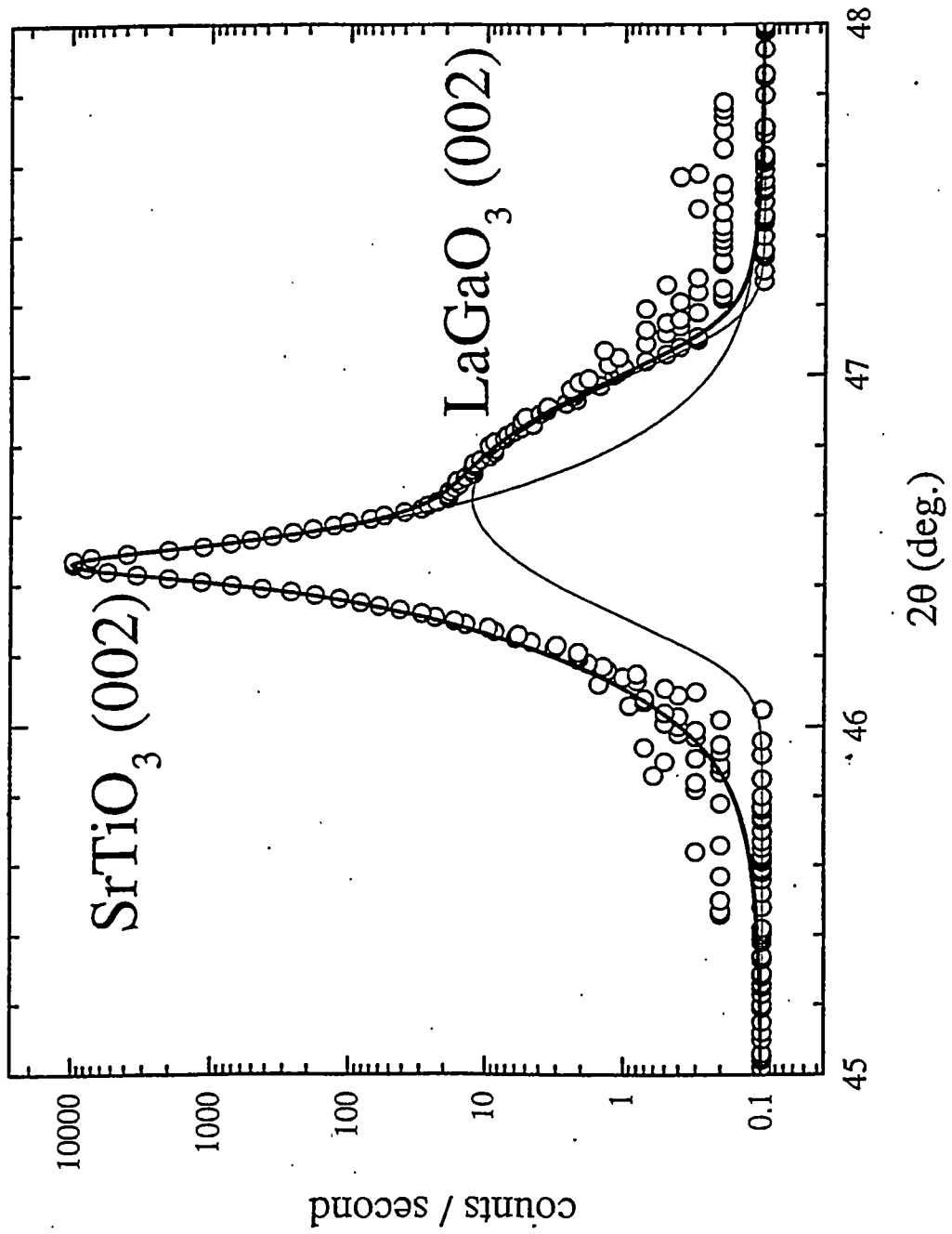


Figure 3.12. Theta/2-theta XRD of LaGaO<sub>3</sub> on SrTiO<sub>3</sub> at 850 °C with a longer dwell time.

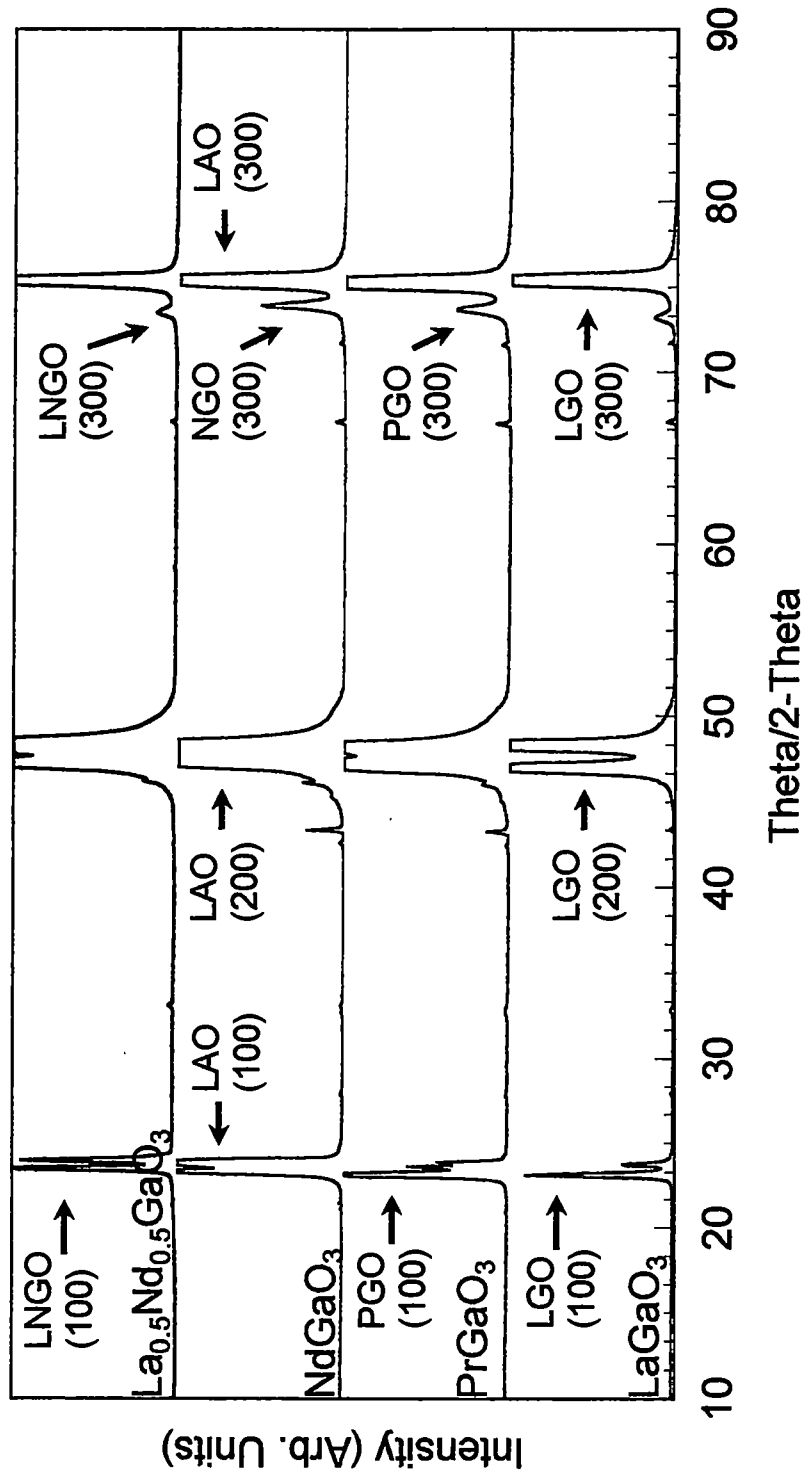


Figure 3.13. Theta/2-Theta XRD of  $\text{LaGaO}_3$ ,  $\text{PrGaO}_3$ ,  $\text{NdGaO}_3$ , and  $\text{La}_{0.5}\text{Nd}_{0.5}\text{GaO}_3$  on  $\text{LaAlO}_3$  at  $850\text{ }^\circ\text{C}$ .

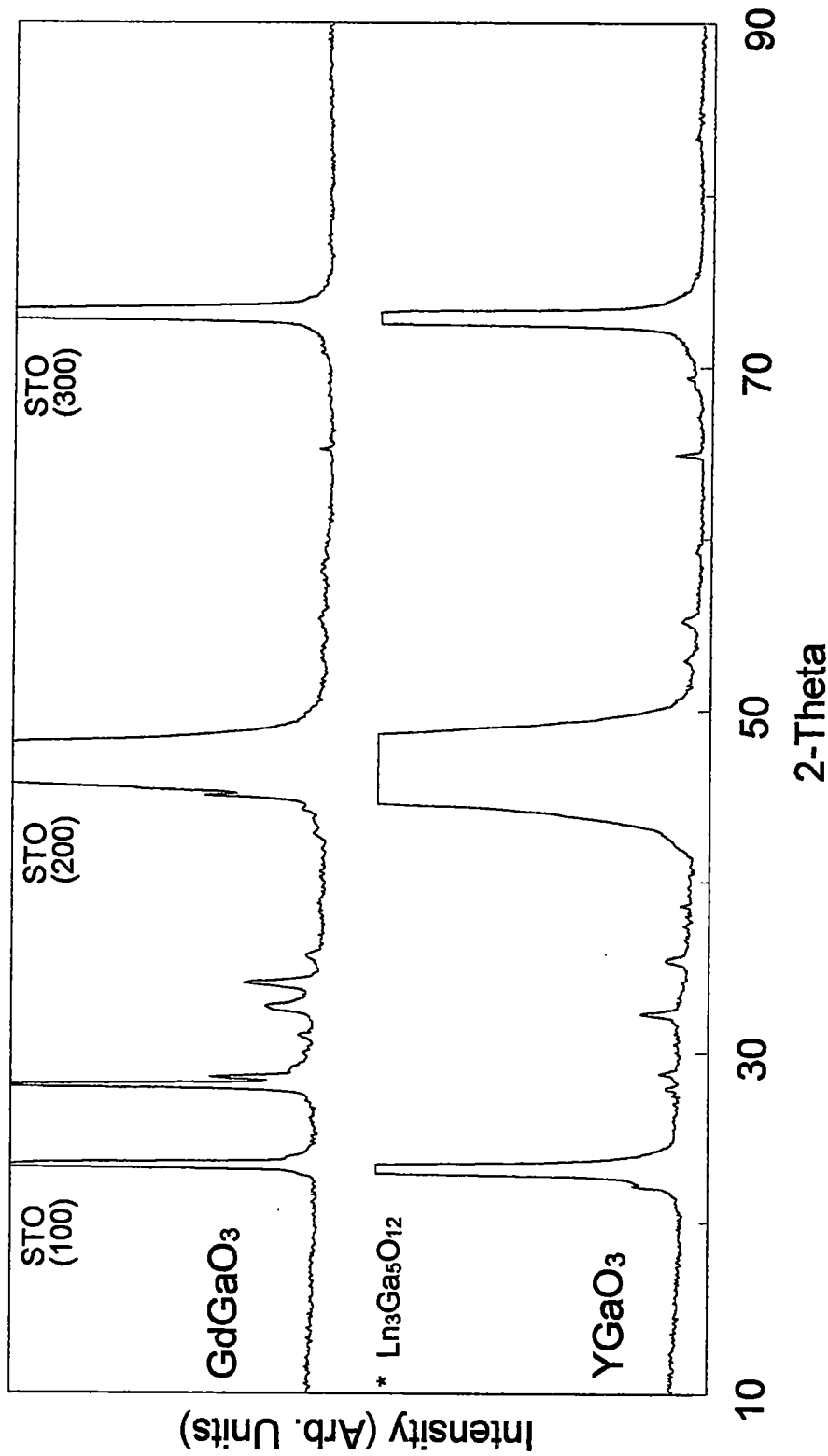


Figure 3.14. Theta/2-theta XRD of GdGaO<sub>3</sub> and YGaO<sub>3</sub> on SrTiO<sub>3</sub> at 850 °C.

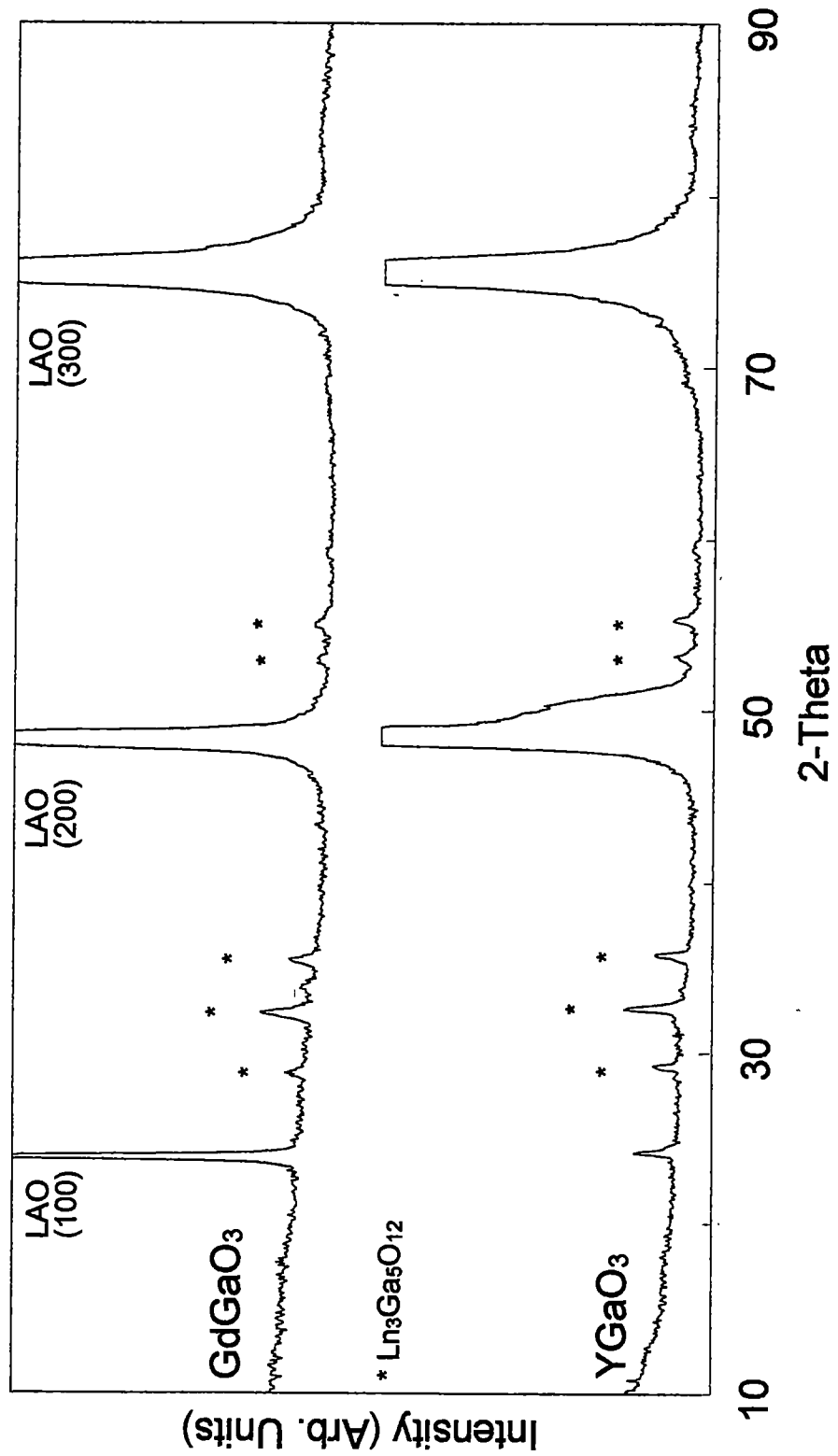


Figure 3.15. Theta/2-theta XRD of GdGaO<sub>3</sub> and YGaO<sub>3</sub> on LaAlO<sub>3</sub> at 850 °C.



illustrates the fact that all of the films on both strontium titanate and lanthanum aluminate showed excellent out-of-plane orientation. A representative omega scan about the (300) reflection of neodymium gallate on (100) strontium titanate is shown in Figure 3.16.

Pole figures about the (220) plane were obtained to help determine the nature of the in-plane epitaxy. Figure 3.17 shows representative pole figures about the (220) reflection of neodymium gallate on strontium titanate and lanthanum aluminate. The pole figures are indicative of cube-on-cube epitaxy showing only four peaks at chi of 45° spaced 90° in phi. In order to access the quality of the in-plane epitaxy, phi scans were obtained. A representative phi scan about the (220) reflection of neodymium gallate on (100) strontium titanate is shown in Figure 3.16. Table 3.1 reports all fwhm values of the phi scans for neodymium gallate, praseodymium gallate, and lanthanum gallate on both strontium titanate and lanthanum aluminate. The in-plane peak widths are proportional to the lattice mismatch between the film and the substrate, and they are significantly larger than those of the out-of-plane peaks.

### **3.3.5. Analysis of $\text{YBa}_2\text{Cu}_3\text{O}_{7-\delta}$ PLD Film on Solution Deposited $\text{NdGaO}_3$ on (100) Strontium Titanate**

A 15.0 x 2.5 mm sample of neodymium gallate on strontium titanate was used as the substrate for a yttrium barium copper oxide ( $\text{YBa}_2\text{Cu}_3\text{O}_{7-\delta}$ , YBCO),

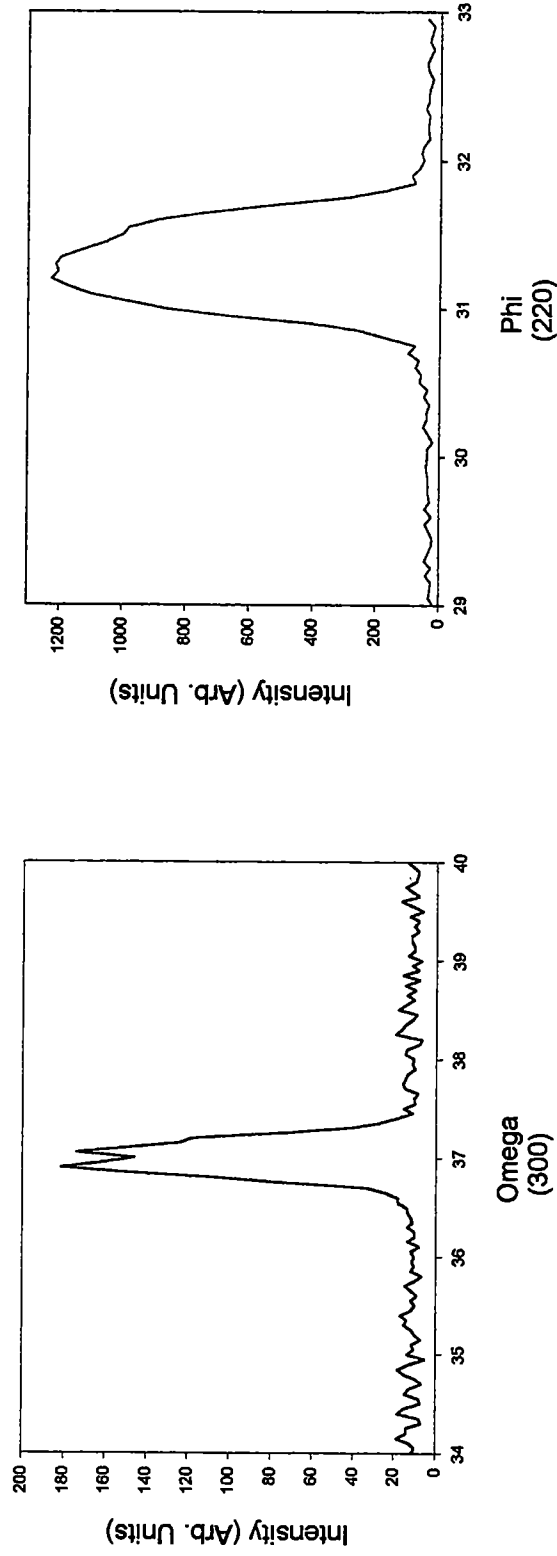
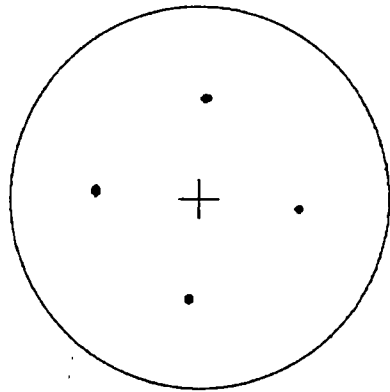
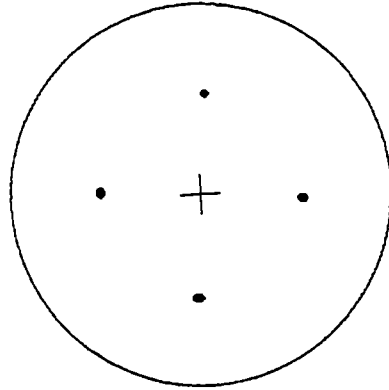


Figure 3.16. Omega scan and phi scan of NdGaO<sub>3</sub> on SrTiO<sub>3</sub>.



NdGaO<sub>3</sub> on SrTiO<sub>3</sub>  
(220)



NdGaO<sub>3</sub> on LaAlO<sub>3</sub>  
(220)

Figure 3.17. Pole figures of NdGaO<sub>3</sub> on SrTiO<sub>3</sub> and LaAlO<sub>3</sub> about the (220) reflection.

superconducting film. A theta/2-theta scan of YBCO on neodymium gallate and strontium titanate was obtained showing only c-axis reflections (Figure 3.18). Out-of-plane alignment, omega scans ( $\omega = 0.46^\circ$ ), and in-plane alignment, phi scans ( $\phi = 1.14^\circ$ ), indicated a highly oriented film. The epitaxial relationship of the superconductor/buffer layer/substrate was cube-on-cube throughout [(100) YBCO// (100) NdGaO<sub>3</sub>// (100) SrTiO<sub>3</sub>]. The YBCO film had a transport critical current density ( $J_c$ ) value of  $10^6$  A/cm<sup>2</sup> (77 K) and is shown in Figure 3.19. Figure 3.20 shows the critical temperature of the YBCO film, which exhibited zero resistivity at 90.3 K.

### 3.4. Conclusion

Solution synthesis provided a simple and extremely low-cost method for producing high quality heteroepitaxial films of rare-earth gallates on readily available single-crystal oxide substrates. It was also possible to engineer lattice mismatch through heteroepitaxial growth of multiple buffer layers so as to minimize crystalline defects. High critical current copper oxide-based superconductors films were obtained on rare-earth gallate buffer layers prepared by a solution deposition method.

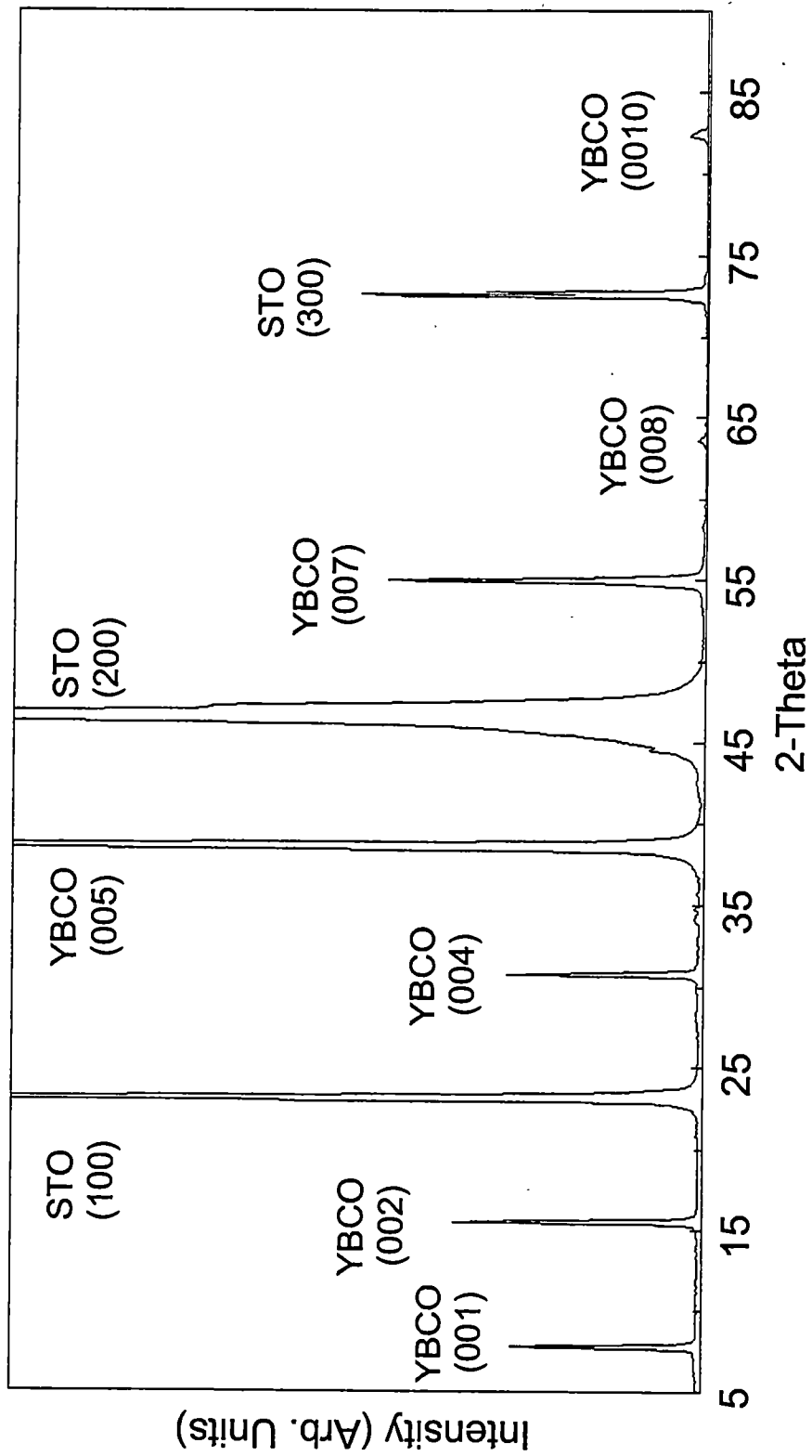


Figure 3.18. Theta/2-theta XRD of YBCO/NdGaO<sub>3</sub> on SrTiO<sub>3</sub>.

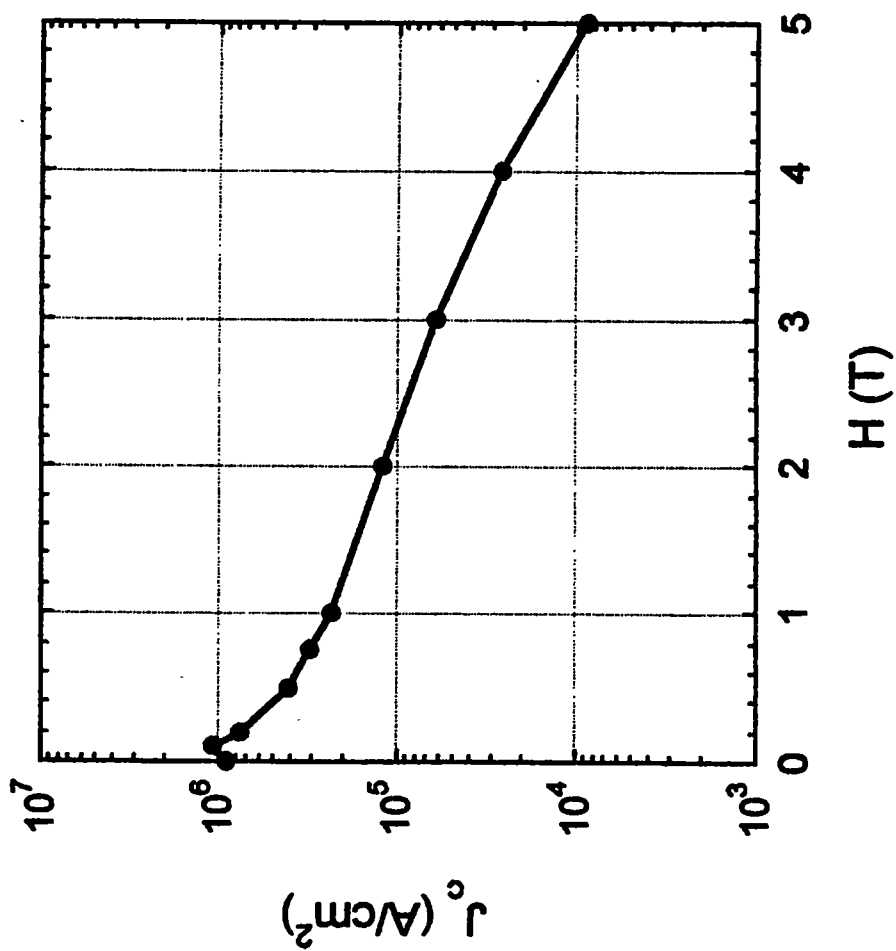


Figure 3.19. Critical current density ( $J_c$ ) vs. applied magnetic field ( $H$ ) at 77K for YBCO/NdGaO<sub>3</sub> film on SrTiO<sub>3</sub>.

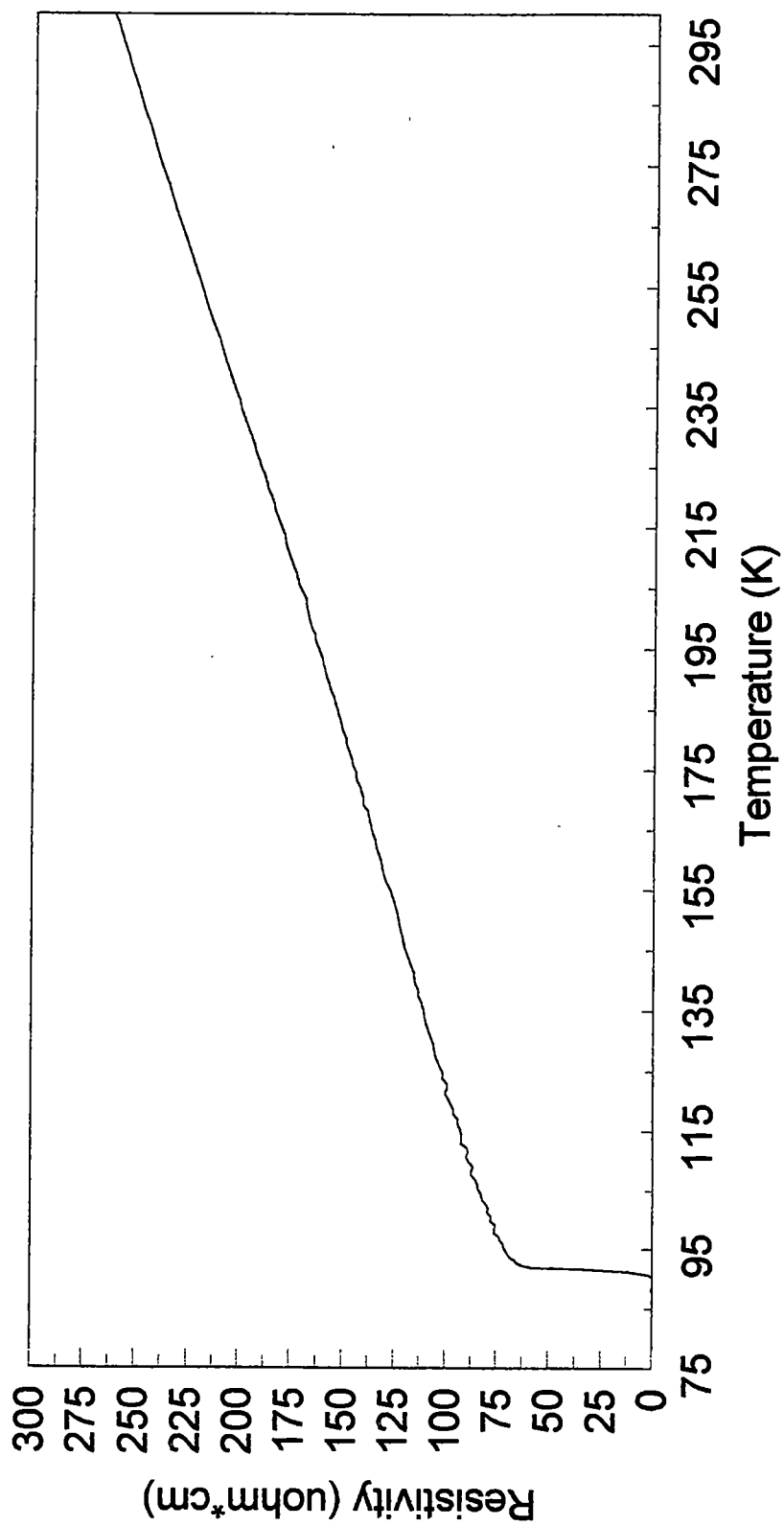


Figure 3.20. Resistivity versus temperature for a YBCO film deposited on SrTiO<sub>3</sub> with a NdGaO<sub>3</sub> buffer layer.

## CHAPTER 4

### EPITAXIAL GROWTH OF RARE-EARTH ALUMINATES AND $A_xA'_{(1-x)}B_yB'_{(1-y)}O_3$ MIXED METAL OXIDE THIN-FILMS

#### 4.1. Introduction

Over the past few years, significant progress has been made in preparing yttrium barium copper oxide (YBCO) superconducting layers. YBCO has attracted much interest due to its high performance in strong magnetic fields at 77 K. This is in contrast to thallium and bismuth containing superconductors, even though the latter two have higher superconducting transition temperatures.<sup>78</sup> For YBCO to function as a high-current carrying layer, it is necessary to have both out-of-plane (*c*-axis) orientation and a fair degree of in-plane (*a* and *b*-axis) orientation.<sup>79</sup> This alignment is made possible through the deposition of the superconductor on single-crystal oxide substrates (or on single crystal oxide substrates through a buffer layer as shown in Chapter 3). However, long length single-crystal oxide substrates cannot be manufactured inexpensively, and this has greatly limited the widespread use of high  $T_c$  superconductors.

Substrates which are chemically inert, flexible, mechanically robust, textured, and latticed-matched to the superconducting layer are an alternative to single-crystal oxide substrates for long length superconductors. Metal



substrates such as Ni are the most logical choice and satisfy the mechanical requirements, but a ceramic buffer layer is necessary to obtain a chemically inert substrate. For this reason, two main approaches have been developed to produce a textured buffer layer: texturing the buffer layer with ion beams (ion beam assisted deposition, or IBAD),<sup>50</sup> or deposition of an epitaxial buffer layer on a roll-textured metal substrate called RABiTS (Rolling Assisted Biaxially Textured Substrates).<sup>54</sup>

Several methods for producing buffer layers on roll-textured nickel are pulsed laser ablation,<sup>54</sup> e-beam evaporation,<sup>80</sup> and solution deposition.<sup>39</sup> The most successful buffer layers used to date are cerium oxide and yttrium stabilized zirconium which have been deposited under reducing conditions to prevent oxidation of the roll-textured nickel substrate. Any solution process for the deposition of epitaxial buffer layers on roll-textured nickel also requires reducing conditions. Rare-earth aluminates on single crystal oxide substrates have been shown to be excellent buffer layers for YBCO.<sup>40</sup> These materials are otherwise extremely difficult to deposit by pulsed laser ablation or sputtering due to preferential ablation or sputtering. Rare-earth aluminates on roll textured nickel have been investigated by Beach *et al.*,<sup>39</sup> but a single in-plane epitaxy was not obtained.

The following sections of this chapter provide the procedures and results for solution deposition of neodymium aluminate, praseodymium aluminate,

lanthanum aluminate, gadolinium aluminate, yttrium aluminate, and mixed rare-earth metal gallium and aluminum oxide films on silver foil, (100) strontium titanate, (100) lanthanum aluminate, and roll-textured nickel. The deposition on single-crystal ceramic substrates was conducted for comparison with that on silver foil and roll-textured nickel. The structures of these films were determined by X-ray diffraction (XRD). The sol-gel chemistry used here was pioneered by Payne *et al.*<sup>19</sup> and employs solutions of metal methoxyethoxide complexes in 2-methoxyethanol.

## **4.2. Experimental Details**

### **4.2.1. General Procedures**

All manipulations were performed under dry argon atmosphere with the use of either standard Schlenk techniques or a glove box. NMR spectra were recorded on a Bruker AC-400 Fourier transform spectrometer, and were referenced to solvent. Lanthanum isopropoxide (Gelest, 99.9%), neodymium metal (Alfa Aesar, 99.9%), praseodymium metal (Alfa Aesar, 99.9%), gadolinium metal (Alfa Aesar, 99.9%), yttrium metal (Alfa Aesar, 99.9%), aluminum isopropoxide (Aldrich, 99.99%) and gallium trichloride (Alfa Aesar, 99.9%) were used as received. Benzene was dried over sodium/benzophenone and distilled before use.

#### 4.2.2. Preparation of Rare-Earth Isopropoxides

Lanthanum, praseodymium, neodymium, gadolinium, and yttrium isopropoxide were prepared by a literature method through the reactions of the metals directly with dry isopropanol in the presence of mercuric catalysts.<sup>77</sup> Commercial powders of these metals failed to react with dry isopropanol in the presence of a catalyst. Metal filings were obtained by using a rasp to file the metal under an inert atmosphere. The appropriate metal filings [1.736 g (12.5 mmol) of lanthanum, 1.76 g (12.5 mmol) of praseodymium, 1.803 g (12.5 mmol) of neodymium, 1.966 g (12.5 mmol) of gadolinium, and 1.112 g (12.5 mmol) of yttrium], were added to a 250 mL Schlenk flask with 90 mL of dry isopropanol, a magnetic stir bar, 5 mg of  $\text{Hg}(\text{OOCCH}_3)_2$ , and 5 mg of  $\text{HgCl}_2$ . The mixtures were allowed to reflux overnight at 85 °C and then filtered. The solvent was removed at reduced pressure to give a solid product. The crude lanthanum, praseodymium, neodymium, gadolinium, and yttrium isopropoxides were extracted using a Soxhlet extractor with dry isopropanol and then purified by recrystallization. Yields ranged between 50-70%.

#### 4.2.3. Preparation of Gallium Isopropoxide, $\text{Ga}(\text{OPr}^i)_3$

Gallium isopropoxide,  $\text{Ga}(\text{i-OC}_3\text{H}_7)_3$ , was prepared from the reaction of gallium trichloride and sodium isopropoxide first reported by Mehrotra.<sup>75</sup> A 250 mL Schlenk flask with a magnetic stir bar and condenser was charged with 4.88

g (0.212 mol) of crushed sodium metal, 18 mL of dry isopropanol, and 100 mL of dry benzene. The mixture was refluxed at 85 °C overnight to insure complete reaction of the sodium and isopropanol. Another 250 mL Schlenk flask was charged with 12.0 g (68 mmol) of GaCl<sub>3</sub> and 50 mL of benzene. The GaCl<sub>3</sub> was allowed to dissolve in benzene, and added dropwise to the NaOPr<sup>i</sup> solution from the top of the condenser via a syringe to maintain a gentle reflux. The mixture then refluxed for 8 h, and filtered afterwards. The volatiles in the filtrate were removed at 23 °C under vacuum to give a viscous oil. A microdistillation apparatus was attached to the Schlenk flask and the solution was distilled under reduced pressure. Approximately 8.8 g (66.8 mmol, 52%) of Ga(*i*-OC<sub>3</sub>H<sub>7</sub>)<sub>3</sub> were collected at 137-141 °C and 0.1 torr. The liquid was placed in a dry box and allowed to harden from a colorless viscous liquid to a semi-solid wax. The gallium isopropoxide was placed in an inert atmosphere dry-box and allowed to harden from a colorless viscous liquid to a semi-solid wax. (Oliver and Worrall<sup>76</sup> have attributed this change in state to conversion of the initially formed trimer to a more stable tetrameric oligomer.)

#### 4.2.4. Preparation of Methoxyethoxide Solutions

Each of the metal isopropoxides was mixed with 90 mL of 2-methoxyethanol to exchange isopropoxide for methoxyethoxide ligands. Each solution was refluxed for 1 h at 140 °C, and 60 mL of the solvent was removed

by distillation at atmospheric pressure. The solvent removed by distillation was replaced with fresh 2-methoxyethanol. The ligand exchange process was repeated two more times to ensure complete ligand exchange. Nuclear magnetic resonance (NMR) was used to verify the ligand exchange. The  $^1\text{H}$  NMR spectra of aluminum isopropoxide/methoxyethoxide are shown in Figure 4.1. The NMR spectra show only proton peaks associated with the methoxyethoxide ligand, implying that the ligand exchange was complete between the two ligands.

Each solution was adjusted to 50 mL, and its molality was calculated based on the moles of isopropoxide used and the weight of the solutions. (The use of molality rather than molarity allowed the gravimetric preparation of small volumes of solutions with high accuracy.) Solutions were mixed from the individual stock solutions with the appropriate stoichiometry and refluxed for 1 h to insure proper mixing. The following rare-earth aluminum oxides were prepared from the stock solutions: lanthanum aluminate ( $\text{LaAlO}_3$ ), praseodymium aluminate ( $\text{PrAlO}_3$ ), neodymium aluminate ( $\text{NdAlO}_3$ ), gadolinium aluminate ( $\text{GdAlO}_3$ ), and yttrium aluminate ( $\text{YAlO}_3$ ). In addition, the following mixed compounds of the formulas  $\text{ABB}'\text{O}_3$  and  $\text{AA}'\text{BB}'\text{O}_3$  were prepared: lanthanum gallium aluminate ( $\text{LaGa}_{0.5}\text{Al}_{0.5}\text{O}_3$ ) and lanthanum neodymium gallium aluminate ( $\text{La}_{0.5}\text{Nd}_{0.5}\text{Ga}_{0.5}\text{Al}_{0.5}\text{O}_3$ ).

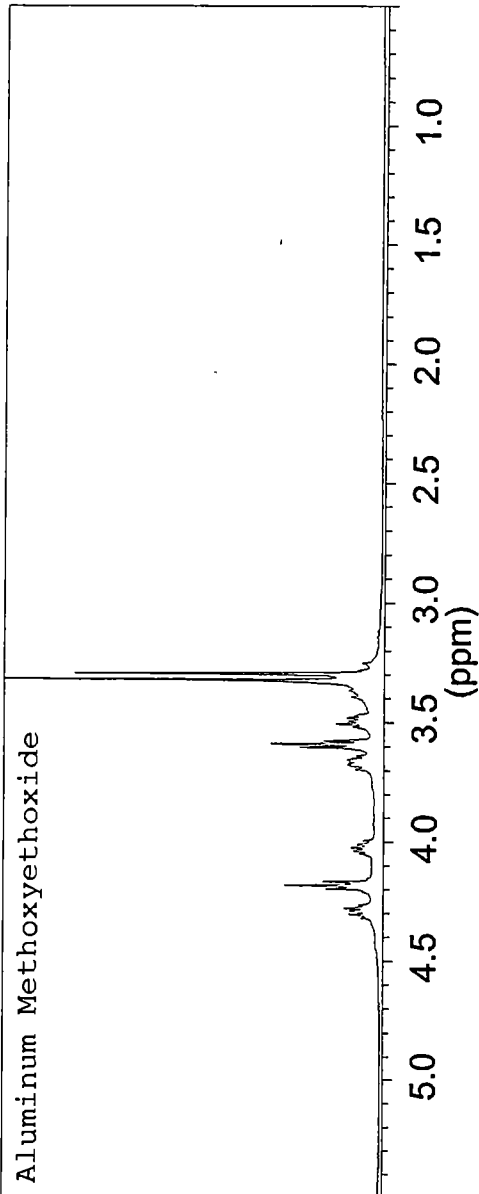
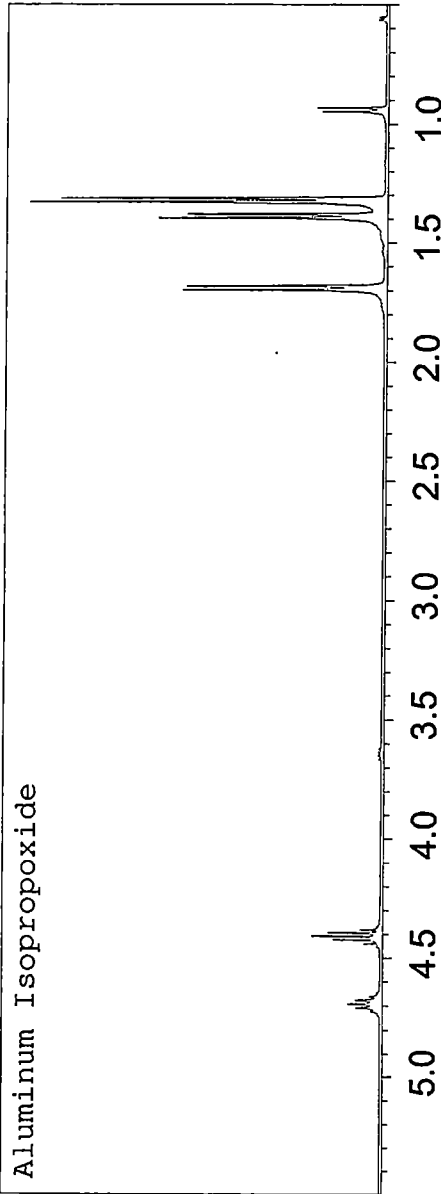


Figure 4.1. <sup>1</sup>H NMR spectra of aluminum isopropoxide and aluminum methoxyethoxide in benzene-d<sub>6</sub>.

#### 4.2.5. Powder and Film Preparation

The stock solutions were mixed in a ratio of one part hydrolysis solution (1.0 M water in 2-methoxyethanol) to four parts of the stock solution, resulting in a partially hydrolyzed coating solution. Powders were prepared by the addition of excess water to the coating solution followed by the decomposition of the resultant gels at 300 °C. The gels were crushed, ground with a mortar and pestle, and fired (for one hour in air) at temperatures between 650 °C and 1050 °C. Each substrate, strontium titanate (100) and lanthanum aluminate (100), was heated for 1 h in oxygen at 1000 °C and 800 °C, respectively, prior to coating. Silver foil was polished with 0.06 micron extra pure alumina abrasive and cleaned in distilled water. Roll-textured nickel was annealed in forming gas (96% Ar/4% $H_2$ ) for 2 h at 650 °C. The nickel was then ultrasonically cleaned for 1 h prior to coating. The hydrolyzed stock solutions were applied to the substrates through a 0.2  $\mu$ m syringe filter and spin coated on a photo-resist spinner for 30 s at 2,000 rpm. The substrates were placed in a preheated Thermolyne muffle furnace at 850 °C for 20 min in air. Each coat was approximately 70 nm thick, and this coating and firing procedure was repeated four times.

### 4.3. Results and Discussion

#### 4.3.1. NMR Study of Lanthanum Aluminum 2-Methoxyethoxide Solution

A key question in the preparation of multi-cation containing solutions is the reactions of the metal alkoxide mixture before hydrolysis. NMR was used to study these reactions in the current systems. Figure 4.2 shows the  $^1\text{H}$  NMR spectra of 2-methoxyethanol,  $\text{Al}(\text{OCH}_2\text{CH}_2\text{OCH}_3)_3$ ,  $\text{La}(\text{OCH}_2\text{CH}_2\text{OCH}_3)_3$ , and  $\text{LaAl}(\text{OCH}_2\text{CH}_2\text{OCH}_3)_6$ . In the  $^1\text{H}$  NMR spectra of both  $\text{La}(\text{OCH}_2\text{CH}_2\text{OCH}_3)_3$  and the mixture of  $\text{La}(\text{OCH}_2\text{CH}_2\text{OCH}_3)_3$  and  $\text{Al}(\text{OCH}_2\text{CH}_2\text{OCH}_3)_3$ , broad peaks were observed, in contrast to those of  $\text{Al}(\text{OCH}_2\text{CH}_2\text{OCH}_3)_3$ . These  $^1\text{H}$  NMR spectra suggest the formation of polymeric adducts and/or dynamic ligand exchange processes in the solutions. Whatever process is operative, it is clear that the solution is not a simple mixture of aluminum and lanthanum methoxyethoxides. In the current study, the formula  $\text{LaAl}(\text{OCH}_2\text{CH}_2\text{OCH}_3)_6$  is used to represent the polymeric adduct or dynamic mixture between  $\text{La}(\text{OCH}_2\text{CH}_2\text{OCH}_3)_3$  and  $\text{Al}(\text{OCH}_2\text{CH}_2\text{OCH}_3)_3$ .

#### 4.3.2. Gelation and Crystallization

One of the more difficult aspects in this research was the study of the progression from hydrolyzed solution, through gel and amorphous preceramic stages, to crystalline ceramic. While a number of well developed techniques exist for the study of solutions and ceramic films, relatively few techniques exist



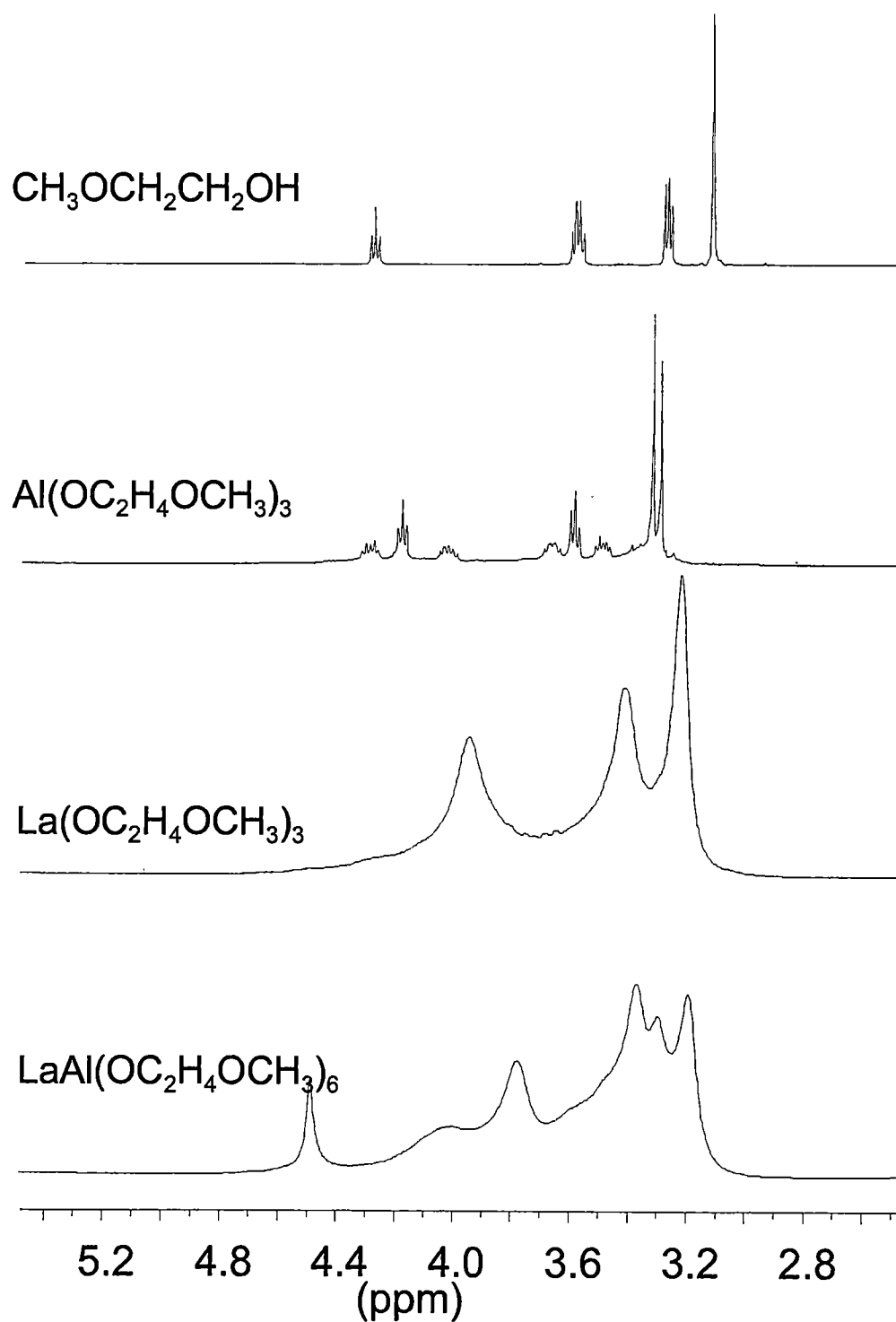


Figure 4.2.  $^1\text{H}$  NMR spectra of mixed metal lanthanum and aluminum alkoxide precursors in benzene- $\text{d}_6$ .

for the study of amorphous material, such as the inorganic-organic mixture formed in the cast gel. One widely used technique was FTIR. IR spectra of the gels formed by the hydrolysis of  $\text{LaAl}(\text{OCH}_2\text{CH}_2\text{OCH}_3)_6$  with two equivalents (top trace) and six equivalents (bottom trace) of water are shown in Figure 4.3. The hydrolysis of alkoxide ligands results in the immediate formation of hydroxide groups in the region  $3300$  to  $3700\text{ cm}^{-1}$ , the disappearance of hydrocarbon bands, with very little formation of oxo bridged species in the region  $400$  to  $800\text{ cm}^{-1}$ . The hydroxy complexes are very soluble in 2-methoxyethanol, and only slight increases in solution viscosity were observed immediately after the hydrolysis.

Another technique to study the amorphous materials was thermal analysis of gel pyrolysis. Figure 4.4 shows thermal gravimetric analysis (TGA) and differential thermal analysis (DTA) plots of lanthanum aluminate gel produced from the addition of two equivalents of water (top trace) and six equivalents of water (bottom trace). The TGA data for the sample hydrolyzed with two equivalents of water indicated three fairly distinct decomposition regimes: at the lowest temperature, the hydroxyl groups were removed; at temperatures between  $400$  and  $600\text{ }^\circ\text{C}$ , alkoxide groups bound to lanthanum were lost; and at temperatures greater than  $800\text{ }^\circ\text{C}$ , alkoxide groups bound to aluminum were lost (based on results from TGA measurements of single metal alkoxide species, not shown). Hydrolysis with six equivalents of water replaces

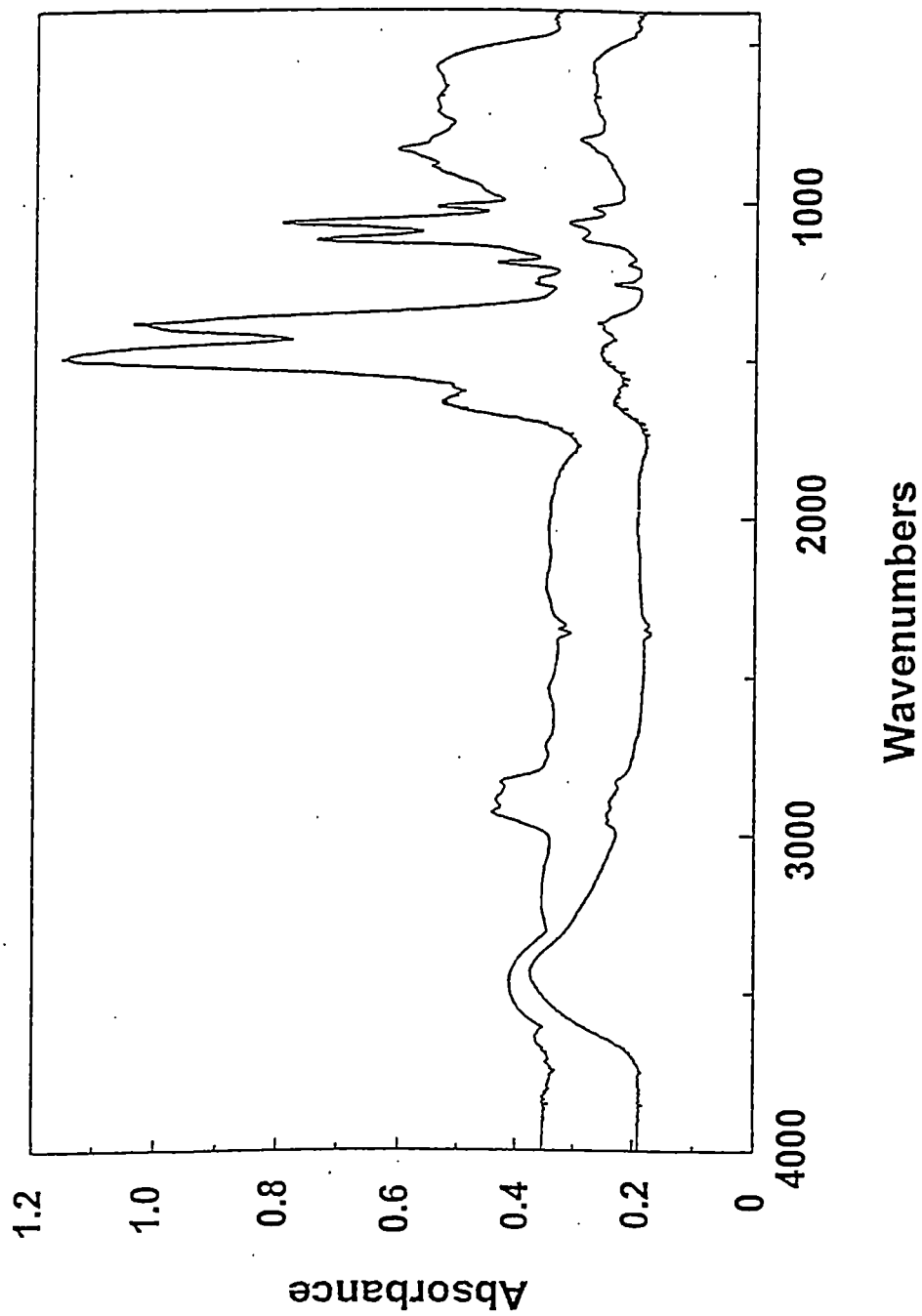


Figure 4.3. IR spectra of lanthanum aluminum methoxyethoxide solutions with 2 equivalents (top trace) and 6 equivalents (bottom trace) of water.

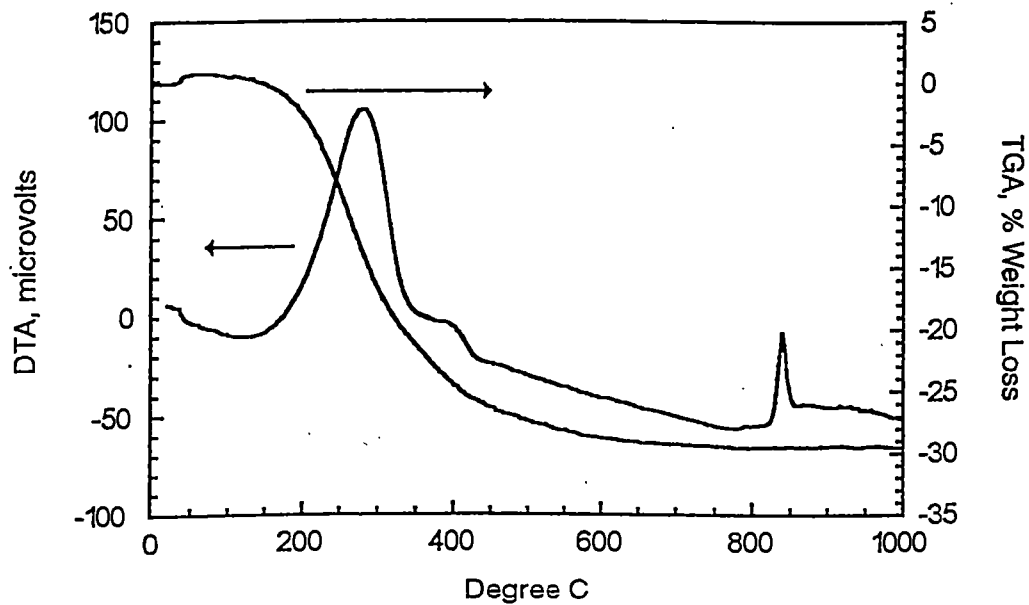
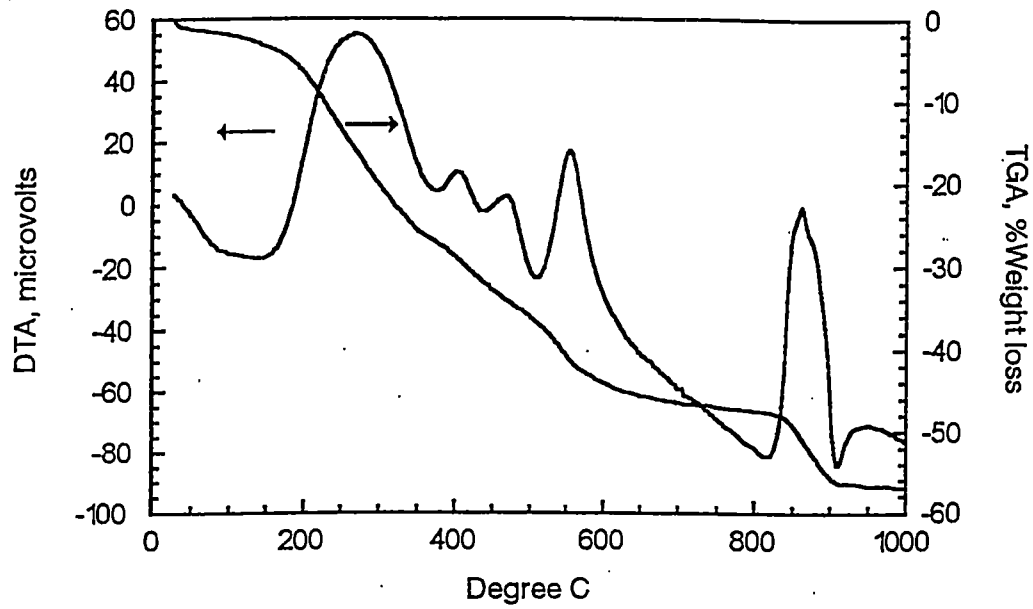
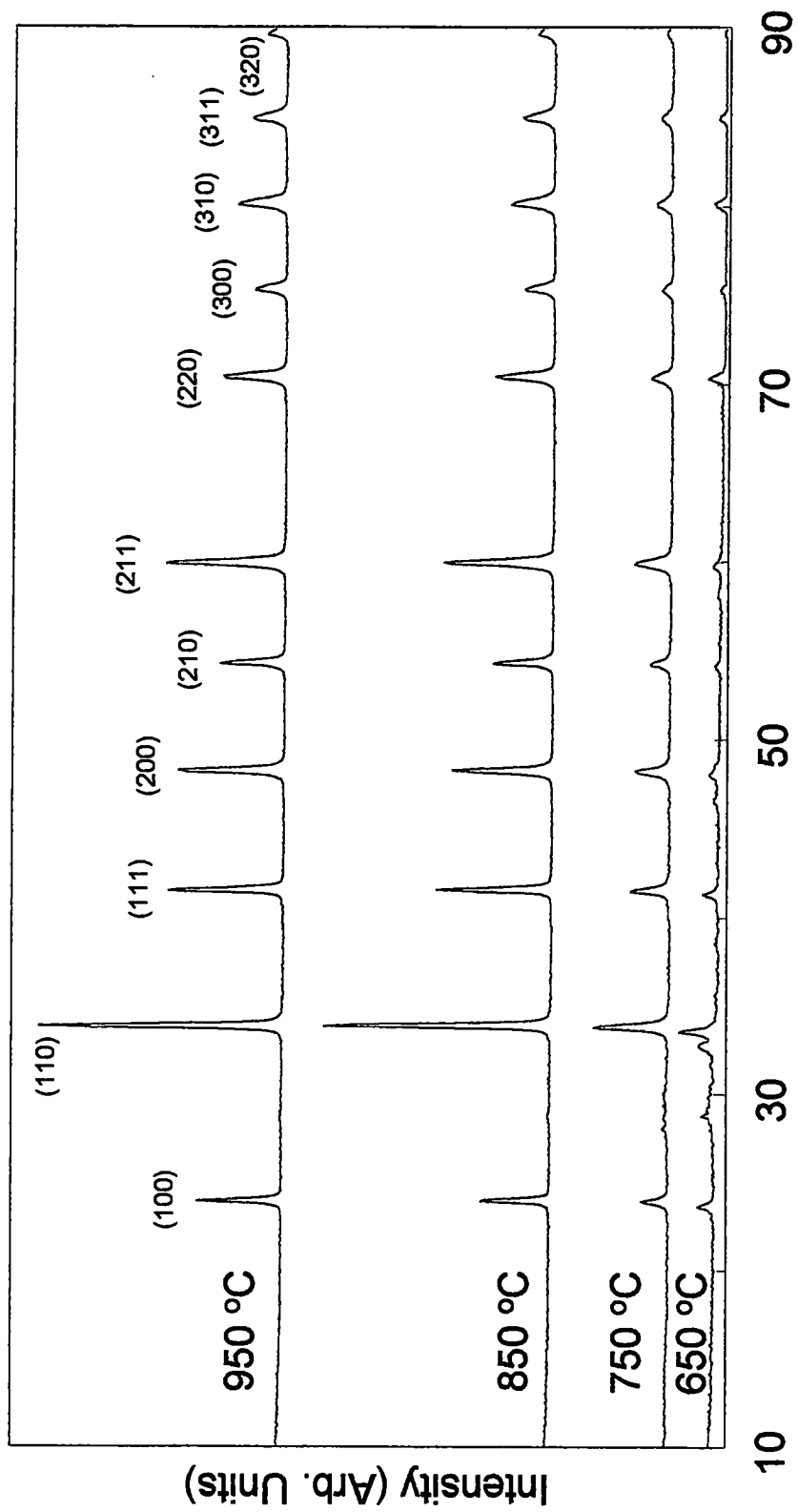


Figure 4.4. TGA/DTA plot of lanthanum aluminate gel with 2 equivalents (top trace) and 6 equivalents (bottom trace) of water.

almost entirely the alkoxide groups with hydroxyl groups as observed in TGA/DTA. These observations are consistent with the IR data. However, the hydrolysis has little effect on the ultimate crystallization at 850 °C as indicated by the spike in the DTA data.

#### **4.3.3. XRD Analysis of Rare-Earth Aluminate Powders**

The annealing behavior of lanthanum aluminate, praseodymium aluminate, neodymium aluminate, gadolinium aluminate, and yttrium aluminate powders were evaluated under both oxidizing and reducing conditions. Annealing under reducing conditions was conducted to compare phase development under the two ambient atmospheres, and to determine if epitaxial growth on substrates sensitive to surface oxidation was possible. Figures 4.5-4.9 show X-ray diffraction data of powders annealed at temperatures from 650 °C to 1050 °C for 1 h in air, and Figures 4.10-4.14 show X-ray diffraction of powders annealed for 1 h in 4% H<sub>2</sub> in Ar (forming gas). When the powders were annealed in air, the crystallization started at 650 °C and full crystallization was observed at 850 °C. The data shows that the onset of crystallization is about 100 °C higher under reducing conditions. All rare-earth aluminates, except gadolinium aluminate and yttrium aluminate, showed a single phase in both oxidizing and reduced atmospheres. Gadolinium aluminate was the predominant phase in a mixture that contained the garnet Gd<sub>3</sub>Al<sub>5</sub>O<sub>12</sub> and a two



2-Theta

Figure 4.5. Theta/2-theta XRD of LaAlO<sub>3</sub> powders.

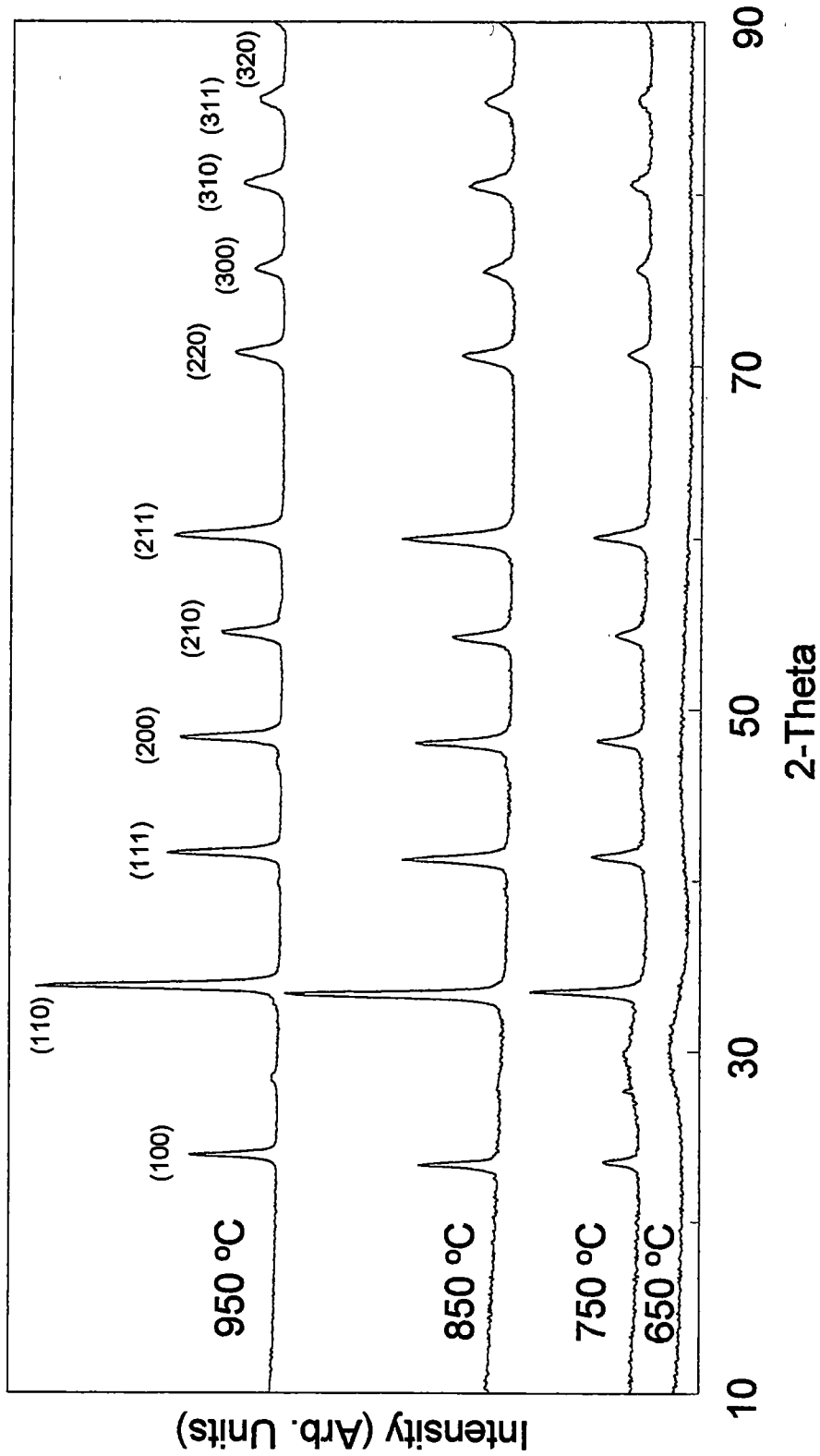


Figure 4.6. Theta/2-theta XRD of PrAlO<sub>3</sub> powders.

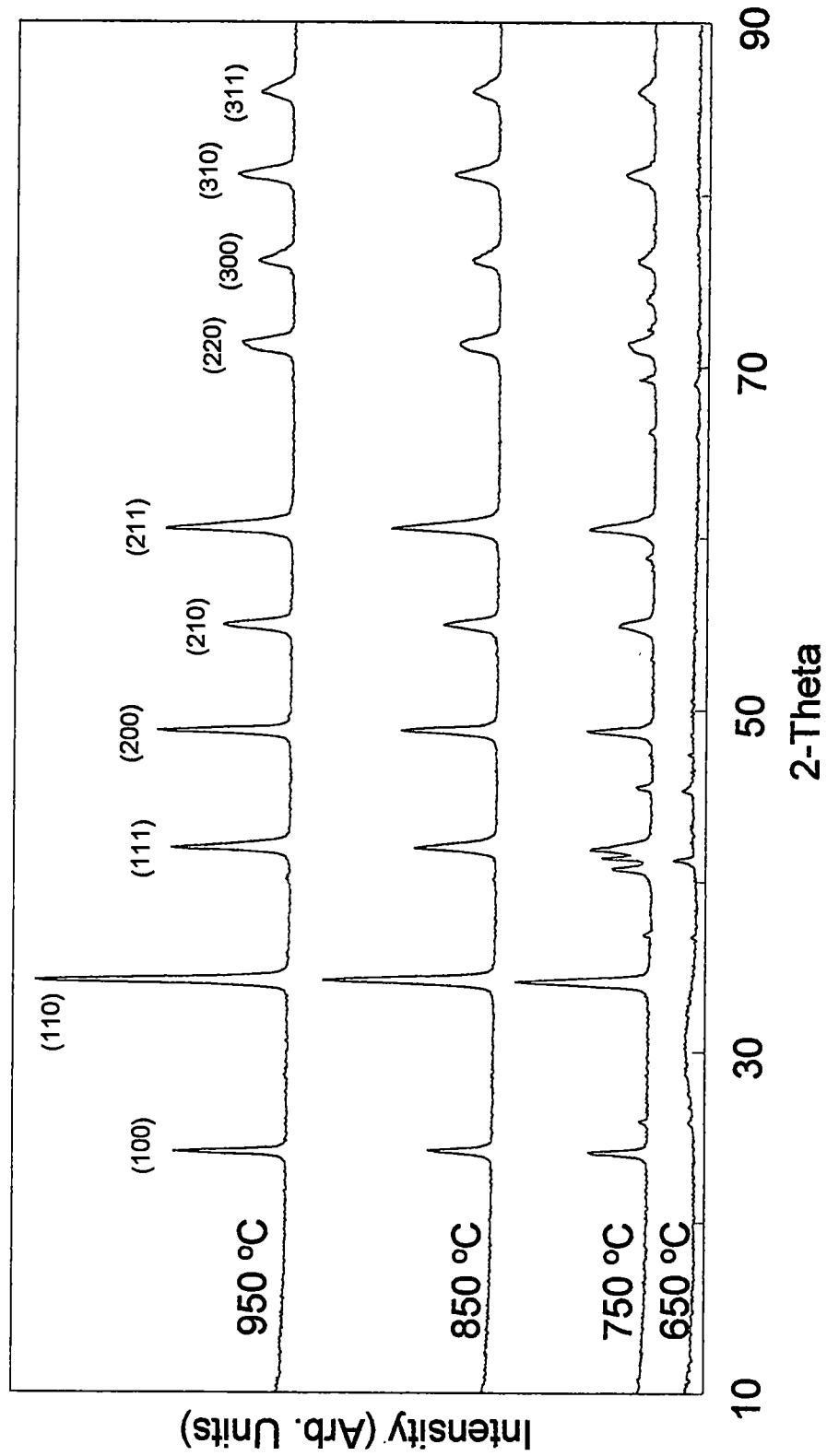
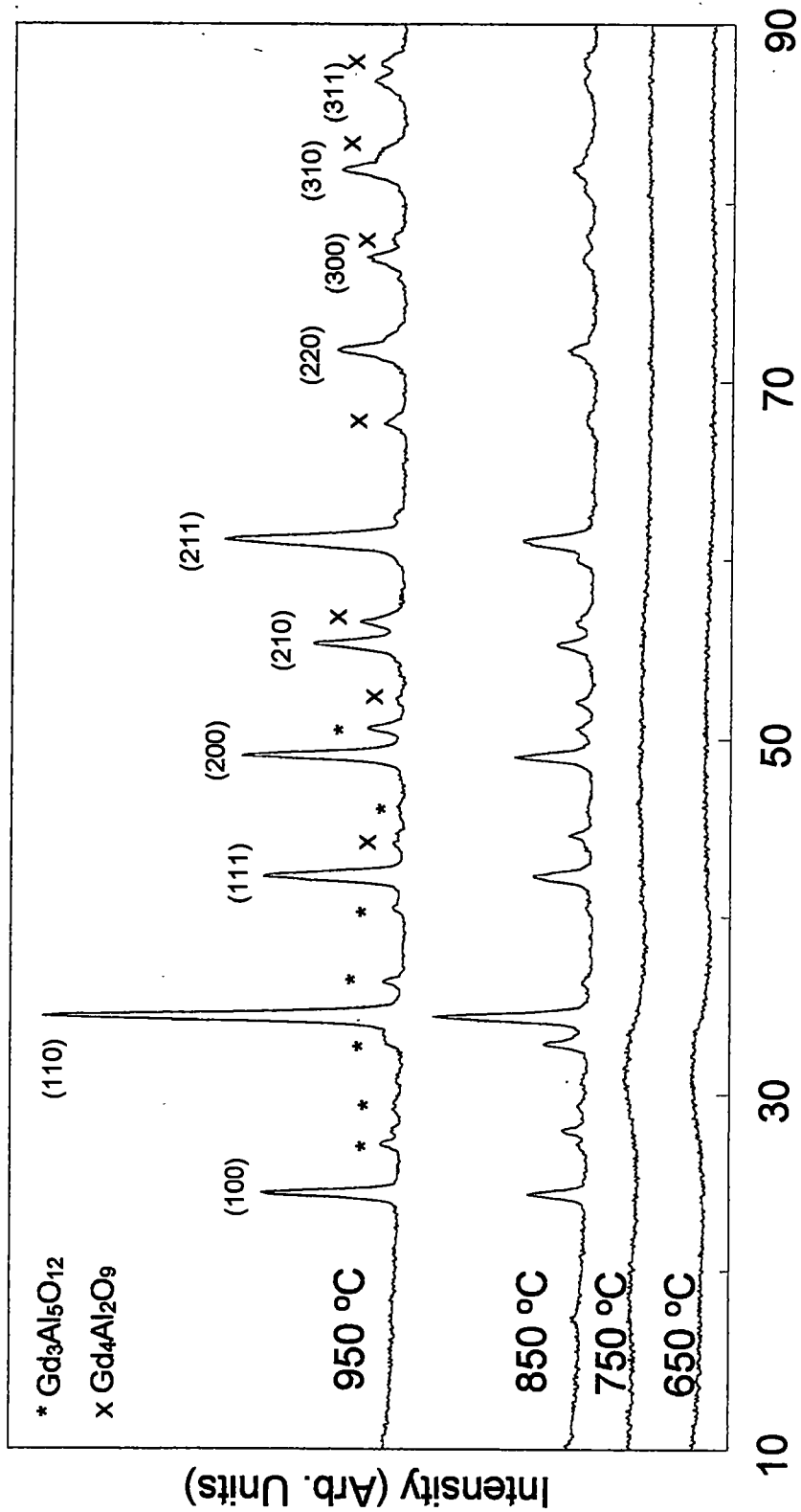


Figure 4.7. Theta/2-theta XRD of NdAlO<sub>3</sub> powders.





2-Theta

Figure 4.8. Theta/2-theta XRD of GdAlO<sub>3</sub> powders.

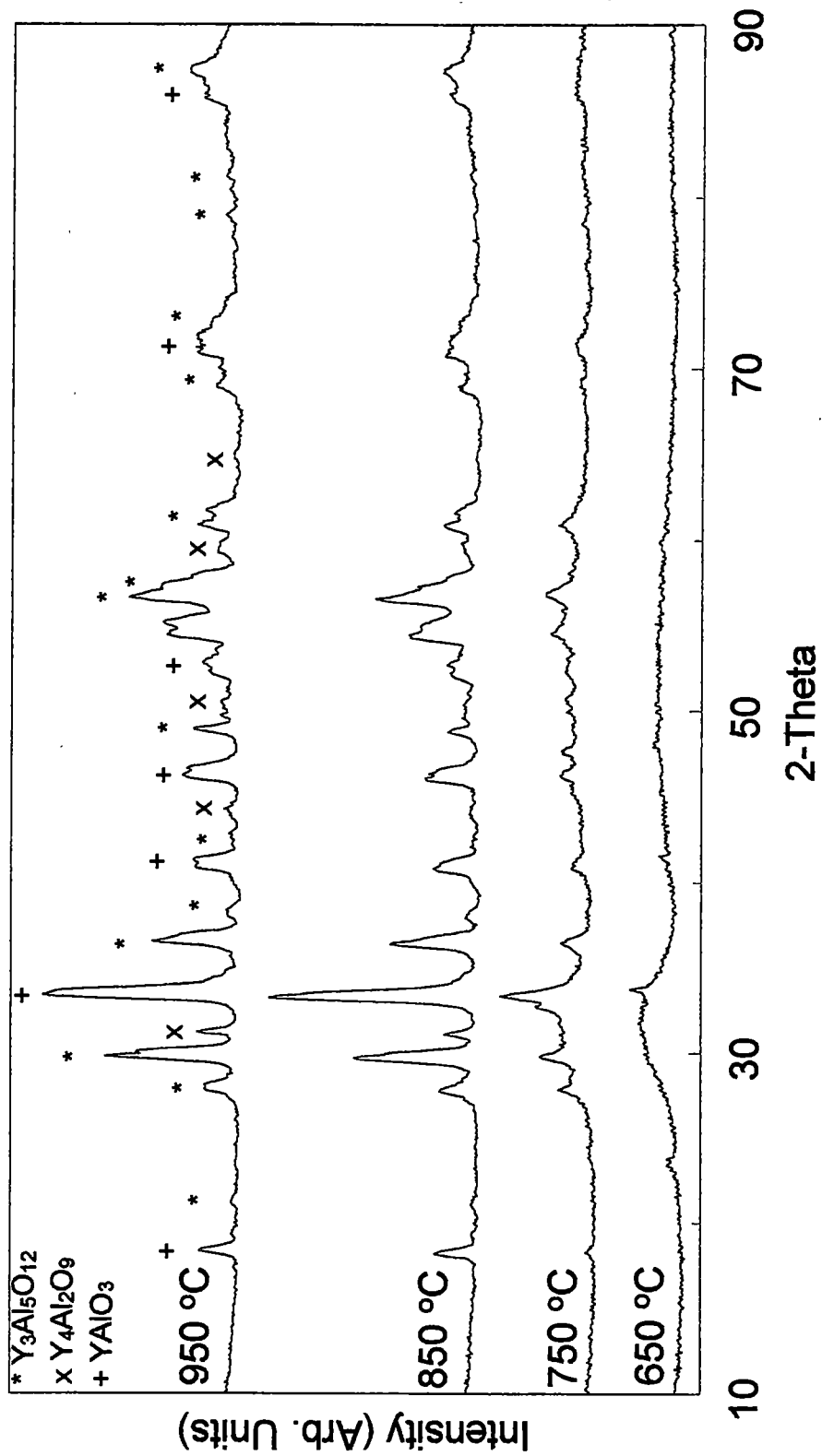


Figure 4.9. Theta/2-theta XRD of  $\text{YAlO}_3$  powders.

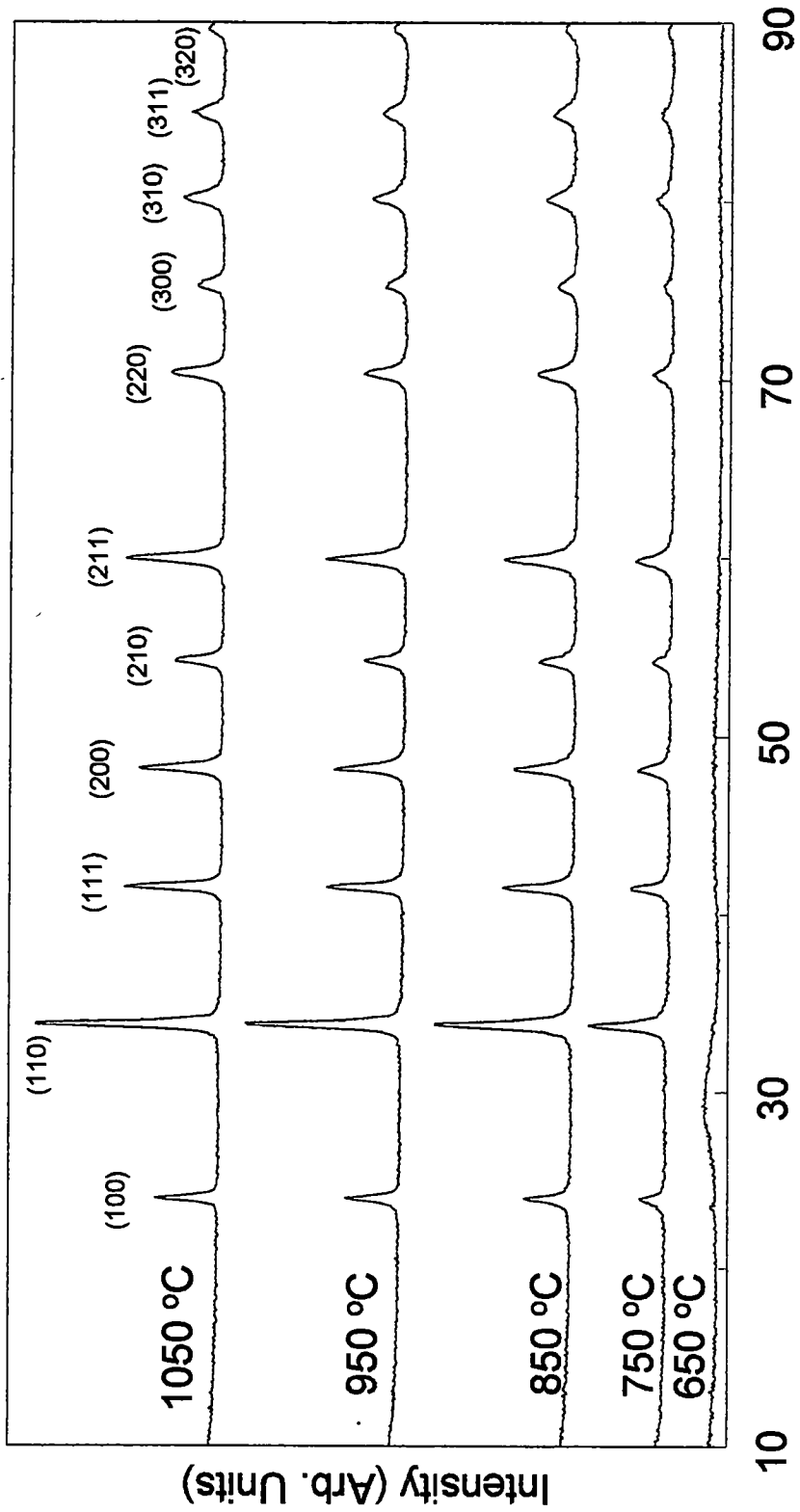


Figure 4.10. Theta/2-theta XRD of LaAlO<sub>3</sub> powders annealed in forming gas.

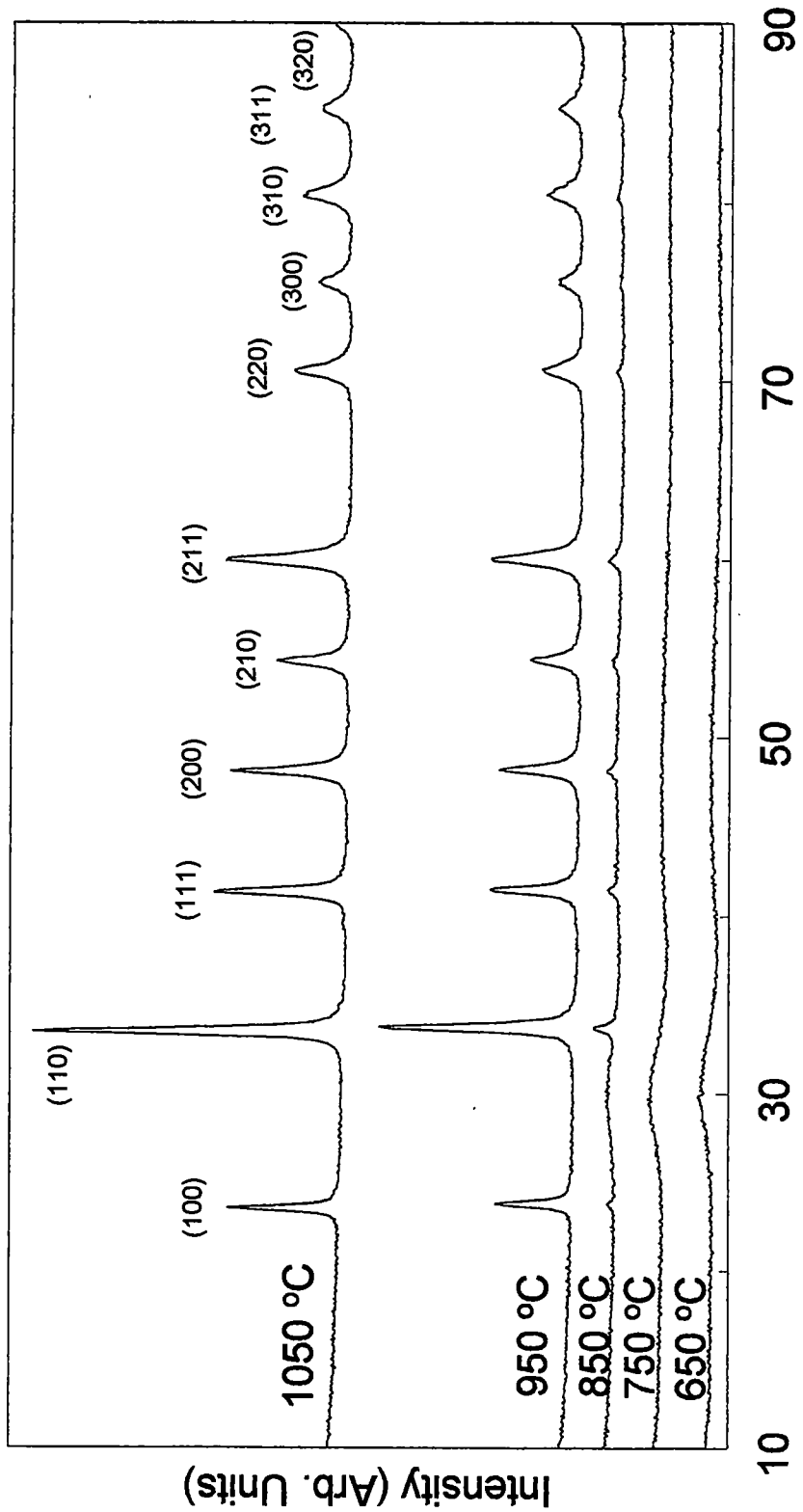


Figure 4.11. Theta/2-theta XRD of PrAlO<sub>3</sub> powders annealed in forming gas.

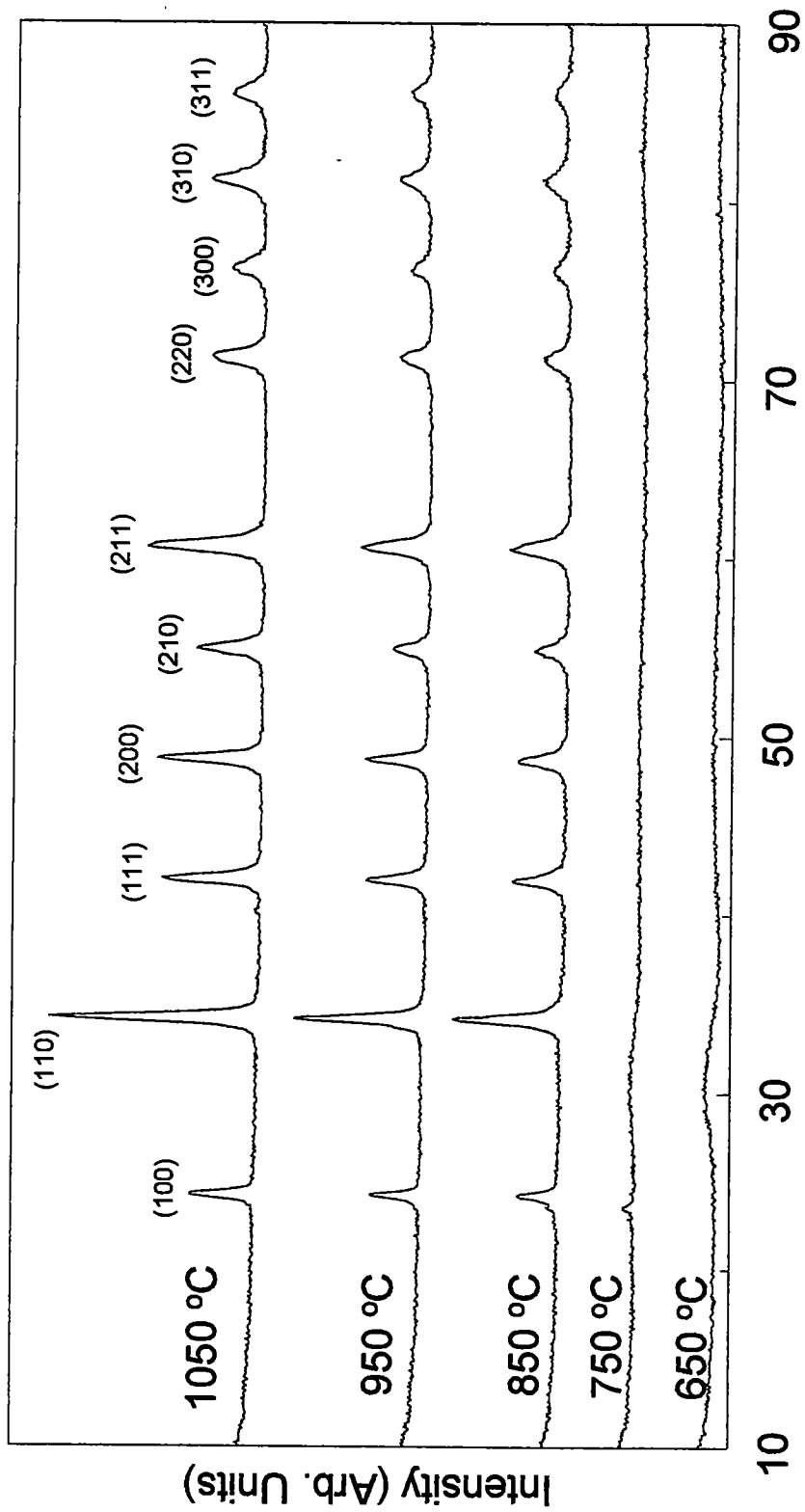


Figure 4.12. Theta/2-theta XRD of NdAlO<sub>3</sub> powders annealed in forming gas.

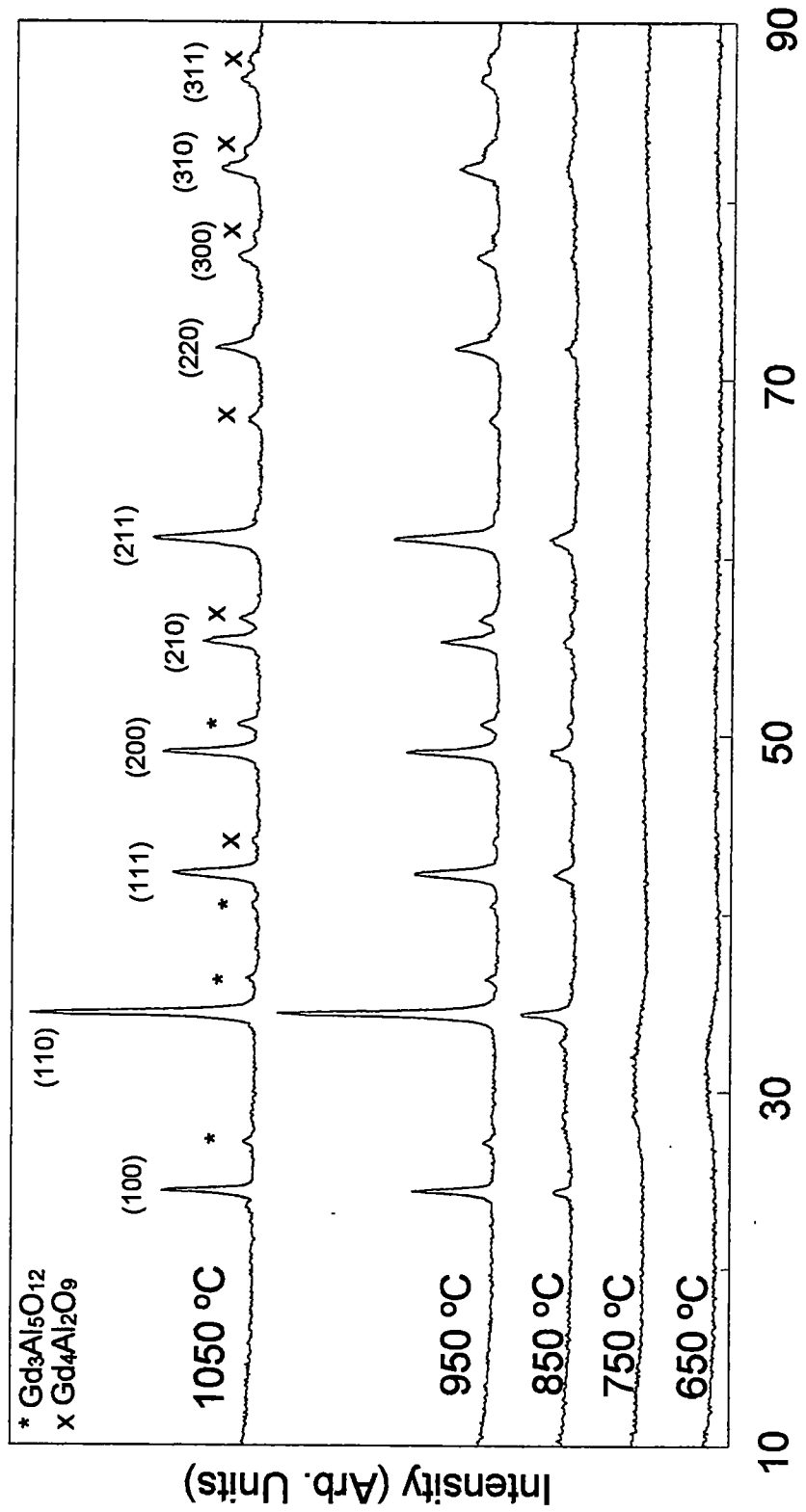


Figure 4.13. Theta/2-theta XRD of  $GdAlO_3$  powders annealed in forming gas.

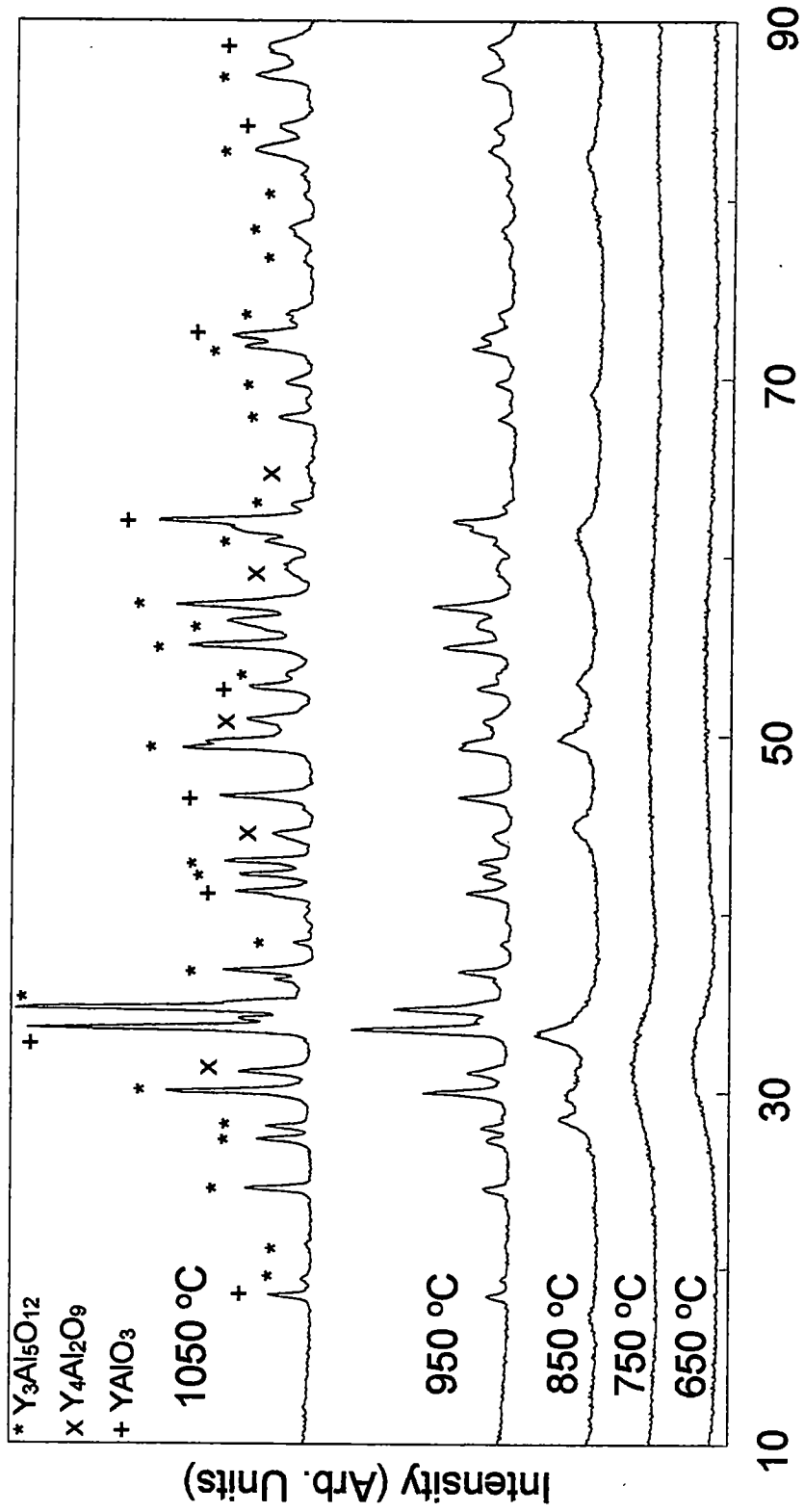


Figure 4.14. Theta/2-theta XRD of  $YAlO_3$  powders annealed in forming gas.

to one phase of the rare-earth aluminate ( $\text{Gd}_4\text{Al}_2\text{O}_9 = 2\text{Gd}_2\text{O}_3:\text{AlO}_3$ ). The yttrium showed a mixture of garnet  $\text{Y}_3\text{Al}_5\text{O}_{12}$ , two to one phase  $\text{Y}_4\text{Al}_2\text{O}_9$ , and  $\text{YAlO}_3$ . Roth<sup>81</sup> reported that the tolerance factor for forming a perovskite decreases when the B cation is large and the A cation becomes smaller. The lanthanide contraction leads to a decrease in size of rare-earth ions and to difficulties in formation of the perovskite across the lanthanide series.

#### **4.3.4. XRD Analysis of Rare-Earth Aluminate Films on Silver Substrates**

Films were deposited on silver coupons using spin-coating in order to determine the coating characteristics of the solutions. The solutions gave films that were crack-free and continuous. Film thickness was built up by deposition of successive layers and each layer was annealed at 850 °C for 20 min in air. The thickness was found to be 600 to 700 Å per layer by etching a step in the films and measuring the step height with an Alpha Step Profilometer. Figure 4.15 shows X-ray diffraction data for polycrystalline films of lanthanum aluminate, praseodymium aluminate, neodymium aluminate, gadolinium aluminate, and yttrium aluminate on silver. There were no secondary phases observed, and the relative intensity ratios were similar to the powder theta/2-theta scans.



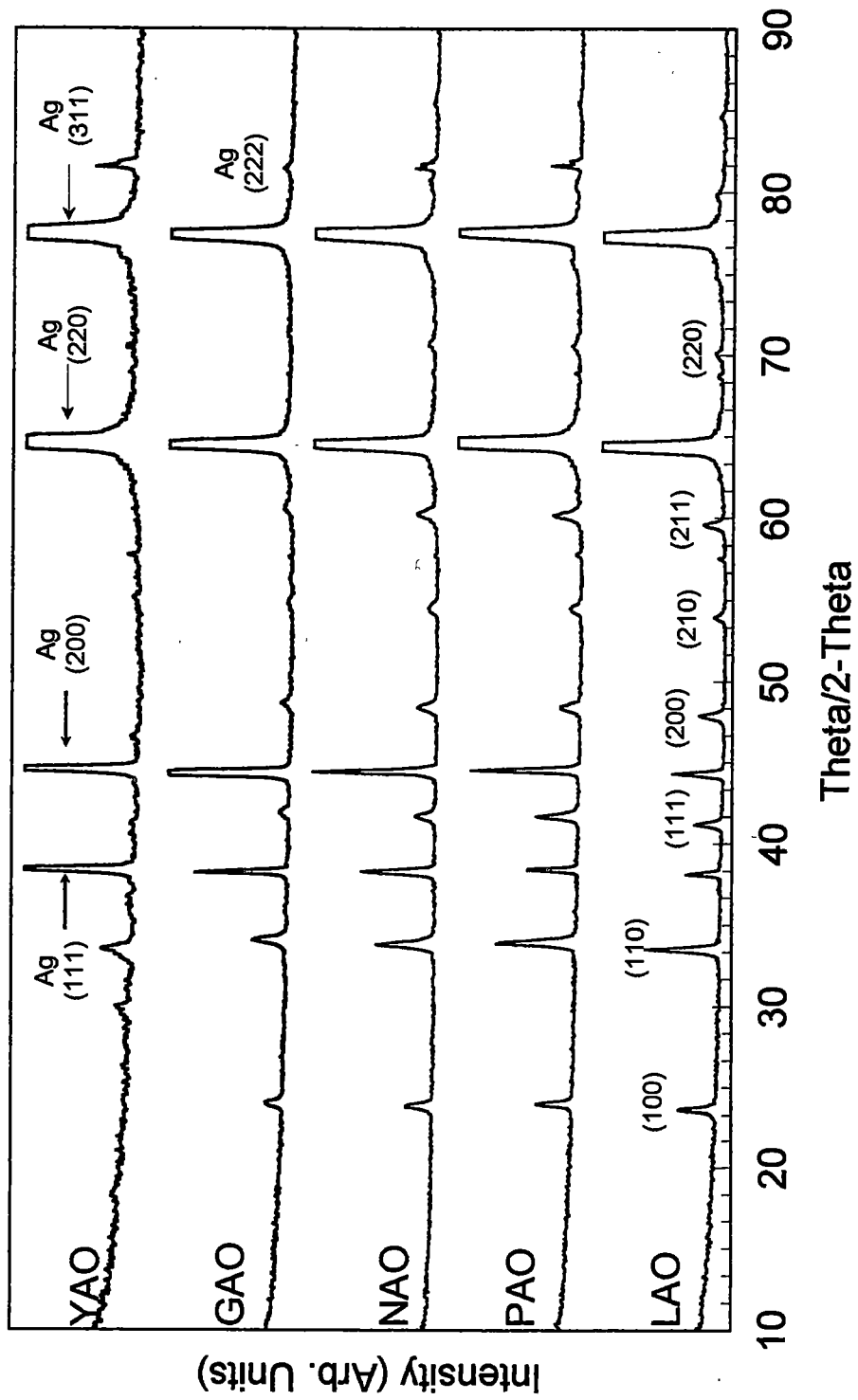


Figure 4.15. Theta/2-Theta XRD of  $\text{LaAlO}_3$ ,  $\text{PrAlO}_3$ ,  $\text{NdAlO}_3$ ,  $\text{GdAlO}_3$ , and  $\text{YAlO}_3$  on Ag at 850 °C.

#### 4.3.5. XRD Analysis of Rare-Earth Aluminate Films on Strontium Titanate and Lanthanum Aluminate

During the course of this investigation, it was observed that commercially obtained single-crystal substrates were mis-cut by 1 to 2°. The XRD peaks of the single-crystal oxide substrates, strontium titanate and lanthanum aluminate, had fwhm values of less than 0.5°. The combination of this mis-cut and the narrowness of the peaks made it difficult to align the (*h*00) peaks of the substrate, and therefore, some of the (*h*00) reflections were not observed in the XRD data.

Optical microscopy was conducted on spin-coated rare-earth aluminate films on single crystal strontium titanate and lanthanum aluminate with a thickness of approximately 280 Å, and the films were smooth and continuous. The out-of-plane orientation of the films was determined by X-ray diffraction and were indexed as pseudo-cubic. Figure 4.16 shows theta/2-theta scans of primarily (*h*00) reflections of the lanthanum aluminate, praseodymium aluminate, neodymium aluminate, gadolinium aluminate, and yttrium aluminate on (100) strontium titanate. Figure 4.17 shows theta/2-theta scans of praseodymium aluminate, neodymium aluminate, gadolinium aluminate, and yttrium aluminate on (100) lanthanum aluminate, demonstrating a high degree of out-of-plane alignment. Lanthanum aluminate on (100) lanthanum aluminate was not prepared since they have the same lattice constant. Rare-earth

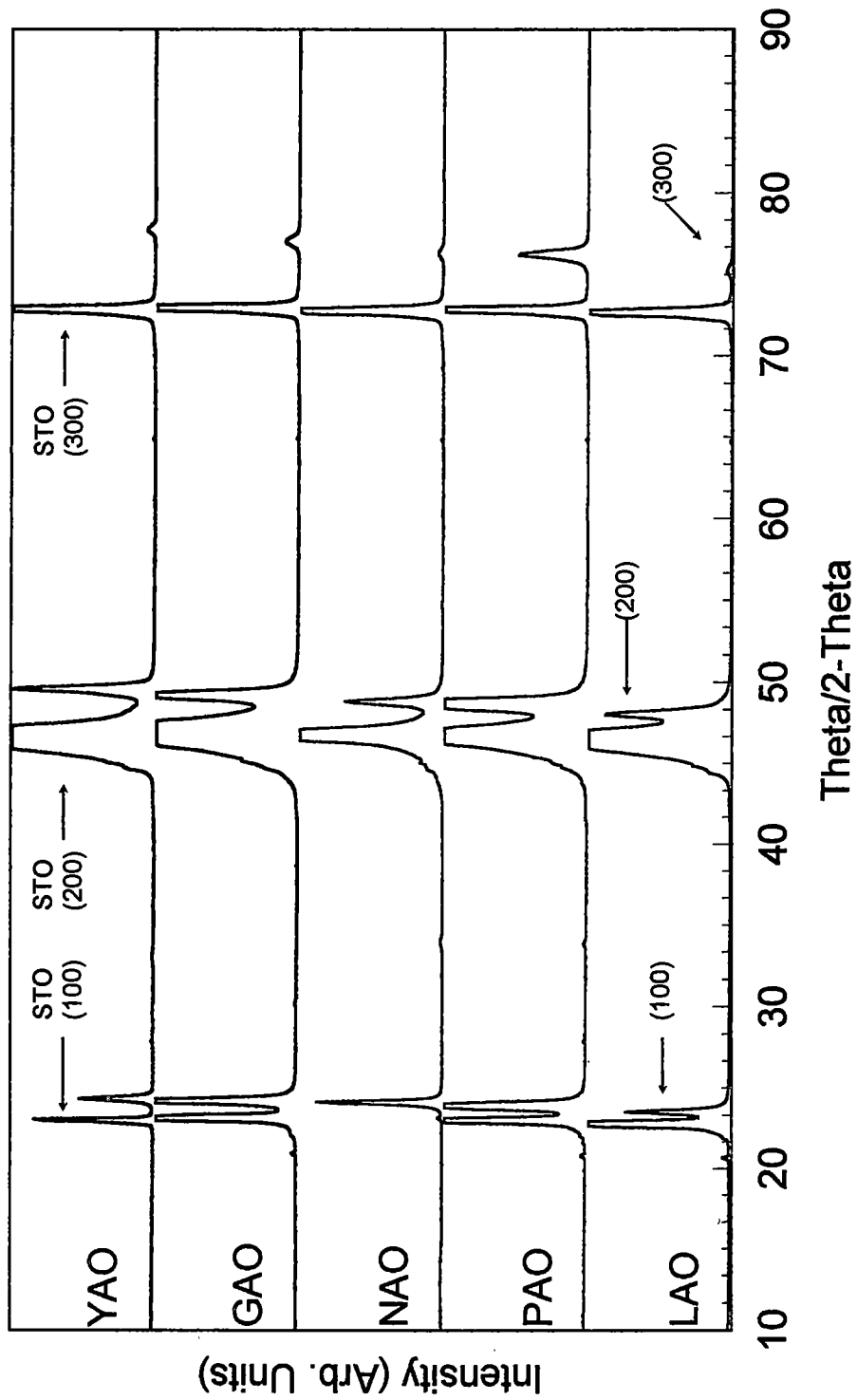


Figure 4.16. Theta/2-Theta XRD of  $\text{LaAlO}_3$ ,  $\text{PrAlO}_3$ ,  $\text{NdAlO}_3$ ,  $\text{GdAlO}_3$ , and  $\text{YAlO}_3$  on  $\text{SrTiO}_3$  at 850 °C.

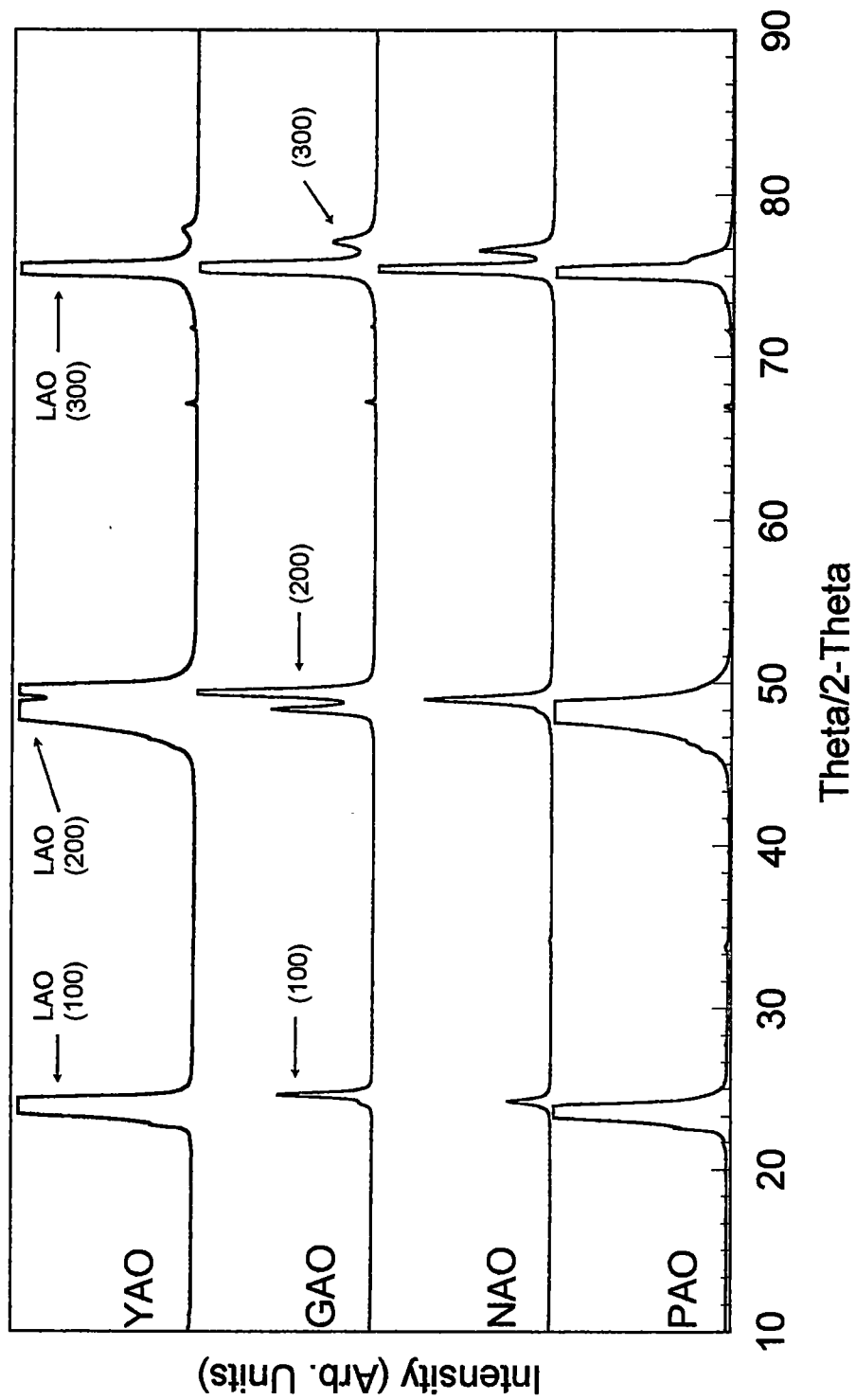


Figure 4.17. Theta/2-Theta XRD of  $\text{PrAlO}_3$ ,  $\text{NdAlO}_3$ ,  $\text{GdAlO}_3$ , and  $\text{YAlO}_3$  on  $\text{LaAlO}_3$  at 850 °C.

aluminates, one on top of another, were grown epitaxially on strontium titanate at 850 °C. Figure 4.18 shows the epitaxial growth of  $\text{YAlO}_3/\text{GdAlO}_3/\text{PrAlO}_3/\text{LaAlO}_3$  on strontium titanate when each layer was applied individually. From left to right in the lanthanide series in the periodic table, the mismatch increases due to lanthanide contractions and leads to larger mismatches. Figure 4.19 shows theta/2-theta scans of epitaxial mixed  $\text{LaAl}_{0.5}\text{Ga}_{0.5}\text{O}_3$  and  $\text{La}_{0.5}\text{Y}_{0.5}\text{Al}_{0.5}\text{Ga}_{0.5}\text{O}_3$  on  $\text{SrTiO}_3$ . Table 4.1 lists the lattice constants of all five rare-earth aluminates:  $\text{LaAlO}_3$ ,  $\text{PrAlO}_3$ ,  $\text{NdAlO}_3$ ,  $\text{GdAlO}_3$ ,  $\text{YAlO}_3$ , and the two substrates  $\text{SrTiO}_3$  and  $\text{LaAlO}_3$ .

#### **4.3.6. Out-of-Plane and In-Plane Texture Analysis of Rare-Earth**

##### **Aluminates on Strontium Titanate and Lanthanum Aluminate**

Rocking curves (omega scans) about the (300) reflections and phi scans about the (220) reflections of all five rare-earth aluminate films on strontium titanate and lanthanum aluminate were performed to determine the quality of the epitaxy. Table 4.1 lists full-width at half-maximum degrees of the omega scans. Phi scans and pole figures about the (220) plane were obtained to determine the quality of in-plane epitaxy. Figure 4.20 shows a representative phi scan of neodymium aluminate on (100) strontium titanate. Figure 4.21 shows a representative pole figure about the (220) reflection of praseodymium aluminate on strontium titanate. The pole figures (showing only four peaks at

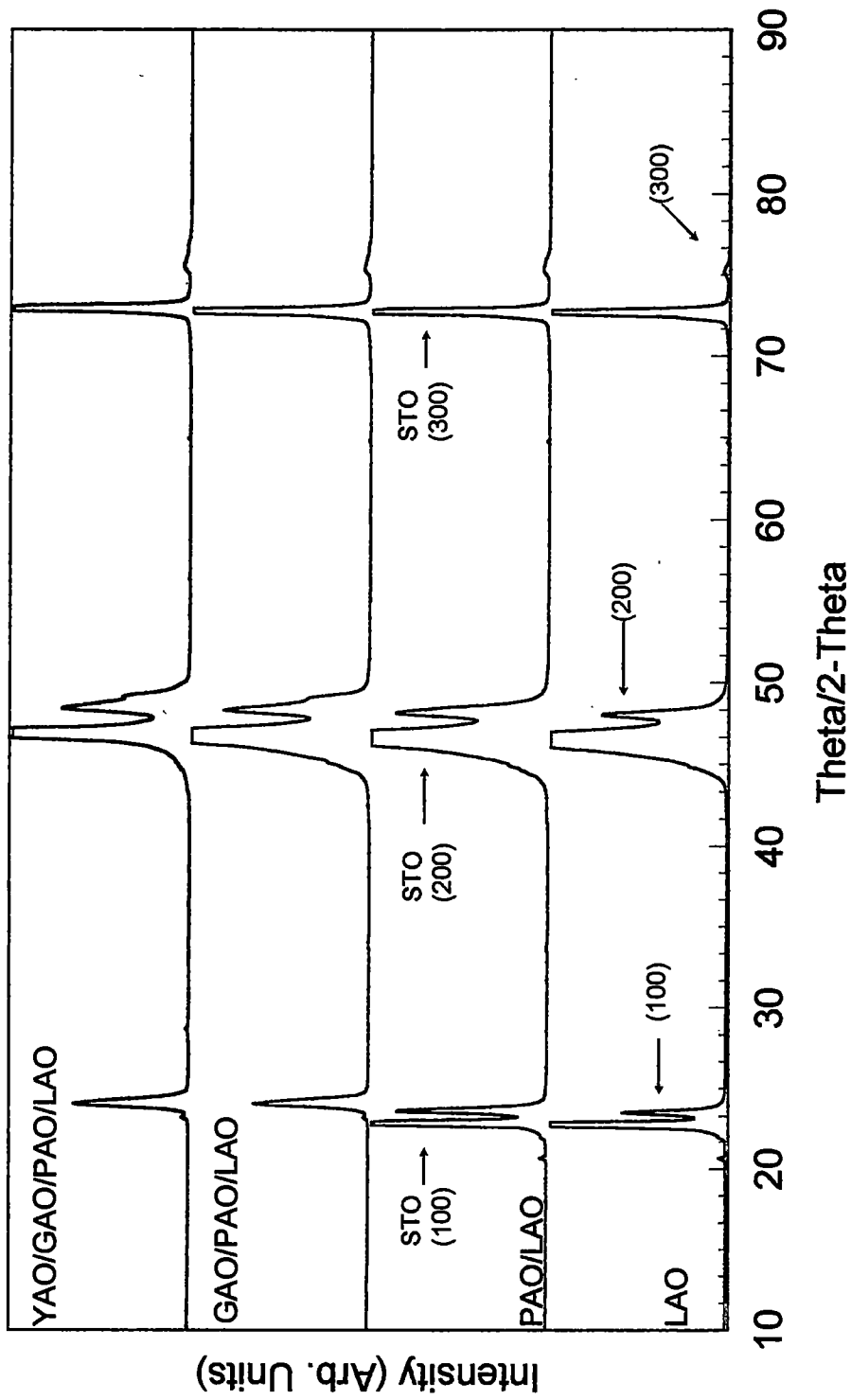


Figure 4. 18. Theta/2-Theta XRD of layered YAlO<sub>3</sub>/GdAlO<sub>3</sub>/PrAlO<sub>3</sub>/LaAlO<sub>3</sub> on SrTiO<sub>3</sub> at 850 °C.

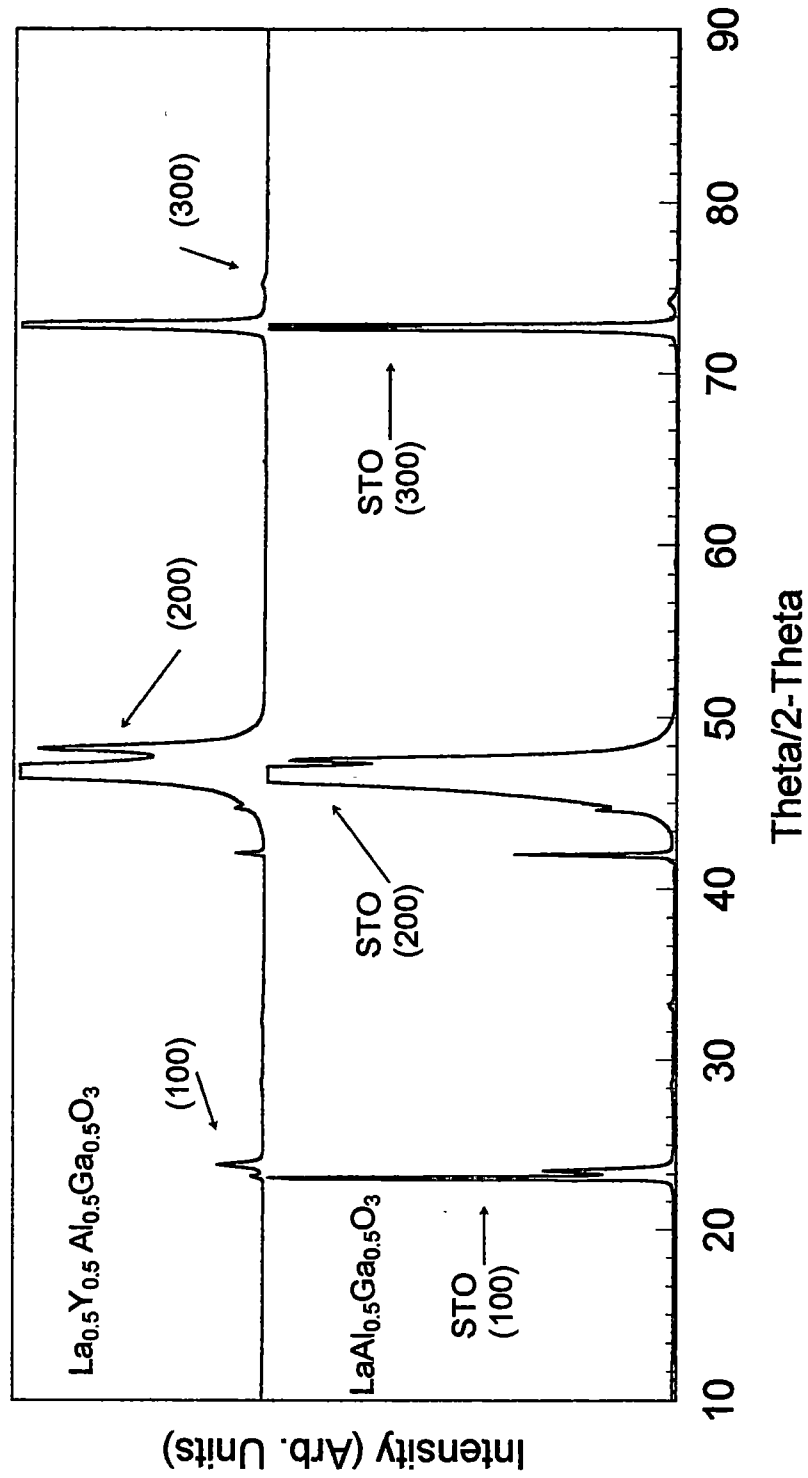


Figure 4.19. Theta/2-Theta XRD of  $\text{LaAl}_{0.5}\text{Ga}_{0.5}\text{O}_3$  and  $\text{La}_{0.5}\text{Y}_{0.5}\text{Al}_{0.5}\text{Ga}_{0.5}\text{O}_3$  on  $\text{SrTiO}_3$  at 850 °C.

Table 4.1. Full-width at half-maximum for rare-earth aluminate films.

	SrTiO <sub>3</sub>	LaAlO <sub>3</sub>	LaAlO <sub>3</sub>	LaAlO <sub>3</sub>	PrAlO <sub>3</sub>	NdAlO <sub>3</sub>	GdAlO <sub>3</sub>	YAlO <sub>3</sub>
Lattice constant <sup>1</sup>	3.905 Å	3.793 Å	3.793 Å	3.793 Å	3.75 Å	3.74 Å	3.71 Å	3.68 Å
fwhm of (300) rocking curve on SrTiO <sub>3</sub>				0.87°	0.9°	1.5°	1.6°	2.8°
fwhm of (300) rocking curve on LaAlO <sub>3</sub>				-	0.50°	0.496°	0.58°	0.40°
fwhm of (220) phi scan on SrTiO <sub>3</sub>				1.07°	1.0°	1.4°	2.1°	4.0°
fwhm of (220) phi scan on LaAlO <sub>3</sub>				-	0.59°	0.80°	0.81°	0.50°
lattice constant mismatch with SrTiO <sub>3</sub>				-2.87%	-3.97%	-4.23%	-4.99%	-5.76%
lattice constant mismatch with LaAlO <sub>3</sub>				0.0%	-1.13%	-1.33%	-2.19%	-2.98%

\*Uncertainty in the last digit indicated parenthetically.

<sup>1</sup>Giess, E. A.; Sandstrom, R. L.; Gallagher, W. J.; Gupta, A.; Shinde, S. L.; Cook, R. F.; Cooper, E. I.; O'Sullivan, E. J. M.; Roldan, J. M.; Segmuller, A. P.; Angiello, J. *IBM J. Res. Develop.* **1990**, *34*, 916.



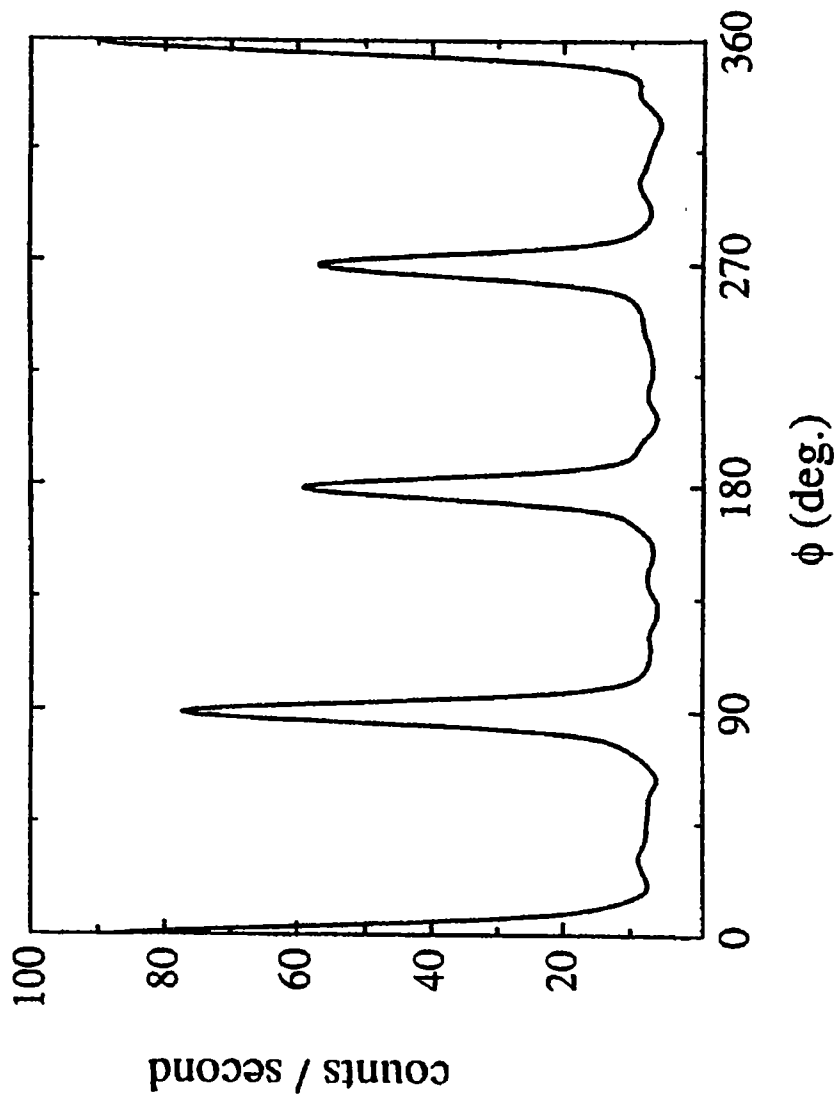
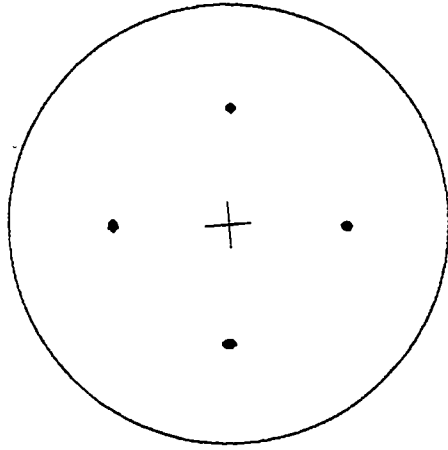


Figure 4.20. Phi scan of NdAlO<sub>3</sub> on SrTiO<sub>3</sub> about the (220) reflection.



PrAlO<sub>3</sub> on SrTiO<sub>3</sub>  
(220)

Figure 4.21. Pole figure of PrAlO<sub>3</sub> on SrTiO<sub>3</sub> about the (220) reflection.

chi of  $45^\circ$  spaced  $90^\circ$  in phi), were indicative of a single in-plane epitaxial relationship between the film and the substrate (cube-on-cube epitaxy). Full-width at half-maximum of the phi scans showed a measure of the quality of the epitaxy (Table 4.1). The lattice constant mismatch for the rare-earth aluminates on strontium titanate and lanthanum aluminate correlated with the full-width at half-maximum values.

#### **4.3.7. Analysis of Rare-Earth Aluminate Films on Roll-Textured Nickel**

Rare-earth aluminates on roll-textured nickel were annealed at  $1150^\circ\text{C}$  for 1 h in forming gas (4%  $\text{H}_2$  in Ar). Figure 4.22 shows theta/2-theta scans of lanthanum aluminate, praseodymium aluminate, neodymium aluminate, gadolinium aluminate, and yttrium aluminate on (100) nickel. Prominent ( $h00$ ) peaks of the lanthanum aluminate, praseodymium aluminate, and neodymium aluminate films were observed as well as a small (110) peak. Gadolinium aluminate and yttrium aluminate on nickel were not epitaxial, and omega and phi scans were thus not performed on these two films. Omega scans about the (200) reflection were obtained on the lanthanum aluminate, praseodymium aluminate, and neodymium aluminate films. The fwhm values were significantly higher than that of the single crystal oxide films but were similar to the fwhm of the rocking curves of the nickel substrate about the (200) reflection. The in-plane epitaxy was determined by a phi scan and a pole figure of the film.

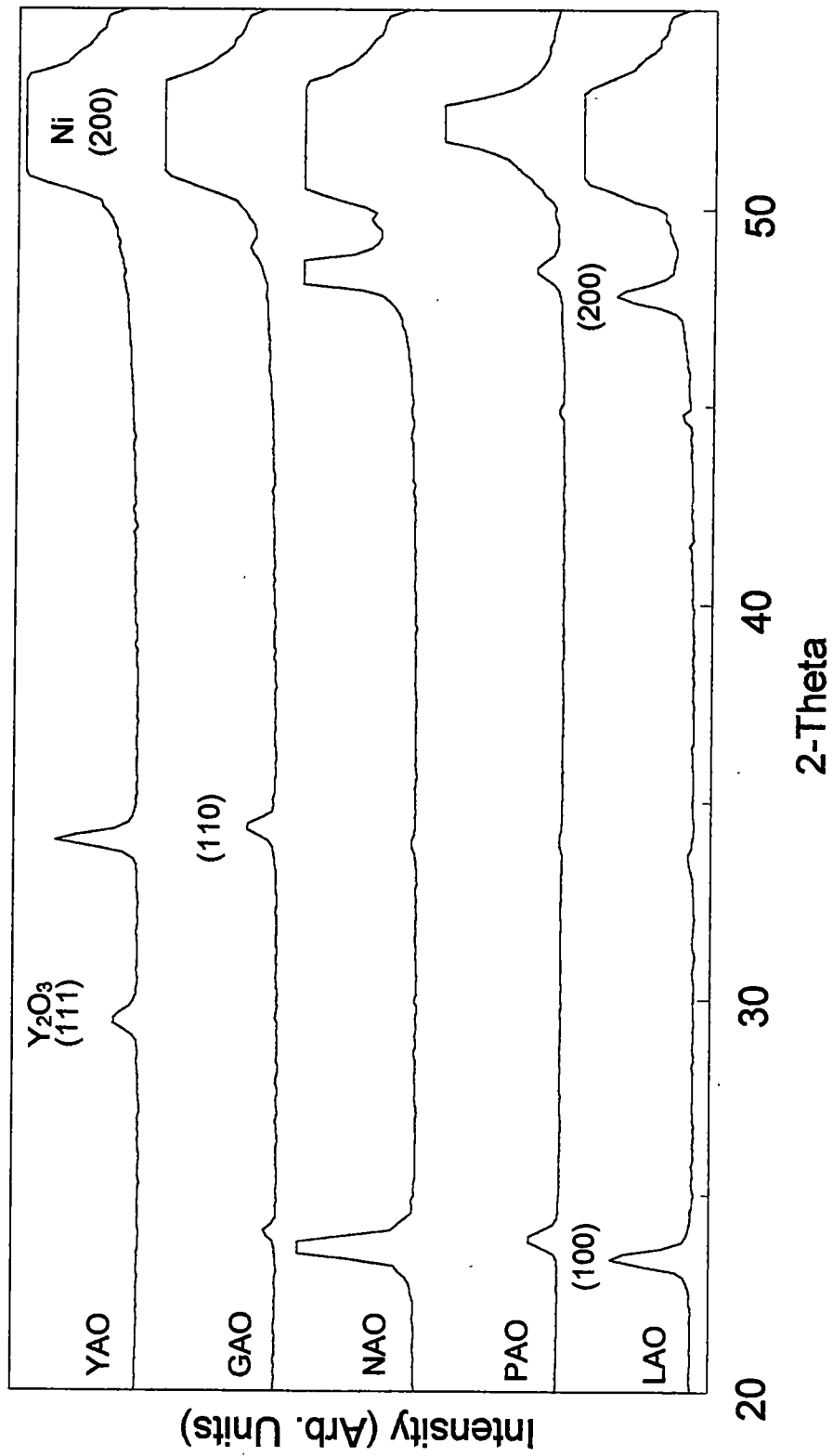


Figure 4.22. Theta/2-theta XRD of LaAlO<sub>3</sub>, PrAlO<sub>3</sub>, NdAlO<sub>3</sub>, GdAlO<sub>3</sub>, and YAlO<sub>3</sub> on Ni.

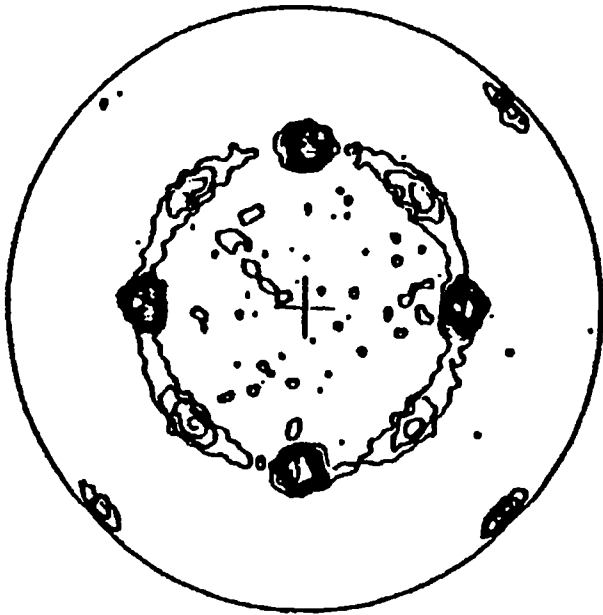
Omega and phi scan fwhm values for the three epitaxial rare-earth aluminate films on nickel are listed in Table 4.2. Figure 4.23 shows a representative pole figure of lanthanum aluminate (110) on nickel. An eight-fold symmetry was observed which indicated that two in-plane epitaxies were present. The major epitaxy was lanthanum aluminate (100) and the minor was lanthanum aluminate (110). Figure 4.24 shows 360° of a phi scan of NdAlO<sub>3</sub> on nickel which had eight peaks. The smaller peaks were the (110) epitaxy and are about half as intense as the (100) epitaxy.

#### **4.4. Conclusion.**

Solution synthesis through novel sol-gel chemistry provides a simple and low-cost method to produce high quality heteroepitaxial films of rare-earth aluminates on readily available single crystal oxide substrates. It is also possible to engineer lattice mismatch through heteroepitaxial growth of multiple buffer layers so as to minimize crystalline defects. This involves either stacking different rare-earth aluminates or mixing rare-earth metal solutions with aluminum and/or gallium solutions. The rare-earth aluminates on roll-textured nickel did not produce single in-plane grain alignment and are not suitable for superconductivity buffer layers produced by a solution route.

**Table 4.2.** Full-width at half-maximum for LaAlO<sub>3</sub>, PrAlO<sub>3</sub>, and NdAlO<sub>3</sub> on Ni.

	Lattice constant	fwhm of (200) rocking curve on Ni	fwhm of (110) phi scan on Ni	Lattice constant mismatch with Ni
Nickel	3.52 Å	7.06°	8.45°	<del> </del>
LaAlO <sub>3</sub>	3.793 Å	7.2°	13.4°	7.76%
PrAlO <sub>3</sub>	3.75 Å	7.2°	12.0°	6.53%
NdAlO <sub>3</sub>	3.74 Å	5.8°	12.2°	6.25%



LaAlO<sub>3</sub> on Ni  
(100) and (110) reflections  
observed

Figure 4.23. Pole figure of LaAlO<sub>3</sub> on Ni about the (110) reflection.

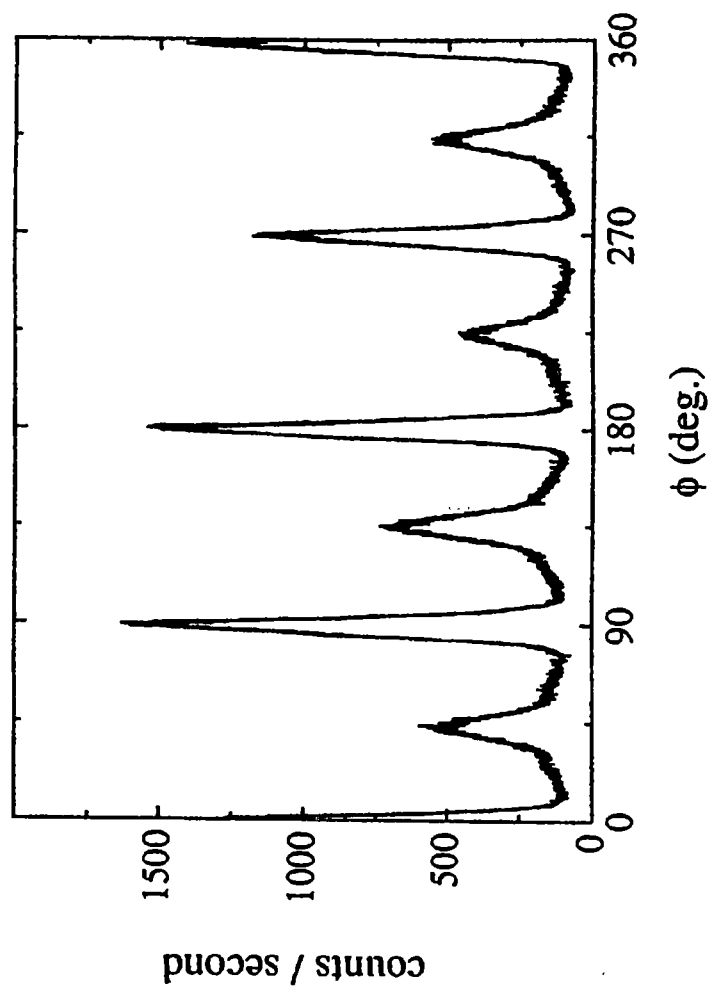


Figure 4.24. Phi scan of NdAlO<sub>3</sub> on Ni about the (220) reflection.



## CHAPTER 5

### EPITAXIAL GROWTH OF TETRAGONAL PEROVSKITES ( $ABCO_4$ ) THIN-FILMS

#### 5.1. Introduction

Oxides of the general form  $ABCO_4$ , where A is an alkali earth metal, B is a rare-earth element, and C is a group III element such as gallium or aluminum, have a tetragonally distorted perovskite structure. They are potentially an important class of substrates for the deposition of electronic ceramics such as the cuprate superconductors, because these oxides have low dielectric constants and good in-plane lattice match to the superconductors. Upon crystallization of the compounds, they adopt the structure of  $K_2NiF_4$ . Figure 5.1 shows the typical tetragonal structure of the  $ABCO_4$  compounds.<sup>82</sup> Previous research has provided more than fifty examples of these compounds, and Pajczkowska and Gloubokov<sup>82</sup> have recently reviewed synthesis and structural properties of these compounds. It is relatively difficult to grow single crystals of these materials, and consequently they are four or five times more expensive than commercial wafers of  $SrTiO_3$  and  $LaAlO_3$  of the same size. However, heteroepitaxial growth of thin-films of the desired material on a commercially available substrate is an alternative to the expensive growth of single-crystal substrates.

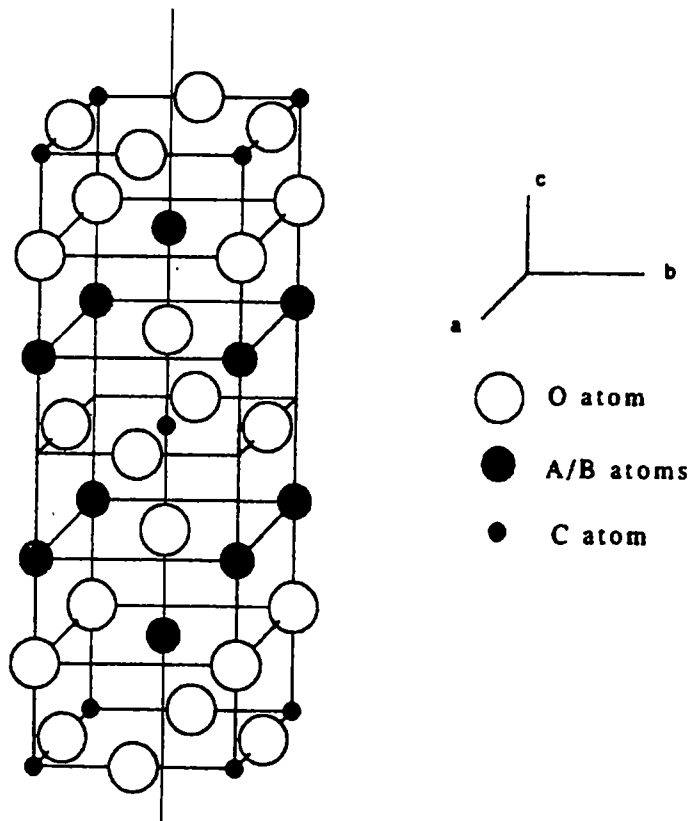


Figure 5.1. Structure of  $ABCO_4$  compounds.

Marks *et al.*<sup>83,84</sup> have reported the heteroepitaxial growth of SrPrGaO<sub>4</sub> and SrLaGaO<sub>4</sub> on LaAlO<sub>3</sub> using metal organic chemical vapor deposition (MOCVD). These authors have also deposited YBa<sub>2</sub>Cu<sub>3</sub>O<sub>7</sub> on the epitaxial films and reported excellent electrical properties for the superconductor. As a simpler alternative to the MOCVD synthesis, solution synthesis can be used to produce epitaxial films on commercially available substrates. Solution synthesis provides accurate control of complex film stoichiometry and the ability to obtain high quality films.

The following sections of this chapter provide procedures and results for solution deposition of tetragonal perovskite thin-films in which the rare-earth element and Group III element were varied. Films were deposited on silver foil, (100) strontium titanate single-crystals, and (100) lanthanum aluminate single-crystals. The effect of these variations on film structure was determined by X-ray diffraction (XRD). Structural and electrical results of copper oxide-based high temperature superconductors with a tetragonal perovskite as a buffer layer were also obtained.

## **5.2. Experimental Details**

### **5.2.1. General Procedures**

All manipulations were performed under dry argon atmosphere with the use of either standard Schlenk techniques or a glove box. Lanthanum isopropoxide (Gelest, 99.9%), praseodymium metal (Alfa Aesar, 99.9%),

aluminum isopropoxide (Aldrich, 99.99%), strontium metal (Alfa Aesar, 99.9%), gallium trichloride (Alfa Aesar, 99.9%), and 2-methoxyethanol (Aldrich, HPLC grade) were used as received. Benzene was dried over sodium/benzophenone and distilled before use. Isopropanol was dried over aluminum isopropoxide and distilled before use. The sol-gel chemistry used was pioneered by Payne *et al.*<sup>19</sup> and is based on solutions of metal methoxyethoxide complexes in 2-methoxyethanol.

### 5.2.2. Preparation of Gallium Isopropoxide $\text{Ga}(\text{OPr}^i)_3$

Gallium isopropoxide,  $\text{Ga}(\text{i-OC}_3\text{H}_7)_3$ , was prepared from the reaction of gallium trichloride and sodium isopropoxide first reported by Mehrotra.<sup>75</sup> A 250 mL Schlenk flask with a magnetic stir bar and condenser was charged with 4.88 g (0.212 mol) of crushed sodium metal, 18 mL of dry isopropanol, and 100 mL of dry benzene. The mixture was refluxed at 85 °C overnight to insure complete reaction of the sodium and isopropanol. Another 250 mL Schlenk flask was charged with 12.0 g (68 mmol) of  $\text{GaCl}_3$  and 50 mL of benzene. The  $\text{GaCl}_3$  was allowed to dissolve in benzene, and added dropwise to the  $\text{NaOPr}^i$  solution from the top of the condenser via a syringe to maintain a gentle reflux. The mixture was then refluxed for 8 h, and filtered afterwards. The volatiles in the filtrate were removed at 23 °C under vacuum to give a viscous oil. A microdistillation apparatus was attached to the Schlenk flask and the solution

was distilled under reduced pressure. Approximately 8.8 g (66.8 mmol, 52%) of  $\text{Ga}(\text{i-OC}_3\text{H}_7)_3$  were collected at 137-141 °C and 0.1 torr. The gallium isopropoxide was placed in an inert atmosphere drybox and allowed to harden from a colorless viscous liquid to a semi-solid wax. (Oliver and Worrall<sup>76</sup> have attributed this change in state to conversion of the initially formed trimer to a more stable tetrameric oligomer.)

### 5.2.3. Preparation of Lanthanum and Praseodymium Isopropoxide

Lanthanum and praseodymium isopropoxide solutions were prepared by reacting the metals directly with dry isopropanol in the presence of mercuric catalysts which was first described by Brown and Mazdidasni.<sup>77</sup> Commercial powders of the metals failed to react with the dry isopropanol in the presence of a catalyst. Metal filings were obtained by using a rasp to file the metal under an inert atmosphere. The appropriate metal filings [1.736 g (12.5 mmol) of lanthanum and 1.76 g (12.5 mmol) of praseodymium] were added to a 250 mL Schlenk flask with 90 mL of dry isopropanol, a magnetic stir bar, 5 mg of  $\text{Hg}(\text{OOCCH}_3)_2$ , and 5 mg of  $\text{HgCl}_2$ . The mixtures were allowed to reflux overnight at 85 °C and then filtered. The solvent was removed at reduced pressure to give an off-white solid. The lanthanum and praseodymium isopropoxides were extracted using a Soxhlet extractor with dry isopropanol and then purified by recrystallization. Yields ranged between 50-70%.

#### 5.2.4. Preparation of Methoxyethoxide Solutions

Each of the metal isopropoxides was mixed with 90 mL of 2-methoxyethanol to undergo exchanges between isopropoxide and methoxyethoxide ligands. Each solution was refluxed for 1 h at 140 °C, and 60 mL of the solvent was removed by distillation at atmospheric pressure. The solvent removed by distillation was replaced with fresh 2-methoxyethanol. The ligand exchange process was repeated two more times to ensure complete ligand exchange. Each solution was adjusted to 50 mL, and its molality was calculated based on the moles of isopropoxide used and the weight of the solutions. (The use of molality rather than molarity allowed the gravimetric preparation of small volumes of solutions with high accuracy.) The following tetragonal perovskite oxides were made from the stock solutions: strontium lanthanum gallate ( $\text{SrLaGaO}_4$ ), strontium praseodymium gallate ( $\text{SrPrGaO}_4$ ), strontium lanthanum aluminate ( $\text{SrLaAlO}_4$ ), and strontium praseodymium aluminate ( $\text{SrPrAlO}_4$ ).

#### 5.2.5. Powder and Film Preparation

The stock solutions were mixed in a ratio of one part hydrolysis solution (1.0 M water in 2-methoxyethanol) to four parts of the stock solution, resulting in a partially hydrolyzed coating solution. Powders were prepared by the addition of excess water to the coating solution followed by the decomposition

of the resultant gels at 300 °C. The gels were crushed, ground with a mortar and pestle, and fired in air for 1 h at the temperatures indicated in the following section. Each substrate, strontium titanate (100) or lanthanum aluminate (100), was heated for 1 h in oxygen at 1000 °C and 800 °C, respectively, prior to coating. Silver foil was polished with 0.06 micron extra pure alumina abrasive and cleaned in distilled water. The hydrolyzed stock solutions were applied to the substrates through a 0.2 µm syringe filter and spin coated on a photo-resist spinner for 30 s at 2,000 rotations per minute (rpm). The substrates were placed in a preheated, Thermolyne furnace at 850 °C for 20 min in air. Each coat was approximately 70 nm thick, and this coating and firing procedure was repeated four times.

#### **5.2.6. Deposition of Yttrium Barium Copper Oxide Superconductor**

The YBCO superconductor was deposited on strontium praseodymium gallate and strontium lanthanum gallate buffer layers by pulsed laser deposition (PLD), using a XeCl excimer laser operating at a wavelength of 308 nm focused to produce a 3 J/cm<sup>2</sup> fluence at the YBCO target. The laser-pulse repetition rate was 5 Hz and 6000 laser pulses were required to obtain a film thickness of 250 nm. During the deposition of the YBCO, the strontium titanate or lanthanum aluminate substrate temperature was maintained at 780 °C and the oxygen pressure was held at 200 mTorr. Additionally, the YBCO target was

rotated at 21 rpm to minimize both the rate of cone formation and the change in stoichiometry on the surface of the YBCO during laser ablation. After the deposition was completed, the samples were cooled at a rate of 5 °C per minute in 300 Torr of oxygen to 500 °C to ensure full oxygen uptake by the YBCO. Once the temperature reached 500 °C, additional oxygen was added to bring the pressure to 500 Torr, and the temperature and pressure were maintained for 1 h. Finally, the substrates were cooled to room temperature at a rate of 1 °C per minute.

#### **5.2.7. Critical Current and Critical Temperature Measurements**

In order to obtain critical current ( $I_c$ ) and critical temperature ( $T_c$ ) measurements, four silver electrical contacts, approximately one-half micrometers thick, were sputtered on the YBCO film surface. The samples were then annealed for 30 min at 500 °C in flowing oxygen to ensure low contact resistance.

The property of resistivity was used to find the critical temperature at a constant current. A four-probe AC measurement was conducted in conjunction with a closed cycle helium refrigerator. Samples were cooled under vacuum to a low temperature, and then slowly warmed. Voltage was measured every 0.2 K during warm up. The  $T_c$  was the temperature reached when resistance first occurred, i.e., when any voltage was detected.



To find the critical current, the sample was put in a constant temperature environment of liquid nitrogen. Current was applied and slowly increased while the voltage was monitored. When a voltage is first detected at a particular current, the sample is no longer considered to be superconducting.

### 5.3. Results and Discussion

#### 5.3.1. XRD Analysis of Tetragonal Perovskite Powders

The annealing behavior of SrLaGaO<sub>4</sub>, SrPrGaO<sub>4</sub>, SrLaAlO<sub>4</sub>, and SrPrAlO<sub>4</sub> powders was evaluated under oxidizing conditions. Figures 5.2 to 5.5 show X-ray diffraction data of powders annealed at temperatures from 650 °C to 1050 °C for 1 h in air. It was observed that crystallization started at 650 °C and full crystallization occurred at 850 °C. Table 5.1 reports the lattice constant values obtained on the powders in the *I4/mmm* space group. These lattice constants are in excellent agreement with those reported by Pajaczkowska and Gloubokov.<sup>82</sup> The lattice constants showed the trend that substitution of La for Pr causes the *c*-axis to expand with little effect on the *a*-axis. Also, substitution of Ga for Al results in an expansion of the *a*-axis with little effect on the *c*-axis.<sup>82</sup>

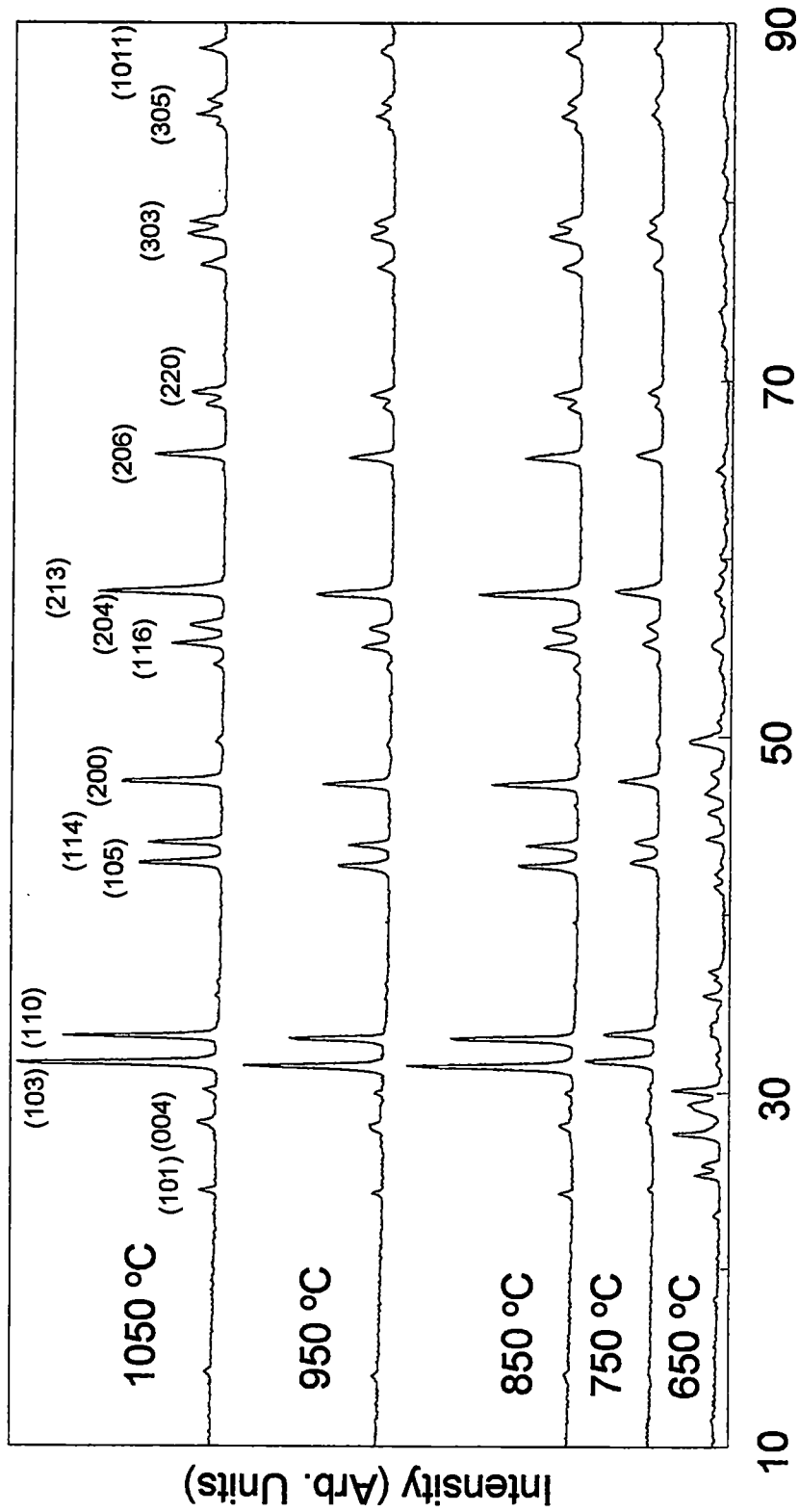
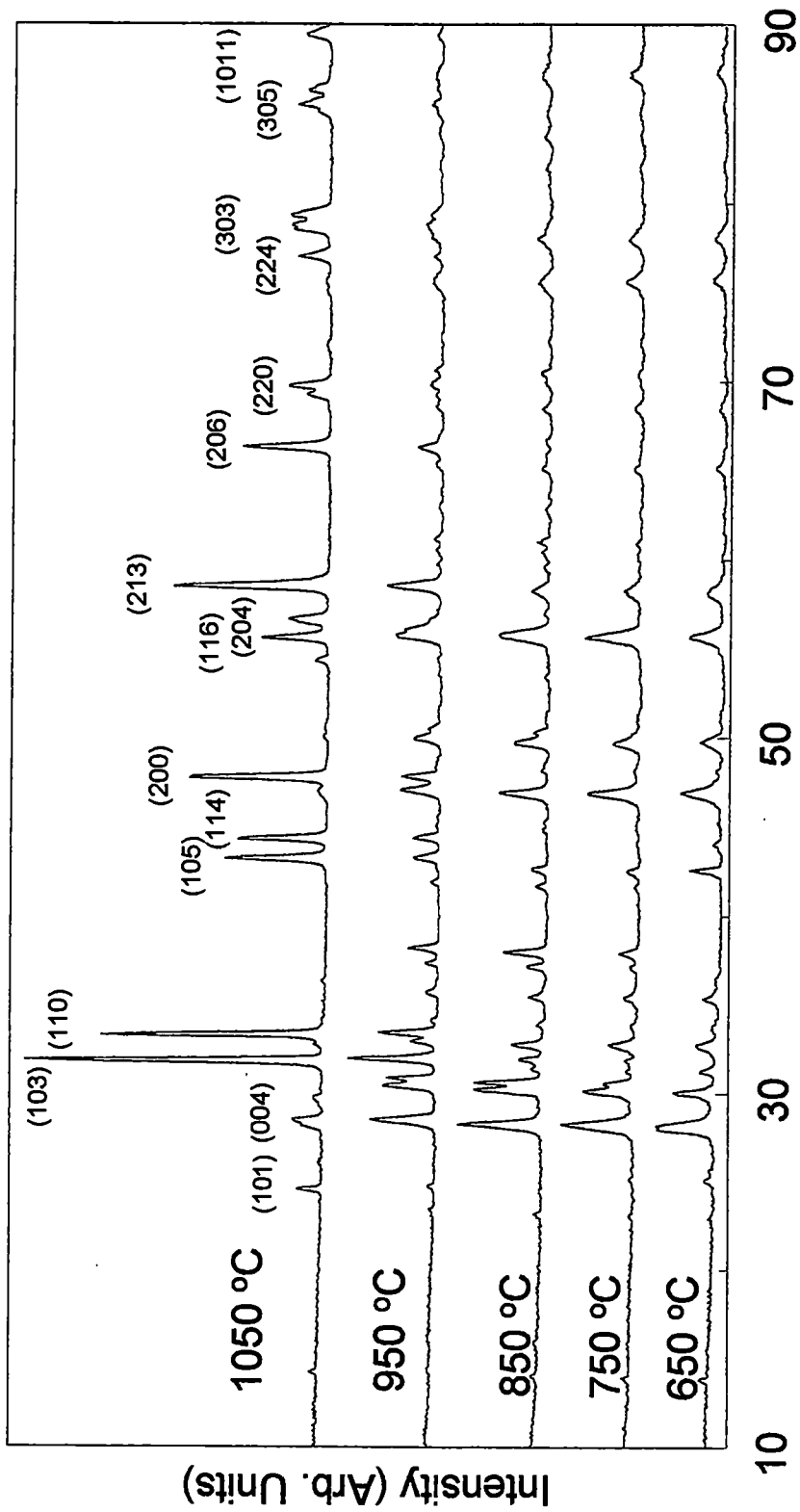


Figure 5.2. Theta/2-theta XRD of SrLaGaO<sub>4</sub> powders.



2-Theta

Figure 5.3. Theta/2-theta XRD of SrPrGaO<sub>4</sub> powders.

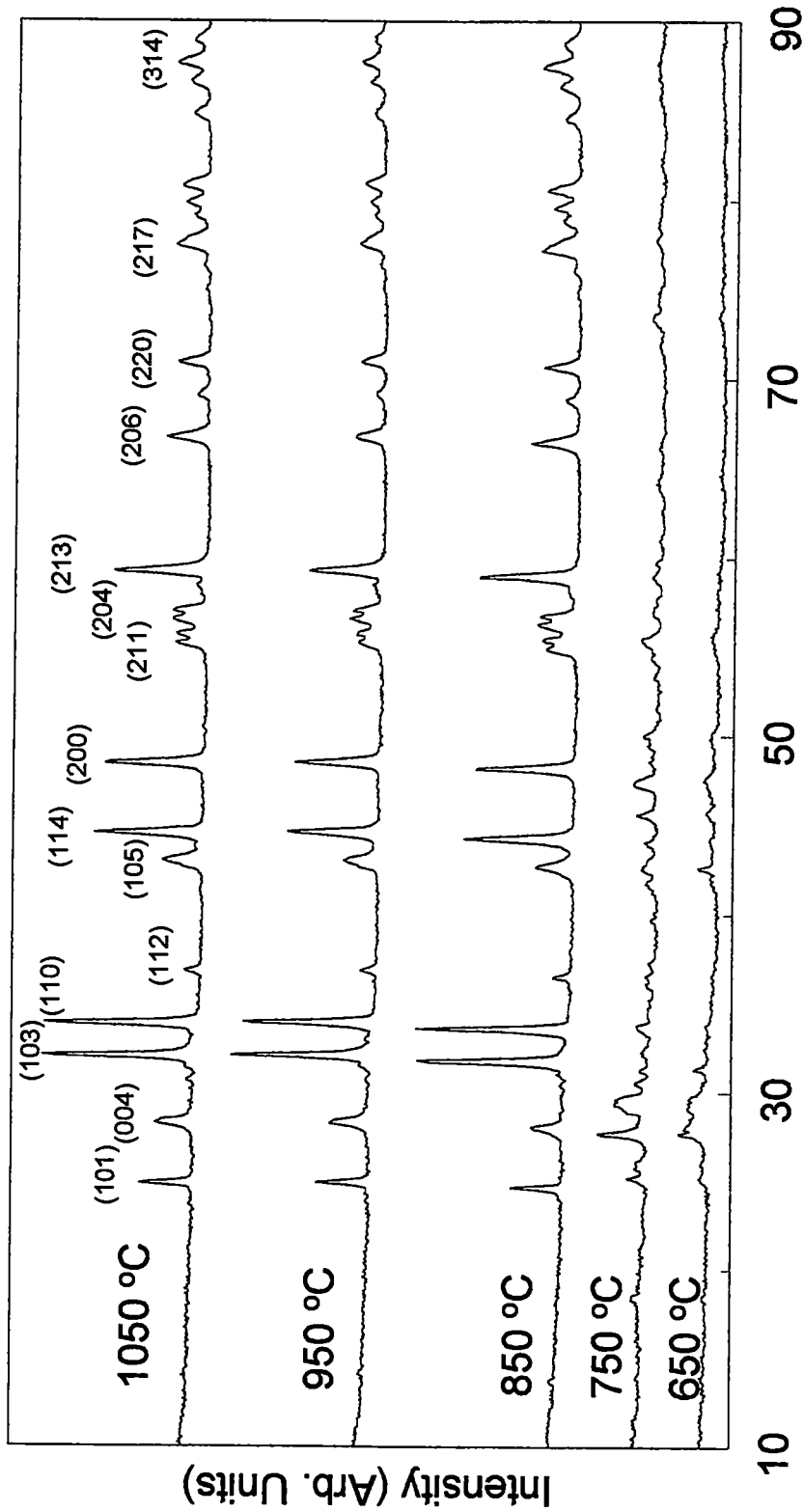
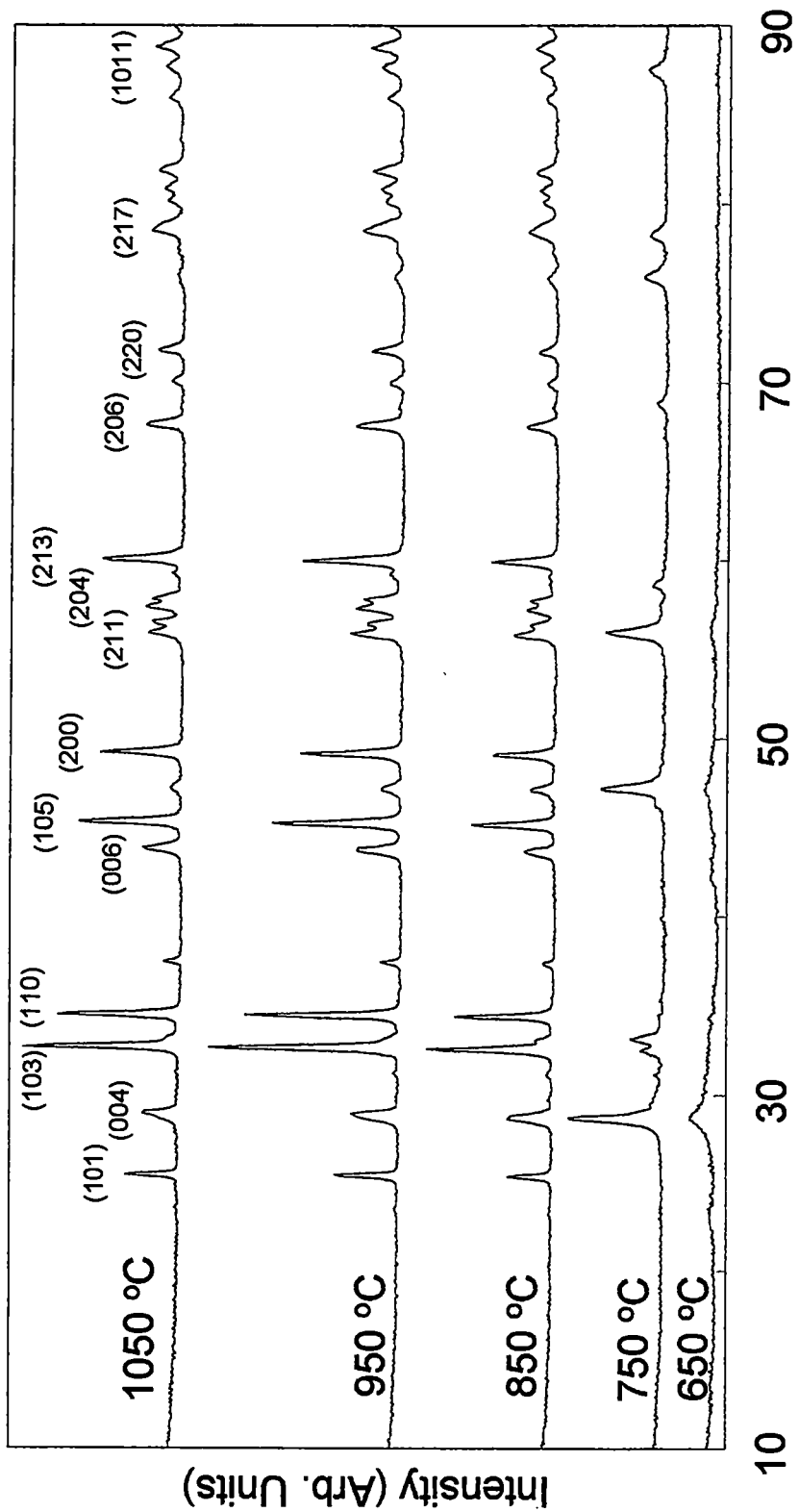


Figure 5.4. Theta/2-theta XRD of SrLaAlO<sub>4</sub> powders.



2-Theta

Figure 5.5. Theta/2-theta XRD of SrPrAlO<sub>4</sub> powders.

**Table 5.1.** Lattice constants for epitaxial tetragonal perovskites, in Å.

Compound	Powders <sup>1</sup> (reported)		Powders (calculated)		Films on SrTiO <sub>3</sub>		Films on LaAlO <sub>3</sub>	
	a	c	a	c	a	c	a	c
SrLaGaO <sub>4</sub>	3.843	12.68	3.834(3)*	12.66(2)	3.83(1)	12.72(5)	3.82(1)	12.74(5)
SrPrGaO <sub>4</sub>	3.813	12.532	3.813(3)	12.56(2)	3.79(1)	12.61(5)	3.84(1)	12.55(5)
SrLaAlO <sub>4</sub>	3.754	12.63	3.756(2)	12.63(2)	3.70(1)	12.68(5)	3.66(1)	12.67(5)
SrPrAlO <sub>4</sub>	<del> </del>	<del> </del>	3.723(3)	12.53(2)	3.70(1)	12.53(5)	3.68(1)	12.56(5)

\*Uncertainty in the last digit indicated parenthetically.

<sup>1</sup>Pajaczkowska, A.; Gloubokov, A. *Prog. Cryst. Growth Charact.* **1998**, *36*, 126.

### 5.3.2. XRD Analysis of Tetragonal Perovskite Films on Silver

Films were deposited on silver coupons using spin-coating in order to determine the coating characteristics of the solutions. Solutions of approximately 0.25 M gave films that were crack-free and continuous. Film thickness was built up by deposition of successive layers and each layer was annealed at 850 °C for 20 min in air. The thickness was found to be 600 to 700 Å per layer by etching a step in the films and measuring the step height with an Alpha Step Profilometer. Figure 5.6 shows X-ray diffraction data for polycrystalline films of SrLaGaO<sub>4</sub>, SrPrGaO<sub>4</sub>, SrLaAlO<sub>4</sub>, and SrPrAlO<sub>4</sub> on silver. There were no secondary phases observed and the intensities were similar to the powder theta/2-theta scans.

### 5.3.3. XRD Analysis of Tetragonal Perovskites on Strontium Titanate and Lanthanum Aluminate

During the course of this investigation, it was observed that commercially obtained single-crystal substrates were mis-cut by 1 to 2°. The XRD peaks of the single-crystal oxide substrates, strontium titanate and lanthanum aluminate, had fwhm values of less than 0.5°. The combination of this mis-cut and the narrowness of the peaks made it difficult to align the (*h*00) peaks of the substrate, and therefore, some of the (*h*00) reflections were not observed in the XRD data.

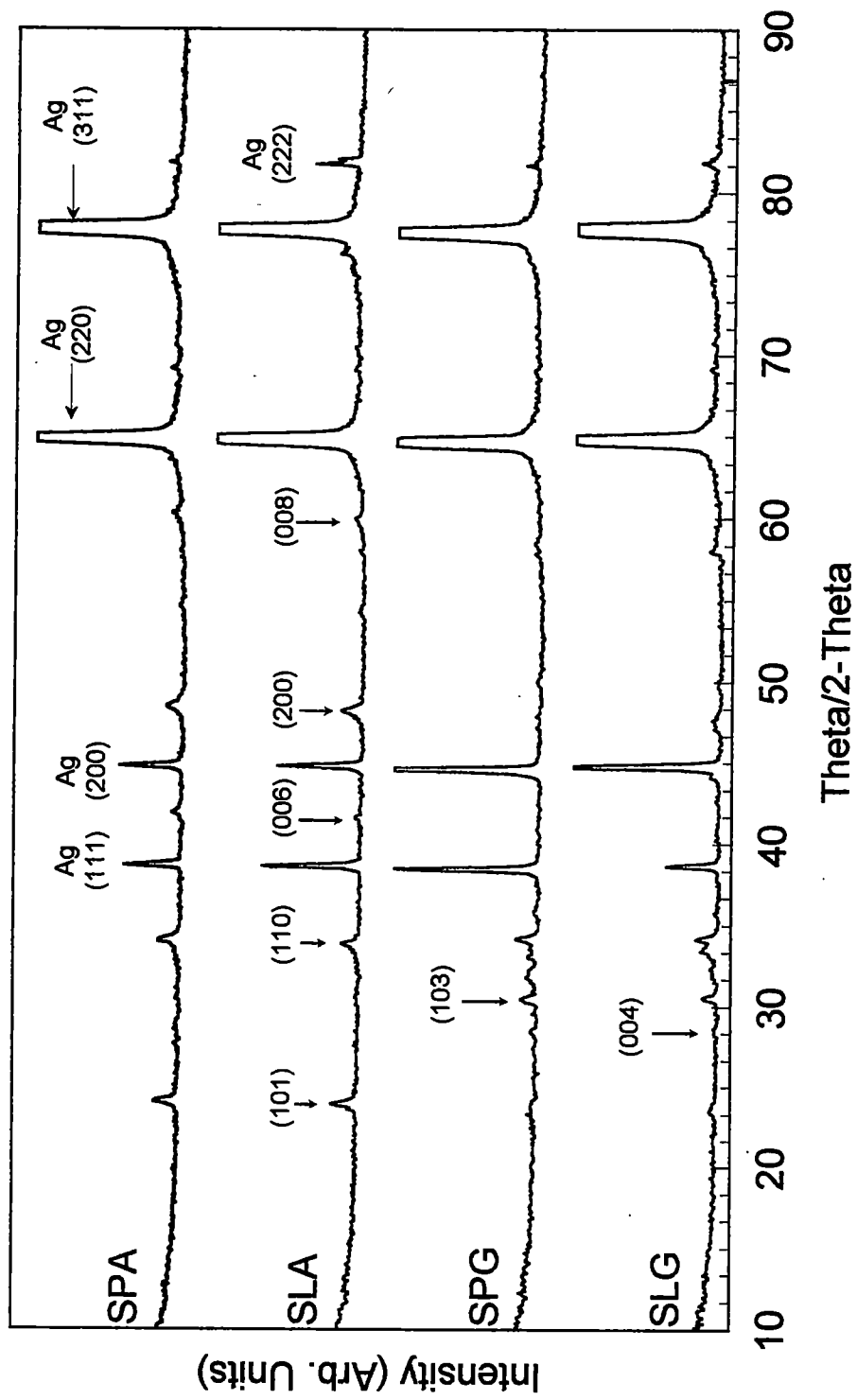


Figure 5.6. Theta/2-Theta XRD of SrLaGaO<sub>4</sub>, SrPrGaO<sub>4</sub>, SrLaAlO<sub>4</sub>, and SrPrAlO<sub>4</sub> on Ag at 850 °C.



X-ray diffraction was used to examine the structure of the films. Each of the four compounds deposited on strontium titanate and lanthanum aluminate showed only even numbered (00*l*) reflections during theta/2-theta scans. Theta/2-theta scans of the four compounds on strontium titanate (100) and lanthanum aluminate (100) are shown in Figures 5.7 to 5.10, demonstrating a high degree of out-of-plane alignment. Using the (*h*00) reflections of the substrate, the (00*l*) peaks of the film were calibrated and the corrected values of *d* were plotted against (1/*l*). The *c*-axis lattice constant of the epitaxial films was obtained from the slope of the plot. Table 5.1 shows lattice constants for tetragonal powders on SrTiO<sub>3</sub> and LaAlO<sub>3</sub> substrates. The *a*-axis lattice constant was determined from the (105) film reflection ( $\chi = 56^\circ$ ) which was calibrated against the (110) substrate reflection ( $\chi = 45^\circ$ ). The lattice constants showed the same trend as did the powders in that substitution of La for Pr causes the *c*-axis to expand with little effect on the *a*-axis. Also, substitution of Ga for Al results in an expansion of the *a*-axis with little effect on the *c*-axis.<sup>82</sup> When the powder lattice constants are compared to the epitaxial films on strontium titanate and lanthanum aluminate, the values for the lattice constant are similar.

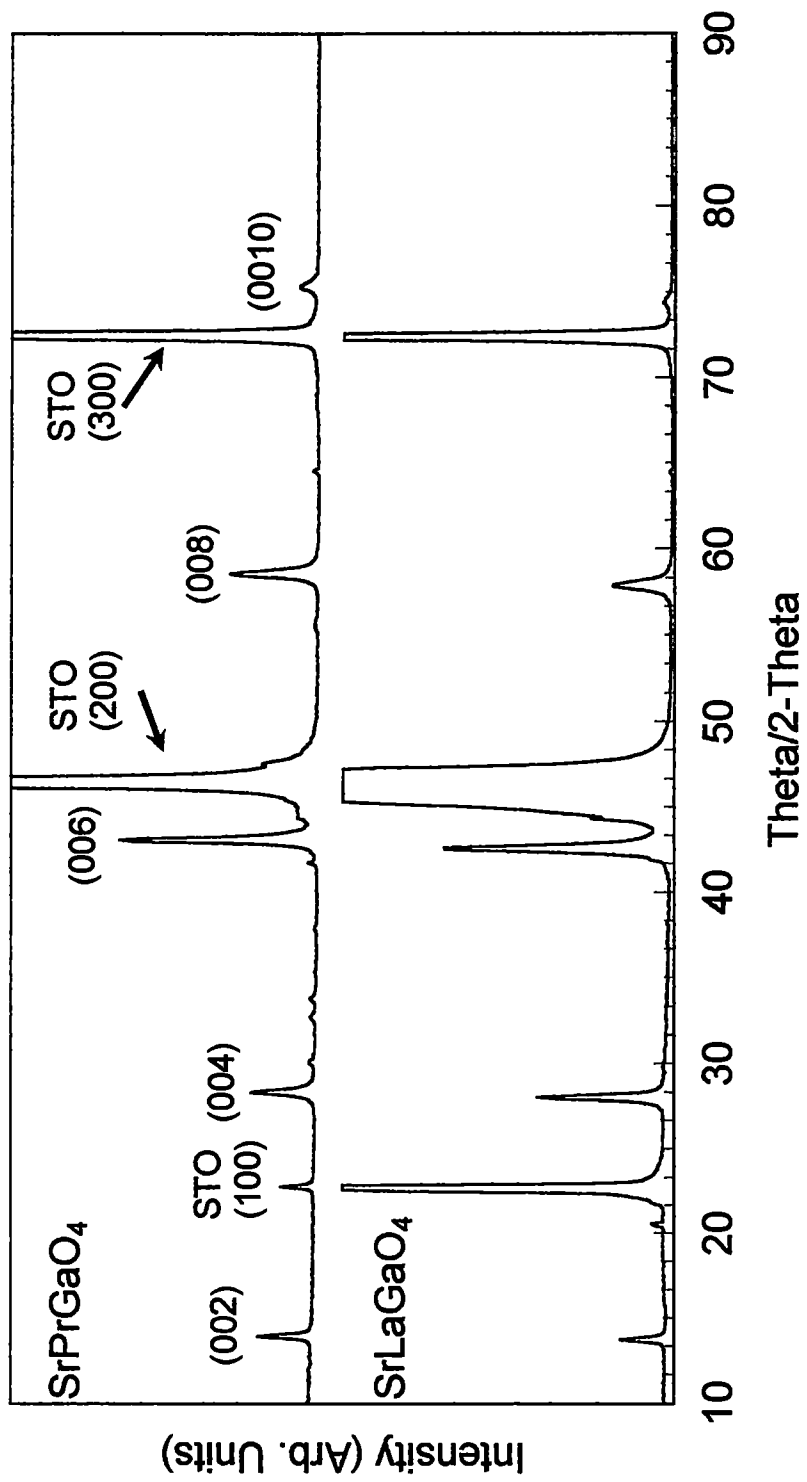


Figure 5.7. Theta/2-Theta XRD of SrLaGaO<sub>4</sub> and SrPrGaO<sub>4</sub> on SrTiO<sub>3</sub> at 850 °C.

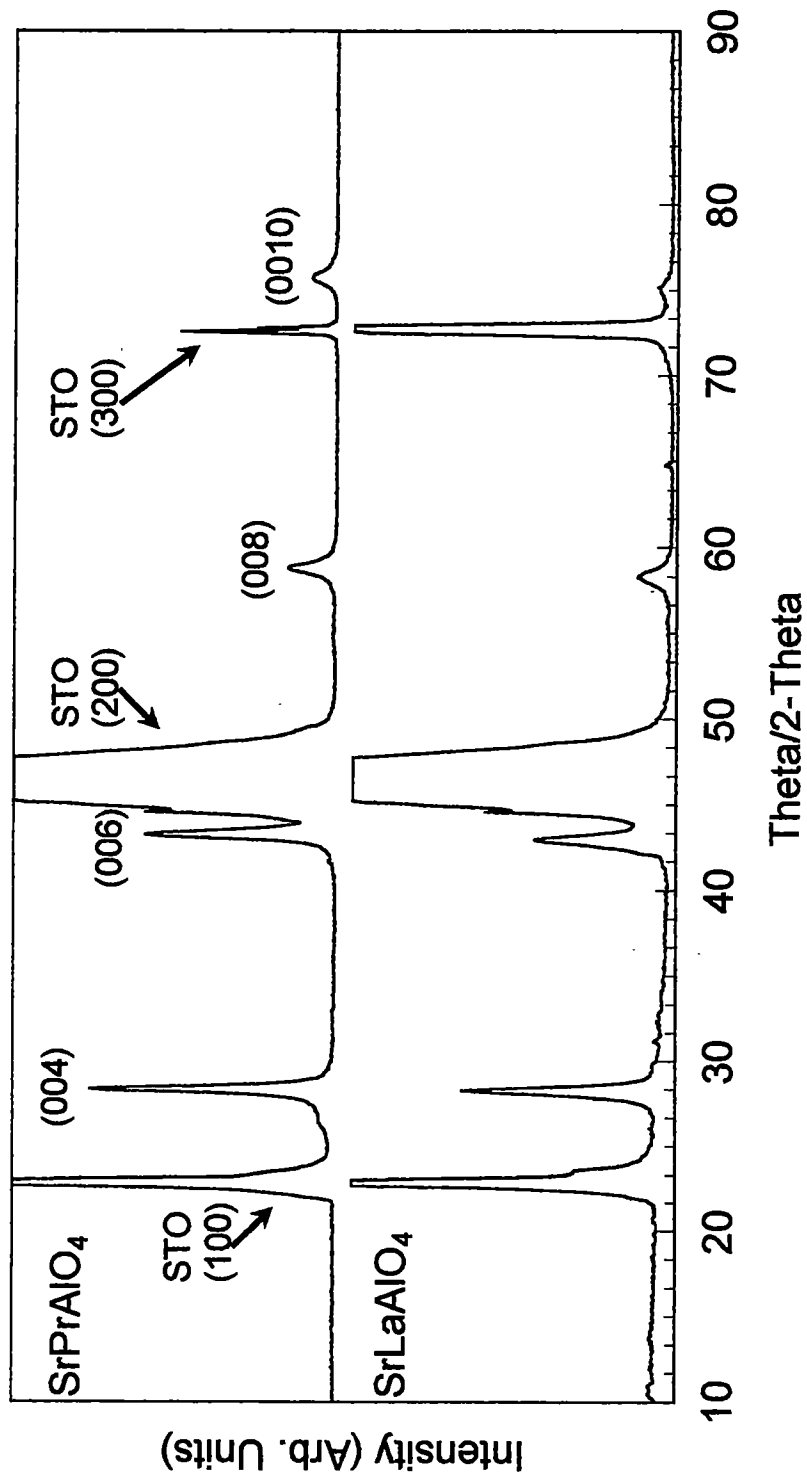


Figure 5.8. Theta/2-Theta XRD of SrLaAlO<sub>4</sub> and SrPrAlO<sub>4</sub> on SrTiO<sub>3</sub> at 850 °C.

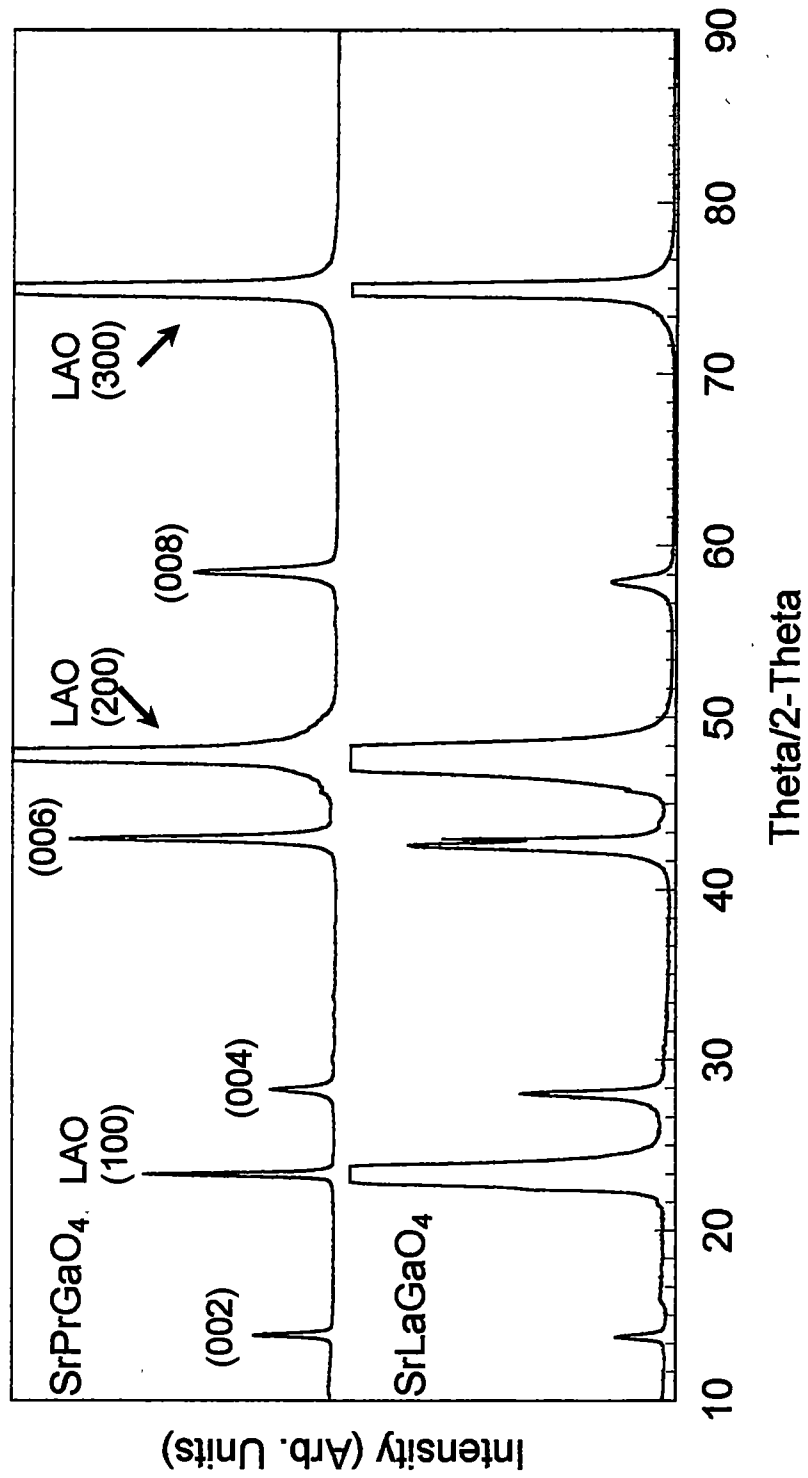


Figure 5.9. Theta/2-Theta XRD of SrLaGaO<sub>4</sub> and SrPrGaO<sub>4</sub> on LaAlO<sub>3</sub> at 850 °C.

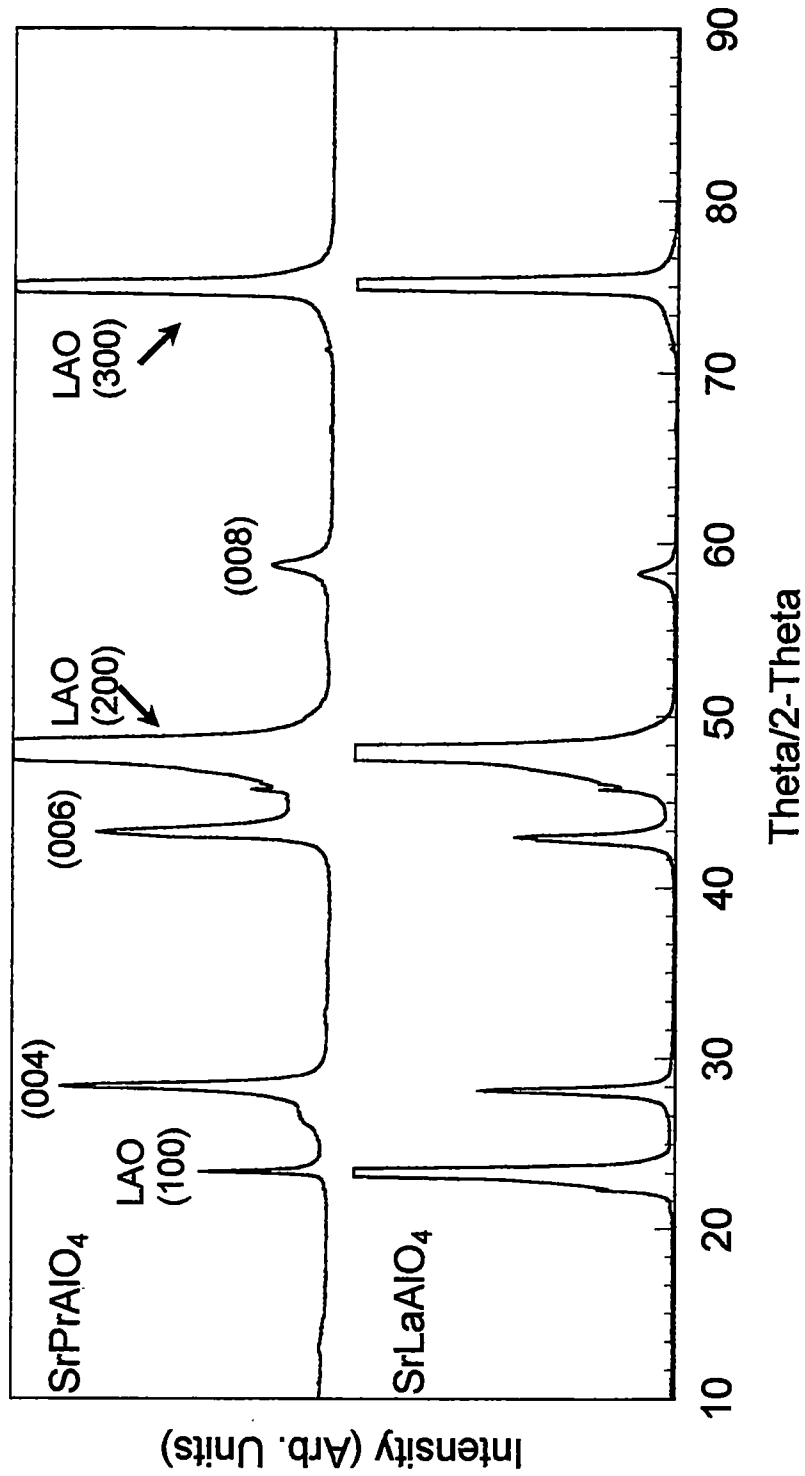


Figure 5.10. Theta/2-Theta XRD of SrLaAlO<sub>4</sub> and SrPrAlO<sub>4</sub> on LaAlO<sub>3</sub> at 850 °C.

#### **5.3.4. Out-of-Plane and In-Plane Texture Analysis of Tetragonal Perovskites on Strontium Titanate and Lanthanum Aluminate**

Omega scans (rocking curves) about the (006) reflection were used to measure the mosaic character (degree of crystallinity) of the film. Table 5.2 shows the full width at half maximum (fwhm) of the out-of-plane peaks and illustrates the fact that all of the films on both strontium titanate and lanthanum aluminate showed excellent out-of-plane orientation. A representative omega scan about the (006) reflection is shown in Figure 5.11.

Pole figures about the (105) plane were obtained to help determine the nature of the in-plane epitaxy. Figure 5.12 shows two representative pole figures about the (105) reflection of strontium lanthanum gallate on strontium titanate and lanthanum aluminate, respectively. The pole figures are indicative of cube-on-cube epitaxy showing only four peaks at  $\chi$  of  $45^\circ$  spaced  $90^\circ$  in  $\phi$ . In order to assess the quality of the in-plane epitaxy,  $\phi$  scans were obtained. A representative  $\phi$  scan about the (105) reflection is shown in Figure 5.11. Table 5.2 reports all fwhm values of the  $\phi$  scans for the tetragonal perovskites on strontium titanate and lanthanum aluminate. The in-plane peak widths are proportional to the lattice mismatch between the film and the substrate and are significantly larger than those of the out-of-plane peaks.

**Table 5.2.** Full-width at half-maximum for tetragonal perovskites on SrTiO<sub>3</sub> and LaAlO<sub>3</sub>.

Compound	SrTiO <sub>3</sub>		LaAlO <sub>3</sub>	
	out-of-plane	in-plane	out-of-plane	in-plane
SrLaGaO <sub>4</sub>	0.38(5) <sup>°*</sup>	1.8(1) <sup>°</sup>	0.39(5) <sup>°</sup>	1.6(1) <sup>°</sup>
SrPrGaO <sub>4</sub>	0.34(5) <sup>°</sup>	2.0(1) <sup>°</sup>	0.30(5) <sup>°</sup>	1.2(1) <sup>°</sup>
SrLaAlO <sub>4</sub>	0.34(5) <sup>°</sup>	3.3(1) <sup>°</sup>	0.30(5) <sup>°</sup>	2.3(1) <sup>°</sup>
SrPrAlO <sub>4</sub>	0.34(5) <sup>°</sup>	3.3(1) <sup>°</sup>	0.30(5) <sup>°</sup>	2.3(1) <sup>°</sup>

\*Uncertainty in the last digit indicated parenthetically.

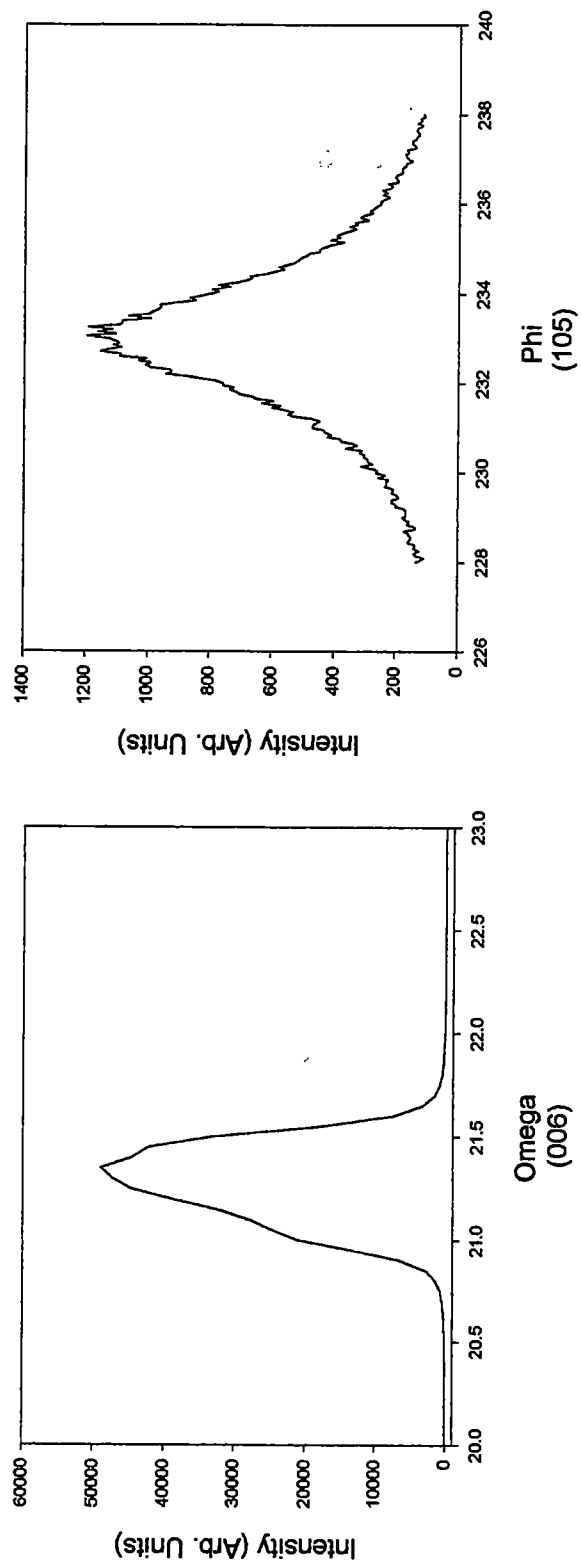
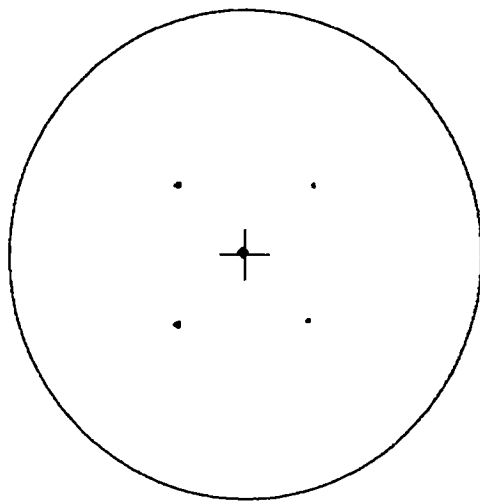


Figure 5.11. Omega scan and phi scan of SrLaGaO<sub>4</sub> on SrTiO<sub>3</sub>.





SrLaAlO<sub>4</sub> on SrTiO<sub>3</sub>  
(105) reflection

Figure 5.12. Pole figure of SrLaAlO<sub>4</sub> on SrTiO<sub>3</sub> about the (105) reflection.

### **5.3.5. Analysis of YBCO PLD Film on Solution Deposited Strontium Praseodymium Gallate on (100) Strontium Titanate and Strontium Lanthanum Gallate on (100) Lanthanum Aluminate**

Samples of (100) strontium titanate and (100) lanthanum aluminate, 12.0 x 3.5 mm, were used as the substrates for yttrium barium copper oxide ( $\text{YBa}_2\text{Cu}_3\text{O}_{7-\delta}$ , YBCO) superconducting films. The strontium praseodymium gallate and strontium lanthanum gallate buffer layers were deposited by spin-coating on (100) strontium titanate and (100) lanthanum aluminate in 0.25 M solutions, respectively, since they had a close lattice constant to their substrates. The samples were annealed in air at 850 °C for 20 min, and the coating procedure was repeated a total of three times. The YBCO superconductor was deposited by pulsed laser deposition (PLD). Figure 5.13 shows theta/2-theta scans of YBCO on strontium titanate substrate with a strontium praseodymium gallate buffer layer and lanthanum aluminate substrate with a strontium lanthanum gallate buffer layer. The epitaxial relationship of the superconductor/buffer layer/substrate was cube-on-cube with (100) YBCO// (100) SPG or SLG// (100)  $\text{SrTiO}_3$  or  $\text{LaAlO}_3$ . Figure 5.14 shows the critical temperature ( $T_c$ ) of the YBCO film on the strontium praseodymium gallate buffer layer, which exhibited zero resistivity at  $91.6 \pm 0.1$  K. The YBCO film on the strontium praseodymium gallate buffer layer had a transport critical current density ( $J_c$ ) value of  $(6.6 \pm 0.1) \times 10^5$  A/cm<sup>2</sup> (77 K), and

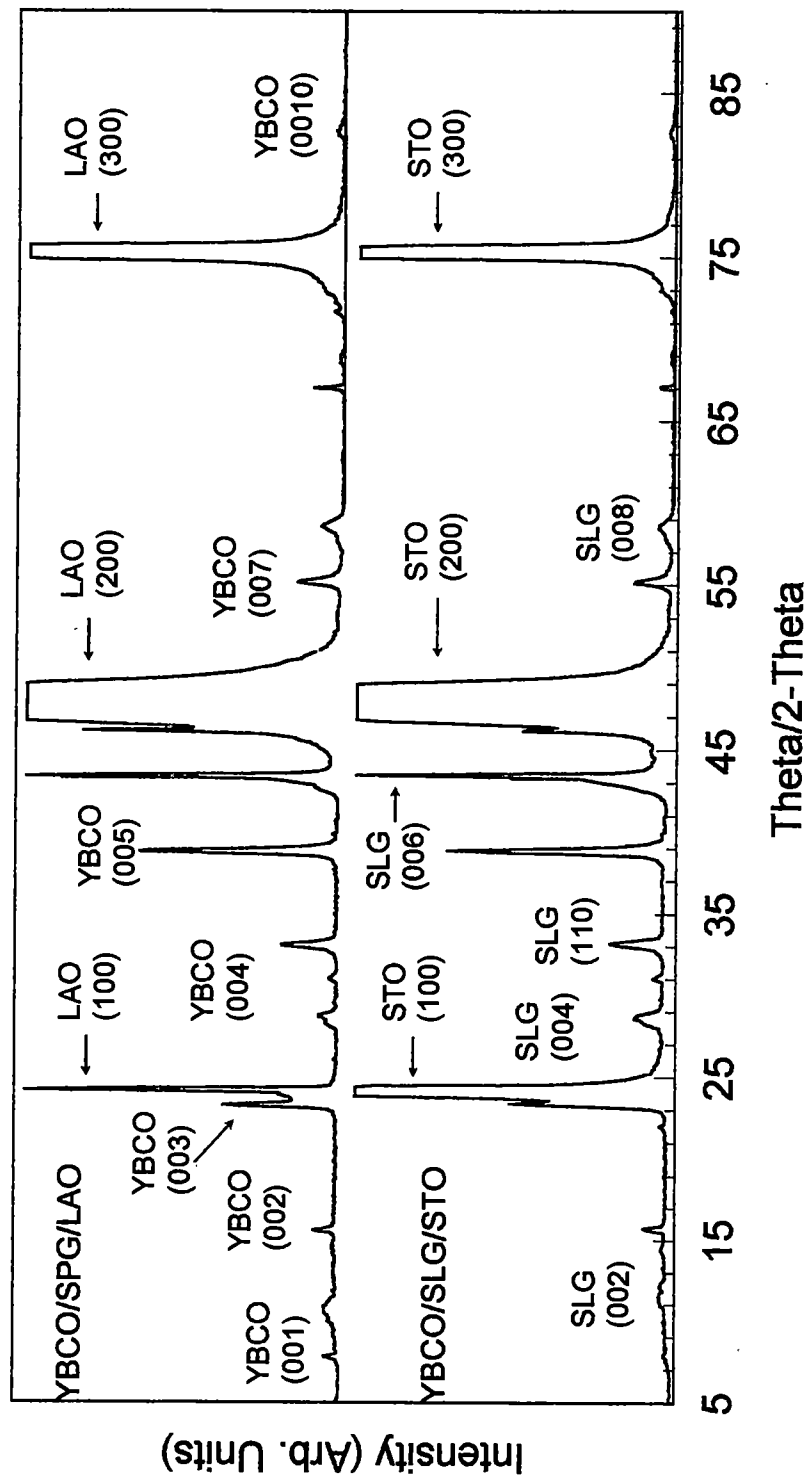


Figure 5.13. Theta/2-Theta XRD of YBCO/SrLaGaO<sub>4</sub>/SrTiO<sub>3</sub> and YBCO/SrPrGaO<sub>4</sub>/LaAlO<sub>3</sub> at 850 °C.

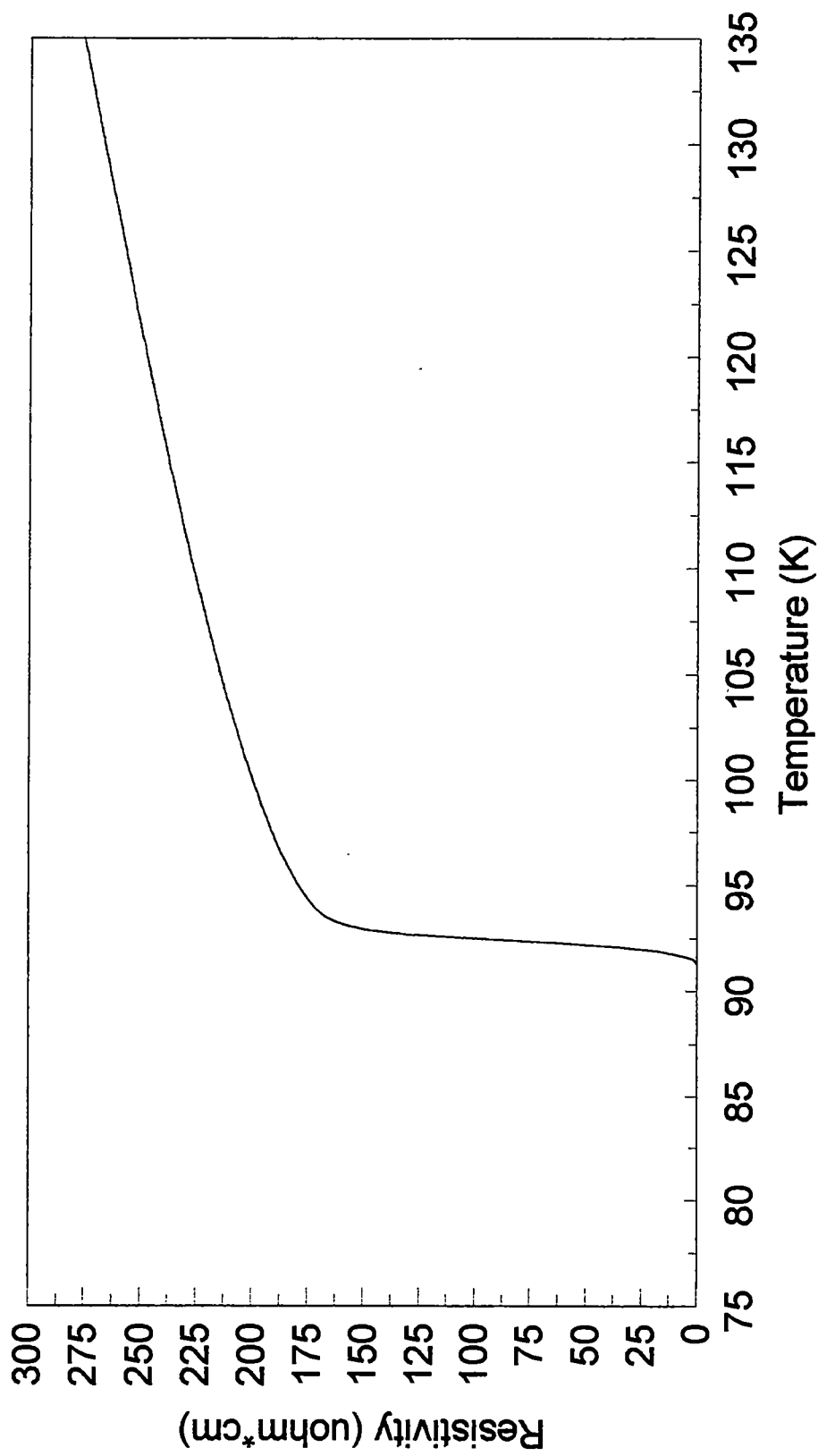


Figure 5.14. Resistivity versus temperature for a YBCO film deposited on SrTiO<sub>3</sub> with a SrLaGaO<sub>4</sub> buffer layer.

the  $I_c$  plot is shown in Figure 5.15. The YBCO film on the strontium lanthanum gallate buffer layer did not act as a superconductor so critical current and critical temperature values were not obtained.

#### **5.4. Conclusion**

Our results indicate that epitaxial  $ABCO_4$  oxide films can be produced using solution synthesis. The excellent control of stoichiometry and relative ease of preparation offered by this technique make it appropriate for the growth of valuable electroceramic devices. Furthermore, it is possible to develop high  $J_c$  superconductors using  $SrPrGaO_4$  as a buffer layer.

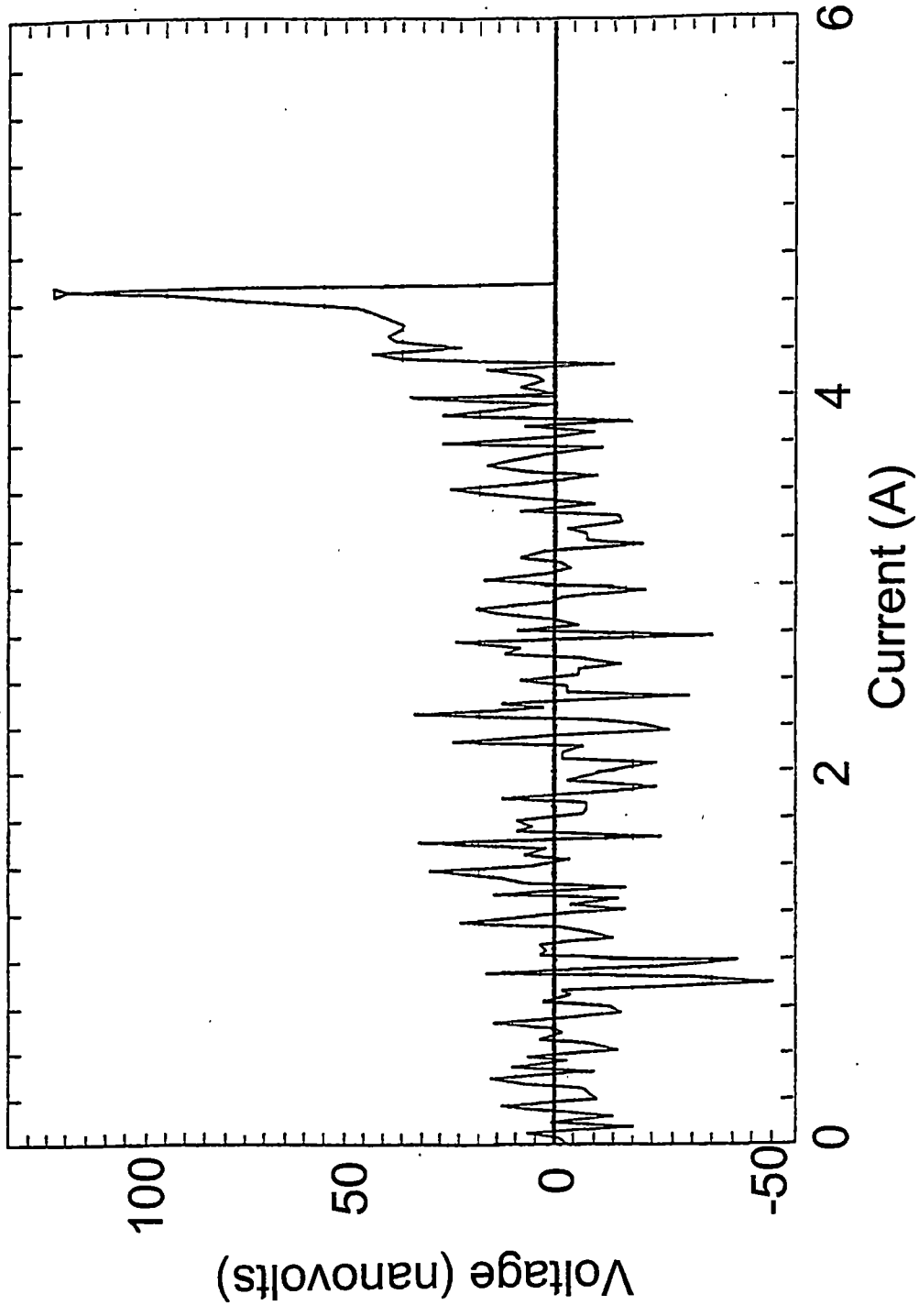


Figure 5.15. Voltage as a function of critical current ( $I_c$ ) of YBCO/SrPrGaO<sub>4</sub> on SrTiO<sub>3</sub>.

## CHAPTER 6

### EPITAXIAL GROWTH OF RARE-EARTH OXIDES ( $\text{Ln}_2\text{O}_3$ AND $\text{CeO}_2$ ) ON ROLL-TEXTURED NICKEL

#### 6.1. Introduction

A "coated conductor" structure consisting of a polycrystalline copper oxide-based superconductor deposited on a mechanically strong metal tape is predicted to be the next generation of superconducting wire operating at liquid nitrogen temperature.<sup>85</sup> High critical currents can only be achieved in copper oxide-based superconducting films if there is both good out-of-plane and in-plane grain alignment. For out-of-plane alignment, *c*-axis texture, the copper oxide planes must lie parallel to the substrate. This *c*-axis texture is often achieved even on amorphous or glassy substrates due to the layered structure of the cuprate superconductors, but in-plane alignment is much more difficult to achieve. Studies of misalignment in bi-crystal substrates have shown that grain boundaries must be aligned to less than 7° mismatch to avoid "weak link" conduction between grains.<sup>79</sup>

Two distinctly different approaches to inexpensive substrates are being pursued in order to achieve this alignment in practical coated conductors. One approach is a technique known as Ion Beam Assisted Deposition (IBAD), which

involves the deposition of a textured buffer layer on a randomly oriented, oxidation resistant metal tape using multiple ion beams.<sup>53</sup> One beam is used to deposit the material, and another beam is used to etch the growth surface at some angle which produces shadowing of atoms in the correct lattice positions leading to an in-plane oriented deposit. The technique requires relatively thick films to develop useable textures, and the process is slow due to the fact that most of the film is removed by etching.

The second approach to epitaxial substrates is a technique known as Rolling Assisted Biaxially Textured Substrates (RABiTS). The RABiTS process involves the deposition of epitaxial buffer layer(s) on a nickel tape which has been mechanically deformed by rolling and heat treated to obtain a highly textured metastable microstructure.<sup>54</sup> Laser ablation was used to produce the first successful RABiTS buffer layer. An epitaxial layer of palladium on roll textured nickel was deposited by laser ablation followed by a layer of cerium oxide and then a layer of yttrium stabilized zirconium (YSZ).<sup>55</sup> Later, the use of the palladium layer was discontinued from the RABiTS architectures.<sup>86</sup>

In addition to the use of pulsed laser ablation, two methods (e-beam evaporation and sputtering) have been used to deposit ceramic layers on the RABiTS to achieve high critical currents.<sup>80</sup> The best results to date for a RABiTS process were obtained with the use of a cerium oxide layer (>500 Å) in contact with the nickel, a yttrium stabilized zirconium (YSZ) oxide layer (1 µm)



on top of the cerium oxide layer, and a cap layer of cerium oxide ( $>500 \text{ \AA}$ ) on top of the YSZ. Figure 6.1 shows a diagram of the RABiTS architecture.

Recently, high critical currents have been obtained with buffer layers using only rare-earth oxides deposited by e-beam evaporation.<sup>87,88</sup>

Another method, different from physical methods of deposition discussed above, to grow epitaxial rare-earth oxide thin-films is solution deposition. Solution deposition has a relatively low cost and uses no vacuum deposition techniques. The following sections of this chapter describe development of epitaxial rare-earth oxide buffer layers using a chemical solution route on roll textured nickel tape. These buffer layers must act as a diffusion barrier against nickel oxidation and act as a template for the superconductor. Coating solutions were prepared consisted of the following rare-earth metals: Ce, Sm, Eu, Gd, Tb, Dy, Ho, Er, Tm, Yb, and Lu. All solutions of the rare-earths were used for spin-coating and dip-coating, and films were crystallized by annealing them for 1 h under a reducing atmosphere of 4%  $\text{H}_2$  / 96% Ar. The cubic phase of the rare-earth oxides was preferred and formed at a temperature range of 850 °C to 1160 °C according to the phase diagram for the rare-earth oxides (Figure 6.2). X-ray diffraction was used to determine the out-of-plane and in-plane grain alignment of the rare-earth oxide buffer layers. Results of YBCO high temperature superconductors with europium oxide and gadolinium oxide as buffer layers are also discussed.

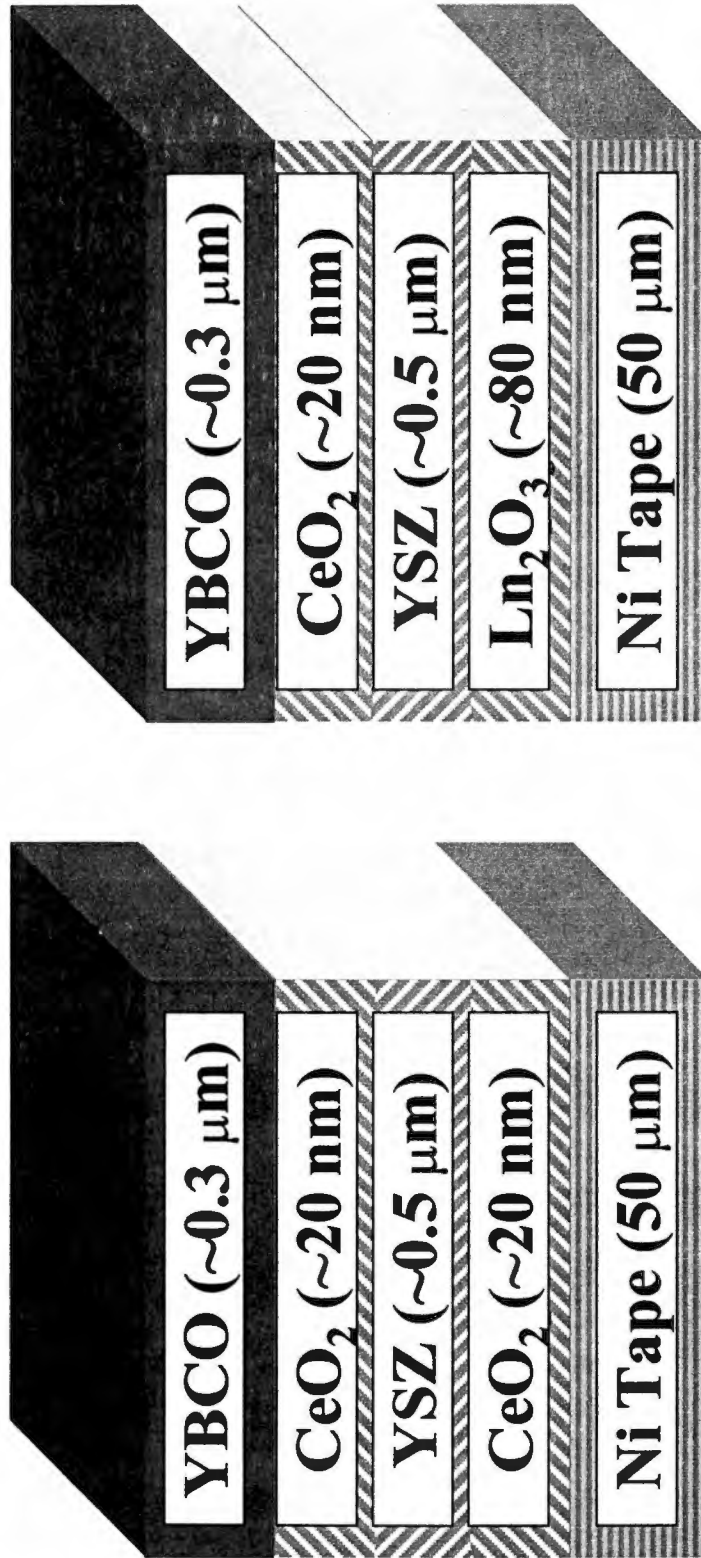


Figure 6.1. RABiTS standard architecture (left) and proposed architecture (right).

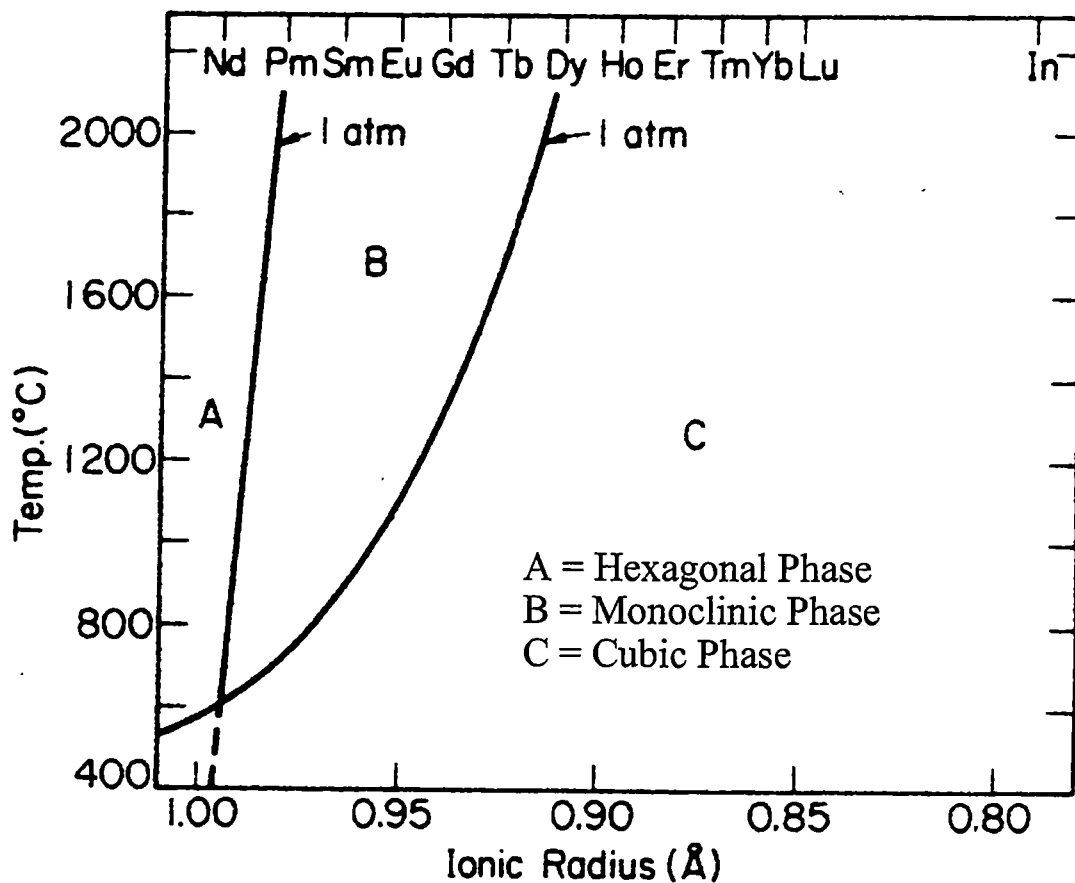


Figure 6.2. Phase diagram of rare-earth oxide transitions as a function of cation radius.

Source: Hoekstra, H. R. *Inorg. Chem.* 1966, 5, 755.

## 6.2. Experimental Details

### 6.2.1. General Procedures

All manipulations were performed under dry argon atmosphere with the use of either standard Schlenk techniques or a glove box. Cerium oxide (Strem, 99.9%), Samarium oxide (Strem, 99.9%), europium oxide (Strem, 99.9%), gadolinium oxide (Strem, 99.9%), gadolinium metal (Alfa Aesar, 99.99%), terbium oxide (Strem, 99.9%), dysprosium oxide (Strem, 99.9%), holmium oxide (Strem, 99.9%), erbium oxide (Strem, 99.9%), thulium oxide (Strem, 99.9%), ytterbium oxide (Strem, 99.9%), ytterbium metal (Alfa Aesar, 99.99%), lutetium oxide (Strem, 99.9%), glacial acetic acid (99.7%), and 2-methoxyethanol (Aldrich, HPLC grade) were used as received. Isopropanol was dried over aluminum isopropoxide and distilled before use. The sol-gel chemistry used was pioneered by Payne *et al.*<sup>19</sup> and is based on solutions of metal methoxyethoxide complexes in 2-methoxyethanol.

### 6.2.1. Preparation of Rare-Earth Isopropoxides

Rare-earth metals were used as received. Rare-earth isopropoxides of gadolinium and ytterbium were prepared by reacting the metals directly with dry isopropanol in the presence of mercuric catalysts which was first described by Brown and Mazdiyasn.<sup>77</sup> Commercial powders of the metals failed to react with the dry isopropanol in the presence of a catalyst. Instead of the commercial

metal powders, 5.0 g of rare-earth metal filings were obtained by using a coarse file on the metal. Each solution was made individually, and the filings were added to a 250 mL Schlenk flask with 90 mL of dry isopropanol, a magnetic stir bar, 50 mg of mercury (II) acetate,  $\text{Hg}(\text{OOCCH}_3)_2$ , and mercuric chloride,  $\text{HgCl}_2$ . The reactions were allowed to reflux overnight at 85 °C and then filtered through a Celite packed column. The solvent was removed at reduced pressure, and the rare-earth isopropoxides were extracted using a Soxhlet extractor with dry isopropanol and then recrystallized to insure the highest purity of the compounds. Yields of purified compound were typically between 50 and 70 percent.

### **6.2.3. Preparation of Rare-Earth Acetates**

Rare-earth oxides were used as received. Since most high purity rare-earth metals such as europium are expensive, rare-earth acetates were prepared from rare-earth oxides. This was accomplished by dissolving rare-earth oxides in 25% of glacial acetic acid in water. The solution was allowed to evaporate and the remaining rare-earth acetates were collected.

### **6.2.4. Preparation of Coating Solutions**

Each isopropoxide (gadolinium and ytterbium) and acetate (samarium through lutetium and cerium) were reacted with 90 mL of 2-methoxyethanol to

undergo ligand exchange of the isopropoxide ligand, as well as partial exchange of the acetate ligand with the methoxyethoxide ligand. Each solution was refluxed for 1 h at 140 °C and 60 mL of the solvent was removed by distillation at atmospheric pressure. The solvent removed by distillation was replaced with fresh 2-methoxyethanol. The ligand exchange process was repeated two more times to insure complete ligand exchange of the isopropoxide ligand and partial exchange of the acetate ligand. Each solution was adjusted to 50 mL, and the molality of each solution was calculated based on the moles of rare-earth isopropoxide or rare-earth acetate used and the weight of the solutions. (The use of molality rather than molarity allowed the gravimetric preparation of small volumes of solutions with high accuracy.) The following rare-earth oxides were made from the isopropoxide route: gadolinium oxide ( $\text{Gd}_2\text{O}_3$ ) and ytterbium oxide ( $\text{Yb}_2\text{O}_3$ ). The rare-earth oxides made from the acetate route were: samarium oxide ( $\text{Sm}_2\text{O}_3$ ), europium oxide ( $\text{Eu}_2\text{O}_3$ ), gadolinium oxide ( $\text{Gd}_2\text{O}_3$ ), terbium oxide ( $\text{Tb}_2\text{O}_3$ ), dysprosium oxide ( $\text{Dy}_2\text{O}_3$ ), holmium oxide ( $\text{Ho}_2\text{O}_3$ ), erbium oxide ( $\text{Er}_2\text{O}_3$ ), tellurium oxide ( $\text{Tm}_2\text{O}_3$ ), ytterbium oxide ( $\text{Yb}_2\text{O}_3$ ), lutetium oxide ( $\text{Lu}_2\text{O}_3$ ), and cerium oxide ( $\text{CeO}_2$ ).

#### **6.2.5. Preparation of Substrates and Films**

Roll-textured nickel substrates were ultrasonically cleaned with filtered, dry isopropanol for 1 h. This process cleans the mechanically deformed nickel

surface of oil from the roller. The cleaned nickel was annealed at 650 °C in a forming gas atmosphere (4% H<sub>2</sub> / 96% Ar) for 2 h to develop a cubic texture. The nickel substrates were coated with rare-earth coating solutions by both spin coating and dip coating techniques. For spin coating, 10 mm by 10 mm samples were flooded with solution (rare-earth methoxyethoxide/acetate), and the excess solution was eliminated by spinning for 30 s at 2000 rpm. For dip coating, strips of nickel approximately 5 mm by 80 mm were submerged in the coating solution and withdrawn mechanically at a rate of 5 cm per min. Coated substrates were placed in a crucible inside a quartz tube fitted with a gas inlet and bubbler outlet. The tube containing the samples was purged for 30 min at room temperature using forming gas (4% H<sub>2</sub> / 96% Ar). The tube was then placed inside a preheated furnace for 1 h at temperatures of 950 °C (samarium oxide), 1050 °C (europium oxide), and 1160 °C for the rest of the rare-earth oxides. Films were approximately 600 Å thick after firing and thicker coats were produced by multiple coatings. The film thicknesses were measured using profilometry.

#### **6.2.6. Application of Yttrium Barium Copper Oxide Superconductor**

The YBCO superconductor was deposited on CeO<sub>2</sub>/YSZ/Eu<sub>2</sub>O<sub>3</sub> and CeO<sub>2</sub>/YSZ/Gd<sub>2</sub>O<sub>3</sub> buffer layers by the barium fluoride precursor process.<sup>89</sup> Figure 6.1 shows a diagram of the buffer layer architecture. This process

involved electron-beam co-evaporation of Y, BaF<sub>2</sub>, and Cu to make a precursor film at a rate of 6 Å/sec. During the evaporation, the substrate temperature was maintained at 400 °C, and the oxygen pressure increased from 0.1 mTorr to 4.0 mTorr. Additionally, the materials were placed inside crucibles in a stainless-steel vacuum chamber and heated with 3 kW e-beam guns (Thermonics 150-0010). Tungsten crucibles were used for the Cu, BaF<sub>2</sub>, and Y sources, and the BaF<sub>2</sub> had a perforated lid to control its deposition. After the deposition was completed, the oxygen pressure was increased to 100 Torr, and the samples were cooled for 1 h to room temperature. The samples were then post-annealed in a controlled atmosphere furnace at 740 °C for 2 h. Water was introduced into the furnace tube at 55 Torr to convert the Y, Cu, and BaF<sub>2</sub> into YBa<sub>2</sub>Cu<sub>3</sub>O<sub>7-δ</sub>.

### 6.2.7. Critical Current and Critical Temperature Measurements

In order to obtain critical current ( $J_c$ ) and critical temperature ( $T_c$ ) measurements, four silver electrical contacts, approximately one-half micron thick, were sputtered onto samples with a YBCO surface. This reduced electrical contact resistance during measurements. The samples were then annealed for 30 min at 500 °C in flowing O<sub>2</sub> to ensure low contact resistance.

The property of resistivity was used to find the critical temperature at a constant current. A four-probe AC measurement was used in conjunction with



a closed cycle helium refrigerator to take data. Samples were cooled in a vacuum to a low temperature, and then slowly warmed. Voltage data was taken every 0.2 K during warm up. The  $T_c$  is the temperature reached when resistance first occurs, i.e., when any voltage is detected.

To find critical current, the sample was put in a constant temperature liquid nitrogen cryostat. Current was applied and slowly increased while monitoring the voltage. When a voltage was first detected at a particular current, the sample is no longer considered to be superconducting.

## **6.3. Results and Discussion**

### **6.3.1. Study of the Coating Solutions**

One of the more difficult aspects of this research was the study of the coating solutions. IR was used to determine if the acetate ligand fully exchanges with the methoxyethoxide ligand. Figure 6.3 shows IR spectra of ytterbium acetate, ytterbium coating solution made by the acetate route, ytterbium isopropoxide, and ytterbium coating solution made by the isopropoxide route. At  $1575\text{ cm}^{-1}$ , it was observed that the carbonyl stretching of the acetate was clearly evident in both the ytterbium acetate and ytterbium coating solution made by the acetate route. This observation indicated that the acetate ligand only partially exchanged with the methoxyethoxide ligand. [It was clear from Chapter 3 (Figure 3.1), that the isopropoxide ligand fully

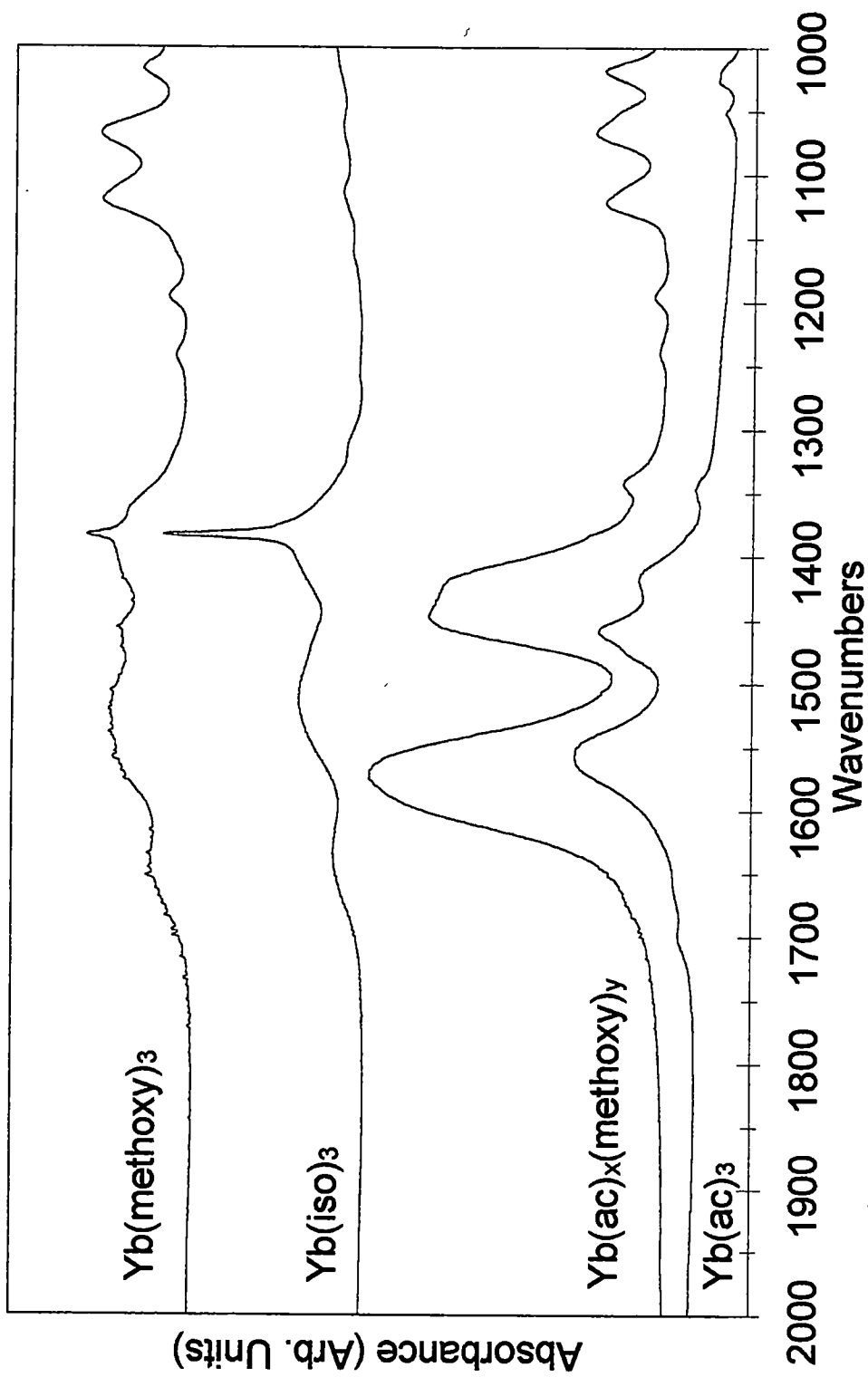


Figure 6.3. IR spectra of ytterbium containing compounds. (ac = acetate, methoxy = methoxyethoxide, iso = isopropoxide)

exchanges with the methoxyethoxide ligand.] In addition, the methoxyethoxide-acetate coating solutions differ in chemical properties from the coating solutions made from the isopropoxide route. The methoxyethoxide-acetate coating solutions did not gel after standing over a period of several months, but rather precipitated. The following XRD data showed that the methoxyethoxide-acetate coating solutions provide a better epitaxy.

### 6.3.2. XRD Analysis of Rare-Earth Oxide Films on Roll-Textured Nickel

X-ray diffraction was the principal tool for determining the structure of the rare-earth oxide thin-films. The gadolinium and ytterbium oxide thin-films, developed from the isopropoxide route, showed a high degree of *c*-axis orientation. The acetate route, however, provided a 100% *c*-axis orientation. Figures 6.4 and 6.5 show theta/2-theta scans of the difference in *c*-axis orientation between the two solution routes (isopropoxide and acetate) of gadolinium oxide and ytterbium oxide. The relative intensity of the (400) reflection versus the (222) reflection in the isopropoxide route is indicative of this high degree of *c*-axis orientation. A randomly oriented film would have an intensity ratio ( $I_{(222)}$  to  $I_{(400)}$ ) of 100 to 30.<sup>90</sup> In the acetate route theta/2-theta scans, the (222) reflection was not seen, indicating full *c*-axis orientation. Figures 6.6-6.8 show theta/2-theta scans of the remaining rare-earth oxides on nickel. Each of these rare-earth oxide thin-films was made from the acetate

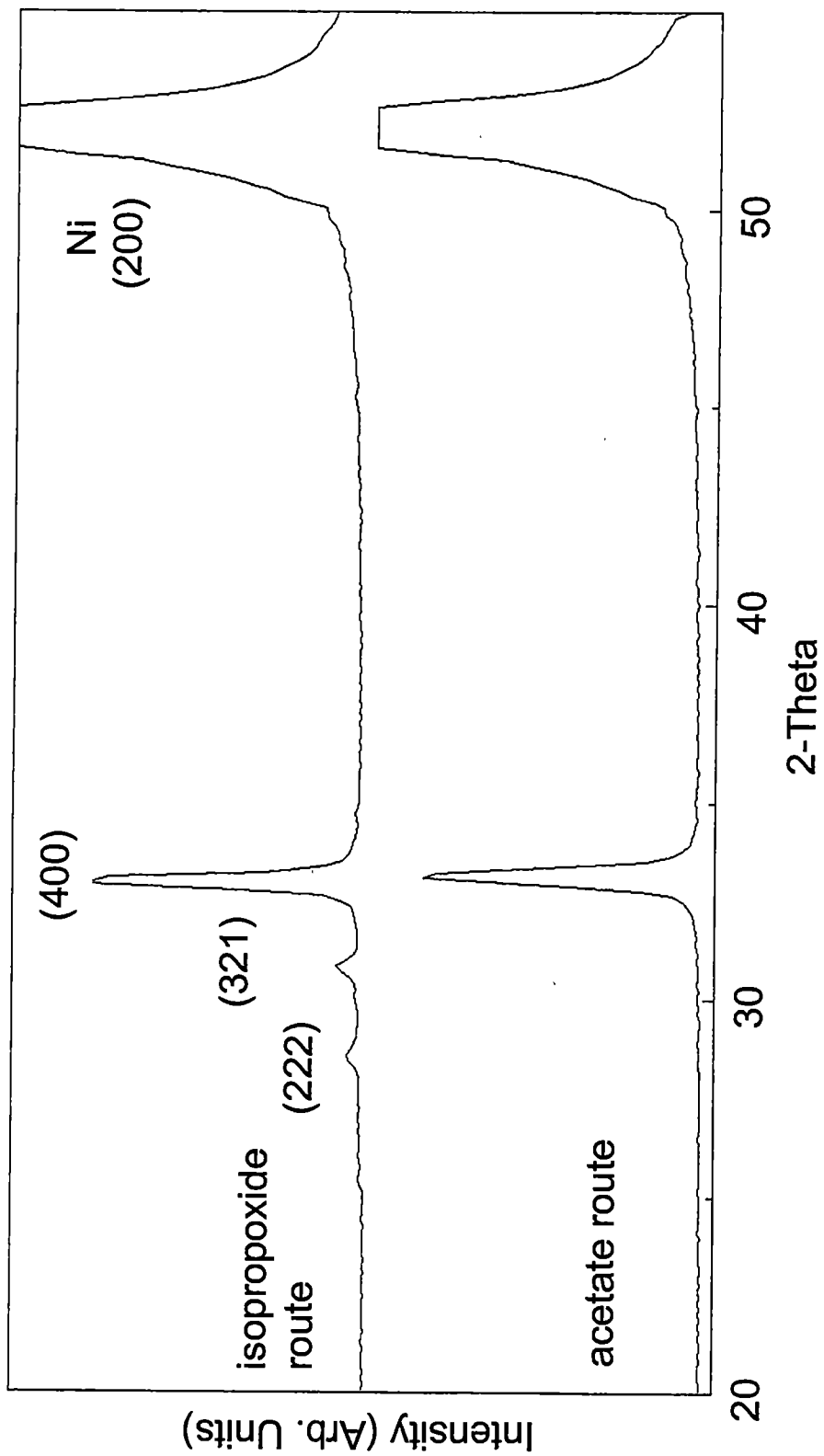


Figure 6.4. Theta/2-theta XRD of Gd<sub>2</sub>O<sub>3</sub> on Ni at 160 °C by two different routes.

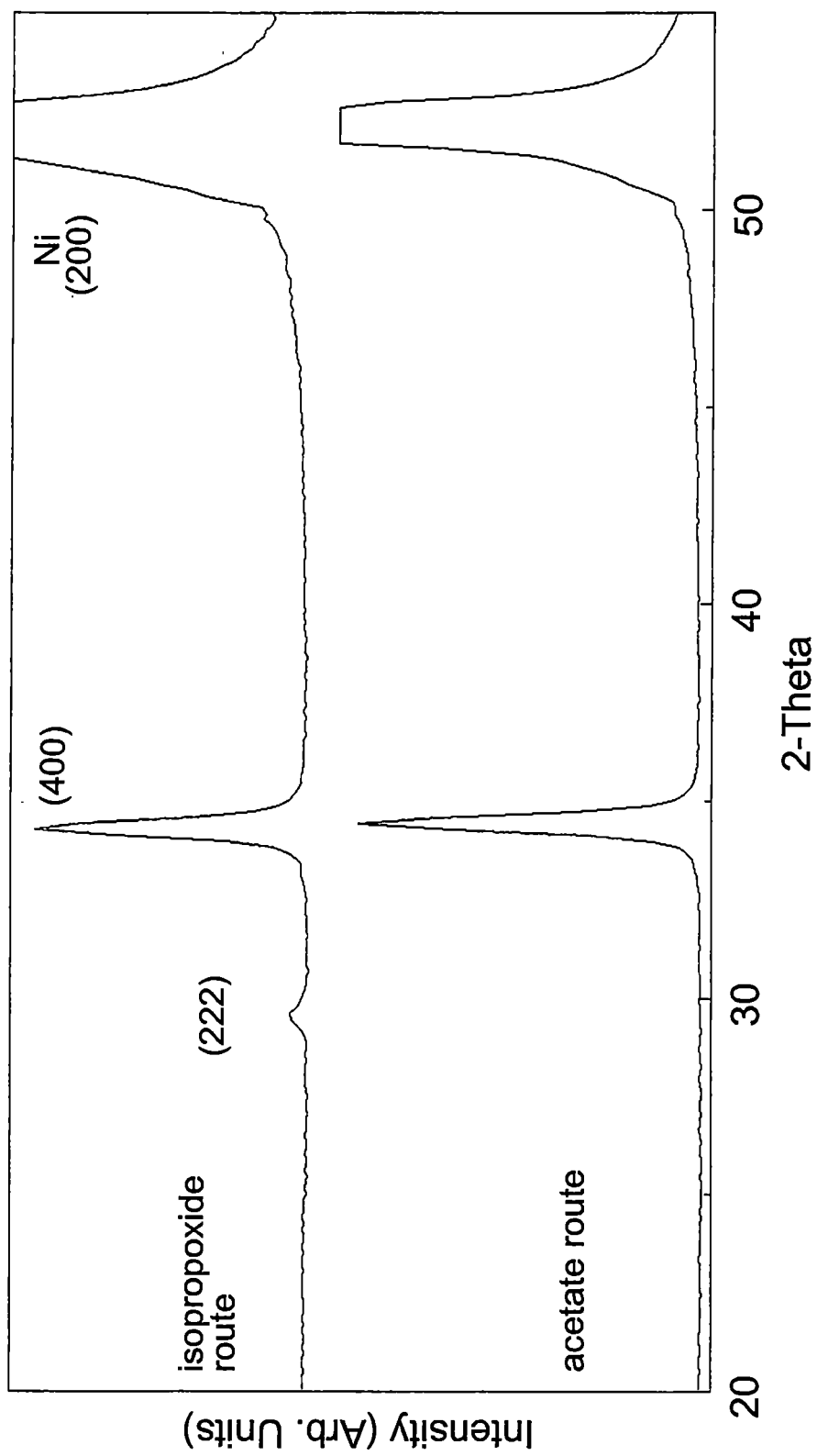


Figure 6.5. Theta/2-theta XRD of Yb<sub>2</sub>O<sub>3</sub> on Ni at 1160 °C by two different routes.

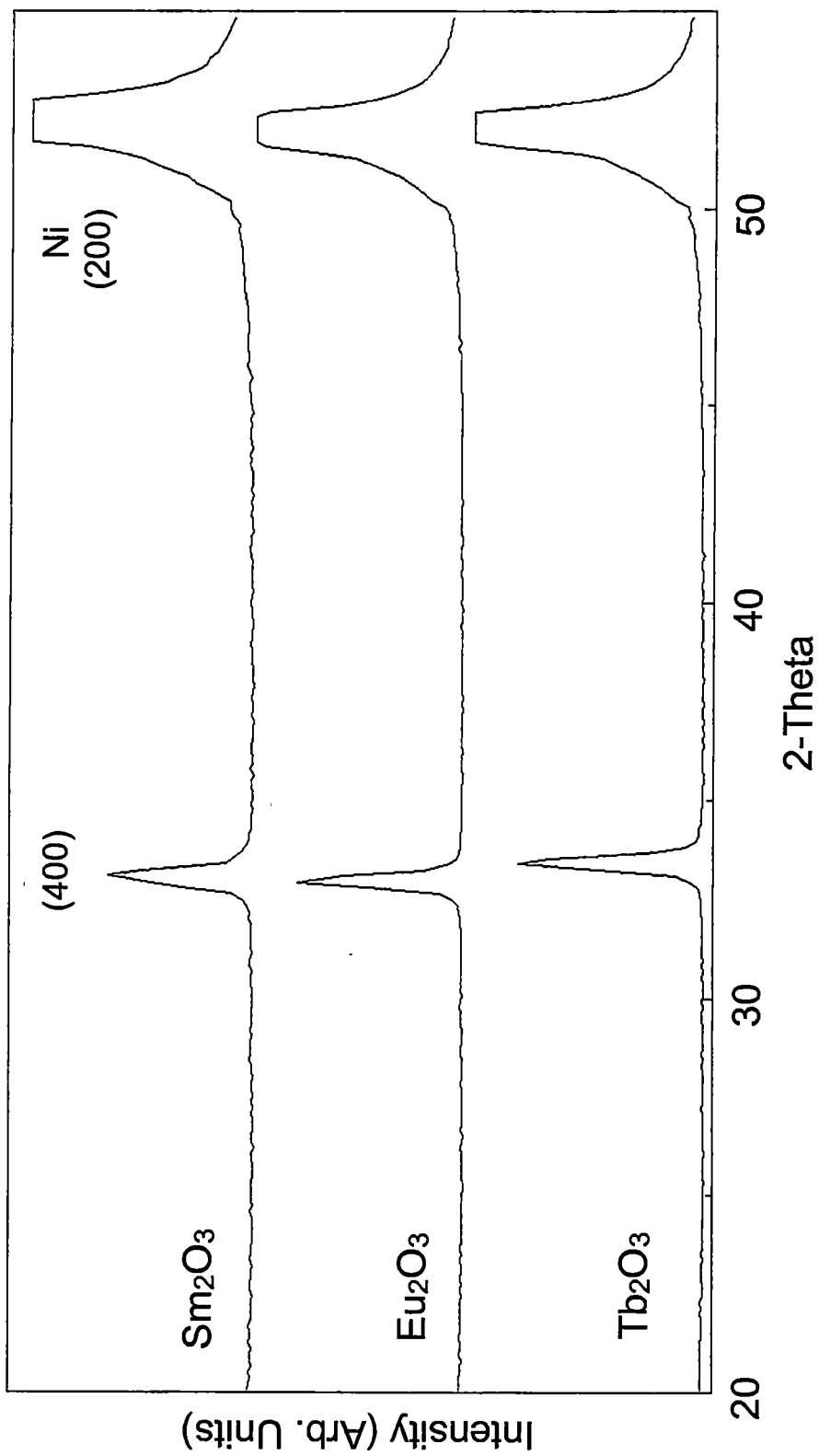


Figure 6.6. Theta/2-theta XRD of  $\text{Sm}_2\text{O}_3$ ,  $\text{Eu}_2\text{O}_3$ , and  $\text{Tb}_2\text{O}_3$  on Ni.

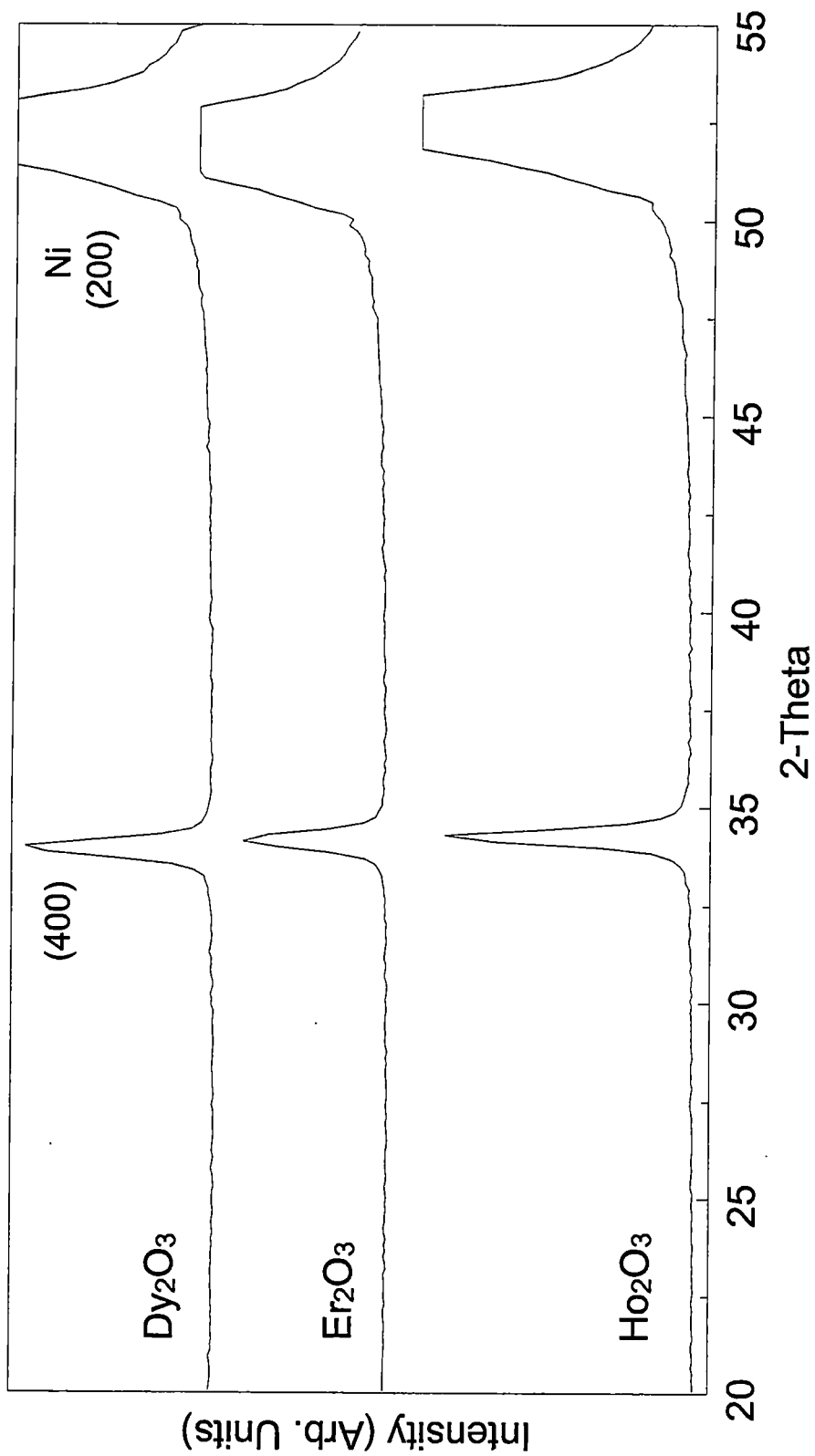


Figure 6.7. Theta/2-theta XRD of Dy<sub>2</sub>O<sub>3</sub>, Er<sub>2</sub>O<sub>3</sub>, and Ho<sub>2</sub>O<sub>3</sub> on Ni.

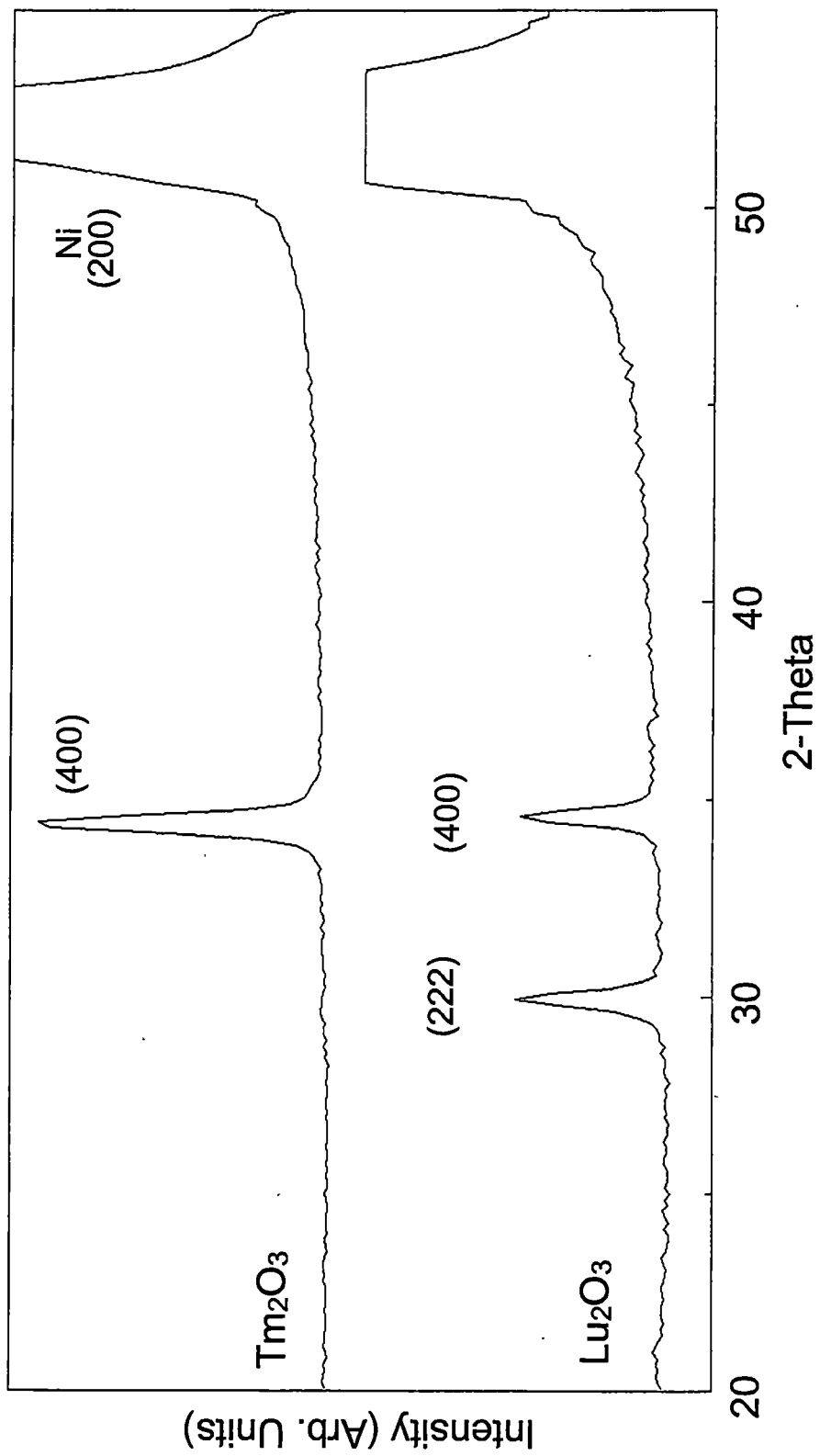


Figure 6.8. Theta/2-theta XRD of  $Tm_2O_3$  and  $Lu_2O_3$  on Ni.



route. Table 6.1 shows the lattice constants of nickel and the rare-earth oxides (samarium through lutetium and cerium oxide). Longer annealing times were studied to rule out sources of the changes in the diffraction pattern. Five single spin-coated films were annealed at 15 min, 30 min, 1 h, 2 h, and 4 h at 1160 °C. Maximum X-ray intensity occurred at 1 h with no change in the (400) intensity with longer annealing times. Only one of the rare-earth compounds showed mixed orientation,  $\text{Lu}_2\text{O}_3$ . This mixed orientation was observed at temperatures between 1050 °C and 1260 °C. When the  $\text{Lu}_2\text{O}_3$  was coated on top of  $\text{Gd}_2\text{O}_3$  on Ni, the mixed orientation was still present. This ruled out a nucleation problem between the  $\text{Lu}_2\text{O}_3$  and the Ni substrate. The most likely reason for the observed mixed orientation could be a kinetic effect in which the film crystallizes from the bulk rather than at the surface.

Thicker films could be produced by multiple coatings, and Figure 6.9 shows four  $\theta/2$ - $\theta$  scans of one to four coats of  $\text{Eu}_2\text{O}_3$  on nickel. It was observed that the X-ray intensity of the (400) reflection increased with each successive coat. It was also possible to grow epitaxial layers of different rare-earth oxides one on top of another. Figure 6.10 shows an example of this with  $\text{Yb}_2\text{O}_3$  and  $\text{Eu}_2\text{O}_3$  on nickel. Each film was applied separately by spin-coating and then annealed.

Besides rare-earth oxides having a formula of  $\text{Ln}_2\text{O}_3$ , it was possible to grow cerium oxide ( $\text{CeO}_2$ ) epitaxially on the nickel. Figure 6.11 shows a

**Table 6.1.** Lattice constants and fwhm values for epitaxial rare-earth oxide thin films on nickel.

	Lattice constants	fwhm of (400) omega scan on Ni	fwhm of (222) phi scan on Ni	Lattice constant mismatch
Nickel	3.523 Å	7.06°	8.45° (111)	<del>                    </del>
Sm <sub>2</sub> O <sub>3</sub>	3.864 Å	<del>                    </del>	<del>                    </del>	9.68%
Eu <sub>2</sub> O <sub>3</sub>	3.843 Å	7.30°	10.10°	9.08%
Gd <sub>2</sub> O <sub>3</sub> (isopropoxide route)	3.824 Å	9.40°	11.95°	8.54%
Gd <sub>2</sub> O <sub>3</sub> (acetate route)	3.824 Å	9.80°	12.06°	8.54%
Tb <sub>2</sub> O <sub>3</sub>	3.794 Å	9.19°	9.96°	7.69%
Dy <sub>2</sub> O <sub>3</sub>	3.771 Å	7.69°	11.48°	7.04%
Ho <sub>2</sub> O <sub>3</sub>	3.750 Å	8.89°	11.37°	6.44%
Er <sub>2</sub> O <sub>3</sub>	3.730 Å	9.02°	11.33°	5.88%
Tm <sub>2</sub> O <sub>3</sub>	3.708 Å	8.44°	9.56°	5.25%
Yb <sub>2</sub> O <sub>3</sub> (isopropoxide route)	3.690 Å	9.89°	10.11°	4.74%
Yb <sub>2</sub> O <sub>3</sub> (acetate route)	3.690 Å	8.17°	9.28°	4.74%
Lu <sub>2</sub> O <sub>3</sub>	3.674 Å	<del>                    </del>	<del>                    </del>	4.29%
CeO <sub>2</sub>	3.827 Å	7.63°	9.14°	8.63%

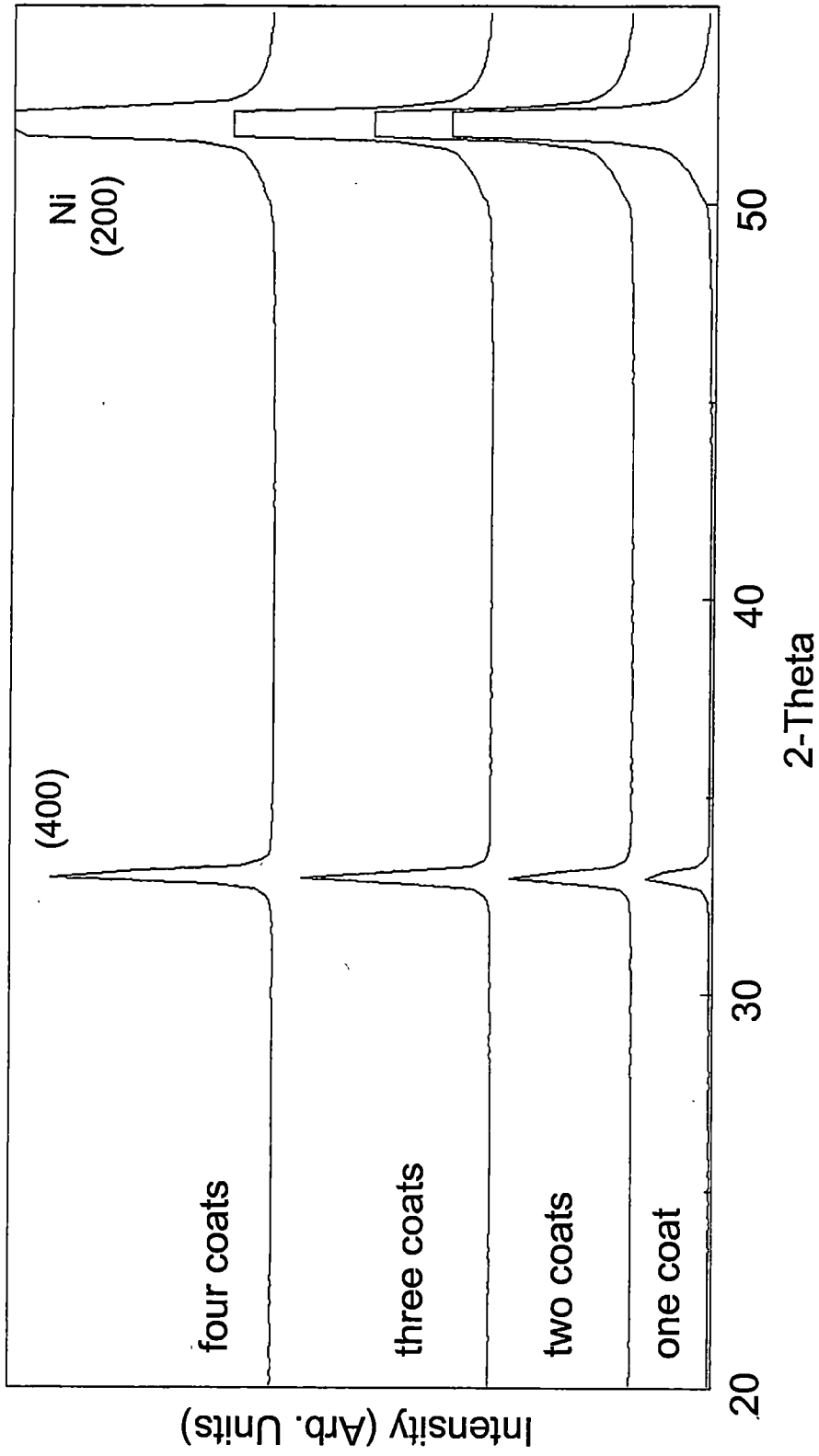


Figure 6.9. Theta/2-theta XRD of  $\text{Eu}_2\text{O}_3$  on Ni at  $1050^\circ\text{C}$  with one to four spin-coats.

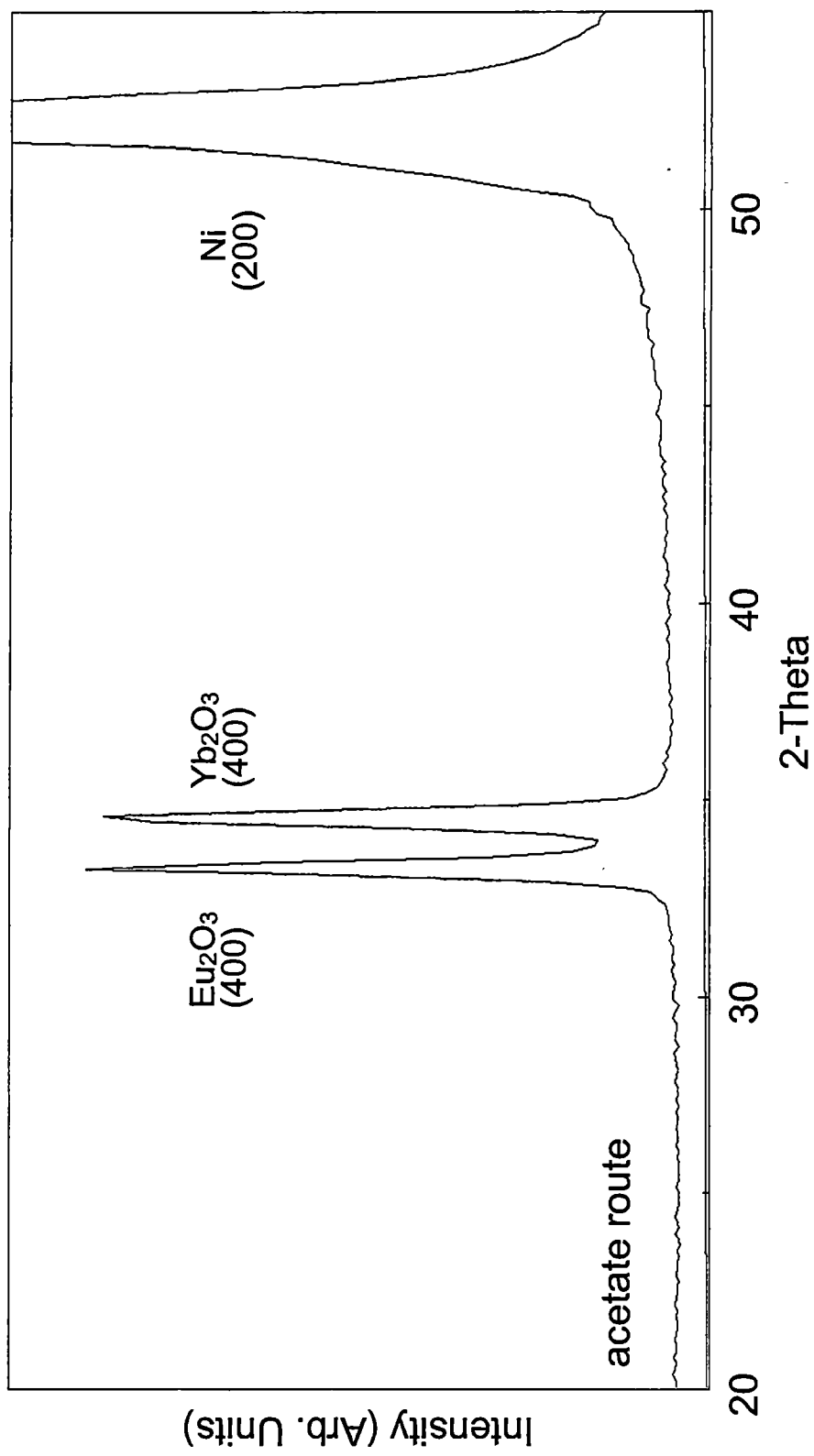


Figure 6.10. Theta/2-theta XRD of Eu<sub>2</sub>O<sub>3</sub> and Yb<sub>2</sub>O<sub>3</sub> on Ni at 1160 °C.

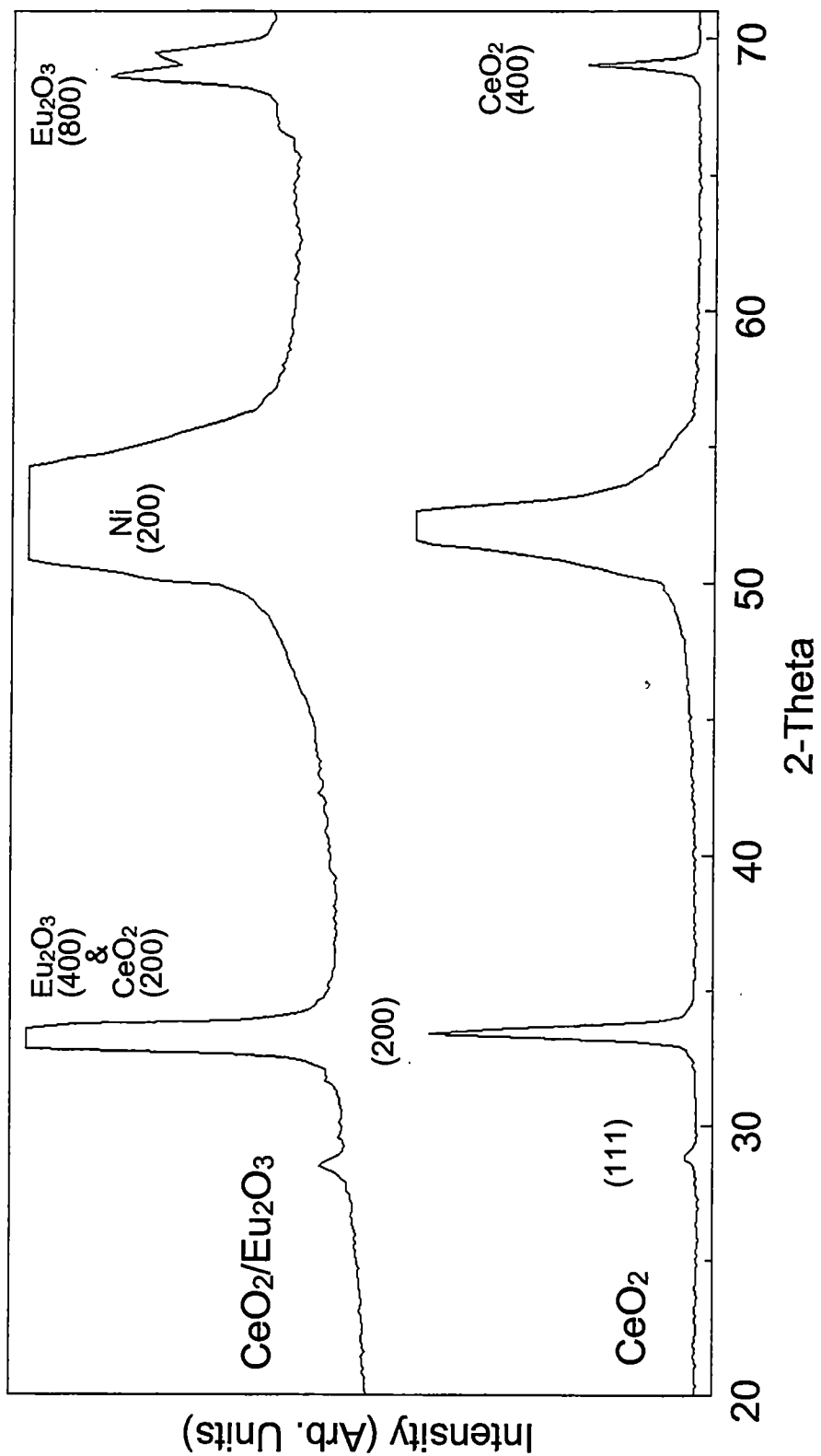


Figure 6.11. Theta/2-theta XRD of CeO<sub>2</sub> and CeO<sub>2</sub>/Eu<sub>2</sub>O<sub>3</sub> on Ni at 1050 °C.

theta/2-theta scan of cerium oxide on nickel. When  $\text{CeO}_2$  was coated on top of a  $\text{Eu}_2\text{O}_3$  film on nickel, it was epitaxial (Figure 6.11). Because the lattice constants for  $\text{Ce}_2\text{O}_3$  and  $\text{Eu}_2\text{O}_3$  are so close, the theta/2-theta scan was extended to  $71^\circ$  in order to distinguish the  $\text{CeO}_2$  (400) peak from the  $\text{Eu}_2\text{O}_3$  (800) peak .

### **6.3.3. Out-of-Plane and In-Plane Texture Analysis of Rare-Earth Oxides on Nickel**

Rocking curves (omega scans) about the (400) reflection and phi scans and pole figures about the (222) reflection of the rare-earth oxides on nickel were performed to determine the quality of the epitaxy. It was observed that the fwhm of the rare-earth oxide rocking curve was slightly smaller than the roll-textured nickel. An example of a rocking curve with  $\text{Gd}_2\text{O}_3$  on nickel can be seen in Figure 6.12. The rocking curves are larger than those encountered in single-crystals, but they indicate a degree of alignment suitable for the deposition of superconducting films with high critical currents. Phi scans and pole figures about the film (222) plane and the nickel substrate (111) plane were obtained in order to determine whether the film was aligned in-plane. A representative phi scan about the (222) of  $\text{Gd}_2\text{O}_3$  on nickel can be seen in Figure 6.12. The fwhm of the phi scans were again larger than those of single-crystals, but were comparable to the fwhm of RABiTS substrates that have

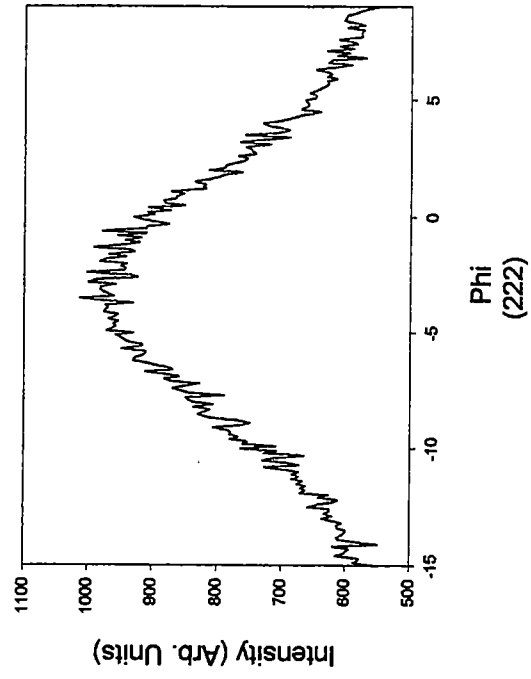
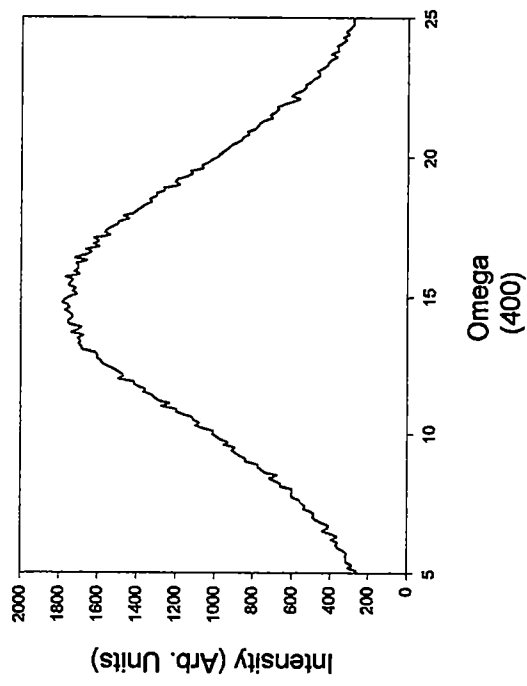


Figure 6.12. Omega scan and phi scan of  $Gd_2O_3$  on Ni.

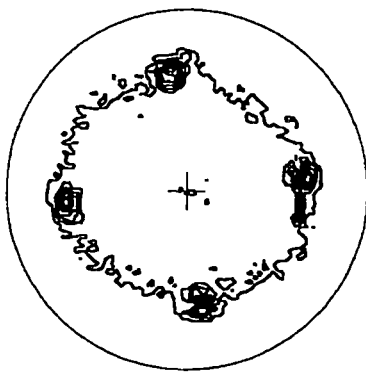
been used to obtain superconducting films with high critical currents. The pole figures indicated an excellent epitaxial relationship between the film and the substrate,  $\text{Ln}_2\text{O}_3(110)\parallel\text{Ni}(100)$ . Figures 6.13-6.15 show pole figures for the rare-earth oxides on nickel (except  $\text{Sm}_2\text{O}_3$  since it had mostly amorphous material due to a low annealing temperature, and  $\text{Lu}_2\text{O}_3$  since it did not have good *c*-axis alignment). Table 6.1 shows a list of full-width at half-maximum degrees of the rocking curves showing excellent out-of-plane orientation of the films and phi scans showing the in-plane texture.

#### **6.3.4. Film Morphology and Surface Structure**

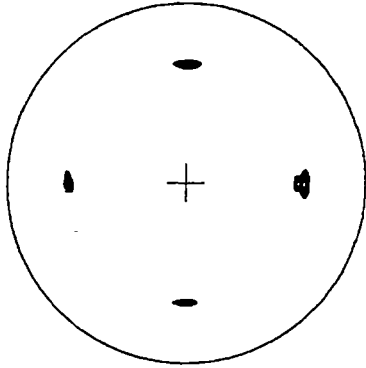
Scanning electron microscopy (SEM) was performed on the rare-earth oxide films. Low magnification SEMs of  $\text{Gd}_2\text{O}_3$  revealed a film morphology very similar to that of nickel substrates. Figure 6.16 shows a low magnification SEM of  $\text{Gd}_2\text{O}_3$  on roll-textured nickel. Grains which are approximately 25  $\mu\text{m}$  across and tightly packed together were observed. Higher magnification revealed a more dense and continuous film of  $\text{Gd}_2\text{O}_3$  as seen in Figure 6.17. Relatively few pin-holes or defects were observed even though the films were not produced in a dust-free environment.

The surface structure of the roll-textured nickel and the gadolinium oxide film were examined, and the average surface roughness was determined using atomic force microscopy (AFM). Figures 6.18 and 6.19 show AFM images of

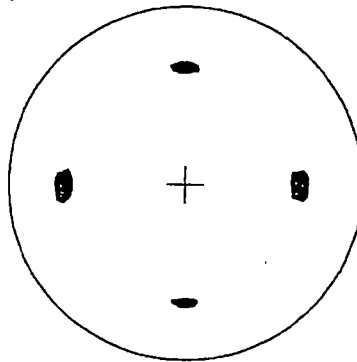




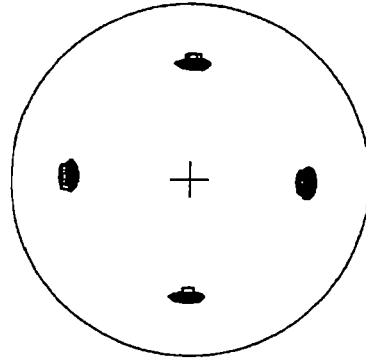
$Gd_2O_3$  (222)  
by isopropoxide route



$Gd_2O_3$  (222)  
by acetate route



$Yb_2O_3$  (222)  
by isopropoxide route



$Yb_2O_3$  (222)  
by acetate route

Figure 6.13.  $Gd_2O_3$  and  $Yb_2O_3$  pole figures about the (222) for two different solution routes.

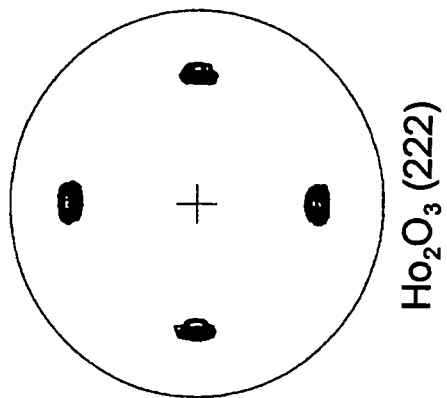
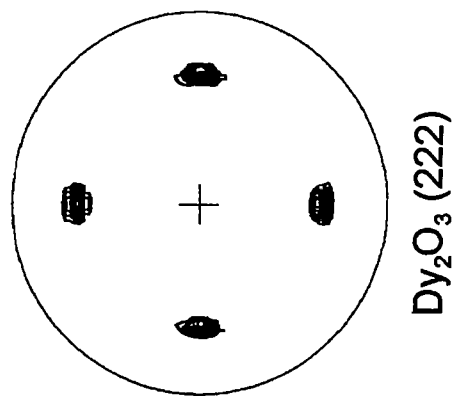
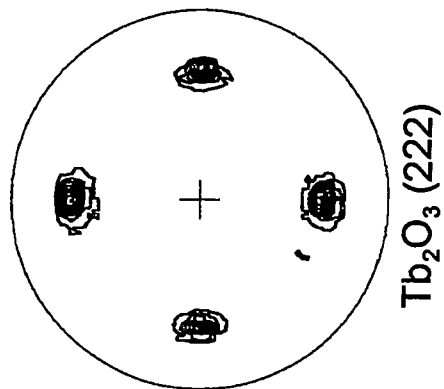
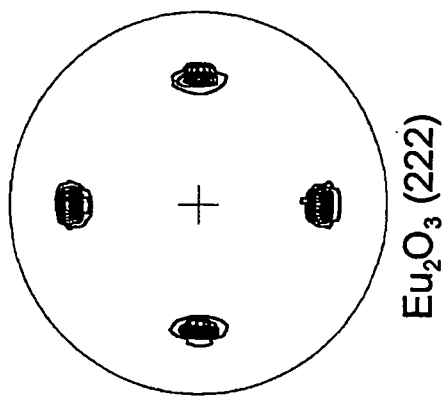
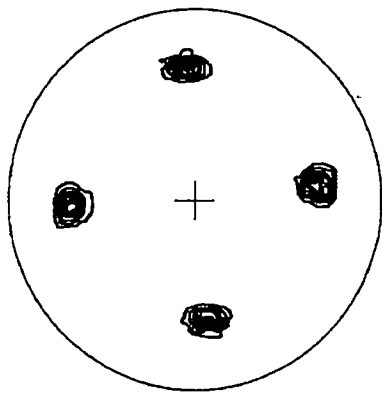
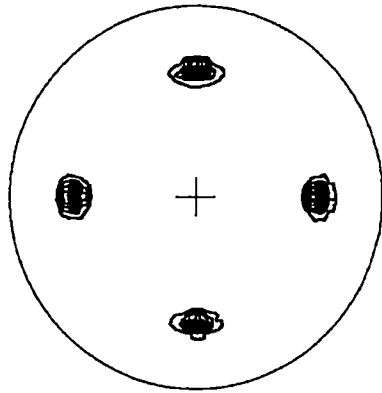


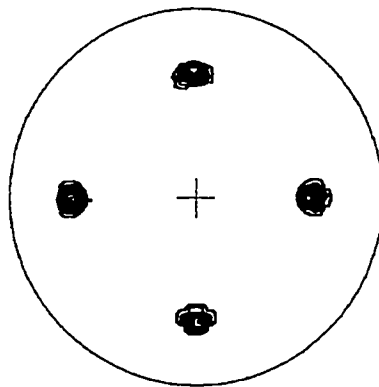
Figure 6.14. Eu<sub>2</sub>O<sub>3</sub>, Tb<sub>2</sub>O<sub>3</sub>, Dy<sub>2</sub>O<sub>3</sub>, and Ho<sub>2</sub>O<sub>3</sub> pole figures about the (222).



$\text{Er}_2\text{O}_3$  (222)



$\text{Tm}_2\text{O}_3$  (222)



$\text{CeO}_2$  (111)

Figure 6.15. Pole figures of  $\text{Er}_2\text{O}_3$  and  $\text{Tm}_2\text{O}_3$  on Ni about the (222), and  $\text{CeO}_2$  on Ni about the (111).

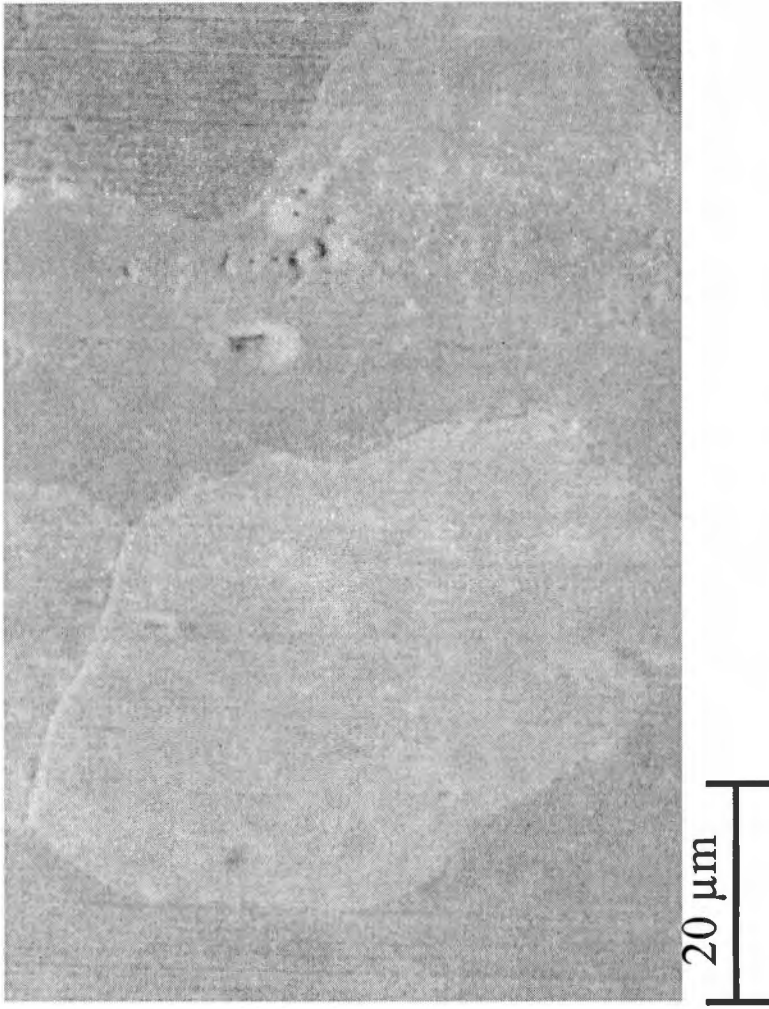


Figure 6.16. Low magnification SEM of Gd<sub>2</sub>O<sub>3</sub> on roll-textured nickel.

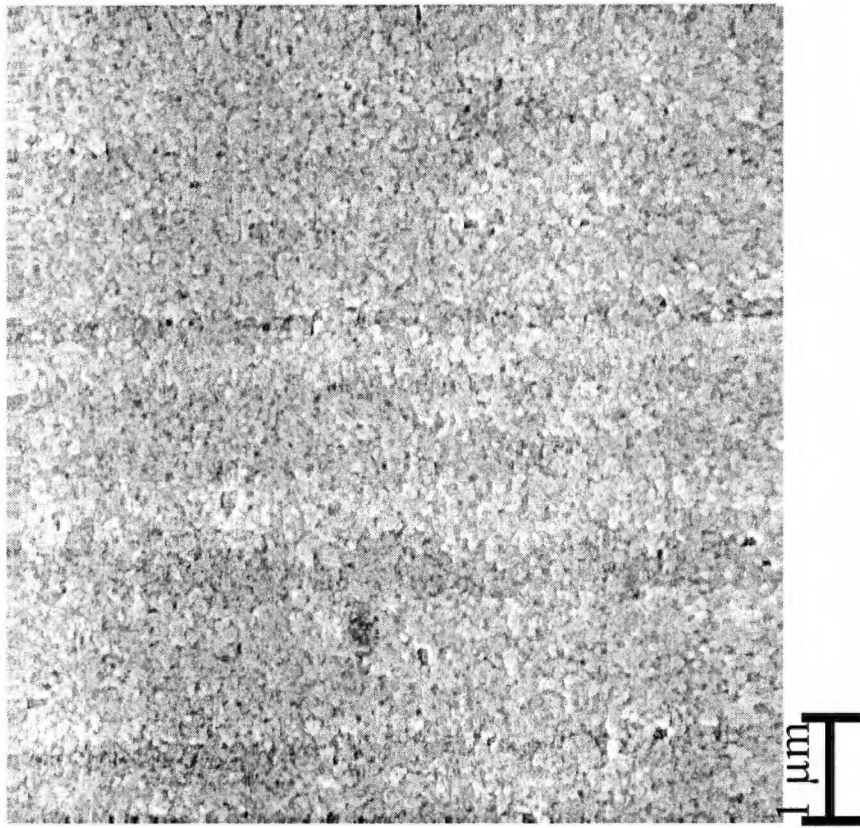


Figure 6.17. High magnification SEM of Gd<sub>2</sub>O<sub>3</sub> on roll-textured nickel.

Roll-textured Ni  
Ra : 47 Å

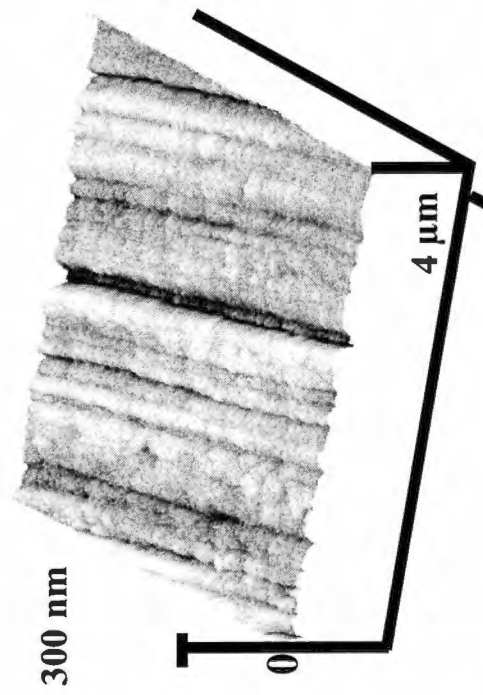


Figure 6.18. AFM of the surface of an annealed roll-textured nickel substrate.

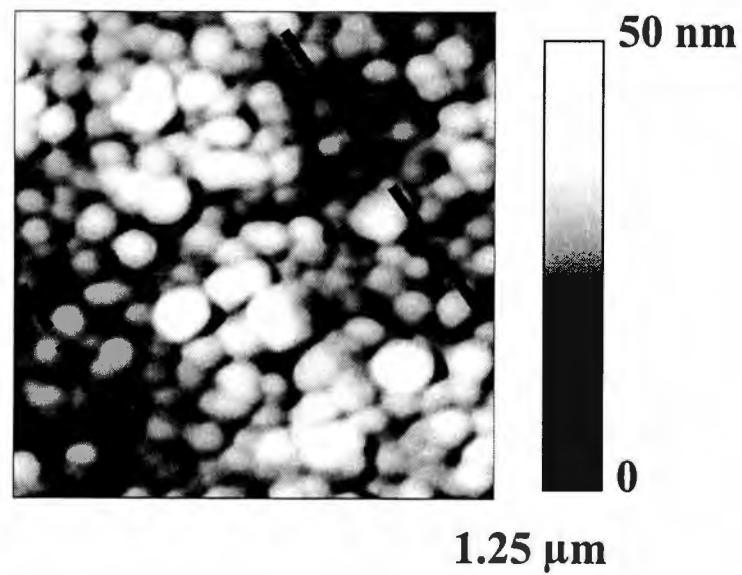
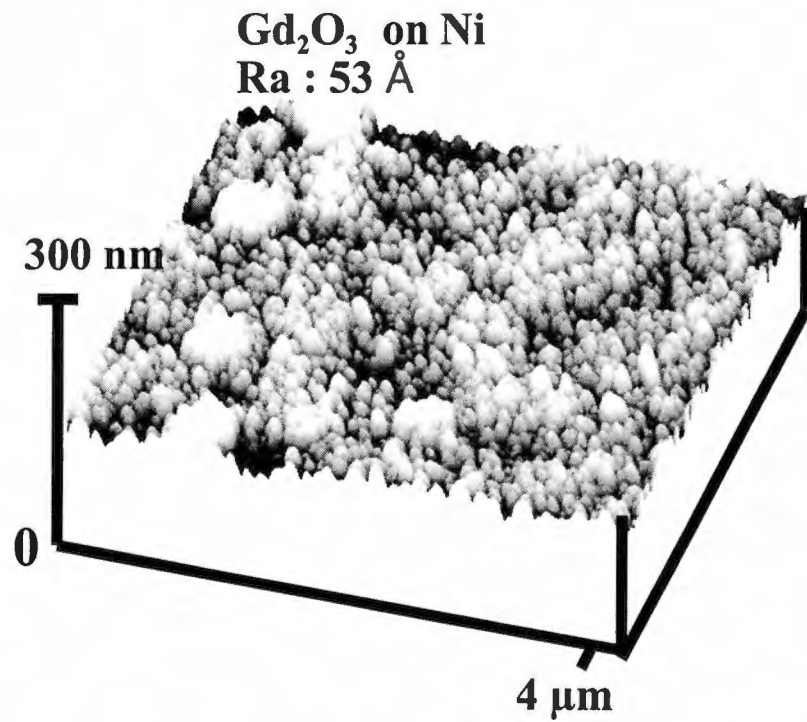


Figure 6.19. AFM of the surface of a 600 Å Gd<sub>2</sub>O<sub>3</sub> film deposited on roll-textured nickel.

nickel after heat treatment and after the application of the  $\text{Gd}_2\text{O}_3$  buffer layer. Heat treatment was used to develop the cubic texture of the nickel. It was observed that the average surface roughness increased from approximately 47 Å (after heat treatment) to approximately 53 Å after application of the buffer layer.

### **6.3.5. Analysis of $\text{YBa}_2\text{Cu}_3\text{O}_{7-\delta}$ Films on Solution Deposited Rare-Earth Oxide Buffer Layers on Roll-Textured Nickel**

Attempts to deposit  $\text{YBa}_2\text{Cu}_3\text{O}_{7-\delta}$  using e-beam evaporated Y,  $\text{BaF}_2$ , and Cu followed by ex-situ heat treatment in water/oxygen<sup>91</sup> directly on sol-gel  $\text{Gd}_2\text{O}_3$ ,  $\text{Yb}_2\text{O}_3$ , and  $\text{Eu}_2\text{O}_3$  buffered nickel were unsuccessful. The XRD of the films showed peak characteristics of nickel oxide, the  $T_c$  was approximately 80 K and the critical current ( $J_c$ ) was low. The low  $T_c$ ,  $J_c$ , and the nickel oxide in the films suggested that the films were not a good barrier layer to the diffusion of nickel from the substrate into the superconducting film. Some reasons for this may be porosity in the buffer layer or the reaction of the buffer layer with the YBCO layer.

Since the rare-earth oxide buffer layers are epitaxial, they can act as a template for further growth of epitaxial films or "cap layers." In a standard RABiTS process, a  $\text{CeO}_2$  (>500 Å) || yttrium stabilized zirconium (YSZ) oxide (1 μm) ||  $\text{CeO}_2$  layer (>500 Å) are deposited on the buffer layer by sputtering.



Since the rare-earth oxide buffer layers grow epitaxially on the nickel, the cerium oxide bottom layer on the nickel was replaced. Approximately 0.5  $\mu\text{m}$  of YSZ was sputtered on top of the rare-earth oxide buffer layer with a 500  $\text{\AA}$  cap layer of  $\text{CeO}_2$ . The YSZ layer acts as a good oxygen diffusion barrier, and the  $\text{CeO}_2$  layer reduces the lattice mismatch between the YSZ and the YBCO layer. The superconductor yttrium barium copper oxide ( $\text{YBa}_2\text{Cu}_3\text{O}_{7.5}$ ), or YBCO, was deposited on the  $\text{CeO}_2/\text{YSZ}/\text{rare-earth oxide}$  buffer layers by the barium fluoride precursor process. Figures 6.20 and 6.21 show  $\theta/2\theta$  diffractograms of the YBCO superconducting layer on  $\text{CeO}_2/\text{YSZ}/\text{Gd}_2\text{O}_3$  buffer layer and  $\text{CeO}_2/\text{YSZ}/\text{Eu}_2\text{O}_3$  buffer layer, respectively (both rare-earth oxide buffer layers were dip-coated). The  $\text{Eu}_2\text{O}_3$  buffer layer sample showed good out-of-plane epitaxy. However, some small NiO,  $\text{CeO}_2$ , and YSZ (111) reflections were observed. The  $\text{Gd}_2\text{O}_3$  buffer layer sample showed several high intensity peaks that were not epitaxial, but rather had random orientation [NiO (111),  $\text{CeO}_2$  (111) and YSZ (111)]. These (111) peaks grew because the  $\text{Gd}_2\text{O}_3$  buffer layer was made by the isopropoxide route, which has a small percentage of (222) (see Figure 6.4), and acted as a template for further growth of the buffer layers.

Critical current and critical temperature measurements were done on the YBCO/ $\text{CeO}_2/\text{YSZ}/\text{Gd}_2\text{O}_3$  or  $\text{Eu}_2\text{O}_3/\text{Ni}$  samples. Figure 6.22 shows a comparison plot of the critical current and critical temperature values obtained

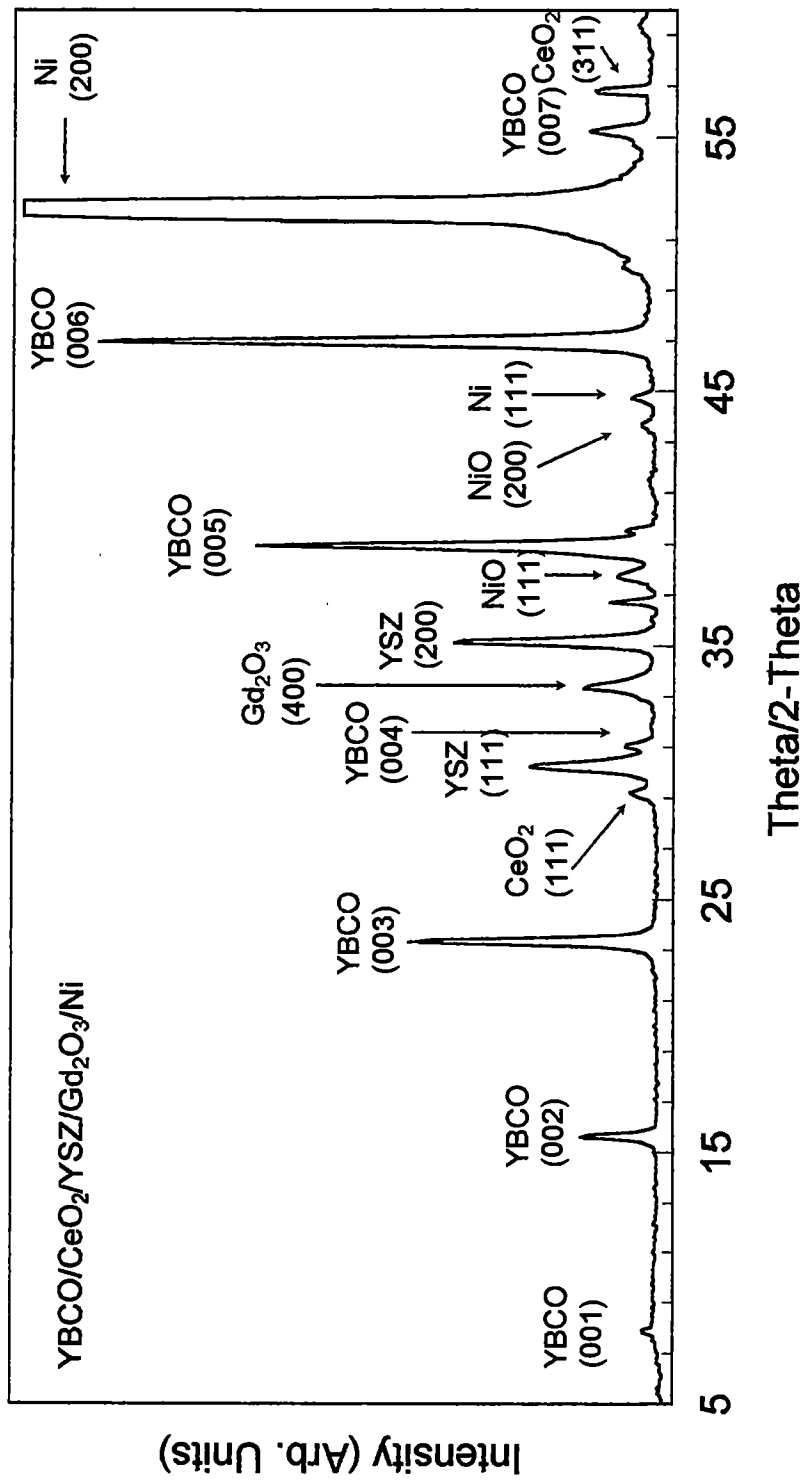


Figure 6.20. Theta/2-Theta XRD of YBCO/CeO<sub>2</sub>/YSZ/Gd<sub>2</sub>O<sub>3</sub> on Ni.

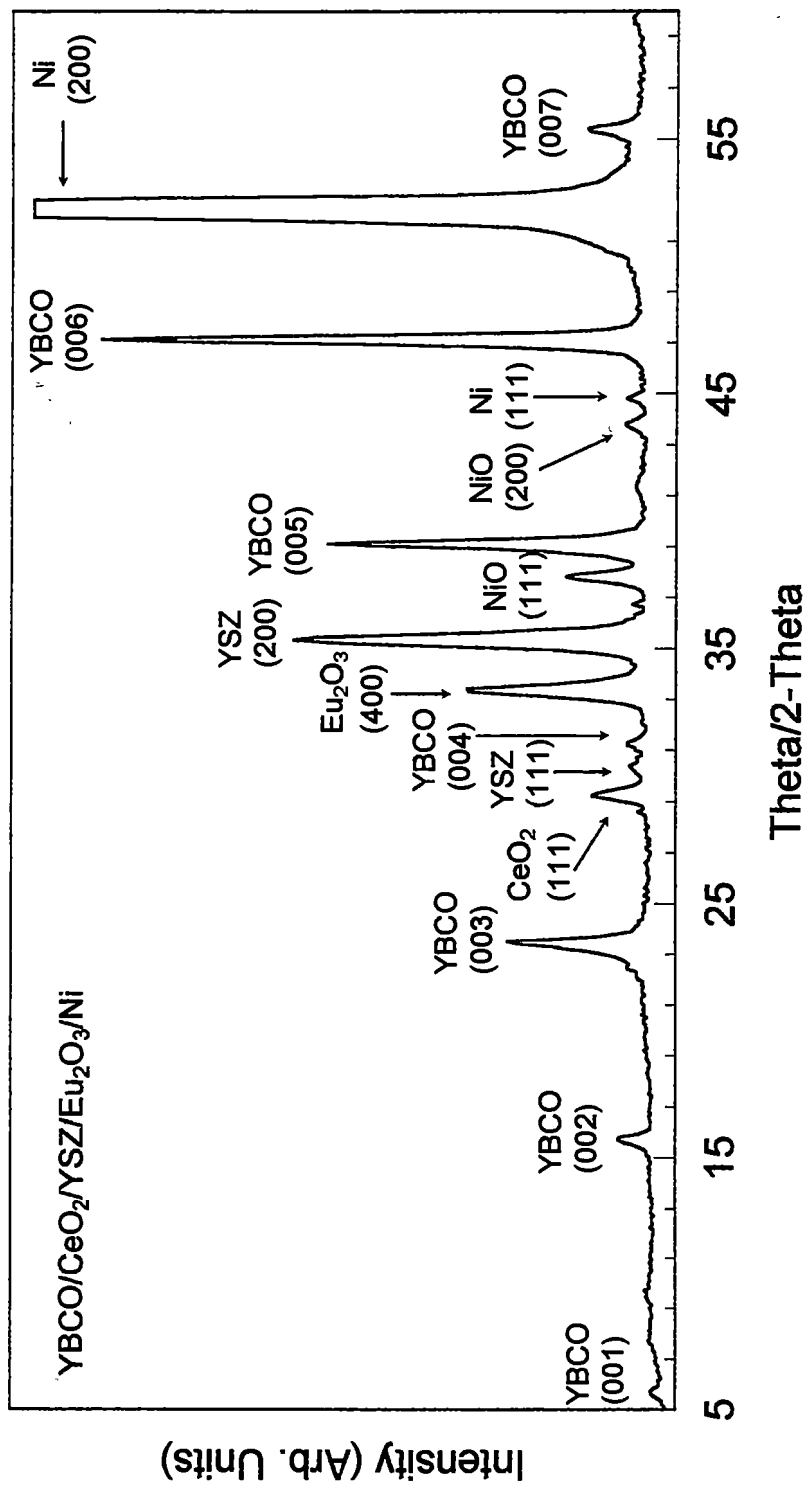


Figure 6.21. Theta/2-Theta XRD of YBCO/CeO<sub>2</sub>/YSZ/Eu<sub>2</sub>O<sub>3</sub> on Ni.

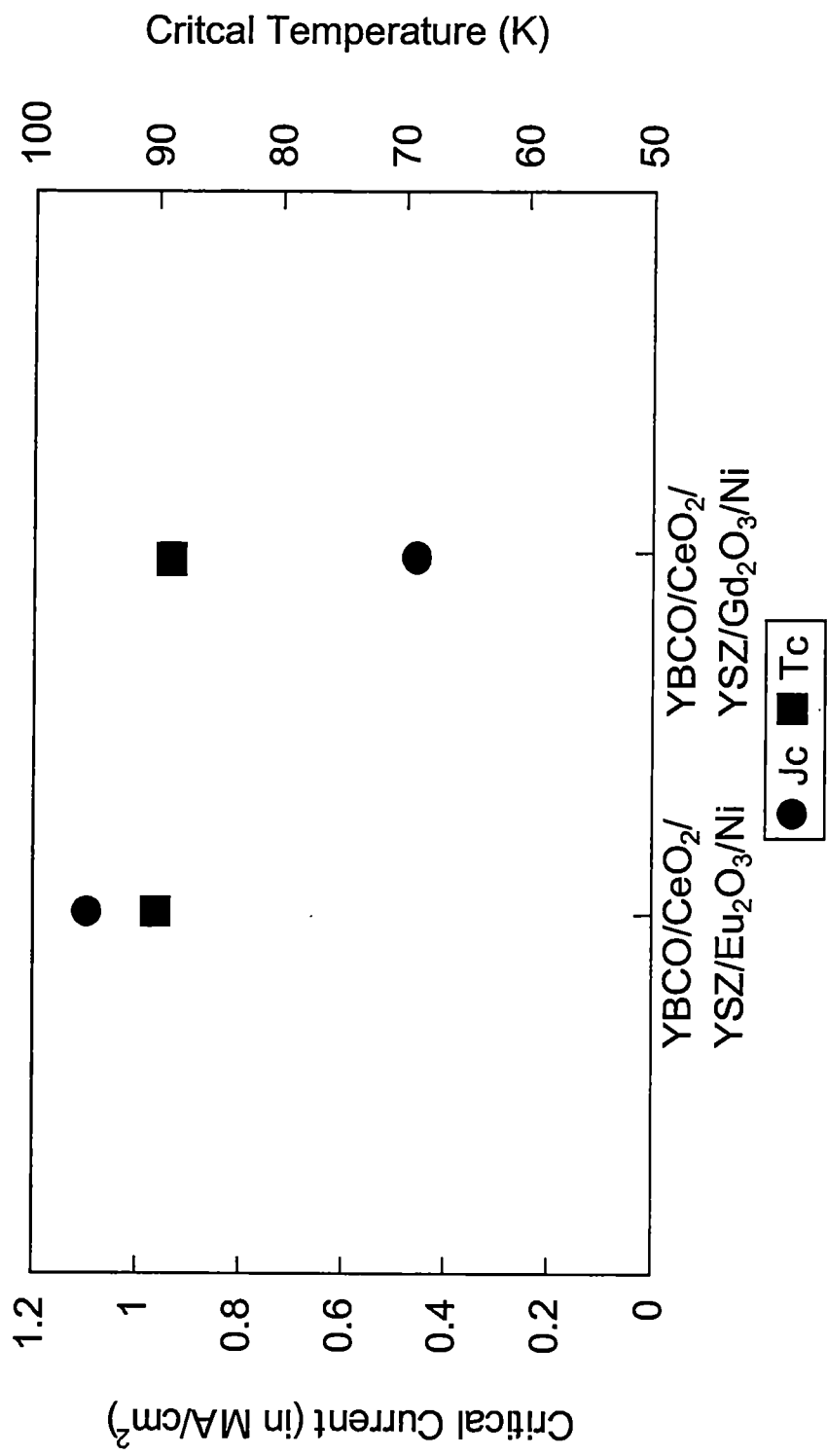


Figure 6.22. Critical current and critical temperature plots of YBCO/CeO<sub>2</sub>/YSZ/Eu<sub>2</sub>O<sub>3</sub>/Ni and YBCO/CeO<sub>2</sub>/YSZ/Gd<sub>2</sub>O<sub>3</sub>/Ni.

for YBCO superconducting layers on CeO<sub>2</sub>/YSZ/Gd<sub>2</sub>O<sub>3</sub> buffer layers and CeO<sub>2</sub>/YSZ/Eu<sub>2</sub>O<sub>3</sub> buffer layers, respectively. The YBCO superconductor with a Gd<sub>2</sub>O<sub>3</sub> buffer layer had a T<sub>c</sub> of 89 K and a J<sub>c</sub> of 0.4 MA/cm<sup>2</sup>. The YBCO superconductor with a Eu<sub>2</sub>O<sub>3</sub> buffer layer had a T<sub>c</sub> of 90 K and a J<sub>c</sub> of 1.1 MA/cm<sup>2</sup>. The YBCO film with a Eu<sub>2</sub>O<sub>3</sub> buffer layer had a significantly higher critical current than the Gd<sub>2</sub>O<sub>3</sub> buffer layer film because it was made with the acetate route rather than the isopropoxide route. This supported the results from the XRD spectra demonstrating that out-of-plane and in-plane grain alignments are essential for buffer layers in order to obtain high J<sub>c</sub> measurements in YBCO films.

#### **6.4. Conclusion**

The results of the process described in this chapter have verified that a solution technique can be used to obtain a single-epitaxy on a roll-textured substrate. Major incentives for this process include simplicity and the low-cost of a non-vacuum process. Substantial improvement to this process will be necessary in order to develop a long length superconductor with high critical current using only solution techniques.

## CHAPTER 7

### SUMMARY

An all-alkoxide solution chemistry utilizing methoxyethoxide-metal complexes in 2-methoxyethanol was developed to deposit epitaxial thin-films of metal oxides on single-crystal oxide substrates, (100) SrTiO<sub>3</sub> and (100) LaAlO<sub>3</sub>, polycrystalline silver substrates, and roll-textured nickel substrates. Speciation within these solutions was studied using Nuclear Magnetic Resonance (NMR), and Fourier Transform Infrared (FT-IR) spectroscopies. Film precursor gels were studied using FT-IR spectroscopy and thermal analysis. Approximate temperature ranges for film crystallization were determined from powders prepared from the film coating solutions. Film structure was determined using X-ray diffraction, and film morphology was studied using scanning electron microscopy (SEM), and atomic force microscopy (AFM).

A number of technologically interesting systems were prepared using this general technique. Bismuth-containing ferroelectric materials of the general formula (Sr or Ba)Bi<sub>2</sub>(Nb or Ta)<sub>2</sub>O<sub>9</sub> were synthesized.  $\{^1\text{H}\}^{13}\text{C}$  NMR was conducted on the metal alkoxides. Double alkoxides of the formula (Sr or Ba)(Nb or Ta)<sub>2</sub>(OCH<sub>2</sub>CH<sub>2</sub>OCH<sub>3</sub>)<sub>12</sub> were observed to form and were present in the bismuth containing coating solution. The formation of these double

alkoxides may be key to the superior annealing characteristics of this all-alkoxide sol-gel route in that the desired crystalline materials consists of layers of bismuth oxide between layers of alkali-earth/transition metal perovskites. Powders annealed in oxidizing conditions were fully crystalline at 850 °C. Films were deposited on polycrystalline silver, (100) strontium titanate, and (100) lanthanum aluminate single-crystal oxide substrates by spin-coating techniques. Both out-of-plane alignment (*c*-axis orientation) and in-plane alignment (*a* and *b*-axis orientation) for SrBi<sub>2</sub>Ta<sub>2</sub>O<sub>9</sub>, SrBi<sub>2</sub>Nb<sub>2</sub>O<sub>9</sub>, and BaBi<sub>2</sub>Nb<sub>2</sub>O<sub>9</sub> were achieved on the oxide substrates. [BaBi<sub>2</sub>Ta<sub>2</sub>O<sub>9</sub> was not epitaxial on (100) LaAlO<sub>3</sub> due to a large lattice constant mismatch.] Pole figures about the (105) reflection showed cube-on-cube epitaxy. An SBT film deposited on a silver substrate had a dielectric constant of 280.

Chapters 3 through 6 of this dissertation dealt with the solution synthesis of buffer layers for high temperature copper oxide-based superconductors (HTS). There are several requirements for buffer layers in order to achieve high critical currents in HTS materials. The buffer layers must be chemically compatible with the superconducting film and the substrate, have good mechanical properties, and, in the case of epitaxial films, have good lattice match to the superconducting layer.

Buffer layers consisting of rare-earth gallates and rare-earth aluminates have been shown to meet these requirements for HTS materials. The rare-

earth gallate and rare-earth aluminate materials are extremely difficult to deposit by pulsed laser ablation or sputtering techniques due to preferential ablation or sputtering. As an alternative to physical methods of deposition, rare earth gallates and rare-earth aluminates (where Ln = La, Pr, Nd, Gd, Y) were synthesized using solution deposition. The crystallization of powders under reducing and oxidizing conditions, deposition of polycrystalline films on silver substrates, and the deposition of epitaxial films on single crystal oxide substrates were studied. Both the rare-earth gallate powders (except  $\text{GdGaO}_3$  and  $\text{YGaO}_3$ ) and rare-earth aluminate powders (except  $\text{GdAlO}_3$  and  $\text{YAlO}_3$ ) showed single phase formations and were fully crystalline at 850 °C in oxidizing conditions. Films on (100)  $\text{SrTiO}_3$  and (100)  $\text{LaAlO}_3$  showed out-of-plane and in-plane alignment. Pole figures about the (220) reflection showed cube-on-cube epitaxy. It was also possible to engineer lattice mismatch through heteroepitaxial growth of multiple buffer layers of different rare-earth gallates and aluminates so as to minimize crystalline defects.

Long-length single-crystal oxide substrates cannot be manufactured inexpensively, and substrates which are chemically inert, flexible, mechanically robust, textured, and latticed-matched to the superconducting layer are highly desirable for practical, long-length superconductors. Metal substrates such as Ni are the most logical choice and satisfy the mechanical requirements, but a ceramic buffer layer is necessary to obtain a chemically inert substrate. Rare-



earth aluminate buffer layers were deposited on roll-textured nickel using spin-coating and dip-coating techniques. Only  $\text{LaAlO}_3$ ,  $\text{PrAlO}_3$ , and  $\text{NdAlO}_3$  showed c-axis orientation. However, pole figures and phi scans about the (110) reflection of  $\text{LaAlO}_3$ ,  $\text{PrAlO}_3$ , and  $\text{NdAlO}_3$  films showed an eight-fold symmetry. This indicated that two in-plane epitaxies were present, and therefore, rare-earth aluminate films on roll-textured nickel are unsuitable as buffer layers for superconductors.

Tetragonal perovskites are potentially an important class of substrates for the deposition of electronic ceramics such as the cuprate superconductors, because these oxides have low dielectric constants and good in-plane lattice match to the superconductors. It is relatively difficult to grow single crystals of these materials, and consequently they are four or five times more expensive than commercial wafers of  $\text{SrTiO}_3$  and  $\text{LaAlO}_3$  of the same size. However, heteroepitaxial growth of thin-films of the desired material on a commercially available substrate is an alternative to the expensive growth of single-crystal substrates. Tetragonal perovskites in the general form  $\text{ABCO}_4$  (where A = Sr; B = La or Pr; C = Al or Ga) were prepared using solution deposition techniques. Powders were annealed in oxidizing conditions to determine their crystallization temperatures, and then coated on polycrystalline silver substrates to understand their coating characteristics.  $\text{SrLaAlO}_4$ ,  $\text{SrPrAlO}_4$ ,  $\text{SrLaGaO}_4$ , and  $\text{SrPrGaO}_4$  thin-films were spin-coated on single crystal oxide substrates of

(100) SrTiO<sub>3</sub> and (100) LaAlO<sub>3</sub> at 850 °C. The tetragonal thin-films showed out-of-plane alignment (*c*-axis texture), and in-plane alignment, about the (105) reflection on the single crystal substrates. Pole figures about the (105) reflection showed cube-on-cube epitaxy.

Since none of the multi-cationic aluminate and gallate films had reproducibly shown a single in-plane alignment, it was necessary to explore other buffer layer materials. Chemical solution epitaxy was used to deposit films of rare-earth oxides (Ln = Ce, Sm, Eu, Gd, Tb, Dy, Ho, Er, Tm, Yb, and Lu) on roll-textured nickel. Rare-earth methoxyethoxide solutions were made by an isopropoxide route and an acetate route. Rare-earth oxide thin-films, produced by the isopropoxide route, showed mostly *c*-axis orientation, where as films produced by the acetate route showed 100% *c*-axis orientation. Solution studies using FT-IR showed that the methoxyethoxide ligand did not fully exchange with the acetate ligand. This solution mixture allows the films to crystallize at the interface of the substrate, and provides full *c*-axis texture. Pole figures about the (222) reflection showed a cube-on-cube texture and single in-plane alignment. SEM images showed pore free, dense and continuous rare-earth oxide thin-films on roll textured-nickel. Superconducting thin-films of yttrium barium copper oxide (YBCO) were grown on several of the solution deposited buffer layers. High critical currents (greater than

1.1 MA/cm<sup>2</sup>) and transition temperatures (around 91 K) were measured, thus demonstrating the viability of the solution deposition technique.

In conclusion, this dissertation has shown that bismuth-containing perovskites, rare-earth gallates and aluminates, tetragonal perovskites, and rare-earth oxide heteroepitaxial thin-films may be grown by solution techniques. General utility of the method has been demonstrated by approximately 25 different thin-films grown on three different types of substrates in oxidizing and reducing conditions. Major incentives for the solution deposition process include simplicity and the low-cost of a non-vacuum process.

## REFERENCES

1. *Wall Street Journal*, February 12, 1998.
2. Berberich, P.; Utz, B.; Prusseit, W.; Kinder, H. *Physica C* **1994**, *219*, 497.
3. Inam, A.; Hedge, M. S.; Wu, X. D.; Venkatesan, T.; Englan, P. *Appl. Phys. Lett.* **1998**, *53*, 908.
4. Eom, C. B.; Sun, J. Z.; Yamamoto, K.; Marshall, A. F.; Luther, K. E. *Appl. Phys. Lett.* **1989**, *55*, 595.
5. Eckstein, J. N.; Bozovic, I.; Schlom, D. G.; Harris, J. S., Jr. *Appl. Phys. Lett.* **1990**, *57*, 1049.
6. Norton, D. P. *Annu. Rev. Mater. Sci.* **1998**, *28*, 299.
7. Cheung, J. T.; Sankur, H. *CRC Crit. Rev. Solid State Mater. Sci.* **1988**, *15*, 63.
8. Peercy, P. S.; Bauer, E. G.; Dodson, B. W.; Ehrlich, D. J.; Feldman, L. C.; Flynn, C. P.; Geis, M. W.; Harbison, J. P.; Petroff, P. M.; Phillips, J. M.; Stringfellow, G. B.; Zangwill, A. *J. Mater. Res.* **1990**, *5*, 852.
9. Leskela, M.; Molsa, H.; Niinisto, L. *Supercond. Sci. Technol.* **1993**, *6*, 627.
10. Sato, K.; Togura, K. *Jap. J. Appl. Phys. Part B* **1991**, *30*, L1964.
11. Shibuta, N.; Katsui, A. *J. Cryst. Growth* **1990**, *101*, 91.
12. Royer, L. *Bull. Soc. Fr. Mineral. Crist.* **1928**, *51*, 7.
13. Dey, S. K.; Barlingay, C. K. *Appl. Phys. Lett.* **1992**, *61*, 1278.
14. Seifert, A.; Lange, F. F.; Speck, J. S. *J. Mater. Res.* **1995**, *10*, 680.
15. Ng, M. F.; Cima, M. J. *J. Mater. Res.* **1997**, *12*, 1306.
16. Thompson, C. V. *Annu. Rev. Mater. Sci.* **1990**, *20*, 245.

17. McIntyre, P. C.; Cima, M.C.; Ng, M. F. *J. Appl. Phys.* **1990**, *68*, 4183.
18. Braunstein, G.; Pax-Pujalt, G. R.; Mason, M. G. *J. Appl. Phys.* **1993**, *73*, 961.
19. Budd, K. D.; Dey, S. K.; Payne, D. A. *Brit. Ceram. Soc. Proc.* **1985**, *36*, 107.
20. Dey, S. K.; Budd, K. D.; Payne, D. A. *IEEE Trans. UFFC* **1988**, *35*, 80.
21. Coffman, P. K.; Dey, S. K. *J. Sol-Gel Sci. Technol.* **1994**, *1*, 251.
22. Schwartz, R. W.; Assink, R. A.; Headley, T. J. *Mater. Res. Soc. Symp. Proc.* **1992**, *243*, 245.
23. Yi, G.; Wu, Z.; Sayer, M. *J. Appl. Phys.* **1998**, *64*, 2717.
24. Takahashi, Y. *J. Mater. Sci.* **1990**, *25*, 3960.
25. Vest, R. W.; Xu, J. *IEEE Trans. UFFC* **1988**, *35*, 711.
26. Haertling, G. H. *Ferroelectrics* **1991**, *119*, 21.
27. Ito, Y. *Int. Ferro.* **1997**, *14*, 123.
28. Lange, F. *Science* **1996**, *273*, 903.
29. Francis, L. H., "Sol-gel Processing, Perovskite Phase Development and Properties of Relaxor-Based Thin Layer Ferroelectrics," Ph.D. Dissertation, University of Illinois at Urbana-Champaign, 1991, p. 36.
30. Livage, J.; Henry, M.; Sanchez, C. *Prog. Solid State Chem.* **1988**, *18*, 259.
31. Brinker, C. J.; Scherer, G. W. *Sol-Gel Science* Academic Press, New York, 1990.
32. Swartz, R. W. *Chem. Mater.* **1997**, *9*, 2325.

33. Bornside, D. E.; Macosko, C. W.; Scriven, L. E. *J. Appl. Phys.* **1989**, *66*, 5185.
34. Brinker, C. J.; Hurd, A. J.; Schunk, P. R.; Frye, G. C.; Ashley, C. S. *J. Non-Cryst. Solids* **1992**, *147*, 424.
35. Scriven, L. E. *Better Ceramics Through Chemistry III* C. J. Brinker: *Mater. Res. Soc. Symp. Proc.*, **1998**, *121*, 717.
36. Yoldas, B. E. *Appl. Opt.* **1980**, *19*, 2960.
37. Landau, L. D.; Levich, B. G. *Acta Physichim* **1942**, *17*, 42.
38. Cullity, B. D. "Elements of X-Ray Diffraction," 2nd edition, Addison-Wesley Publ. Co.: Reading, MA, 1978; Chapters 1 and 3.
39. Shoup, S. S.; Paranthaman, M.; Goyal, A.; Specht, E. D.; Lee, D. F.; Kroeger, D. M.; Beach, D. B. *J. Am. Ceram. Soc.* **1998**, *81*, 3019.
40. Giess, E. A.; Sandstrom, R. L.; Gallagher, W. J.; Gupta, A.; Shinde, S. L.; Cook, R. F.; Cooper, E. I.; O'Sullivan, E. J. M.; Roldan, J. M.; Segmuller, A. P.; Angilello, J. *IBM J. Res. Develop.* **1990**, *34*, 916.
41. Bondurant, D. W.; Gnadinger, F. P. *IEEE Spectrum* **1989**, *26*, 30.
42. Artl, G.; Robels, U. *Integ. Ferroelect.* **1993**, *3*, 247.
43. Paz de Aruajo, C. A.; Cuchiario, J. D.; McMillan, L. D.; Scott, M. C.; Scott, J. F. *Nature* **1995**, *374*, 627.
44. Artl, G.; Pertsev, N. A. *J. Appl. Phys.* **1991**, *70*, 2283.
45. Scott, J. F.; Araujo, C. A. *Science* **1989**, *246*, 1400.

46. Duiker, H. M.; Beale, P. D.; Scott, J. F.; Araujo, C. A.; Melnick, B. M.; Cuchiaro, J. D.; McMillan, L. D. *J. Appl. Phys.* **1990**, *68*, 5783.
47. Lohkamper, R.; Neumann, H.; Arlt, G. *J. Appl. Phys.* **1990**, *68*, 4220.
48. Bednorz, J. G.; Müller, K. A. *Z. Phys. B.* **1986**, *64*, 189.
49. Goyal, A.; Norton, D. P.; Christen, D. K.; Specht, E. D.; Paranthaman, M.; Kroeger, D. M.; Budai, J. D.; He, Q.; List, F. A.; Feenstra, R.; Kerchner, H. R.; Lee, D. F.; Hatfield, E.; Martin, P. M.; Mathis, J.; Park, C. *Appl. Supercond.* **1996**, *4*, 403.
50. Wu, X. D.; Foltyn, S. R.; Arendt, P. N.; Blumenthal, W. R.; Campbell, I. H.; Cotton, J. D.; Coulter, J. Y.; Hults, W. L.; Maley, M. P.; Safar, H. F.; Smith, J. L. *Apply. Phys. Lett.* **1995**, *67*, 2397.
51. Klemenz, C.; Scheel, H. J. *Physica C* **1996**, *265*, 126.
52. Testardi, L. R.; Moulton, W. G.; Mathais, H.; Ng, H. K.; Rey, C. M. *Phys. Rev. B* **1988**, *37*, 2324.
53. Iijima, Y.; Tanabe, N.; Kohno, O. *Proc. 4th Int. Symp. Supercond. (ISS)* Springer Verlag, **1992**, 679.
54. Norton, D. P.; Goyal, A.; Budai, J. D.; Christen, D. K.; Kroeger, D. M.; Specht, E. D.; He, Q.; Saffian, B.; Paranthaman, M.; Klabunde, C. E.; Lee, D. F.; Sales, B. C.; List, F. A. *Science* **1996**, *274*, 755.



55. Goyal, A.; Norton, D. P.; Budai, J. D.; Paranthaman, M.; Specht, E. D.; Kroeger, D. M.; Christen, D. K.; He, Q.; Saffian, B.; List, F. A.; Lee, D. F.; Martin, P. M.; Klabunde, C. E.; Hatfield, E.; Sikka, V. K. *Appl. Phys. Lett.* **1996**, *69*, 1795.
56. Aurivillius, B. *Arkiv. For Kemi.* **1949**, *1*, 463.
57. Rentschler, T. *Mater. Res. Bull.* **1997**, *32*, 351.
58. Shebanov, L. A.; Korzunova, L. V. *Mater. Res. Bull.* **1985**, *20*, 781.
59. Desu, S. B.; Vijay, D. P.; Zhang, X.; He, B. *Appl. Phys. Lett.* **1996**, *69*, 1719.
60. Song, T. K.; Lee, J. K.; Jung, H. J. *Appl. Phys. Lett.* **1996**, *69*, 3839.
61. Amanuma, K.; Hase, T.; Miyasaka, Y. *Appl. Phys. Lett.* **1995**, *66*, 221.
62. Boyle, T. J.; Buchheit, C. D.; Rodriguez, M. A.; Al-Shareet, H. N.; Hernandez, B. A.; Scott, B.; Ziller, J. W. *J. Mater. Res.* **1996**, *11*, 2274.
63. Zhu, Y.; Desu, S. B.; Li, T.; Ramanathan, S.; Nagata, M. *J. Mater. Res.* **1997**, *12*, 783.
64. Nagahama, T.; Manabe, T.; Yamaguchi, I.; Kumagai, T.; Tsuchiya, T.; Mizuta, S. *Thin Solid Films* **1999**, *353*, 52.
65. Nagahama, T.; Manabe, T.; Yamaguchi, I.; Kumagai, T.; Tsuchiya, T.; Mizuta, S. *J. Mater. Res.* **1999**, *14*, 3090.
66. Lange, F.; Kim, J. H.; Cheon, C. *J. Mater. Res.* **1999**, *14*, 1194.
67. Moon, S. E.; Song, T. K.; Back, S. B.; Kwun, S. I.; Yoon, J. G.; Lee, J. S. *Appl. Phys. Lett.* **1999**, *75*, 2827.

68. Ishikawa, K.; Funakubo, H. *Appl. Phys. Lett.* **1999**, *75*, 1970.
69. Massiani, M. C.; Papiernik, R.; Hubert-Plazgraf, L. G.; Daran, J. C. *Polyhedron* **1991**, *10*, 437.
70. Ramamurthi, S. D.; Payne, D. A. *Mat. Res. Soc. Symp. Proc.* **1990**, *180*, 79.
71. Rodriguez, M. A.; Boyle, T. J.; Hernandez, B. A.; Bucheit, C. D.; Eatough, M. O. *J. Mater. Res.* **1996**, *11*, 2282.
72. Gutleben, C. D.; Ikeda, Y.; Isobe, C.; Machida, A.; Ami, T.; Hironaka, K.; Morita, E. *Mat. Res. Symp. Proc.* **1996**, *415*, 201.
73. Han, B.; Neumeyer, D. A.; Schultz, D. L.; Marks, T. J.; Zhang, H.; Dravid, V. P. *Appl. Phys. Lett.* **1992**, *61*, 3047.
74. Han, B.; Neumeyer, D. A.; Marks, T. J.; Rudman, D. A.; Zhang, H.; Dravid, V. P. *Appl. Phys. Lett.* **1993**, *63*, 3639.
75. Mehrotra, R. C. *J. Chem. Soc. (A)* **1969**, 863.
76. Oliver, J. G.; Worrall, I. J. *Inorg. Nucl. Chem. Lett.* **1969**, *5*, 455.
77. Brown, L. M.; Mazdiyansi, K. S. *Inorg. Chem.* **1970**, *9*, 2783.
78. Kirchner, H. R.; Norton, D. P.; Goyal, A.; Budai, J. D.; Christen, D. K.; Kroeger, D. M.; Specht, E. D.; He, Q.; Paranthaman, M.; Lee, D. F.; Sales, B. C.; List, F. A.; Feenstra, R. *Appl. Phys. Lett.* **1997**, *71*, 2029.
79. Dimos, D.; Chaudhari, P.; Mannhart, J. *Phys. Rev. B* **1990**, *41*, 4038.

80. Paranthaman, M.; Goyal, A.; List, F. A.; Specht, E. D.; Lee, D. F.; Martin, P. M.; He, Q.; Christen, D. K.; Norton, D. P.; Budai, J. D.; Kroeger, D. M. *Physica C* **1997**, 275, 266.
81. Roth, R. S. *J. Res. Nat. Bur. Stand.* **1957**, 58, 75.
82. Pajaczkowska, A.; Gloubokov, A. *Prog. Cryst. Growth Charact. Mater.* **1998**, 36, 123.
83. Marks, T. J.; Belot, J. A.; Hinds, B. J.; Chen, J.; Strudebaker, D.; Lei, J.; Chang, R. P. H.; Schindler, J. L.; Kannewurf, C. R. *Mat. Res. Soc. Symp. Proc.* **1996**, 415, 67.
84. Belot, J. A.; Hinds, B. J.; Chen, J.; Wang, Y. Y.; Draid, V.; Marks, T. J. *Chem. Vap. Depos.* **1997**, 3, 78.
85. MacManus-Driscoll, J. L. *Annu. Rev. Mater. Sci.* **1998**, 28, 421.
86. Norton, D. P.; Park, C.; Prouteau, C.; Christen, D. K.; Chisholm, M. F.; Budai, J. D.; Pennycook, S. J.; Goyal, A.; Sun, E. Y.; Lee, D. F.; Kroeger, D. M.; Specht, E. D.; Paranthaman, M.; Browning, N. D. *Mater. Sci. Eng., B. Sol. State Mater. Adv. Tech.* **1998**, 56, 86.
87. Lee, D. F.; Paranthaman, M.; Mathis, J. E.; Goyal, A.; Kroeger, D. M.; Specht, E. D.; Williams, R. K.; List, F. A.; Martin, P. M.; Park, C.; Norton, D. P.; Christen, D. K. *Jpn. J. Appl. Phys. Part 2* **1999**, 38, L178.
88. Paranthaman, M.; Lee, D. F.; Goyal, A.; Specht, E. D.; Martin, P. M.; Cui, X.; Mathis, J. E.; Feenstra, R.; Christen, D. K.; Kroeger, D. M. *Supercond. Sci. Tech.* **1999**, 12, 319.

89. Feenstra, R.; Lindemer, T. B.; Budai, J. D.; Galloway, M. D. *J. Appl. Phys.* **1991**, *69*, 6569.
90. Swanson, H. E.; Morris, M. C.; Stinchfield, R. P.; Evans, E. H. *Natl. Bur. Std. (U.S.) Monogr.* **1962**, *25*, 56.
91. Paranthaman, M.; List, F. A.; Lee, D. F.; Goyal, A.; Feenstra, R.; Norton, D. P.; Park, C.; Verebelyi, D. T.; Christen, D., K.; Martin, P. M.; Specht, E. D.; Kroeger, D. M. *Science and Engineering of HTC Superconductivity* edited by Vincenzi, P. (Advances in Science and Technology 23, Techna Srl, **1999**), p. 185.

## VITA

Jonathan Sherman Morrell was born in Bristol, Tennessee, on November 3, 1973. He attended schools in the public school system of Sullivan County, Tennessee. In May 1992, he graduated from Sullivan East High School in Bluff City, Tennessee, and entered King College in Bristol, Tennessee. He conducted his undergraduate research on whether gene L5 or L17 causes temperature sensitivity and hypersensitivity in ribosomal proteins of *E. coli* cells, under the guidance of Dr. Scott Champney, Department of Biochemistry, Quillen College of Medicine, Johnson City, Tennessee. He received his dual Bachelor of Science degrees in Chemistry and Biology from King College in May 1996. He then entered the graduate program in the Department of Chemistry, The University of Tennessee, Knoxville, and received his Ph.D. degree in May 2000.